Atomistic Simulation Studies of Nano-Structural Titanium Dioxide and its Lithiation

by

Malili Gideon Matshaba

Thesis submitted in fulfilment of the requirements for the degree of

Doctor of Philosophy (PhD)

in

Physics

in the

FACULTY OF SCIENCE AND AGRICULTURE

(School of Physical and Mineral Sciences)

at the

UNIVERSITY OF LIMPOPO

Supervisor: Prof. P. E. Ngoepe

Co-Supervisor: Dr. D. C. Sayle

2013

DECLARATION

I declare that the thesis hereby submitted to the University of Limpopo, for the degree of Doctor of Philosophy in Physics has not previously been submitted by me for a degree at this or any other University; that it is my work in design and in execution, and that all material contained herein has been duly acknowledged.

---------- ----------

Matshaba, M. G. (Dr) Date

Dedication

To my wife Kobe Grace,

my two sons Motlatšo and Nkgaru,

lastly to my late brother Letladi Richard and

to my late father Motlatšo George.

Acknowledgements

Firstly, I would like to express my gratitude to my supervisor Professor P.E. Ngoepe for being helpful throughout the research. I appreciate his guidance in the planning and execution of the research project, especially crystallisation of nanostructures, including the time spent discussing the draft of the thesis. I really appreciate time we spent on this work especially after working hours, weekends and holidays. It was a heavy work but he made it easy for me to get all the resources that helped me to finish this work. My co-supervisor Dr D. C. Sayle from Crainfield United Kingdom (UK) helped me to understand the importance of my research in the industry level. He introduced me to some intriguing aspects of amorphisation and recrystallisation. I really appreciate your help and for the time you took to help me on my work. Dr T.X.T. Sayle also from Crainfield UK played a key role in mentoring me on the process of applying the amorphisation and recrystallisation technique starting with MgO. Thanks to Professor C. R. A. Catlow for inviting me to do some of this work in the UK. He gave me a good working space at the University College London. Alastair Smith helped me with the systems and to find accommodation during my stay in London.

I am deeply indebted to my colleagues at Material Modelling Centre (MMC), where all my calculations in this thesis were done. Your discussions have helped me a lot to achieve this degree. Thanks to Mr K. M. Kgatwane for introducing me to the programme of lithiation, it really helped me especially in chapter four. I also thank Professor R. R. Maphanga for helpful discussions.

Thanks to the University of Limpopo community for giving me a wonderful environment throughout my research study. My stay at postgraduate student's village

throughout my study was wonderful. I was able to study at any time without any disturbances. All the trips that I have travelled throughout my study locally and internationally have helped me a lot in contribution to my research work. University of Limpopo have arranged them well including accommodations.

The Centre for High Performance Computing (CHPC) in Cape Town, I would like to say thank you for allowing me to use your systems throughout my research. All calculations of this work were done using their cluster systems. I really appreciate their help especially during the times where I have to visit Cape Town to collect data.

I would like to acknowledge financial assistance from the National Research Foundation (NRF), The Royal Society (London) and Department of Science and Technology-Hydrogen South Africa (DST – HySA) Lithium Ion Batteries and Supercapacitor Programme.

Most of all, I thank the Mighty Creator for giving me strength and good life throughout my study. Finally, I would like to thank my family for being with me throughout my study. Your presence and support helped me a lot to achieve this degree.

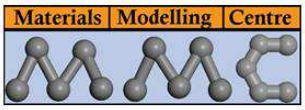

Abstract

Titanium dioxide (TiO_2) nanoparticles, nanowires, nanosheets and nanoporous are of great interest in many applications. This is due to inexpensive, safety and rate capability of the material. It has being considered as a replacement of graphite anode material in rechargeable lithium batteries. Much experimental work on pure and lithiated nanostructures of TiO_2 has been reported, mostly with regards to their complex microstructures. In this work we employ molecular dynamics (MD) simulation to generate models of TiO_2 nano-architectures including: nanosheet, nanoporous, nanosphere and bulk. We have successfully recrystallised all four nanostructures from amorphous precursors; calculated radial distribution functions (RDFs), were used to confirm crystallinity. Configuration energies, calculated as a function of time, were used to monitor the recrystallisation. Calculated X-Ray Diffraction (XRD) spectra, using the model nanostructures, reveal that the nanostructures are polymorphic with TiO_2 domains of both rutile and brookite in accord with experiment.

Amorphisation and recrystallisation was successful in generating complex microstructures. In particular, bulk and nanoporous structures show zigzag tunnels (indicative of micro-twinning) while nanosphere and nanosheet shows zigzag and straight tunnels in accord with experiment. All model nanostructures of TiO_2 were lithiated with different lithium content. RDFs, microstructures, configuration energies, calculated as a function of time and XRDs of all lithiated structures are presented.

Contents

List of figures

List of Tables

Chapter 1
INTRODUCTION

1.1 General introduction

Titanium dioxide is an oxide that is chemically stable, inexpensive, nontoxic and photocatalytic (Liang et al. 2001). It is a wide-bandgap semiconductor with high refractive indices. Most studies on TiO_2 have been on well-known novel applications (Chen et al. 2007). Owing to their unique properties, nanomaterials of TiO_2 are used in a wide range of applications such as dye-sensitized solar cells (Hagfeldt et al. 1995, Hoffmann M. R. 1995, Linsebigler et al. 1995 and Chen et al. 2007), nanostructured solar cells (Henrich et al. 1993, Fujishima et al. 1972 and Haller et al. 1989), ceramics, pigments and optoelectronics (Fujishima et al. 1972, Ollis et al. 1989, Sorantin et al. 1992 and Tang et al. 1994). Previously, extensive work was conducted on TiO_2 as used in solar cells (Park et al. 2000), and in particular dye-sensitized solar cells involving nanoporous TiO_2 thin films (Okuya et al. 2002). Rechargeable lithium-ion batteries are important in power portable electronic devices (PED) such as laptops, mobile phones, and computers and recently for electric vehicles. Their electrochemical properties (Fukushima et al. 1989) and electrodes (Kavan et al. 1996) have been studied. Novels ways of enhancing energy and power densities, long cycle life and safety of lithium ion batteries are needed. TiO_2 has been chosen for this application since it serves as an excellent lithium battery electrode, has large lithium intercalation capacity, low toxicity and is inexpensive. In particular, nanostructures of TiO_2 have high rate performance, are good for lithium insertion and mostly have fast charge and discharge capacity. In this chapter structural properties of TiO_2 and literature review on how its various nanostructures are used in

lithium ion batteries will be presented. This will be followed by the intentions of the study and the thesis outline.

1.2 Structural properties

TiO_2 consists of mainly three distinct polymorphs rutile, anatase and brookite (which are presented in figure1.1 and their physical properties are presented in table1. Anatase and rutile (Vegard et al. 1916) in general are two stable crystalline structures. Besides these three polymorphs, TiO_2 has more modifications which are not that much common: TiO_2 (B) monoclinic (Marchand et al. 1980), TiO_2 (H) hollandite (Latroche et al. 1989), TiO_2(R) ramsdellite (Akimoto et al. 1994), TiO_2 (II)-(α) columbite (Simons et al. 1967), TiO_2 (III) baddeleyite (Tang et al. 1993 and Olsen et al. 1999) and TiO_2 with α-PbO_2 structure (Zaslavskii et al. 1952). Many of these structures occur under very particular conditions.

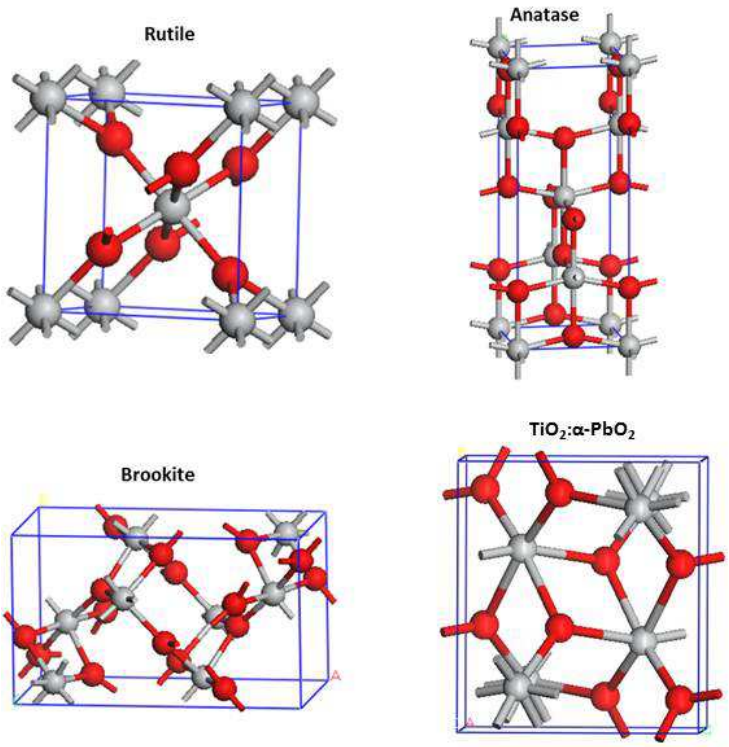

Figure 1.1: Four distinct polymorphs of TiO_2.

Most electronic and optical properties (Tang et al. 1994a, Tang et al. 1994b, Sanjines et al. 1994, Tang et al. 1995, Hosaka et al. 1997, Sekiya et al. 1998 and Sekiya et al. 200) of anatase single crystals (Berger et al. 1993) have been systematically investigated. Anatase is metastable at room temperature and transforms irreversibly to rutile, while rutile is the most stable phase (Haines et al. 1993) of TiO_2. X-ray diffraction of polymorphs of TiO_2 and TiO_2: α-PbO_2 are shown in figure 1.2 (Djerdj et al. 2006).

Table 1.1: Physical properties of three polymorphs of TiO_2 and TiO_2: α-PbO_2.

	Rutile	Anatase	Brookite	TiO_2: α-PbO_2
Form. Wt.	79.890	79.890	79.890	
Z	2	4	8	4
Crystal System	Tetragonal	Tetragonal	Orthorombic	Orthorombic
Space group	$P4_2/mnm$	$I4_1/amd$	Pbca	Pbcn
a (Å)	4.5845	3.7842	9.184	4.5292
b (Å)	4.5845	3.7842	5.447	5.5022
c (Å)	2.9533	9.5146	5.145	4.9034
Volume ($Å^3$)	62.07	136.25	257.38	122.20
Density (g/cm^3)	4.2743	3.895	4.123	

Also XRDs patterns of TiO_2 nanoparticles prepared by hydrothermal treatment for anatase, rutile and brookite are depicted in figure 1.3 (Reyes-Coronado et al 2008). XRD studies of the products obtained from hydrothermal treatment of the amorphous starting material under a variety of experimental conditions showed that phase-pure anatase, rutile and brookite can be obtained under the following conditions: anatase was prepared using 1, 5 M acetic acid at 200 °C, rutile was obtained using 4 M HCL at 200 °C and brookite was obtained with 3 M HCL at 175 °C. Under these conditions the phase purity was over 95 % as determined from the integrated intensity of the XRD peaks for the phases (Zhang et al 2000). These XRDs will help us to assign the peaks of our simulated XRDs in chapter three and four in order to find the corresponding model.

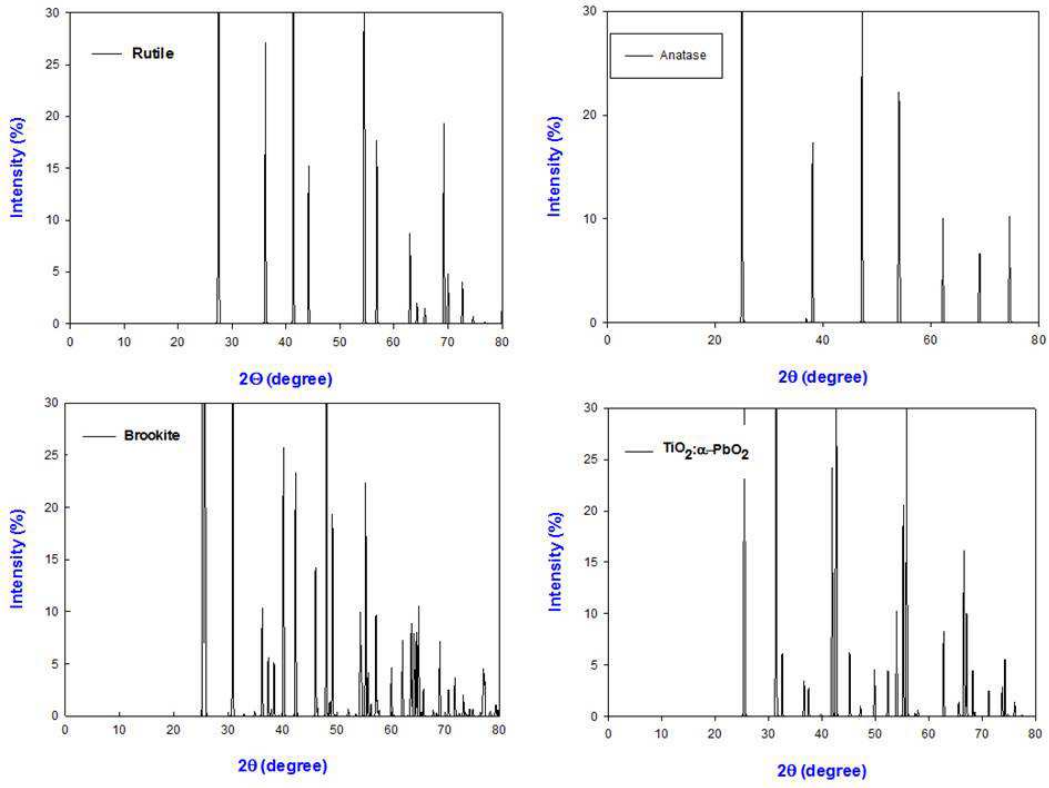

Figure 1.2: XRDs of TiO_2 polymorphs and TiO_2: α-PbO_2.

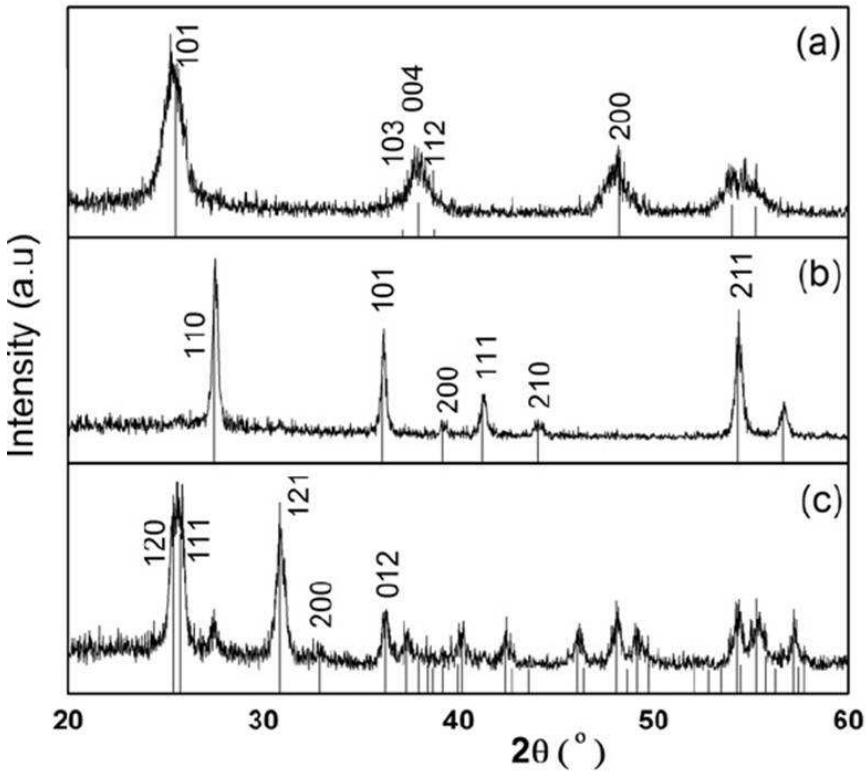

Figure 1.3: XRD patterns of TiO_2 nanoparticles (a) anatase, (b) rutile and (c) brookite (Reyes-Coronado et al 2008)

Comparison of XRD patterns of TiO_2 brookite and TiO_2: α-PbO_2 structure show close resemblance but with minor differences. Sayle and Sayle (2007) reported that the TiO_2: α-PbO_2 structure was closest to their simulated TiO_2 nanosphere than the anatase and rutile structures. Slight deviations from simulated could be ascribed to nanospherical form; hence flexibility of TiO_2: α-PbO_2 should be closer to that of brookite. In the orientations displayed in figure 1.4, the middle portion in the dashed rectangle of TiO_2 brookite, with space group Pbca, has a similar arrangement of atoms as the TiO_2 with the α-PbO_2 structure and space group Pbcn, and differs mainly in the displacement of the oxygen's.

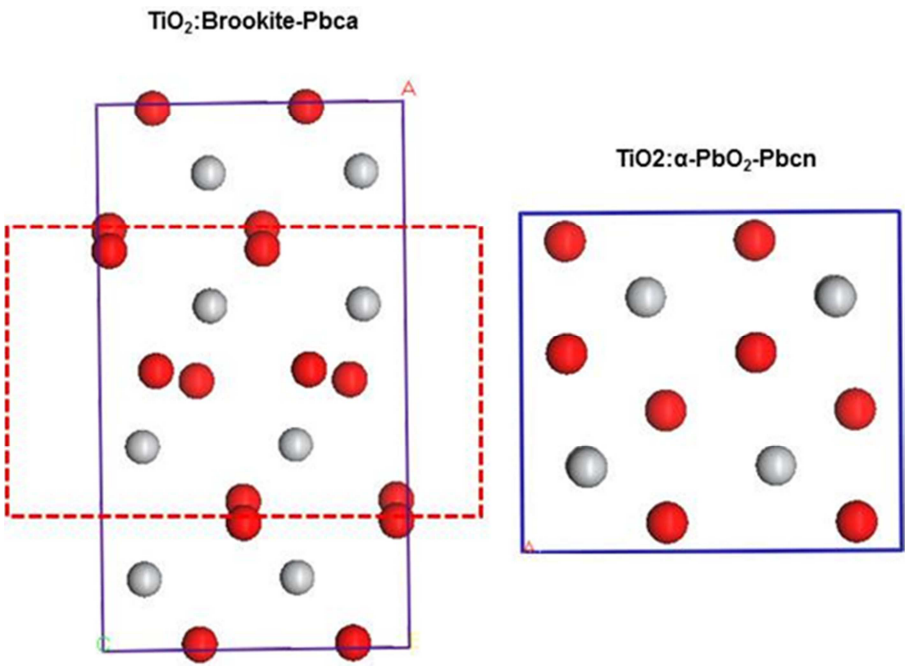

Figure 1.4: Orientations of TiO_2: brookite -Pbca and TiO_2: α - PbO_2 - Pbcn.

1.3 Literature review

1.3.1 Applications

TiO_2 is one of the most extensively studied metal oxide and has been widely used in photocatalysis, photosplitting of water, photochromic devices, gas sensing, dye-sensitized

solar cells (DSSCs) (energy conversion) and rechargeable lithium ion batteries (LIB) (electrochemical storage) (Fujishima et al. 1972, O'Regan et al. 1991, Chen et al. 2007, Liu et al. 2010a, Liu et al. 2011 and Liu et al. 2009). Over the last two decades, the increasing demand of energy and shifting to the renewable energy resources, has rendered LIBs to be considered as promising alternative and green technology for energy storage applied in hybrid electric vehicles (HEVs), plug-in hybrid electric vehicles (PHEVs), and other electric utilities. TiO_2 is being considered as one of the most attractive anode materials of LIBs owing to the following distinct characteristics: (i) its potential vs. Li ^{o} (~1.5-1.7 V) prevents the plating of metallic lithium at the negative electrode, thus enhancing the safety and extending the life of the cell, (ii) it exhibits relatively high practical capacity (~200 mAh/g), certainly smaller than graphite, but greater than its lithiated form $Li_4Ti_5O_{12}$, and (iii) it is environmentally benign, abundant, inexpensive and has stable structure. Its most significant advantage, however, is the ability to be charged and discharged at a high current rate (high power). The above-mentioned points are of great importance since large-scale batteries for hybrid electric vehicles and other applications require prolonged life, improved safety, and reduced cost. In general, the properties of TiO_2 greatly depend on the crystal sizes, phases, exposed facets, and morphologies (Chen et al. 2007, Liu et al. 2010b and Liu et al. 2011).

1.3.2 TiO_2 Bulk Polymorphs

As it has been demonstrated in section 1.2, TiO_2 has different polymorphs, and the eight that are well known are anatase, rutile, brookite, TiO_2-B, TiO_2-H, TiO_2-II and TiO_2-III (Deng el al. 2008). Regardless of various polymorphs of TiO_2, the insertion reaction of Li-ion into TiO_2 can be expressed as (van de Krol et al. 1999)

$$TiO_2 + xLi^+ + xe^- \rightarrow Li_xTiO_2$$

With the insertion of positive Li the overall charge compensation is achieved by the introduction/presence of Ti^{III} cations in the Ti^{IV} sublattice, which usually results in a sequential phase transformation occurring in original TiO_2 as a function of Li^+ content. This has been predicted by theoretical calculations (Olson et al. 2006, Stashans et al. 1996, Mackrodt et al. 1999, Koudriachova et al. 2002, Muscat et al. 2002, Koudriachova et al 2004a and Koudriachova et al. 2004b) and was observed in X-ray photoelectron spectroscopy (XPS) experiments (Soedergren et al. 1997 and Henningsson et al. 2003). Anatase is considered the most suitable candidate for Li-insertion host, while Li insertion into the bulk rutile is usually negligible at room temperature (Kavan et al. 1996, Kavan et al. 1999, Ohzuku et al. 1979 and Zachau-Christiansen et al. 1988). For instance, while the particle sizes are in the micrometers range, only 0.1-0.25 mol Li per mol TiO_2 can be inserted into bulk rutile at room temperature (Hu et al. 2006).

In order to understand the extent to which different TiO_2 polymorphs can accommodate lithium insertion, it is necessary to consider their structural features more closely (Yang et al. 2009, van de Krol et al. 1999 and Payne et al. 1992), and those of anatase and rutile will be discussed in particular. The structure of anatase TiO_2 can be regarded as a stacking of one dimensional zigzag chains consisting of distorted edge-sharing TiO_6 octahedrals. Along [100] and [010] directions, this stacking is equivalent and composed of empty zigzag channels in the whole framework, which provides paths for Li-ion insertion occupying the interstices of TiO_6 octahedrals to form Li_xTiO_2 (Kavan et al. 1996, Zachau-Christiansen et al. 1988 and Cava et al. 1984). Since the Li–Li are interacting strongly (Zachau-Christiansen et al. 1988), the originally tetragonal anatase phase (space group I41/amd) undergoes a phase transition with an orthorhombic distortion (Cava et al. 1984) as the ratio of Li-ion insertion is larger than 0.05 (Zachau-Christiansen et al. 1988). The change of symmetry involves a decrease of the unit cell

along the c axis and an increase along the b axis (Ohzuku et al. 1979). The overall distortion of the atom positions accompanying the phase transition is relatively small, which leads to the volume change of unit cell less than 4% (Deng et al 2009).

In the lattice framework of an ideal rutile crystal, TiO_6 octahedra share edges in the c-direction, and corners in the ab-plane (Koudriachova et al. 2003). Therefore, Li^+ diffusion in rutile is highly anisotropic and fast along the c-direction (diffusion coefficient is about 10^{-6} cm^2s^{-1}), while in the ab planes it is very slow (diffusion coefficient is approximately 10-14 cm2s-1 (Koudriachova et al. 2004a, Gligor et al. 2006 and Johnson et al. 1964). The anisotropic diffusion of Li ions in rutile limits the amount of Li ions distributed along ab-planes and separates Li^+ in the c channels (Stashans et al. 1996, Koudriachova et al. 2002 and Koudriachova et al. 2003). Even along the c-direction, further Li-ion insertion would be blocked owing to the repulsive forces between Li ions in c-direction and trapped Li-ion pairs in the ab-planes (Koudriachova et al. 2001). Consequently, Li-ion insertion into the bulk rutile TiO_2 is very difficult and only a negligible number of Li ions have been reported to be accommodated in this polymorph except those operated at high temperature up to 120 °C (Macklin et al. 1992).

The idealized TiO_2-B has the same structure as a shear derivative of the ReO_3-type structure, which is composed of corrugated sheets of edge- and corner-sharing TiO_6 octahedrals (Feist et al. 1992, Marchand et al. 1980 and Zukalova et al. 2005). In this special framework, TiO_2-B possesses a one-dimensional infinite channel, which indicates that the structure of TiO_2-B is more open than other polymorphs (Yang et al. 2009). Furthermore, the existence of parallel infinite channels in TiO_2-B lattice can also accommodate volume change without any significant distortion of the structure during Li^+ insertion (Pyne et al. 1992). In addition, Zukalova et al. (2005) proposed that, the diffusion of Li^+ in TiO_2-B is a pseudocapacitive faradic process, which is a faster process

compared with the solid-state diffusion process, which controls the Li^+ diffusion in anatase (Zukalova et al. 2005) All such properties suggest that TiO_2-B is an outstanding candidate as anode materials of LIBs.

As mentioned in section 1.2, TiO_2 brookite is naturally occurring and has an orthorhombic structure with symmetry Pbca and consists of edge- and corner-sharing TiO_6 octahedra, which form channels along the c axis (Bauer 1961). The dimensions of the channels are suitable to accommodate lithium ions (~0.76 Å). Reports on direct insertion of Li in the bulk TiO_2 brookite are currently scarce. However, DFT and atomistic simulations indicated that among the naturally occurring bulk polymorphs of TiO_2 (Kerisit et al. 2010) anatase, brookite, and ramsdellite are energetically favoured over rutile upon lithium insertion. As a confirmation to previous structural discussions (Reddy et al. 2008) the calculations indicates that the main factors controlling the relative stability of the lithiated titania polymorphs are the lithium bonding environment, the arrangement of LiO_x and TiO_6 polyhedra, and the extent of lattice deformation upon lithiation.

1.3.3 Nanosizing

Irrespective of various polymorphs, the practical attainable capacities of bulk TiO_2 are reported as only half of the theoretical value (330 mAh g^{-1}), based on the full electrochemical activation of the Ti^{4+}/Ti^{3+} redox couple and still needs to be sustained over long-term cycling. The main reason is that the further Li-ion insertion in TiO_2 is blocked because of the strong repulsive force between Li ions as the insertion ratio is greater than 0.5 (as $x>0.5$ in Li_xTiO_2) (Nuspl et al. 1997, Kavan et al. 2000 and Kavan et al. 1995), hence leading to low diffusion coefficient of Li in TiO_2 which greatly limits the applications and development of TiO_2 as electrode materials in LIBs. Consequently, intensive experiments and limited theoretical simulations have been conducted which

demonstrated that the lithium-insertion/deinsertion activity and cycling stability of titania-based electrode can be improved dramatically as the scale of employed materials moves into the region of nanometers (Yang et al. 2009, Kavan et al. 2000, Tang et al. 2009, Sudant et al. 2005, Jiang et al. 2007, Fattakhova-Rohlfing et al. 2007 and Kubiak et al. 2008). The main factors behind such improvement can be due to: (i) an increased electrode/electrolyte contact area, which allows higher cycling rates, and (ii) a decrease in the mean diffusion lengths for both electrons and lithium cations, allowing the use of "low" electronic and/or ionic conducting materials. We will now review certain nano-architectures, (viz. nanoparticles, nanorods, nanotubes, nanoporous, nanosheets) that have been adopted by different polymorphs of TiO_2 and explore the extent to which lithium can be inserted in them and the related electrochemical performance. There is a great deal of interest in TiO_2 nanoparticles, nanowires and nanotubes due to their potential advantages (safety, rate) as anodes replacing graphite in a new generation of rechargeable lithium batteries (Sudant et al. 2005, Jiang et al. 2007, Wagemaker et al. 2007, Hardwick et al. 2007, Armstrong et al. 2005b, Armstrong et al. 2005c, Bruce et al. 2008 and Deng et al. 2009).

1.3.4 Nanoparticles

We now consider lithium insertion in nanoparticles of anatase TiO_2, which as the size of TiO_2 falls in the nanometers, tends to be more stable than other polymorphs, owing to differences in particle surface tension, size, and shape (Barnard et al. 2004 and Ranade et al. 2002). A larger Li-ion conductivity is deduced from simulation results for particle size smaller than 20 nm, and lower conductivity for larger nanoparticles (Sushko et al. 2010). An experimental confirmation was put forward by Wang et al (Wang et al. 2007) which depicted that the total energy storage, emanating from double layer effects and intercalation process, increased with decreasing the size of nanocrystalline anatase from 5

nm to 10 nm. In addition, reducing particle size to the nanoscale regime leads to faster charge/discharge rates because the diffusion-controlled Li-ion intercalation process is replaced by faradic reactions which occur at the surface of the material TiO_2 (Wang et al. 2007). This phenomenon is also observed on the anatase TiO_2 with smallest primary particle size of approximately 8 nm which was obtained from a hydrothermal treatment on sol–gel precipitates of TiO_2 (Wilhelm et al. 2004). Such particles with the smallest primary size deliver the highest charge capacity as 140 $mAhg^{-1}$, and the capacity decreased with increasing the primary particle size (Wilhelm et al. 2004). A higher initially discharge capacity of 203 $mAhg^{-1}$ is reported for anatase TiO_2 nanoparticles with a particle size of approximately 20 nm, which were prepared by hydrolysis of titanium tetraisopropoxide in pure water, and followed by calcined at high temperature. However, the initial loss of capacity is as high as 14% between the insertion and the extraction of Li ions, and the reversible capacity after 40 cycle's decreases to 148 $mAhg^{-1}$ (Liu et al. 2005). Higher reversible capacity is reported on the anatase TiO_2 powders with same size ~20 nm, which were prepared hydrothermally, yielding a specific capacity on the first discharge of 180 $mAhg^{-1}$, and only 5% loss was observed after the second cycle, and there is no appreciable capacity fading even after 100 cycles (Oh et al. 2006).

Electrochemical performances do not always benefit from decreasing particle sizes. Poizot et al. (2000) studied metal oxide systems and found an optimal size range for the metal-oxide particles to exhibit the best electrochemical properties. Exnar et al. (1997) also noted that the optimal anatase particles size in practical $TiO_2/LiCo_{0.5}Ni_{0.5}O_2$ button cells is approximately 10–15 nm. Recently, Kang et al. (2011) presented the so-called polyol-based method to fabricate anatase TiO_2 nanoparticles and they suggested that, under certain experimental conditions, 8–25 nm appears to be the critical particle size for anatase TiO_2 with sufficient crystallinity and significant electrochemical performances.

TiO_2-B nanoparticles have also been studied where, as an example, Estruga et al. (2010) produced such nanoparticles through the hydrolysis of an ionic liquid with titania precursor at ambient pressure and low temperature. However, no electrochemical characterization was reported. Wessel et al. (2011) proposed that pure TiO_2-B nanoparticles with 20–25 nm in diameter can be produced which yielded a considerable high capacity of 100 $mAhg^{-1}$ even at a high current rate of 10 C.

Lithium insertion into nanoparticles of other TiO_2 common polymorphs, such as rutile and brookite, was not well known until very recently, when a high Li electroactivity was reported in nanometer sized rutile and brookite TiO_2 at room temperature (Reddy et al. 2006 and Reddy et al. 2008). However, several groups have shown that, in nanoparticles of rutile TiO_2, one Li/TiO_2 can be inserted at room temperature (Hu et al. 2006, Baudrin et al. 2007 and Jiang et al. 2007a). More recently, it was demonstrated that reasonable amounts of lithium can be inserted into nanocrystalline brookite TiO_2 (Reddy et al. 2007); as an example 0.9 Li/TiO_2 was inserted into a 10 nm sized nanoparticles of brookite, and it was shown that the structure is stable for reversible lithium insertion. Subsequently, Lee et al. (2008) also observed that it is possible to insert Li into nanophase brookite TiO_2 at room temperature. Furthermore, it was observed that crystallized size of brookite TiO_2 has a remarkable effect on lithium insertion (Dambournet et al. 2010).

One of the advantages of brookite, unlike other polymorphs, is an apparent absence of phase transformation with lithiation. However, XRDs studies on different stages in lithium insertion and deinsertion reactions suggest that the Brookite framework amorphised during discharge, with a partial recovery of the crystallinity upon (re)charging (Reddy et al. 2008). A further investigation, involving a combined PDF and DFT approaches, clearly indicated that the TiO_2 connectivity within the Brookite

framework remains intact upon lithium intercalation (Dambournet et al. 2011). The flexibility of the framework with five-fold coordination environment for the Li ion, which, in part, allows it to accommodate the Li ions, is also responsible for the broadening of the Bragg reflections and apparent reported amorphisation. An observation that the framework remains intact is ultimately linked to the property of the material to retain its capacity over many cycles. Typically, the observation of amorphisation is correlated with the assumption of changes in connectivity.

1.3.5 Nanorods, Nanowires and nanowhiskers

The impact of nanorod, nanowire and nanowhisker TiO_2 architectures on electrode performance will now be considered. Since the diffusion coefficient of Li ions along c-direction is almost eight orders higher than that along ab-plane (Koudriachove et al. 2002, Gligor et al. 2006 and Johnson et al. 1964), the Li-ion insertion into rutile TiO_2 can be considered as a nearly one-dimensional diffusion. Consequently, the restricted diffusion into three-dimensional volume makes poor electrochemical performance of the bulk rutile TiO_2 as anodes of LIBS. However, the Li-ion intercalation capacity can be significantly improved as rutile TiO_2 possesses morphologies as nanorods, nanowires, or nanowhiskers, especially as particles grow along the c-direction (Hu et al. 2006, Jiang et al. 2007 and Reddy et al. 2006). The fabrication of rutile TiO_2 nanoneedles, with a width of 20–25 nm and length of 100 nm, was reported by Khomane (2011) and electrochemical measurements show that they deliver an initial capacity of 305 $mAhg^{-1}$, and the capacity value retains as high as 128 $mAhg^{-1}$ after 15 cycles.

Qiao et al. (2010) developed a method to prepare flower-like rutile TiO_2 nanorods. These flower-like structures were composed of many nanorods with 10–15 nm in diameter and 50–70 nm in length, and the growth direction of nanorods was found to be parallel to (110) crystal planes. Such flower-like rutile TiO_2 nanorods demonstrated a stabilized

charge capacity of 183 $mAhg^{-1}$ after 30 cycles. Most recently, Dong et al. (2011) reported a method to fabricate rutile TiO_2 nanorod arrays (grew along c-axis) on Ti foil substrates using a template-free method. These nanorods exhibited significantly electrochemical performance with capacity of about ten times higher than that of rutile TiO_2 compact layer. The higher capacity was ascribed to the greatly improved contacts between electrode materials and electron collectors leading to a significant reduction in resistance.

It was earlier mentioned that TiO_2-B is, generally, a better intercalation host for lithium ions compared to rutile and anatase polymorphs (Armstrong et al. 2006). A three-step synthesis procedure by Marchand et al. (1980) was adopted and well developed by other researchers to prepare TiO_2-B nanowires, and nanorods aimed at providing high capacities in lithium ion batteries (Inaba et al. 2009, Zhu et al. 2011 and Wang et al. 2011). More interestingly, Liu et al. (2010) grew vertically oriented single-crystalline TiO_2-B nanowire arrays on titanium foil over large areas by placing titanium substrates in hydrothermal solution during hydrothermal process. Such arrays exhibited a high capacity of 120 $mAhg^{-1}$ even as the charge/discharge rate is up to 1.8 C and excellent cycling stability beyond 200 cycles.

Lan et al. (2005) reported a facile way of preparing anatase TiO_2 nanorods from rutile powders directly, which exhibit improved capacity of 198 $mAhg^{-1}$. Using similar procedures, Kim et al. observed that the nanotubes transformed to nanorods as the temperature of thermal treatment on the as-prepared nanotubes increased from 300 to 400 ^oC (Kim et al. 2007). However, nanorods exhibited lower initial discharge capacity (178 $mAhg^{-1}$ at the 0.5 C rate) and faster capacity decay (110 $mAhg^{-1}$ at 10 C rate) compared to nanotubes (205 and 180 $mAhg^{-1}$ at 5 and 10 C, respectively) (Kim et al. 2007). The significance of this approach is that it provides a facile route to fabricate anatase TiO_2 nanorods directly from industrial raw materials, which always exists in the rutile phase.

1.3.6 Nanoporous

Much as the TiO_2 nanoparticles introduce good electrochemical performance of anodes for LIB they also have limitations. It is well known that nanoparticles possess high surface energy compared with the bulk counterpart and incline to aggregate either during synthesis or galvanostatic cycling. The aggregation of nanoparticles decreases the surface area and increases the difficulty for electrolyte solution diffusion within aggregates reaching the surface of particles; it results in the reduction of the total storage energy. Consequently, a better way to avoid this situation is to prepare nanoporous TiO_2 (Hwang et al. 2012).

Mesoporous or nanoporous TiO_2 have been studied by several authors (Zhou et al. 2005, Moriguchi et al. 2006, Guo et al. 2007 and Wang et al. 2007) and the micrometre-sized mesoporous materials have characteristic grains as well as pores nearly in the same scale. Electrodes of mesoporous materials for lithium batteries have short transport lengths for Li^+ ions due to their nano-sized grains (10–20 nm), and easy access for electrolytes due to their nanopores (5–10nm). Such mesoporous materials have high packing densities unlike nanopowders, nanowires, nanorods and nanotubes. Despite such advantages, electronic conduction over micrometre-sized particles limits the rate performance of mesporous materials. We will briefly discuss some of the recent studies.

Methods of fabrication of mesoporous TiO_2 can be roughly categorized to template-assistant (Wang et al. 2008, Saravanan et al. 2010, Fu et al. 2007 and Wang et al. 2007) and template-free (Yoon et al. 2011, Lai et al. 2011, Wang et al. 2011, Jung et al. 2009 and Guo et al. 2006). In template-free routines, hydrothermal treatment was always utilized to create a core–shell mesoporous TiO_2 spheres with micrometres in diameter (Yoon et al. 2011, Lai et al. 2011 and Jung et al. 2009). Among all products fabricated from template-free approach, microspheres produced by Wang et al. (2009) demonstrated

the highest initial discharge capacity of 265 and 151 $mAhg^{-1}$ at 0.06 and 1.2 C, respectively, even after 50 cycles.

Compared to the template-free approach, the employment of templates can create well-ordered and uniform mesoporous which can more effectively accommodate the volume change during Li-ion insertion/deinsertion process. In general, surfactants including tri-block polymers (Wu et al. 2011a and Wu et al. 2011b), cationic surfactant molecules (Saravanan et al. 2010), anionic surfactant molecules (Wang Z et al. 2007), and polystyrene (PS) colloids (Fu et al. 2007), etc. are widely used as templates for generating mesopores. Some of the recent studies will be briefly discussed.

Ren et al. (2010) synthesized an ordered 3D mesoporous anatase using a hard template and investigated lithium intercalation. The structural changes are similar to those observed for nanoparticles, with continuous Li insertion into tetragonal anatase up to $Li_{0.05}TiO_2$, then a two-phase process between anatase and orthorhombic $Li_{0.45}TiO_2$ followed by continuous insertion into the orthorhombic phase up to $Li_{0.96}TiO_2$. Despite the intrinsic porosity of the mesoporous phase, the volumetric capacity is higher than the best results for nanoparticulate anatase reported previously, a two-fold increase being observed at the highest rates (24 Ag^{-1}). The rate capability is better than disordered mesoporous anatase even when the latter is metallized, suggesting that the ordered pore structure is important in achieving high rate capability.

The relationship between mesopores properties and electrochemical performances has been elaborated by Saravanan et al. (2010). Mesoporous TiO_2 anatase was synthesised using a soft-template method, and through varying the chain length of surfactants, the average pore size of mesoporous TiO_2 increases from 5.7 to 7.0 nm with increasing the specific surface area from 90 to 135 m^2g^{-1}. It is believed that a high specific surface area benefits electrochemical reactions because of the enhanced active sites for electrolytes,

and it is found that the reversible capacity increases with increasing pore size and specific surface area reaching the maximum capacity of 268 $mAhg^{-1}$ for the samples with a specific surface area of 135 m^2g^{-1} and pore size of 7 nm. A remarkable high rate performance of 107 $mAhg^{-1}$ up to 30 C is also exhibited by this sample (Saravanan et al. 2010). The storage performance and the packing density of the as-synthesized mesoporous TiO_2 are respectively five times and 6.6 better than the commercially available TiO_2 nanopowder.

Liu et al. (2011) reported design and synthesis of a titanium dioxide material with novel architecture, which combines the features of the TiO_2–B polymorph with mesoporous structure (uniform mesopores of 12 nm) and microsphere morphology (microspheres of diameter 11 μm and nanosized crystal grains of ~ 6 nm). (a) The TiO_2–B polymorph ensures the material will have fast kinetics of lithium transport due to its pseudocapacitive mechanism. (b) The mesoporous structure results in adequate contact electrode-electrolyte contact and facile electronic transport along the boundary of sintered nanograins. (c) The microsphere morphology accommodates traditional electrode fabrication art and creates compact electrode layers. The integration of these features enables this material to have superior lithium storage performance, which could meet the needs of electric vehicle batteries and other high power applications.

1.3.7 Nanosheets

Studies of TiO_2 nanosheets for energy storage and conversion, including anode in LIB and electrode in DSC respectively, are not as abundant as those of nanoparticle and nanoporous structures. Such nanosheets are ideal owing to exposure of highly reactive surfaces, which unfortunately are usually unstable during crystal growth. Most available anatase TiO_2 crystals are dominated by the thermodynamically stable {101} facets (more than 94 per cent, according to the Wulff construction (Lazzeri et al. 2001), rather than the

much more reactive {001} facets (Gong et al. 2005). However, recently, approaches of stabilising such surfaces have been put forward; which paved a way for the synthesis of anatase TiO_2 nanosheets with 47% of the {001} surfaces (Yang et al. 2008). Electrochemical investigations reveal that the exposed (001) high-energy facets of the nanosheet result in enhanced rate capability which originates from both the shortened diffusion path and lowered insertion energy barriers on the active surface for Li^+ ions (Knauth et al. 1999). Furthermore, the electrolyte/electrode contact is enhanced via hollow structures; and such features collectively allow for more efficient lithium diffusion in anodes of LIB.

Liu et al. (2012) designed and synthesized hierarchical porous TiO_2–B with thin nanosheets, which combines the superiorities of the TiO_2–B polymorph with porous structure as well as thin nanosheet. TiO_2–B polymorph ensures the fast insertion and extraction of Li-ion due to its pseudocapacitive mechanism, while the porous structure with thin nanosheet wall effectively extends the interfacial zone and thus can greatly promote ionic transport and electrode reaction. The joint advantages endow this material with high reversible capacity, excellent cycling performance, and superior rate capability.

DFT+U calculations show unique lithiation mechanisms for the different nano-architectures, where TiO_2-B nanosheets incrementally fill C sites, followed by A2 and A1 (Dylla et al. 2012). The calculations suggest that this lithiation mechanism is related to the elongated geometry of the nanosheet along the a-axis that reduces Li^+−Li^+ interactions between C and A2 sites. The calculated lithiation potentials and degree of filling agree qualitatively with the experimentally observed differential capacity plots.

TiO_2 films of photoanodes for dye sensitized solar cells (DSSC) play a key role in the improvement of the light to electricity conversion. Not with standing demonstration of O-terminated {100} facets as having the lowest surface energy, Wei et al. 2011) reported a

novel method, which includes O-terminated synthesis – thermal activation – O (dye)-terminated processes, to fabricate and apply stable single crystal anatase TiO_2 nanosheets with exposed {100} facets for dye solar cell applications.

1.3.8 Large scale simulations

Theoretical studies that are capable of modelling complex nanostructures are scarce. Recent studies on MnO_2 (Sayle et al. 2009a) have yielded a systematic strategy for simulating nanomaterials - analogous to atomistic methods, which are widely and routinely used to model crystal structure. The nanoparticle (0D), nanorod (1D), nanosheet (2D) and nanoporous (3D) were considered. The particular polymorphic structure was evolved using simulated amorphisation and crystallization (Sayle et al. 2005). The model was validated using nanoporous MnO_2 and it was shown that they are in accord with experiment. It was demonstrated that, the nanoporous MnO_2 can expand and contract linearly and crucially elastically under charge/discharge cycling thus retaining its structural. Morphological and mechanical properties of simulated lithiated bulk (Maphanga et al. 2011) and nanoporous (Sayle et al. 2009b) MnO_2 have clearly illustrated why the nanoporous structures have high rate capability and preferable for usage in Li ion batteries. High pressure crystallisation of TiO_2 nanoparticles have been studied (Sayle et al. 2007). They generated a full atomistic model of a TiO_2 nanocrystal by simulating TiO_2 crystallisation. Consequently such simulation techniques will be most suitable to study the various nanostructures of TiO_2 and their lithiated forms.

1.4 Intentions of the study

The literature review in section 1.3 has clearly indicated the significance of energy storage in a variety of devices and in particular its demand for vehicle traction recently. TiO_2 is being considered as one of the most attractive anode materials of LIBs owing to distinct characteristics, which have been outlined, as compared to some of the existing

commercial anode materials such as graphite. The advantages of the various TiO_2 nano-architectures have been clearly elucidated, and in order to maximise their usage in enhancing the rate capability and energy density their further fundamental understanding is necessary. Generally, atomistic simulation studies play an important role in this regard; and in particular, amorphisation recrystallisation approach is one of the few methods that are capable of spontaneously generating such nano-architectures. We are currently not aware of other simulation methods that are capable of producing complex architectures, such as the nanoporous phase, in a similar manner. In addition to creation of such nano-architectures it is also of essence to unravel complex microstructures, that can accommodate and provide paths for lithium ions in such architectures and to predict the extent to which such structures can accommodate high concentrations of lithium before depicting undesirable mechanical changes and failure. Previous studies by amorphisation recrytallisation methods on nanosphere TiO_2 and all nano-architectures of MnO_2 and their lithiated versions have provided valuable insights on related microstructures. Lastly, the types of polymorphs that occur in the various nano-architectures have to be identified since they determine possible pathways of lithium ion transport in electrodes. Correlation between atomistic details and performance of batteries is not yet fully explored.

In the proposed study, simulated amorphisation recrystallisation method will be employed to generate various nano-architectures of TiO_2, i.e. nanosphere, nanoporous, nanosheet and bulk structures which have been widely studied experimentally. Such structures will be characterized and lithiated and the fundamental understanding of atomistic structural and microstructural details that are crucial for enhancement of energy density and power, charge discharge time, number of charge/discharge cycles of high power rechargeable batteries, will be explored.

This will help in the acceleration of usage of related batteries in EV and HEV. An example of an EV is shown in figure 1.5 and this was manufactured by Optimal Energy in Cape Town, South Africa, while HEV is shown in figure 1.6 below. Some technology devices are depicted in figure 1.7.

Figure 1.5: Electric vehicle (EV) from Optimal Energy (Joule).

Figure 1.6. Hybrid electric vehicle (HEV).

Figure 1.7: Some modern technology devices.

Our main objective in this work is to have lithiated nanostructures of TiO_2 used as an anode. We want to use computational modelling methods in the enhancement of cost effectiveness, energy density and power, charge discharge time.

1.5 Outline of the dissertation

This thesis presents the study of titanium dioxide nanostructures and lithiated structures and it consists of five chapters.

Chapter one presents the general background of titanium dioxide nanostructures. It presents the previous work that has been studied experimentally and theoretically. It also gives the main applications of our system in some devices and reviews the motivation and intentions of the study.

In chapter two, we review the theoretical methodologies that have been employed throughout our study including code that was employed.

Chapter three presents the results on growth of nanostructures of TiO_2. It also presents amorphisation and recrystallisation, radial distribution functions (RDFs) microstructures and XRDs of some of the nanostructures. We compare our calculated results with the

experimental and theoretical results.

Chapter four presents the results on lithiated nanostructures of TiO_2. Amorphised and recrystallized structures are presented with their RDFs.

Chapter five presents the conclusions on the results that were obtained in chapter three and chapter four, also we present the recommendation and future work. After chapter five we present a bibliography and finally we have appendix A (list of publications) and appendix B (papers presented at the conferences).

Chapter 2

THEORETICAL METHODOLOGY

In this chapter we present the method that was used throughout the study. We describe the simulation code that was employed, potential models used and the simulated amorphisation and recrystallisation technique that was used to allow the spontaneous growth of titanium dioxide nanostructures. We will present the discussion of the potential models for atomic simulation technique since it was the only technique that was employed throughout this work. Some potential models were not used like shell model, since it is a sub-potentials of Buckingham potential. Shell model is computationally very expensive preventing simulation of large systems, such as a mesoporous TiO_2 host. Moreover the potentials become unstable at high temperatures leading to potential catastrophic failure.

2.1 Simulation codes

Molecular dynamics simulations were all performed using the computer code DL_Poly (Smith et al. 1996). DL_Poly is a general purpose molecular dynamics simulation package continually developed at Daresbury Laboratory by W. Smith and I. T. Todorov under the auspices of EPSRC and NERC in the support of CCP5. It simulates a wide variety of molecular systems of ionic liquids and solids, simple liquids, small polar and non-polar molecular systems, bio- and synthetic polymers, ionic polymers and glasses solutions, simple metals and alloys. In this work we used this code to simulate the nanostructures of titanium dioxide. The input files for DL_Poly are CONTROL, FIELD and CONFIG which helps us to carry our calculations together with the run script. These are mandatory files that must be present in the directory when DL_Poly is run.

CONTROL - this file specifies the control conditions for a run of the program. In this file we specify timestep, temperature, pressure, ensemble, ewald precision etc.

FIELD – defines the force field for the simulation and details of the molecular structures.

CONFIG – defines the positions of all the atoms in the system (in Angstroms) and specifies the simulation cell. It also specifies the atomic velocities and forces.

2.2 Potential models

Calculations are based on the Born model (Born et al. 1954) of ionic solids, where ions interact via long-range Coulomb and short range interactions. Rigid ion potentials with partial charges were used and these were developed by Matsui for isostructural rutile TiO_2. In this section we are going to describe the potential models.

2.2.1 Short range two body potential functions

The short range two body potentials is an interaction between two charge clouds. That is the short range attractive and repulsive interactions of the ions. Attractive interaction contains van der Waals. The short range interaction energies are described well by simple parameterised analytical functions. Below we give descriptions of short range interactions potentials.

2.2.1.1 Harmonic potentials

The simplest potential that is used to model interactions between bonded ions is harmonic potential. The harmonic potential is given by,

$$U_{ij}(r_{ij}) = \frac{1}{2} k_{ij}(r_{ij} - r_0)^2 \qquad 2.1$$

In which k_{ij} is the harmonic force constant, r_{ij} is the distance (bond length) between the two ions i and j, r_o is the equilibrium bond distance. This potential cannot be used when the bond length vary much from the equilibrium. But when the bond length vary much then an alternative potential can be used, that is Morse potential, which is discussed

below.

2.2.1.2 Morse potentials

As mentioned above Morse potential is used for interactions at bond distances which display anharmonicity. Morse potential can be able to model systems away from their equilibrium bond distances such as point defects and surfaces or when temperature or pressure is applied. Morse potential is given by,

$$V(r_{ij}) = A_{ij}\left(1 - e^{[-B_{ij}(r_{ij}-r_0)]}\right)^2 - A_{ij} \qquad 2.2$$

Where A_{ij} is the bond dissociation energy, B_{ij} is a function of slope of the potential energy and r_o is the equilibrium bond distance. The Morse potential is often used with subtraction of the Coulomb interaction due to its inclusion of the bond energy, which completely describe the bond for the nearest neighbours. And it takes the form,

$$V(r_{ij}) = A_{ij}\left(1 - e^{[-B_{ij}(r_{ij}-r_0)]}\right)^2 - A_{ij} - \frac{q_i q_j}{4\pi\varepsilon_0 r} \qquad 2.3$$

This equation will reduce to the Morse potential when the fraction of the coulombic subtraction is equal to zero. Morse potentials are generally used to describe the bonded interaction between two nearest neighbours, where interactions between the next nearest neighbours and those further away are represented by different potential functions for non-bonded interactions.

2.2.1.3 Lennard Jones Potentials

The Lennard-Jones is a mathematically simple model that approximates the interaction between a pair of neutral atoms or molecules. But firstly it was developed for the interactions of noble gases and later was uses for intermolecular interactions. Lennard-Jones potential is given by the equation,

$$\Phi_{ij}(r_{ij}) = \frac{A_{ij}}{r_{ij}^{12}} - \frac{B_{ij}}{r_{ij}^{6}} \qquad 2.4$$

Where r_{ij}^{12} presents repulsive part and r_{ij}^{6} represent an attractive part. Lennard-Jones

potential is a non-bonded potential. The term r_{ij}^{12}, dominating at short distance, models the repulsion between atoms when they are brought very close to each other. Its physical origin is related to the Pauli principle: when the electronic clouds surrounding the atoms start to overlap, the energy of the system increases abruptly. The term r_{ij}^{6} , dominating at large distance, constitute the attractive part. This is the term which gives cohesion to the system. A r_{ij}^{6} attraction is originated by van der Waals dispersion forces, originated by dipole-dipole interactions in turn due to fluctuating dipoles. These are rather weak interactions, which however dominate the bonding character of closed-shell systems, that is, rare gases

2.2.1.4 Buckingham Potentials

Buckingham potential is a formula that describes the van der Waals energy $\Phi_{ij}(r)$ for the interaction of two atoms that are indirectly bonded as a function of the interatomic distance (r). It is used to model two body non-bonded interactions in ionic solids. The general form of Buckingham potential is given by

$$\Phi_{ij}(r) = A_{ij} exp^{\frac{-r_{ij}}{\rho_{ij}}} - \frac{C_{ij}}{r_{ij}^{6}} \qquad 2.5$$

Where A_{ij} is the size of the ions, ρ_{ij} is the hardness and C_{ij} is the dispersion parameter. The repulsive interaction between the ions is represented by the first term while the second term is the van der Waals attractive interaction of the ions.

2.2.1.5 Shell model potentials

The shell model is the approach with the inclusion of dipolar polarisation firstly introduced by Dick and Overhauser (Dick et al. 1958). This simple mechanical model describes a core which represents the nucleus and the inner electrons of the ion. This core has the mass associated with it and a shell that represents the valence electrons. The schematic representation of shell model is presented in figure 2.1. All ions in the shell

model consist of a shell and a core, which are coupled to each other by a harmonic spring with constant force. Total interaction energy is given by:

$$U(r_i) = \frac{1}{2} k_i r_i^2 \qquad 2.6$$

where r_i is the distance between the core and the shell, and k is the force constant for the harmonic spring. The spring constant and the charges of core and shell describe the polarisability of the free ion which is given by:

$$\alpha_i = \frac{q^2}{4\pi\varepsilon_o k_i} \qquad 2.7$$

where ε_o is the permittivity of free space and q is the charge on the shell. The units of the force constant k are $eV\text{Å}^2$. The parameters of shell model are obtained by empirical fitting to the dielectric constants, phonon dispersion curves and defect energies.

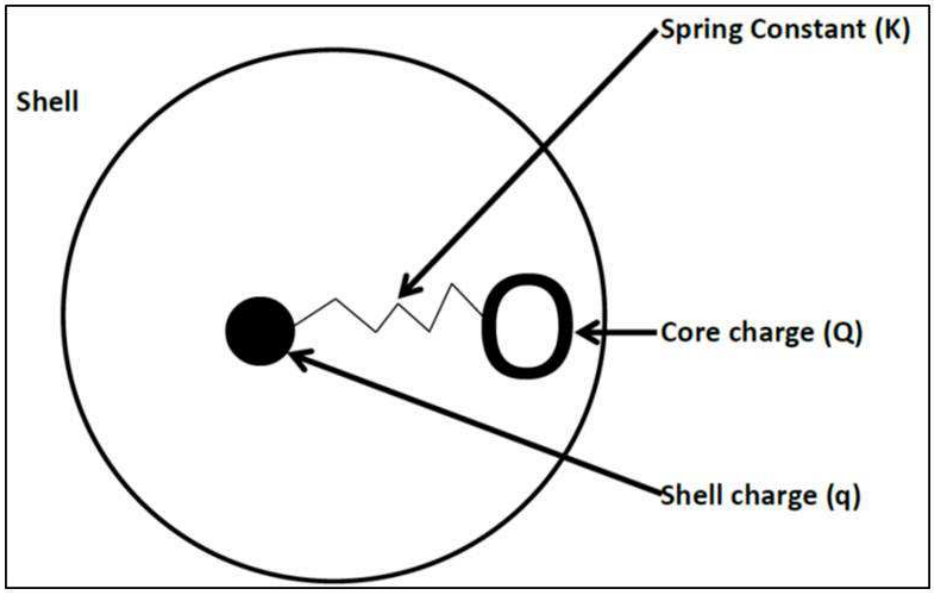

Figure 2.1: Schematic representation of the shell model.

Short-range forces act on the shells while the columbic forces act on both shells and cores, but not for the same ion. In Molecular Dynamics the use of shell model is a bit different since they often use Rigid Ion Models.

2.2.1.6 Rigid Ion model

Rigid ion model is where electronic polarisation is ignored in ionic solids and gives

acceptable results. This model treats ions as a point charge, so it is acceptable in reproducing structural parameters for a rigid system. But in this case the lattice vibrations will be poorly modelled as they are strongly coupled to polarisability. This model will give poor results for defect energies, but in this condition we can be able to handle the problem by fitting short range parameters to model static dielectric constants and overestimating the polarisation due to lattice relaxation to compensate for the shortfall due to neglecting the polarisability. This correction will help us to obtain correct defect energies but it will not work for all calculations involving potentials, that is where time and various models are included.

2.2.2 Long range interaction

The long-range interaction energy is the sum of interaction energies between the charges of a central unit cell and all the charges of the lattice. The long range interaction energy of two ions (ion *i* and ion *j*) with charges q_i and q_j is given by

$$\Psi(r_{ij}) = \sum \frac{q_i q_j}{4\pi\varepsilon_o (r_{ij}+l)} \qquad 2.8$$

where r_{ij} is the displacement separating the two ions, ε_o is the permittivity of free cell and *l* is the set of lattice vectors representing the periodicity of the crystal lattice. In particular long range interactions describe the coulombic summation. It is not easy to use equation 2.7 since it converges with the displacement of ion, so we are going to describe two methods that will help in making this simpler to derive the equations. Two methods are Ewald summation and Parry method where their theory will be described in section 2.2.4 and 2.2.5 respectively.

2.2.3 Coulombic summation

The coulombic interaction potential is represented by the term after summation symbol in equation 2.7. This corresponds to the potential energy of long range interactions. The coulomb energy is given by a conditionally convergent series were the coulomb energy is

ill-defined for an infinite 3-D material unless certain additional conditions are specified.

2.2.4 Ewald summation

The Ewald summation (Ewald et al. 1921) is a technique used to sum the long range interactions between particles and all their infinite periodic images efficiently, particularly electrostatic energies. The description of the coulombic interaction shows that the charge density (ρ) of a point charge (q_i) is

$$\rho_i = q_i \Delta(r_i - r_{lattice}) \tag{2.9}$$

The delta function can take the value of 0 or 1 and basically the Ewald method is replaced by a Gaussian function:

$$\rho_i = q_i e^{\left(-\frac{(r_i - r_{lattice})^2}{\eta^2}\right)} \tag{2.10}$$

where η is the half width of the Gaussian. The original charge density takes the form

$$\rho_i(r) = \left[\Delta(r_i - r_{lattice}) - e^{\left(-\frac{(r_i - r_{lattice})^2}{\eta^2}\right)}\right] + e^{\left(-\frac{(r_i - r_{lattice})^2}{\eta^2}\right)} \tag{2.11}$$

The potential field ϕ (Kittel et al. 1971) generated by this charge distribution is the solution of the Poisson's equation. The potential of the first part takes the form

$$\phi(r) = q_i \sum_j \left(q_i \frac{1}{r_{ij}} erfc(\eta r_{ij})\right) \tag{2.12}$$

where erfc (ηr_{ij}) is the complementary error function. This sums up all the interactions of ions *i* and *j* over the whole lattice.

The second part of equation 2.10 is a Fourier transformed to converge rapidly in reciprocal space of Gaussians and is given by

$$\rho(r) = q_i \sum_k \left(C_k e^{(iK.R)}\right) \tag{2.13}$$

Where K is the reciprocal lattice vectors and R is $r_i - r_{lattice}$ for all ions in the unit cell. Using Poisson's equation then the potential of the second term becomes

$$\phi_i(r) = q_i \sum \left[q_i \frac{1}{\pi K_K} \sum_k \left(\frac{e^{(-\pi^2 k^2 \eta^2)} e^{(iKR)}}{k^2} \right) \right] \quad 2.14$$

By summing up the periodic array we combine the potentials of the first and second terms of equation 2.10 then the equation becomes

$$\phi_i(r) = q_i \sum \left[q_i \frac{1}{V_k} \sum_k \left(\frac{1}{K^2} e^{-\pi^2 K^2 \eta^2} \cdot e^{ik.r} \right) \right] + q_i \sum_j \left(q_i \frac{1}{r_{ij}} erfc(\eta r_{ij}) \right) - q_i^2 \frac{2\eta}{\sqrt{\pi}} \quad 2.15$$

where the final term is the self-interaction.

2.2.5 Parry method

A special application of the Ewald method (Ewald et al. 1921) for two dimensional crystals is called Parry method (Parry et al. 1975). The crystal is assumed to consist of a series of charged planes of infinite size rather than a finite lattice. In the summation of the electrostatic interactions, the vectors are now divided into two planes in-plane vectors, ρ_{ij} and vectors perpendicular to the plane, u_{ij}. In the three dimensional case it is assumed that the total charge of the simulation cell is zero, however the assumption is no longer valid and hence k =0 term has to be evaluated. Thus the summation of the coulombic energy is given as

$$\phi = \frac{\pi}{A} \left\{ -2u_{ij} erf(\eta u_{ij}) - \frac{2e^{\left(-\eta^2 u_{ij}^2\right)}}{\eta\sqrt{\pi}} + \sum_{k \neq 0} \frac{e^{ik\rho_{ij}}}{k} \left[e^{ku_{ij}} erfc\left(\frac{k}{2\eta} - \eta u_{ij}\right) + e^{(ku_{ij})} erfc\left(\frac{k}{2\eta} - \eta u_{ij}\right) \right] \right\} \quad 2.16$$

where K is the two dimensional reciprocal lattice vector, A is the surface area, erf and erfc are the standard and complementary error functions respectively.

2.3 Molecular dynamics

Molecular dynamics (MD) is a computer simulation of physical movements of atoms and molecules. It is the most natural method of performing equilibrium statistical-mechanical calculations via simulation. The atoms and molecules are allowed to interact for a period of time, giving a view of the motion of the atoms. The trajectories of molecules and atoms are determined by numerically solving the Newton's equations of motion for a system of interacting particles, where forces between the particles and potential energy

are defined by molecular mechanics force fields. In molecular dynamics we follow the laws of classical mechanics, and most notably Newton's law:

$$F_i = m_i a_i \tag{2.17}$$

for each atom *i* in a system constituted by N atoms. Here, m_i is the atom mass, Fi is the force acting upon it, due to the interactions with other atoms and ai is the acceleration of the atom given by

$$a_i = \frac{d^2 r_i}{dt^2} \tag{2.18}$$

Therefore, molecular dynamics is a deterministic technique: given an initial set of positions and velocities, the subsequent time evolution is in principle (Alder et al. 1957) completely determined. In more pictorial terms, atoms will ``move" into the computer, bumping into each other, wandering around (if the system is fluid), oscillating in waves in concert with their neighbours, perhaps evaporating away from the system if there is a free surface, and so on, in a way pretty similar to what atoms in a real substance would do. The computer calculates a trajectory in a 6N-dimensional phase space (3N positions and 3N momenta). However, such trajectory is usually not particularly relevant by itself. Molecular dynamics is a statistical mechanics method. Like Monte Carlo, it is a way to obtain a set of configurations distributed according to some statistical distribution function, or statistical ensemble. According to statistical physics, physical quantities are represented by averages over configurations distributed according to a certain statistical ensemble. A trajectory obtained by molecular dynamics provides such a set of configurations. Therefore, a measurement of a physical quantity by simulation is simply obtained as an arithmetic average of the various instantaneous values assumed by that quantity during the MD run.

Statistical physics is the link between the microscopic behaviour and thermodynamics. In the limit of very long simulation times, one could expect the phase space to be fully

sampled, and in that limit this averaging process would yield the thermodynamic properties. In practice, the runs are always of finite length, and one should exert caution to estimate when the sampling may be good (``system at equilibrium'') or not. In this way, MD simulations can be used to measure thermodynamic properties and therefore evaluate, say, the phase diagram of a specific material. Beyond this ``traditional'' use, MD is nowadays also used for other purposes, such as studies of non-equilibrium processes, and as an efficient tool for optimization of structures overcoming local energy minima (simulated annealing). To advance the atomic positions and velocities that describe the dynamical behaviour we integrate Newton's equations. Some work on the new molecular dynamics method was studied in the canonical ensemble (Nose et al. 1984).

2.3.1 Energy

The internal energy is easily obtained from a simulation as the ensemble average of the energies of the states that are examined during the course of the simulation:

$$U = \langle E \rangle = \frac{1}{M} \sum_{i=1}^{M} E_i \qquad 2.19$$

The average potential energy V is obtained by averaging its instantaneous value, which is obtained at the same time as the force computation is made. Thus, the potential energy is given by:

$$V(t) = \sum_i \sum_{j>1} \phi \left(\left| r_i(t) - r_j(t) \right| \right) \qquad 2.20$$

The kinetic energy is given by:

$$K(t) = \frac{1}{2} \sum_i m_i [\bar{v}_i\ (t)]^2 \qquad 2.21$$

where m_i is the mass of atom i and $\bar{v}_i$ is the velocity of atom i. The total energy of the system can be represented as the sum of the kinetic energy and the potential energy and the total energy of the system with a given set of positions and velocities is represented by:

$$T_{tot} = K(t) + V(t) \qquad 2.22$$

2.3.2 Temperature

Temperature depends on a certain kind of ensemble for a particular simulation. In a canonical ensemble the total temperature is constant whereas in the microcanonical ensemble the temperature is fluctuating. The temperature is directly related to the kinetic energy of the system as follows:

$$K = \sum_{i=1}^{N} \frac{|\acute{p}_i|}{2m_i} = \frac{k_B T}{2}(3N - N_c) \quad 2.23$$

Where Pi is the total of particle i, mi is its mass and N_c is the number of constraints on the system. Each degree of freedom contributes $k_BT/2$ this is according to the equipartition of energy. If there are N particles, each with three degrees of freedom, then the kinetic energy should be equal to $3Nk_BT/2$. Total linear momentum of the system is often constrained to a value of zero in a molecular dynamics simulation, which has the effect of removing three degrees of freedom from the system and N_c would be equal to 3.

2.3.3 Pressure

Calculation of pressure is usually in a computer simulation via the virial theorem of Clausius. The virial is defined as the expectation value of the sum of the products of the coordinates of the particles and the forces acting on them. Usually this is written as

$$W = \sum x_i \acute{p}_{x_i} \quad 2.24$$

Where xi is a coordinate (e.g. the x or y coordinate of an atom) and $\acute{p}_{xi}$ is the first derivative of the momentum along that coordinate ($\acute{p}_i$ is the force, by Newton's second law). The virial theorem states that the virial is equal to $-3Nk_BT$. In an ideal gas, the only forces are those due to interactions between the gas and the container and it can be shown that the virial in this case equal to -3PV. This result can be obtained directly from

$$PV = Nk_BT \quad 2.25$$

Forces between the particles in a real gas or liquid affect the virial, and thence the pressure. The total virial for a real system equals the sum of an ideal gas part (-3PV) and

a contribution due to interactions between the particles. The result obtained is:

$$W = -3PV + \sum_{i=1}^{N}\sum_{j=i+1}^{N} r_{ij}\frac{dv(r_{ij})}{dr_{ij}} = -3Nk_BT \qquad 2.26$$

If $d(r_{ij})/dr_{ij}$ is written as f_{ij} the force acting between $_i$ and j then pressure can be written as follows:

$$P = \frac{1}{V}\left[Nk_BT - \frac{1}{3k_BT}\sum_{i=1}^{N}\sum_{j=i+1}^{N} r_{ij}f_{ij}\right] \qquad 2.27$$

The forces are calculated as part of a molecular dynamics simulation, and so little additional effort is required to calculate the virial and thus the pressure. In the NPT ensemble the total pressure of the system is constant while in NVT ensemble the pressure is fluctuating throughout the simulation.

2.3.4 Radial distribution functions

Radial distribution functions (RDFs) also known as pair correlation function g(r) a measure of the probability that, given the presence of an atom at the origin of an arbitrary reference frame, there will be an atom with its centre located in a spherical shell of infinitesimal thickness at a distance, r, from the reference atom. In a solid, the radial distribution function has an infinite number of sharp peaks whose separations and heights are characteristic of the lattice structure. Consider a spherical shell of thickness δr at a distance r from a chosen atom, see figure 2.2. The volume of the shell is given by

$$V = \frac{4}{3}\pi(r+\delta r)^3 - \frac{4}{3}\pi r^3 \approx 4\pi r^2\delta r \qquad 2.28$$

If the number of particles per unit volume is ρ, then the total number in the shell is $4\pi\rho r^2\delta r$, and the number of atoms in the volume element varies as r^2. The radial distribution function of a liquid is intermediate between the solid and the gas, with a small number of peaks as short distances, superimposed on a steady decay to a constant value at longer distances.

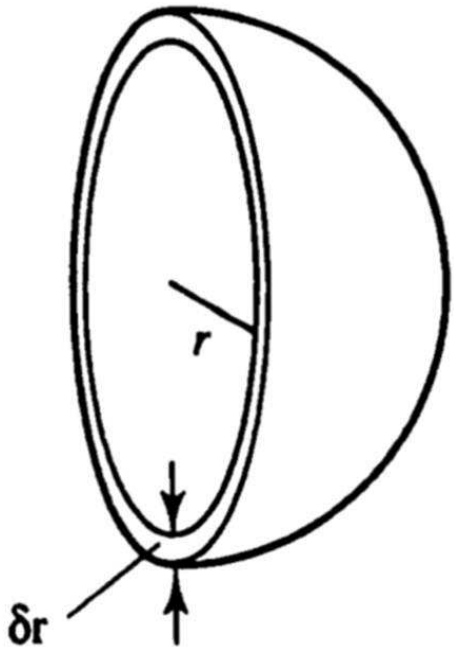

Figure 2.2: Radial distribution function uses a spherical shell of thickness δr.

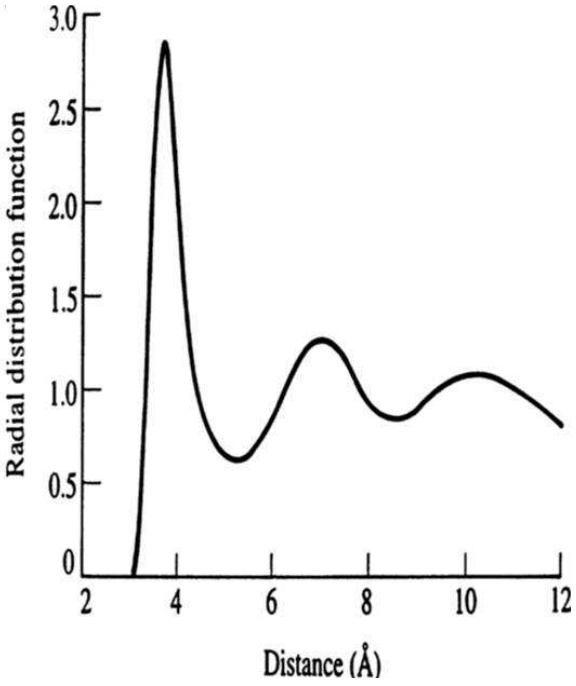

Figure 2.3: Radial distribution function determined from a 100ps molecular dynamics simulation of liquid argon.

A typical radial distribution function calculated from a MD simulation is shown in figure 2.3. At short distances (less than atomic diameter) g(r) is zero. This is due to the strong repulsive forces. The first (and large) peak occurs at approximately 3.7 Å, with g(r) having a value of about 3. This means that it is three times more likely that two molecules

would be found at this separation. The radial distribution function then falls and passes through a minimum value around approximately 5.4 Å. The chances of finding two atoms with this separation are less. At long distances, g(r) approaches one which indicates there is no long-rang order. To calculate the pair distribution function from a simulation, the neighbours around each atom or molecule are sorted into distance bins. The number of neighbours in each bin is averaged over the entire simulation. For example, a count is made of the number of neighbours between 2.5 and 2.75, 2.75 and 3.0 Å and so on for every atom or molecule in the simulation. This count can be performed during the simulation itself or by analysing the configurations that are generated.

The RDF is useful in other ways. For example, it is something that can be deduced experimentally from X-ray or neutron diffraction studies, thus providing a direct comparison between experiment and simulation. It can also be used in conjunction with the interatomic pair potential function to calculate the internal energy of the system, usually quite accurately. The radial distribution function is an important measure because several key thermodynamic properties, such as potential energy and pressure can be calculated from it. This concept also embraces the idea that the atom at the origin and the atom at distance r may be of different chemical types, say α and β. The resulting function is then commonly given the symbol gαβ(r) and is defined by Hansen and McDonald (Hansen et al 1990):

$$x_\alpha x_\beta \rho g_{\alpha\beta}(r) = \frac{1}{N}\langle \sum_{i=1}^{N_\alpha} \sum_{i=1}^{N_\beta} \delta(r - r_i + r_j)\rangle \qquad 2.29$$

where x_i is the mole fraction of chemical type *i*, N_i is the number of atoms of chemical type *i*, N is the total number of atoms, and ρ is the overall number density. The prime indicates that terms where *i* = *j* are excluded when the chemical types are the same.

2.3.5 Ensembles

Integrating Newton's equations of motion allows you to explore the constant energy

surface of a system. However, most natural phenomena occur under conditions where the system is exposed to external pressure and/or exchanges heat with the environment. Under these conditions, the total energy of the system is no longer conserved and extended forms of MD are required. Several methods are available for controlling temperature. Depending on which state variables - the energy, E, enthalpy, H (i.e., E + PV), number of particles, N, pressure, P, stress, S, temperature, T, and volume, V - are kept fixed, different statistical ensembles can be generated. A variety of structural, energetic, and dynamic properties can then be calculated from the averages or the fluctuations of these quantities over the ensemble generated. There are three most common ensembles that are often used in MD simulations NVT, NVE and NPT ensembles.

NVT ensemble is also known as canonical ensemble where temperature and volume are kept constant. NVT ensemble in statistical mechanics is a statistical ensemble representing a probability distribution of microscopic states of the system. For a system taking only discrete values of energy, the probability distribution is characterized by the probability of finding the system in a particular microscopic state with energy level, conditioned on the prior knowledge that the total energy of the system and reservoir combined remains constant.

NVE ensemble is also known as microcanonical ensemble where energy and volume are kept constant. NVE ensemble is obtained by solving the standard Newton equation without any temperature and pressure control. Energy is conserved when this (adiabatic) ensemble is generated. However, because of rounding and truncation errors during the integration process, there is always a slight fluctuation, or drift, in energy.

NPT ensemble is also known as isothermal-isobaric ensemble. This ensemble plays an important role in chemistry as chemical reactions are usually carried out under constant

pressure condition. In NPT ensemble, pressure and temperature are kept constant. The NPT ensemble is used for comparison of MD simulations with experiments. Temperature in NPT ensemble is controlled using Langevin method. The partition function can be written as the weighted sum of the partition function of canonical ensemble, Z (N, V, T).

$$\rho(N,P,T) = \int Z(N,V,T)e^{(-\beta PV)CdV} \quad 2.30$$

where

$$\beta = \frac{1}{k_B T} \quad 2.31$$

k_B is the Boltzmann constant and V is the volume of the system.

2.3.6 Periodic boundary conditions

Periodic boundary conditions (PBC) are a set of boundary conditions that are often used to simulate a large system by modelling a small part that is far from its edge. A periodic boundary is an important technique in a molecular dynamics simulation. It is a clever trick to make a simulation that consists of only a few hundred atoms behave as if it was infinite in size. The main reason this is required is to remove the effects of the surface, which any finite sample of matter must have, and which ensure that the internal structure of the sample is dominated by surface rather than bulk forces (like surface tension - recall how a small drop of water tries to assume a spherical shape, in such cases the surface forces overwhelm the structure of the bulk liquid). Figure 3.4 illustrates the concept of periodic boundary conditions in two dimensions. The shaded box represents the system we are simulating, while the surrounding boxes are exact copies in every detail - every particle in the simulation box has an exact duplicate in each of the surrounding cells. Even the velocities (indicated by the arrows) are the same. This arrangement is imagined to fill the whole of space. A result of this is that whenever an atom leaves the simulation cell, it is replaced by another with exactly the same velocity, entering from the opposite cell face. So the number of atoms in the cell is conserved. Furthermore, no atom feels any

surface forces, as these are now completely removed. In the figure r_{cut} is the cutoff radius that is normally applied when calculating the force between two atoms.

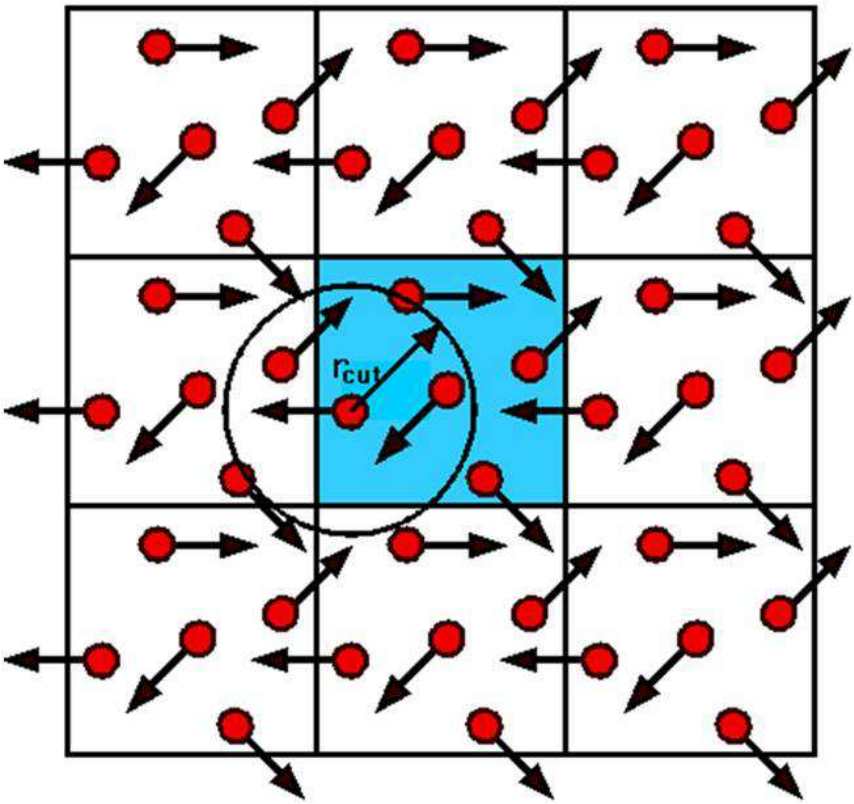

Figure 2.4: Illustration of the concept of periodic boundary conditions.

2.4 Amorphisation and Recrystallisation technique

Amorphisation and recrystallisation technique (Sayle et al. 2002a) is the strategy that has being used in atomistic simulation where the complex structures evolve during a pseudo-recrystallisation from an amorphous starting point. Amorphisation and recrystallisation is an evolutionary simulation technique where compression or tension is applied to the system to displace atoms from equilibrium positions. When pressure is released atoms are accelerated to equilibrium positions having high ionic mobilities as molten systems. To generate realistic models of supported oxide thin films one must consider various factors including the epitaxial relationships, defects and reduced interfacial ion densities. The defects, which evolve in respond to misfit accommodation,

may include dislocations arrays, vacancies, substitutions and interstitials including clustering of such defects. These structural features must be achieved in order to generate a realistic model even though some are challenging. To overcome the problems associated with the starting structure, the supported thin film is forced to undergo an amorphous transition before recrystallising into a final structure. Such a procedure eliminates any possibility of the final structure reflecting artificially the starting structure. Essentially the system loses all memory of the preparatory configuration and dynamical simulation, as applied to an amorphous structure, allows a more comprehensive exploration of the configurational space, which is likely to results in an energetically more favourable, and hence more realistic, final interface structure. This methodology allows interfacial structures to evolve during the course of the simulation influenced solely by the substrate material and associated lattice misfit. Various mechanisms for inducing amorphisation have been explored for supported metal-oxide thin films associated with both positive and negative lattice misfits. These include performing dynamical simulation at very high temperatures to melt the thin film and constraining the thin film under conditions of compression or tension: under dynamical simulation, the considerable strain within the thin film results in an amorphous structure. The latter can be achieved either by modifying artificially the potential parameters during the amorphisation step or by constructing an interface system with a particular associated lattice misfit (positive or negative) based upon, for example, some particular near coincidence site lattice (Sutton et al 1987 and Sayle et al 1993). The amorphisation is induced by straining the support thin film under high compression. The application of high-temperature dynamical simulation to this strained system results in the amorphisation of the thin film overlayer. Prolonged dynamical simulation is required to allow the system to recrystallise under the influence of the support. This methodology is

purely a simulation technique to derive low energy structures and the structural evolution of the system bears no physical significance. The main driving force to the amorphisation is the strain under which the thin film is constrained, while the temperature at which the dynamical simulation is run is secondary to inducing amorphisation. For example, the procedure can be performed equally as well at 20 K as at 200 K. However, the recrystallisation process at 20 K is much slower. In essence, the optimum temperature is one that allows the structure to evolve but that falls of melting the thin film. This would be detrimental as it would prevent recrystallisation and require an additional quenching step (Sayle et al 2001a). An important feature of the methodology is that the amorphous transition enables all memory of the preparatory configuration to be lost (radial distribution functions for the amorphous thin film are broad (Sayle et al 2001a) indicating no long range ordering) and therefore the final structures cannot reflect artificially the starting structure. The recrystallisation is deemed complete when the system is no longer evolving structurally or energetically, the duration of which is system dependent. In addition, dynamical simulation, as applied to an amorphous structure, allows a more comprehensive exploration of the configurational space, which is likely to result in an energetically more favourable, and hence more realistic, final interface structure (Sayle et al 2001b).

This technique has been implemented on various materials such as thin films and nanoparticles (Sayle et al. 2003), generate models for CeO_2 nanocrystallites (Sayle et al. 2002c), microstructure in MnO_2 (Sayle et al. 2006), shape of CeO_2 nanoparticles (Sayle et al. 2004), MgO cluster supported on BaO (100) (Sayle et al. 2002a) and lithium insertion into MnO_2 (Maphanga et al. 2011). In this work we will employ this technique on the nanostructures and lithiated nanostructures of TiO_2. In order to lithiate the various nano-architectures, lithium ions will be inserted at random positions in the amorphous

TiO_2; and coordinates will be chosen to ensure that Li ions are not positioned on top of other atoms in the simulation cell. To facilitate charge neutrality, an equivalent number of Ti^{4+} species were reduced to Ti^{3+}. The method was previously used successfully in the bulk MnO_2 (Maphanga et al. 2011). We will also present the radial distribution functions of the systems to verify the process of amorphisation and recrystallisation.

2.5 X- Ray Diffractions

2.5.1 Diffraction from powder samples

X-ray crystallography is a method used for determining the atomic and molecular structure of a crystal, in which the crystalline atoms cause a beam of X-rays to diffract into many specific directions. We use a reflex powder diffraction to calculate radiation of X-ray diffractions. A powder sample is a collection of individual crystallites, ideally having a random distribution of orientations. This complete powder averaging has two conditions: those crystallites with each set of planes, *hkl*, are suitably aligned for diffraction to occur and that each such collection of crystallites spans a random collection of orientations of the planes about the incident beam direction. When these conditions are met, then diffracted intensity can be observed that is continuous in a cone around the straight-through beam direction, with a radius determined by Bragg's law, rather than the discrete spots obtained from the single crystal in figure 2.5.

As for single crystal diffraction, an essential ingredient for the simulation of a powder diffraction experiment is the calculation of the structure factors F_{hkl}, which are related to the atomic positions and atomic scattering factors via equation below

$$F_{hkl} = \sum_1^N f_n e^{2\pi i(hu_n+kv_n+lw_n)} \qquad 2.32$$

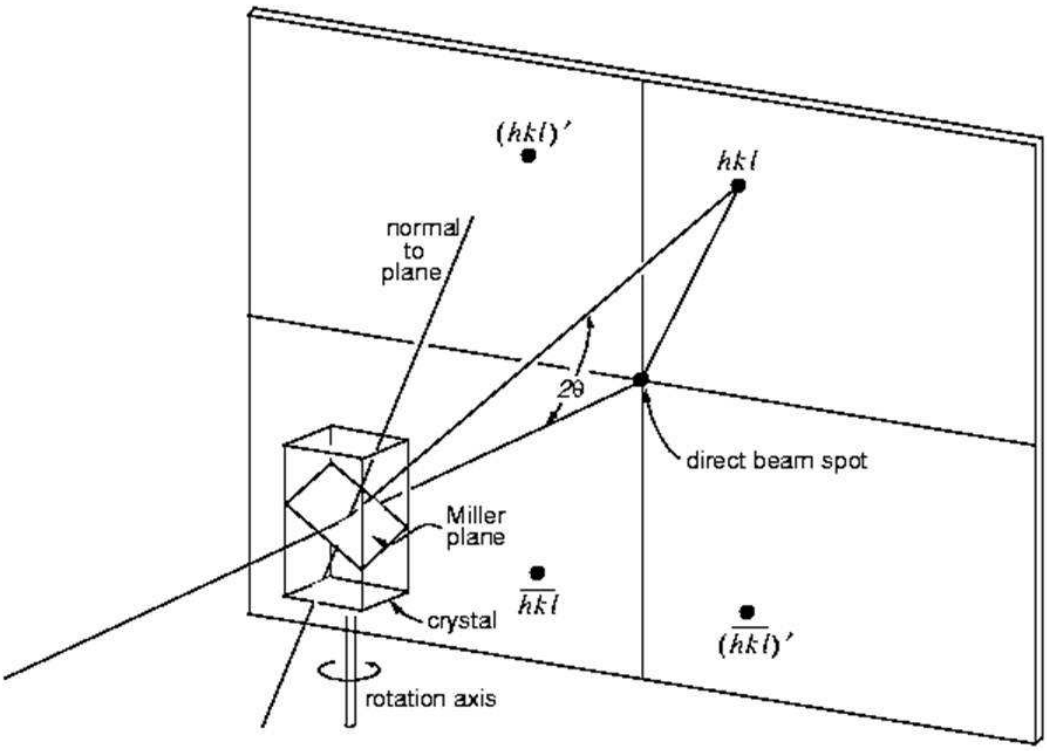

Figure 2.5: Diffraction from a Single Crystal Measured in a Rotation Exposure.

The powder diffraction intensity observed at diffraction angle 2θ is then given as:

$$I(\theta) = \sum_{hkl} p_{hkl}(2\theta - 2\theta_{hkl}) I_{hkl} \qquad 2.33$$

where the Integrated Bragg Intensity I_{hkl} is related to the structure factors F_{hkl} via:

$$I_{hkl} = M_{hkl} P_{hkl} L_{hkl} |F_{hkl}|^2 \qquad 2.34$$

Here

M_{hkl} is the multiplicity of reflection *hkl*

P_{hkl} is the preferred orientation correction for reflection *hkl*

L_{hkl} is the Lorentz and polarization correction for reflection *hkl*.

$p_{hkl}(2\theta - 2\theta_{hkl})$ is an appropriate profile function.

The profile function may include an asymmetry correction, and its width depends on instrument resolution and sample broadening effects.

2.5.2 Multiplicity and systematic absences

2.5.2.1 Multiplicity

In the single crystal rotation geometry shown in figure 2.5, two distinct reflections, *hkl* and *-h-k-l* are each recorded twice in the rotation exposure. Were the crystal, say, to be cubic, with rotation about [001], the planes 100, -100, 010, and 0-10 would all pass through the diffraction condition and be recorded at the same Bragg angle, 2θ. The random collection of orientations in powders implies that all the equivalent reflections contribute to a given diffraction cone, so that the intensity recorded at the appropriate Bragg angle simultaneously contains contributions from the 100, -100, 010, 0-10, 001, and 00-1 planes. The system symmetry in this case dictates that the intensity contributed by each of these planes is equal, but since there are six of them, the measured intensity must be divided by a multiplicity factor of six in order to obtain a relative measure of the 100 intensity. This multiplicity factor depends on the symmetry of the structure and on the nature of the indices, *h*, *k*, and *l*. For a general index plane, *hkl*, the multiplicity varies from 2 in the lowest triclinic symmetry to 48 in the highest symmetry cubic case. Friedel's law states that the intensity of radiation scattered from a given plane *hkl* is equal to that from its inverse, *-h-k-l*. Although this law breaks down when anomalous scattering effects are significant, it is assumed to apply uniformly here.

2.5.2.2 Systematic absences

Bragg reflections occur when the radiation scattered by each of the atoms, in the unit cell, do so in phase, i.e., constructive interference. For a primitive cell, the intensities of

the reflections are easily predicted. In the case, however, of non-primitive cells there are special conditions which result in reflections of zero intensity. These are called systematic or space group absences.

In the case of an I-lattice with lattice points at (0,0,0) and (1/2,1/2,1/2), it is observed that for reflections where the sum of the indices (h + k + l) is odd, no reflection is detected. This can be explained by the diffraction process from the (100) plane, where the combined scattering from the (0,0,0) lattice points do so completely in phase at the specific Bragg angle, but those at the (1/2,1/2,1/2) actually interfere. As there are equal occurrences of the two lattice points, they will cancel out. For centred systems the following equation can be used to predict the presence/absence of Bragg peaks; reflections will only be observed when *n* is an integer.

$$hx_n + ky_n + lz_n = n \qquad 2.35$$

Where: *h*, *k* and *l* refer to reflection (hkl)

X_n, Y_n and Z_n refer to the *n*th lattice point's location in the lattice.

In addition to centred cells, systematic absences will occur in non-primitive systems when glide planes and/or screw axes are present. The method employed to determine whether a reflection is absent in these circumstances requires knowledge of the rotational and translational operators which define the crystal symmetry.

If a reflection, H = (hkl), is unchanged by applying a rotation operator, R, and if the scalar product with the corresponding translation operator, T, is not an integer, then the reflection is absent.

$$H.T = ht_x + kr_y + lt_z = H \qquad 2.36$$

$$H.T = ht_x + kt_y + lt_y \neq n \quad 2.37$$

If both of these conditions are satisfied then the reflection is computed to have zero intensity.

2.5.3 Correction factors in Powder Diffraction

The powder diffraction trace represents a 1D projection of the 3D scattering intensities of each of the atoms in the unit cell. Translating the calculated reflection intensities into a continuous spectrum that accurately predicts the experimental trace requires knowledge of the conditions that existed during data collection. Using this knowledge a number of corrections are applied to the intensity list to produce a realistic trace. These corrections are as follows: Lorentz and polarization correction, instrumental broadening, sample broadening, asymmetry corrections, preferred orientation and line shift correction.

2.6 Lithiation of nanostructures

This section discuss on how the Li ions were introduced into the titania nanostructures in chapter four. The lithiation program used in the current study was written by Kgatwane (2011).

2.6.1 Lithiating at Octahedral Sites

The pristine TiO_2 nanostructures are large and comprise 15972 atoms; 5324 titanium atoms and 10648 oxygen atoms. Additionally, they are heavily twinned and non-crystalline making it difficult to easily compute the coordinates of the 1x1 tunnel sites by using the knowledge of symmetry and lattice constants. However, each tunnel is enclosed by four walls of linked edge-sharing TiO_6 octahedral chains with slightly

varying distance between the chains. The program uses these twinning octrahedral chains to estimate the tunnel sites where lithium ions will be intercalated.

Slicing the TiO_6 octahedral chain planes and rendering min polyhedral view reveals different the 1x1 tunnel configurations (figure 2.6). During intercalation, lithium ions are placed at specific locations in the tunnels which we denote lithium insertion sites. The estimation of the coordinates of these lithium insertion sites is calculated with the midpoint formula for different tunnel configurations shown in a figure below.

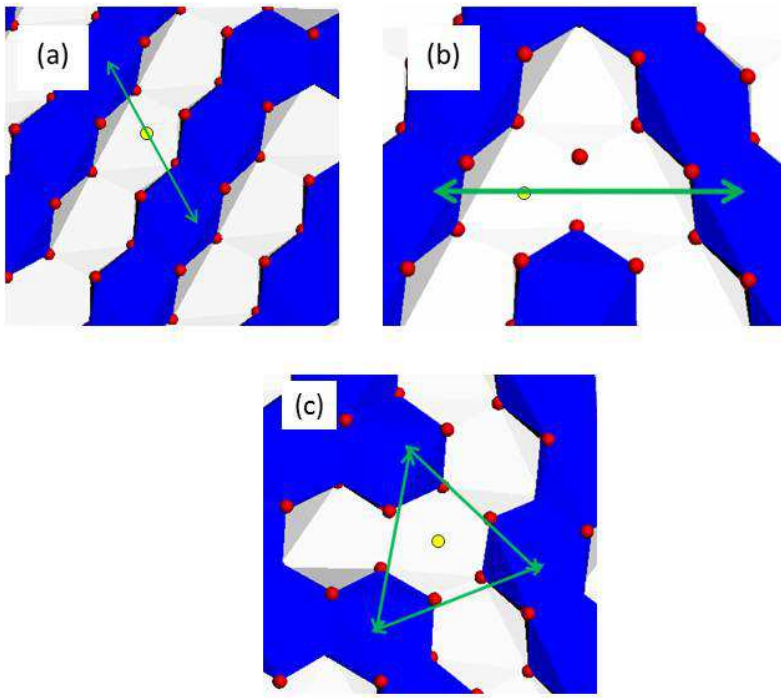

Figure 2.6: A slice through the nanostructure showing different tunnel configurations. The yellow circle is the lithium insertion site.

The coordinates of the lithium insertion site (x, y, z) for a tunnel structure in figure 2.6 (a) is estimated by using the two or three titanium atoms on the same TiO_6 octahedral planes, depicted by the ends of the arrow in the midpoint formula:

$$(x, y, z) = \left(\frac{x_1+x_2}{2}, \frac{y_1+y_2}{2}, \frac{z_1+z_2}{2}\right) \quad 2.38$$

In figure 2.6 (b) the estimation of the insertion sites is achieved by applying the midpoint formula twice. Applying the midpoint formula once result in a coordinate in the middle of the two tunnel sites. Using the newly computed coordinate with the coordinate of one of the manganese atoms at the ends of the arrow in the formula gives the coordinate of the tunnel site (yellow circle):

$$(x,\ y,\ z) = \left(\frac{x_1}{2} + \frac{x_1+x_2}{4}, \frac{y_1}{2} + \frac{y_1+y_2}{4}, \frac{z_1}{2} + \frac{z_1+z_2}{4}\right) \quad 2.39$$

In the last case i.e. in figure 2.6 (c) the computation of the tunnel sites is accomplished by using the coordinates of three manganese atoms in the triangle midpoint formula:

$$(x,\ y,\ z) = \left(\frac{x_1+x_2+x_3}{3}, \frac{y_1+y_2+y_3}{3}, \frac{z_1+z_2+z_3}{3}\right) \quad 2.40$$

The decision of whether two manganese atoms can be used to compute an insertion site depends on the separation distance between them. The Ti-Ti radial distribution function of the nanostructure provides us with a good estimate of these separation distances.

The program computes the lithium insertion sites by checking the separation distance between each pair of titanium atoms in the range specified by the third, fifth and ninth peaks in the radial distribution function of a rutile-type structure and using the appropriate form of the midpoint formula. The insertion site is then validated by checking its distance from all atoms within a small cube constructed around the insertion site with dimensions that are slightly larger than the minimum Ti-O (Ti – titanium in rutile-type structure) separation distance. If there is an atom (Ti, O, or Li^+) which is closer to the insertion site by more than 1.6 Å (for pyrolusite) then the insertion site is not valid and it is discarded. All valid insertion sites are then saved in a file that will be used during lithium insertion into the various nanostructures.

2.6.2 Lithium Insertion

The program uploads the lithium insertion sites from the file produced in the previous step, randomly selects a tunnel site and inserts a lithium ion at its coordinates. Charge compensation in the structure is achieved by changing the titanium (4+ oxidation state) closest to the lithium cation into the Jahn-Teller active titanium (3+ oxidation state). This process is repeated for all the lithium ions inserted in the structure. Note that the program randomly selects an insertion site and the corresponding closest trivalent titanium cation and this can result in different lithium-titanium configurations with different energies. The lithiated structure is not of the lowest energy. To obtain the lowest energy structure one could lithiate in a monte carlo way and then run molecular dynamics simulations on each configuration which would be very time consuming considering the massive size of the nanostructures.

Chapter 3
Nanostructures of Titanium Dioxide

3.1 Introduction

In this chapter we present and discuss the growth of titanium dioxide nanostructures using atomistic simulation methods. We will introduce the interatomic potentials used throughout this work and their theoretical background was discussed in chapter 2. We further present the simulation technique employed to generate models of various nano-architectures i.e. nanosheet, nanosphere and nanoparticles of TiO_2; i.e. amorphisation and recrystallisation technique. Microstructures and radial distribution functions (RDFs) will also be presented, and some microstructures will be compared with experimental results, where available. XRDs of the various nano-architectures are calculated and compared with existing experimental results.

3.2 Methodology

Calculations are based on the Born model of ionic solids, where Titanium (Ti) and Oxygen (O) ions interact via long-range Coulomb and short range interactions. The potentials used in this study were optimized by Matsui (Matsui et al. 1991) for the four polymorphs of TiO_2 (rutile, anatase, brookite and TiO_2 II [α-PbO_2 structure]), and are presented in table 3.1. The short range interactions are described by Buckingham potentials (discussed in chapter 2) and the interaction energy takes the form

$$U_{ij} = \frac{q_i q_j}{4\pi\varepsilon\varepsilon_0 r_{ij}} + A_{ij} exp\left(-\frac{r_{ij}}{\rho_{ij}}\right) - \frac{C_{ij}}{r_{ij}} \quad 3.1$$

The model uses partial atomic charges. The core charges used in this work are presented in table 3.2.

Table 3.1 Buckingham Potentials used.

Ion pair ($_{ij}$)	A_{ij} (eV)	ρ_{ij} (Å)	C_{ij} (eV.Å6)
Ti-O	16957.530	0.1940	12.5900
Ti-Ti	31120.200	0.1540	5.2500
O-O	11782.760	0.2340	30.2200

Table 3.2 Core charges used.

Species	Core (e)
Ti^{4+}	2.196
O^{2-}	-1.098

XRDs measurements were performed using Bragg-Brentano Geometry. The calculations were performed under different sources; i.e. iron and copper. For iron we used the wavelength λ1 of 1.936042 Å and λ2 of 1.93998 Å, and the wavelength λ1 of 1.540562 Å and λ2 of 1.54439 Å were employed for copper. We used pseudo-Voigt function for both sources.

3.3 Growth of TiO_2 nanostructures

Starting from a single crystal structure of titanium dioxide we have constructed a supercell which consists of 15972 atoms (5324 titanium and 10648 oxygen atoms), as shown in figure 3.1. A nanostructure of TiO_2 was simulated in a cell with a lattice vector of 101 Å, using an NVE ensemble, where volume and energy are kept constant. The system was amorphised and a related nanosphere is given in figure 3.5 (a) and other forms of nanostructures were deduced from the nanosphere.

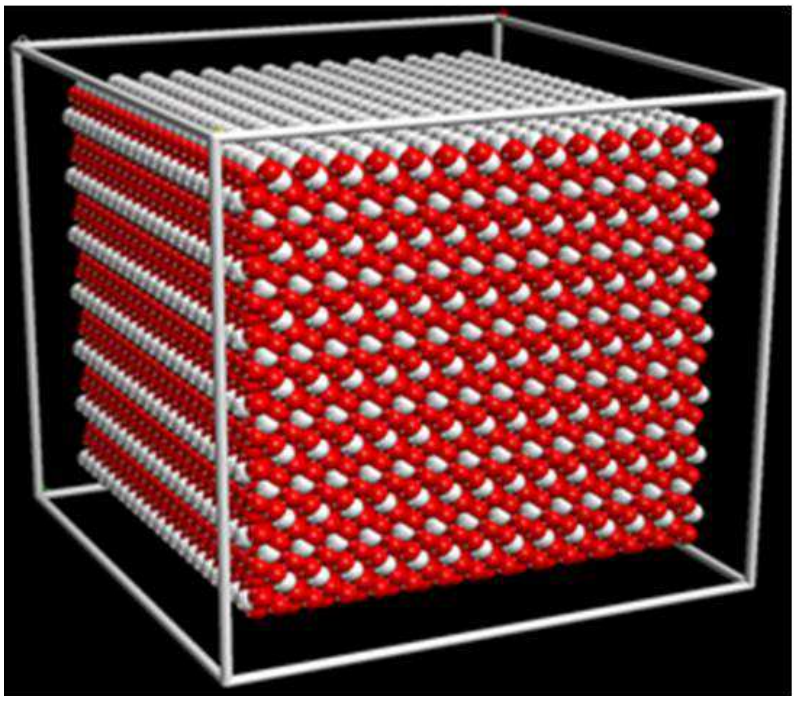

Figure 3.1: Starting supercell for generating nanostructures of TiO_2.

In the current study we followed a strategy that has been devised by Sayle and Sayle (2007), for generating full atomistic models of TiO_2 nanocrystals, by simulating crystallisation at high pressure starting from a molten precursor. They prepared a simulation cell where the TiO_2 nanoparticle was surrounded by a monoatomic 'gas', and the latter were included in order to enhance chances of crystallisation under pressure. In particular, a molten TiO_2 nanoparticle was generated at 6000 K and then crystallised at 2000 K with 20 GPa under the NPT ensemble. We took the nanoparticle at 2000 K, whilst in an amorphous phase, and crystallised it under pressure in accordance with Sayle and Sayle (2007). In addition we carried out a calculation under the NVT ensemble, where crystallisation of the nanosphere was also achieved. This is evidenced by the corresponding variation of the configuration energy with time, in figure 3.2, where the energy changes from -1.759×10^5 eV in the amorphous and nucleation stages to -1.775×10^5 eV after crystallisation. The structures of the nanoparticles crystallised with gas atoms at 20 GPa, and 150 GPa, under the NVT, are depicted in figure 3.3 (a) and (b)

and do not differ much.

We further carried out an MD calculation for 25000 timesteps with the NVT ensemble to initiate nucleation and paused just before crystallisation commenced. The gas molecules were removed from such an ensemble, and the pressure on the nanoparticle was increased

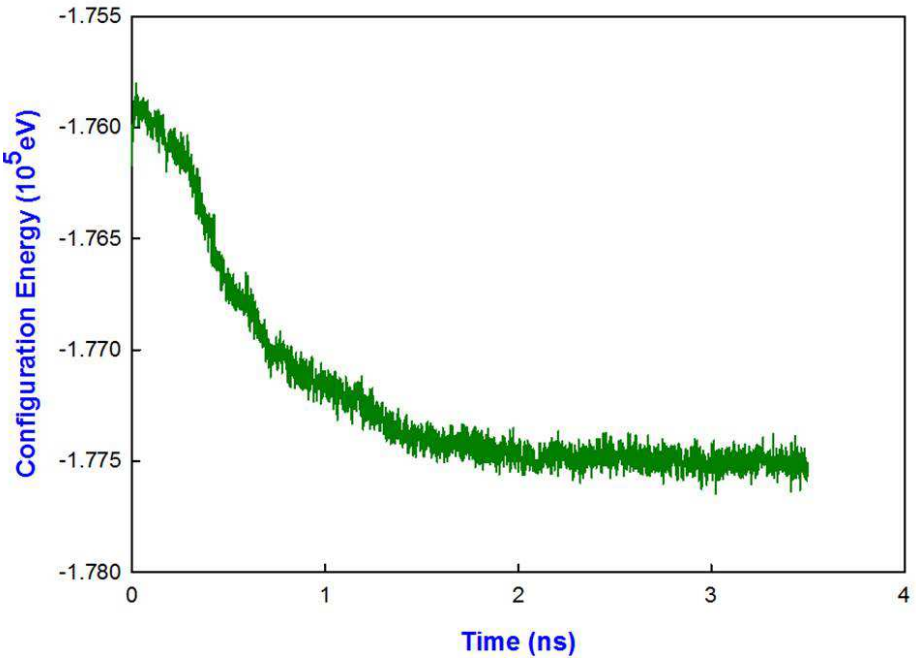

Figure 3.2: Calculated configuration energy as a function of time for the TiO_2 nanosphere with gas atoms.

to 150 GPa in order to stabilise it. Continuation of the run under the NVT ensemble changed the configuration energy of the amorphous nanosphere from -1.76 $x10^5$ to -2.014 $x10^5$ eV and the associated initial RDFs are shown in figure 3.7, indeed confirming that the nanoparticle is still amorphous. After full crystallisation, the configuration energy was reduced to -2.040 $x10^5$ eV as shown in figure 3.8. The structure of the nanoparticle without gas atoms at 150 GPa is given in Figure 3.3 c and is not much different from those of figures 3.3 (a) and (b).

We further attempted to ascertain how the extent of nucleation would affect the microstructures of crystallised nanosphere; Hence the amorphous and nucleation phase,

in the presence of gas atoms, was also allowed to run beyond 25000 timesteps, mentioned above, which pushed the nanosphere into the early stages of crystallisation (where a partially amorphised nanosphere was generated). The gas atoms were then removed and the simulation allowed to proceed as was done in the previous paragraph; changes to the structure and microstructure were hardly noticeable from those in observed figures 3.3.

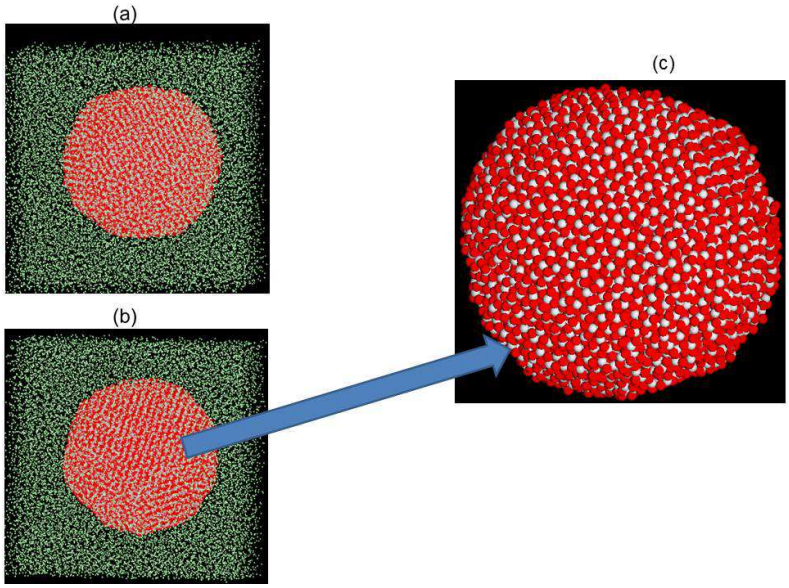

Figure 3.3: Nanostructures of TiO_2, (a) with gas atoms at 20 GPa, (b) with gas atoms at 150 GPa and (c) without gas atoms.

The purpose of generating a nanosphere that is capable of crystallising in the absence of gas atoms was to utilise such a nanosphere in the production other nano-architectures, such as the nanosheet, nanoporous and bulk structures of TiO_2 under the NPT ensemble as was done by Sayle et al. (2009) on MnO_2. They crystallise MnO_2 under NPT with gas atoms to prevent the structure to change and without gas atoms the structure will change under NPT ensemble.

A schematic illustrating the strategy used to construct extended nanostructures is shown in figure 3.4 Top: a periodic array of nanoparticles is constructed in which the nanoparticles are introduced into simulation cells of size a1× a2. The simulation cell

sizes are then reduced to 0.85 a1× a2, top middle. The close proximity between nanoparticles along a1 causes the nanoparticles, under MD, to start to agglomerate, top right, facilitating the evolution of a one-dimensional nanorod. On the other hand, if the sizes of the simulation cells are reduced to 0.85a1 and 0.85a2, bottom left, the nanoparticles can agglomerate in two directions facilitating the evolution of a nanosheet, bottom right. If the nanoparticles agglomerate in all three directions, a porous architecture will result. In our case we allowed it to agglomerate in two dimensions to form a nanosheet. Clearly, if the distance between neighbouring nanoparticles is high, then the nanoparticles are not able to agglomerate. Reproduced with permission from ACS copyright 2009.

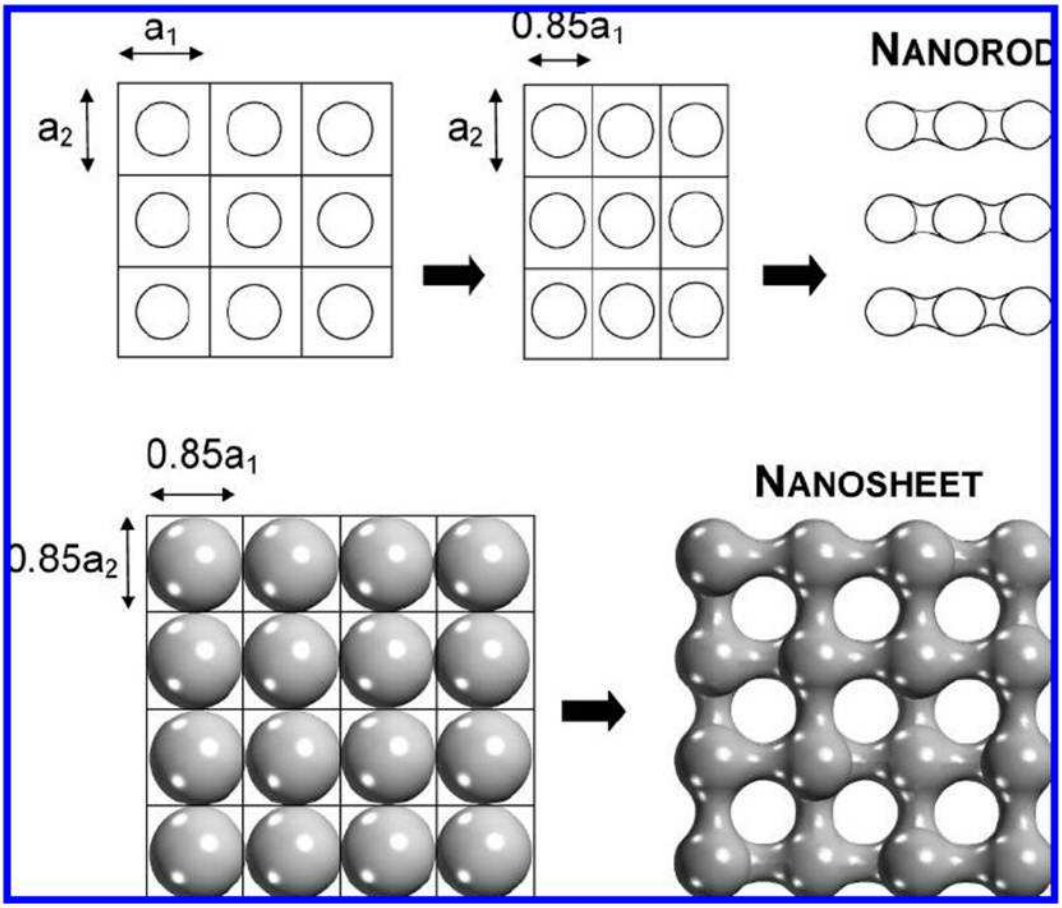

Figure 3.4: Schematic illustrating the strategy used to construct extended nanostructures. (From Sayle et al. 2009).

A general and systematic simulation strategy for creating models (atom coordinates) of nanomaterials has been developed (Sayle et al. 2006). In particular, amorphised nanoparticles are assembled into periodic arrays, using crystallographic rules, and facilitate their aggregation and crystallisation into framework nano architectures, as illustrated in Figure 3.2. As mentioned earlier, the major reason for removing the gas atoms early in the simulation (before crystallisation), unlike at a later stage as executed by Sayle and Sayle (2007), is to enable production of different nano-architectures of TiO_2 i.e. nanosheet, nanoporous, and bulk structures, under NPT ensemble. The nanostructures were obtained at the different box sizes and are presented in figure 3.5. Table 3.3 features the parameters of nanostructures obtained.

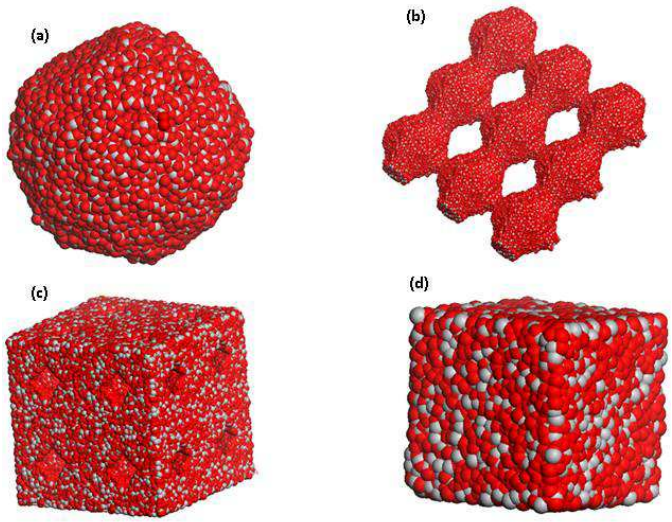

Figure 3.5: Nanostructures of TiO_2 produced during an MD simulation with an NPT ensemble (a) nanosphere, (b) nanosheet, (c) nanoporous and (d) bulk.

Two nanoporous structures at different box sizes, were considered, the first one was deduced from a lattice box of 60 Å while the second one is associated with a lattice box of 66 Å. The main difference between the two nanoporous structures is that the one corresponding to smaller box size has small channels while the other has larger channels; both are shown in figure 3.6. In the next section we will perform long molecular dynamics simulations in order to crystallise all generated nano-architectures.

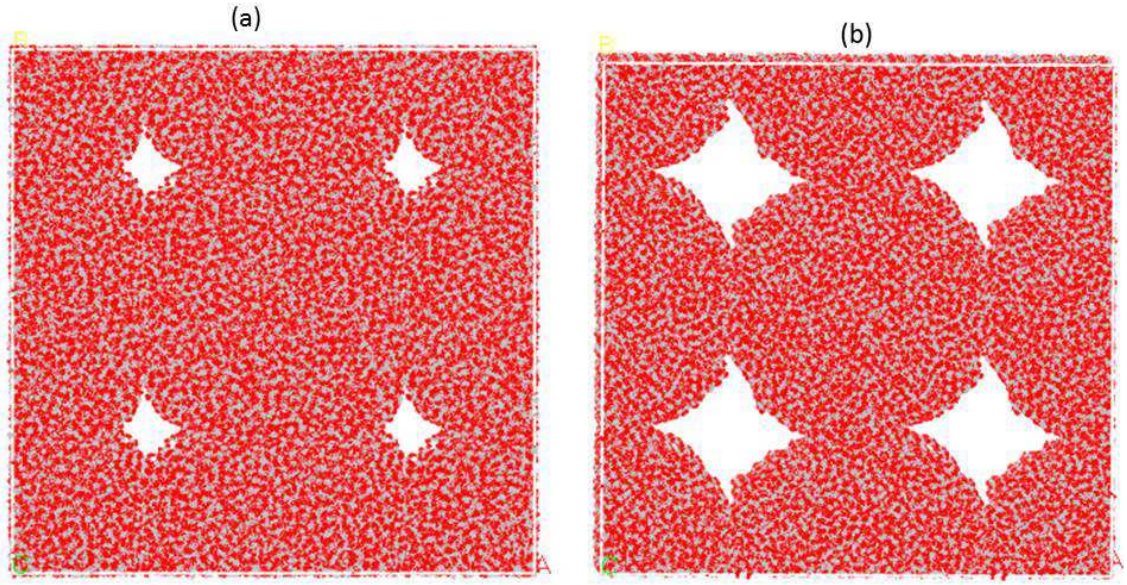

Figure 3.6: Amorphous nanoporous structures of different box size (a) Box size of 60 Å and (b) box size of 66 Å.

Table 3.3: Nano-architectures of titanium dioxide

	Nanoparticle	**Nanosphere**	**Nanosheet**	**Nanoporous**	**bulk**
Structural notation	nano	sphere	sheet	meso	bulk
Box size	100*100*100	101*101*101	75*75*75	60*60*60 (66*66*66)	53*53*53
Dimensions	0-D	0-D	2-D	3-D	3D

3.4 Amorphisation and recrystallisation of nanostructures

In this section we present the amorphised and recrystallised grown nanostructures of TiO_2. Radial distribution functions, microstructures and XRDs patterns of the nanostructures are also introduced and discussed. A graph of the configuration energy as a function of time will be shown, since it indicates how the nanostructures change from

an amorphous to a crystallised phase and will features the time required for the system to recrystallise. A comparison of structural properties will be made with the available experimental results.

3.4.1 Titanium dioxide nanosphere structure

The A+R method was applied to a nanosphere discussed in section 3.3 and the radial distribution functions of amorphised nanosphere are shown in figure 3.7. They depict broader peaks after 4 Å, indicating that the nanosphere is in an amorphous phase. We performed a molecular dynamics simulation using the NVT ensemble, at a temperature of 2000 K for 700000 steps with a time step of 0.005 ps, in order to recrystallise the nanosphere of TiO_2. The associated configuration energy as a function of time is given in figure 3.8.

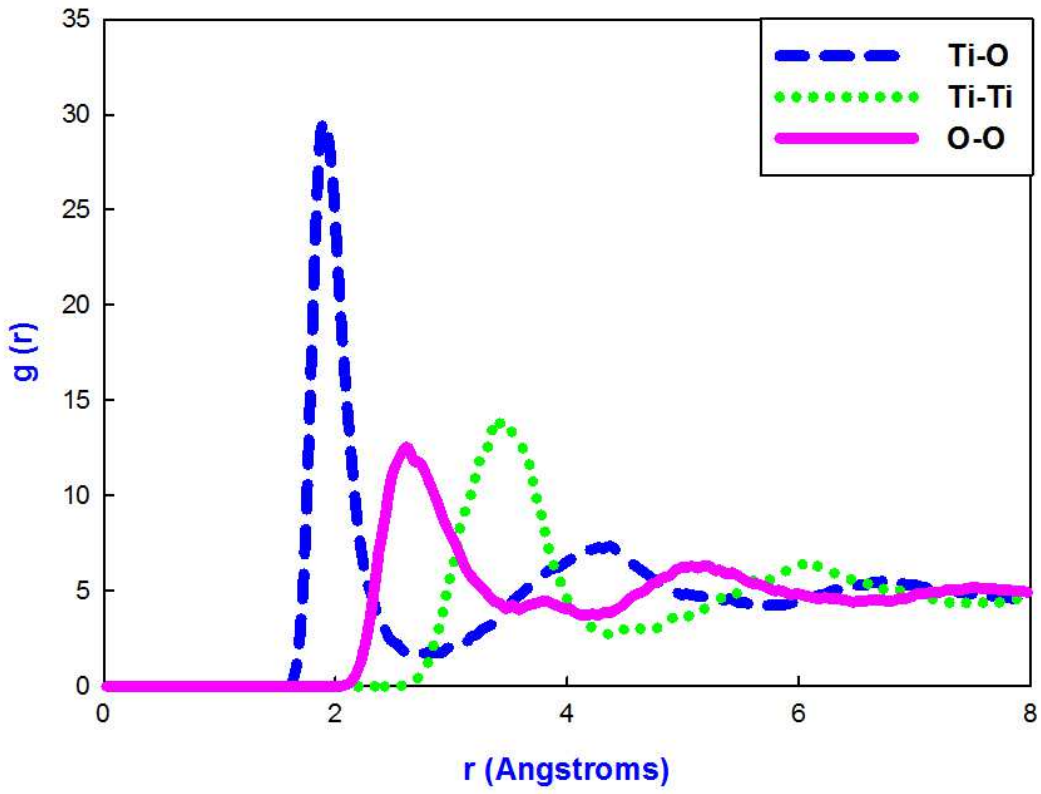

Figure 3.7: RDFs of the amorphous TiO_2 nanosphere before recrystallisation at 2000 K.

The change of the configuration energy from -2.015x10^5 to -2.043 x10^5 eV corresponds to the latent heat of crystallisation and is associated with the transition from an amorphous to a crystalline phase. Beyond 0.6 ns the change in the configuration energy is very small, which indicates that the nanosphere has recrystallised. At 2 ns the energy starts to be near constant which reveals that complete recrystallisation has been achieved. The graph of the configuration energy against time, for the nanosphere, behaves similarly to that of the bulk MnO_2 (Sayle et al. 2009).

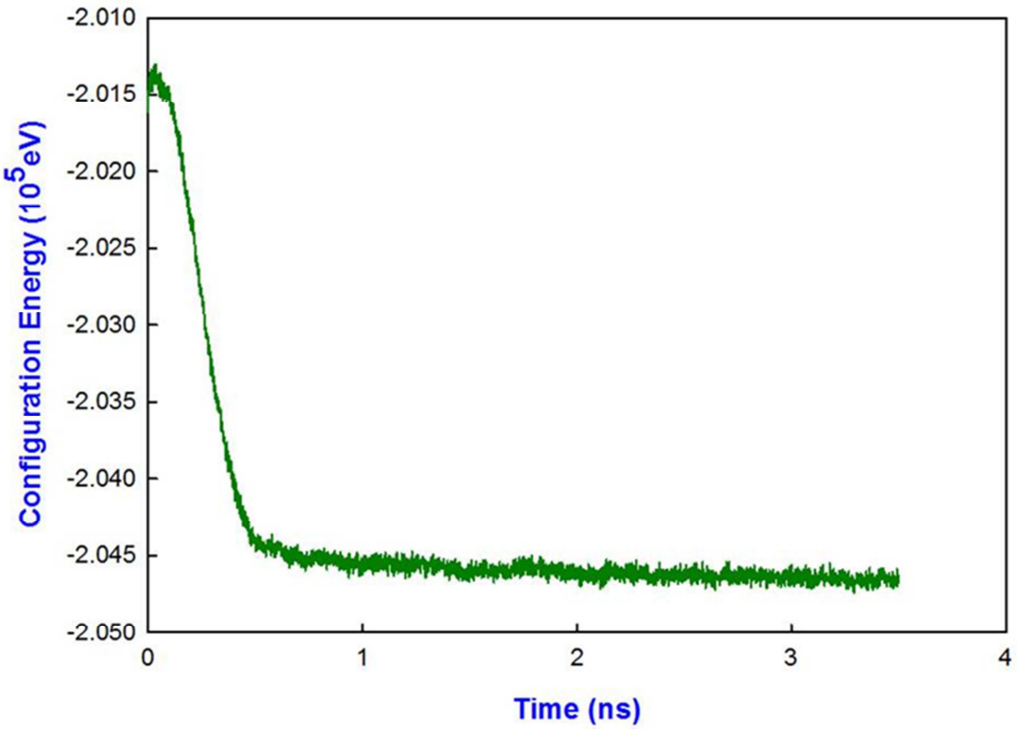

Figure 3.8: Calculated configuration energy as a function of time for the TiO_2 nanosphere.

Figure 3.9 (a) and (b) features amorphised and recrystallised structures of the nanosphere respectively, and crystalline patterns can be observed in figure 3.9 (b). We have cut a slice from the recrystallised nanosphere (Figure 3.9) in order to depict twinning patterns and grain boundaries, which are given in figure 3.10. Snapshots of the nanosphere, illustrated in appendix D, show a clear progress of the nucleation and crystal growth.

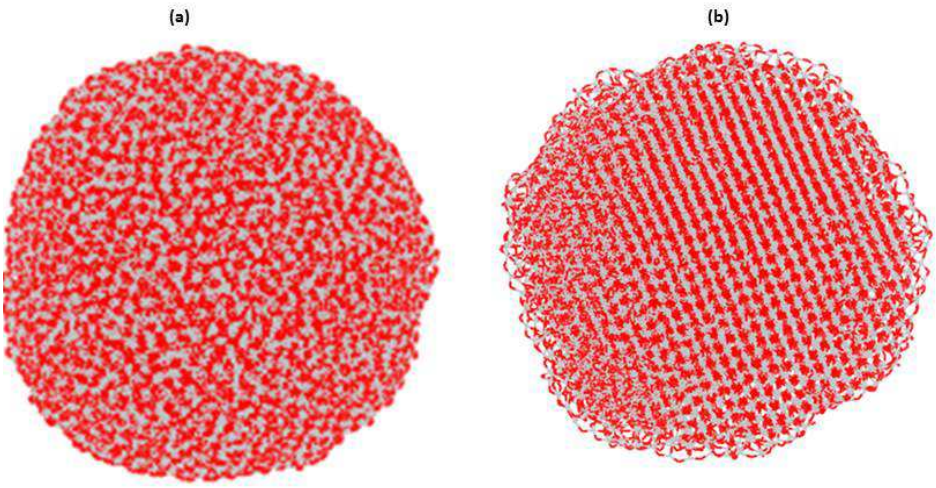

Figure 3.9: Structure of TiO_2 nanosphere (a) amorphised and (b) recrystallised.

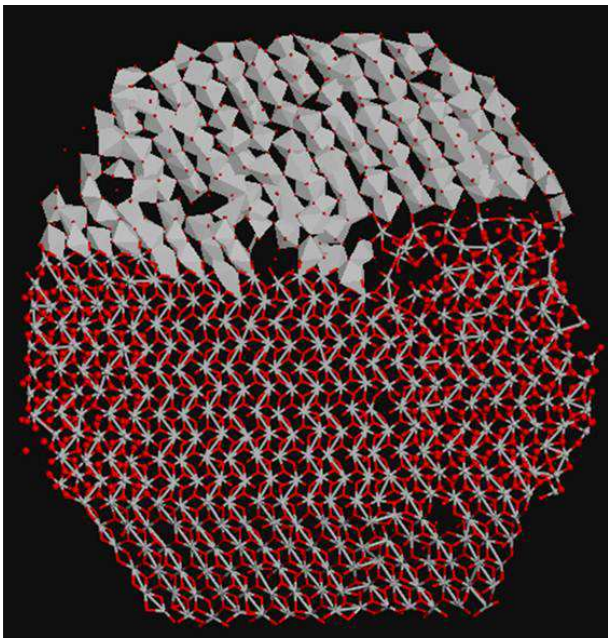

Figure 3.10: Structure of a recrystallised TiO_2 nanosphere showing twinning patterns.

The radial distribution functions (RDFs) of TiO_2 nanosphere after recrystallisation for Ti-O, Ti-Ti and O-O interactions, are given in figure 3.11. We observe more peaks than those of figure 3.7, and at approximately 2.0 Å there is a maximum peak which is attributable to the Ti-O interactions. Between 2 and 4 Å there are peaks related to Ti-Ti and O-O interactions. Beyond 4 Å the peaks emanate from Ti-O, Ti-Ti, and O-O interactions. In the presence of more and sharper peaks it can be concluded that the TiO_2 nanosphere has recrystallised.

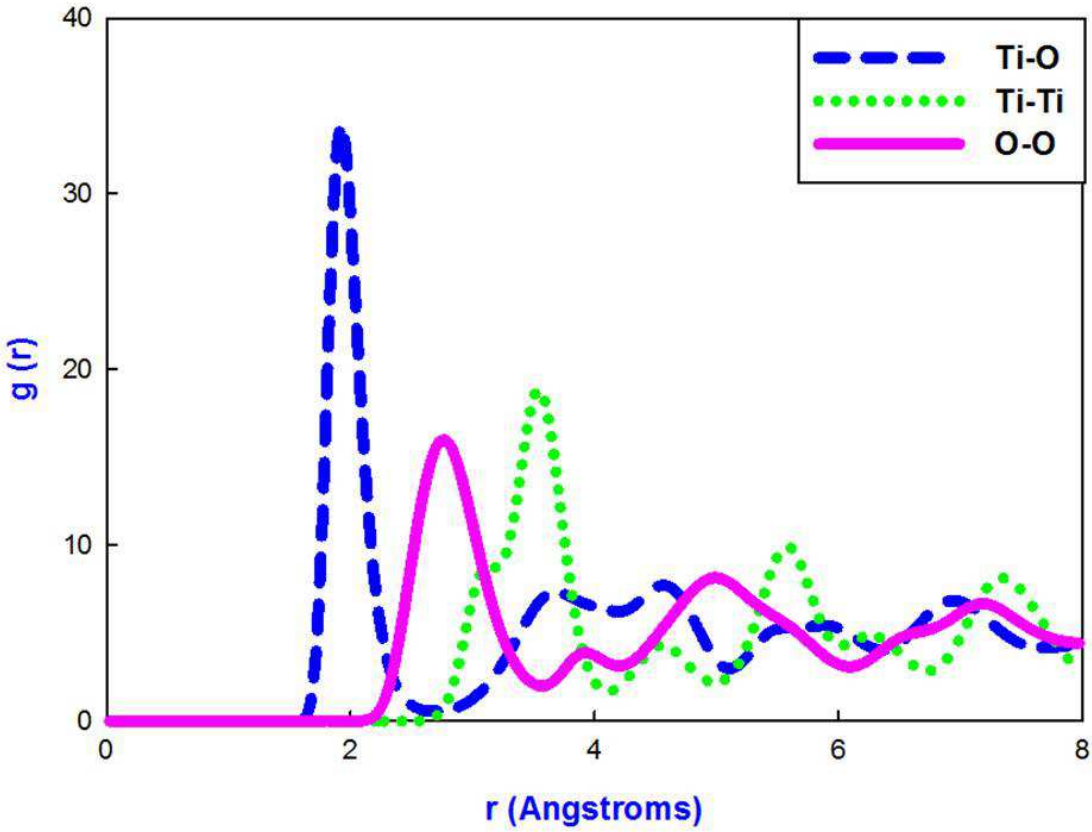

Figure 3.11: RDFs of the TiO_2 nanosphere after recrystallisation at 2000 K.

The recrystallized structure was cooled by running molecular dynamics (MD) simulation for 500 ps at 1500 K, followed by 250 ps at 1000 K, 250 ps at 500 K, and lastly 500 ps at 0 K. A similar process was employed in generating the MnO_2 nanosphere (Sayle et al. 2005). A cooled structure of the nanosphere is depicted in figure 3.12, where more patterns are visible, and tunnels on the side of the structure are shown while the crystalized structure, at elevated temperatures, does not reflect tunnels. The total RDFs of a TiO_2 nanosphere at different temperatures are given in figure 3.13. As the temperature is lowered, from 1500 to 0 K, the broadness of the peaks decreases and their height increases, and this is particularly distinct at the radial distance of 1.8 Å, which implies that the system is crystalline.

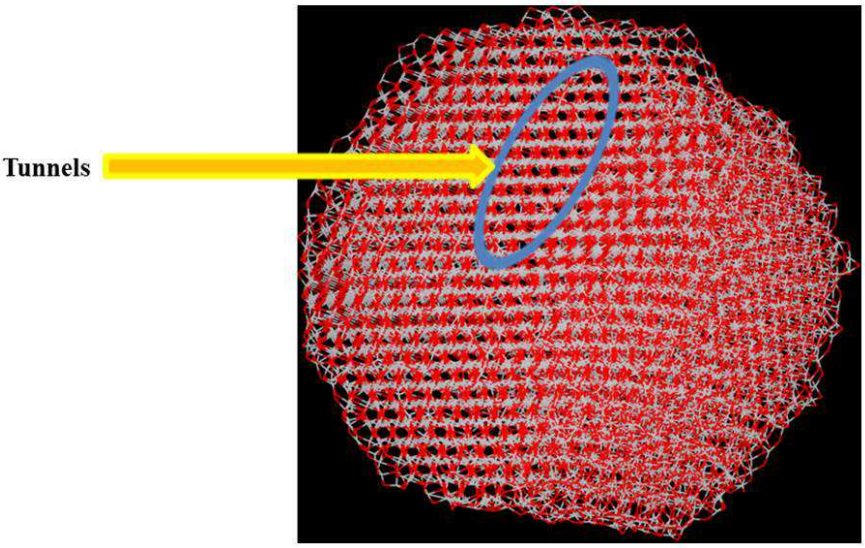

Figure 3.12: A cooled structure of a TiO_2 nanosphere at 0 K.

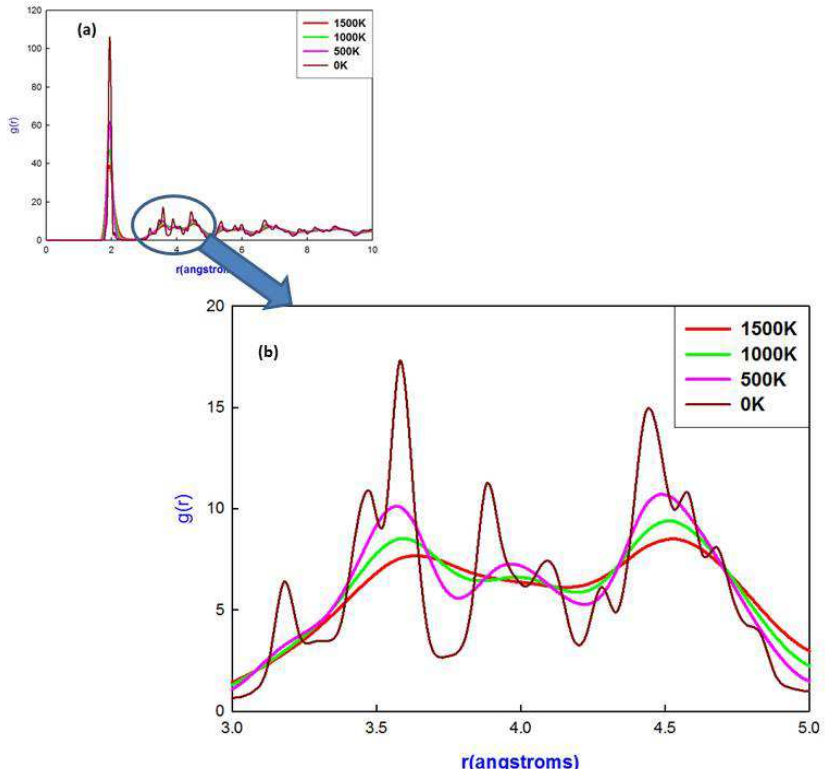

Figure 3.13: Total RDFs of the nanosphere at (a) different temperatures and (b) the magnified portion of (a).

Calculated and measured XRDs of nanosphere together with that of TiO_2: α-PbO_2 are depicted in figure 3.14, where calculated XRDs with copper Kα radiation source illustrate more resolved peaks than the ones with iron Kα radiation source. By comparing them we observe that calculated XRDs show peaks similar to the experimental results, particularly

for the brookite and to a less extent the rutile structural arrangement. At 30 ° we observe two peaks corresponding to brookite, 37 and 43 ° peaks harmonize with brookite and rutile, 55 ° peak accords with brookite and rutile but predominantly with rutile, 68 ° peak associates with brookite whilst rutile is at 70 °. This shows that the nanosphere is predominantly of brookite and rutile structural arrangement and has peaks associated with TiO_2: α-PbO_2 structure. Calculated XRDs show broader peaks as compared to those in figure 1.2.

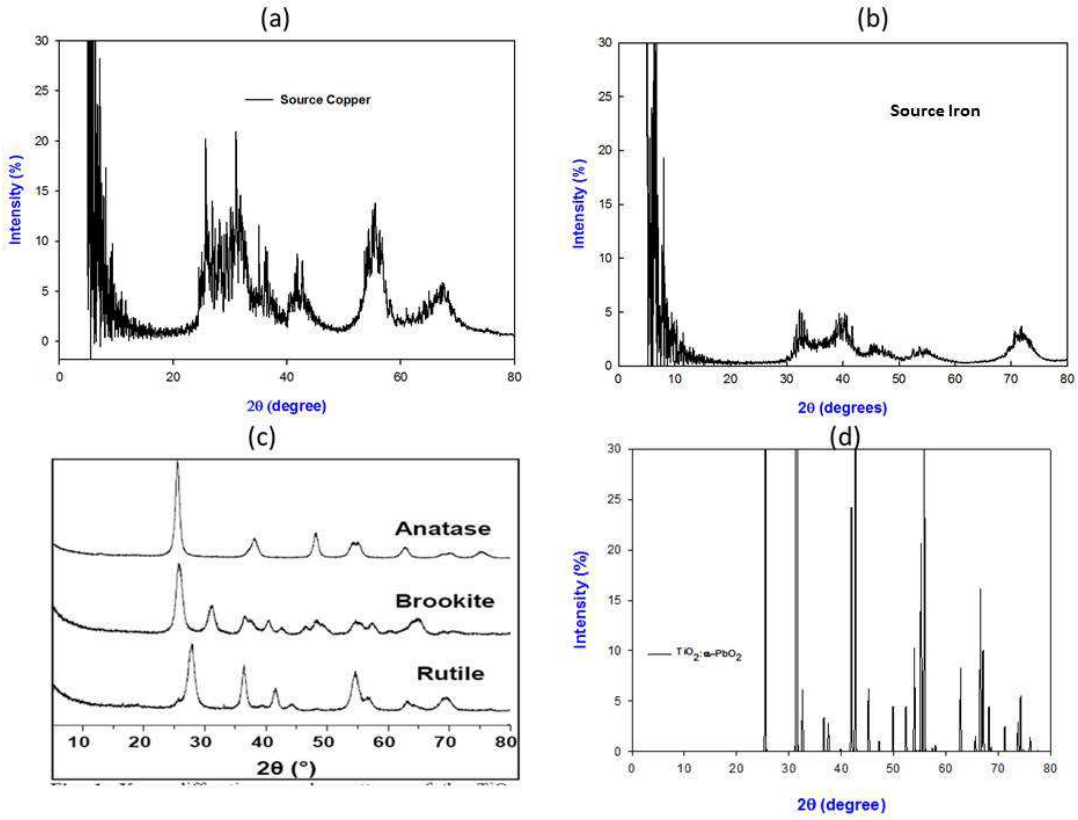

Figure 3.14: XRDs of nanosphere with source (a) copper and (b) iron, (c) experimental (Dambournet et al. 2009) and (d) TiO_2: α-PbO_2.

On superimposing XRD patterns of the experimental brookite, TiO_2: α-PbO_2, rutile polymorphs and the simulated TiO_2 nanosphere, corresponding peaks can be deduced. At 27, 33 and 37 ° there are sharp peaks that correspond well with the brookite and TiO_2: α-PbO_2 structure, whilst at 42 ° only the simulated, brookite and TiO_2: α-PbO_2 peaks are aligned. The simulated XRD pattern at 50 ° has a smooth curve which tally well with the

rutile structure. The peaks at 37 and 57 ° correspond with all polymorphs and the one at 67 ° accords more reasonably with the rutile and TiO_2: α-PbO_2 structures. We used figure 1.3 to assign peaks and they correspond to rutile and brookite model.

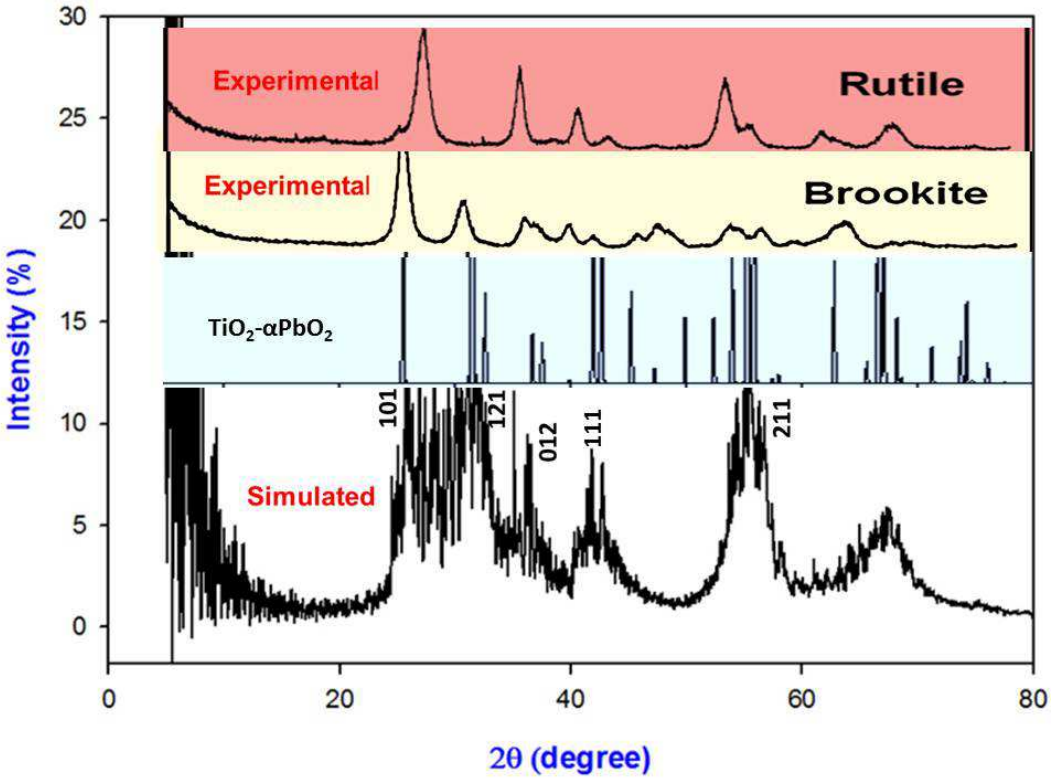

Figure 3.15: A comparison of simulated TiO_2 nanosphere, calculated TiO_2:α-PbO_2 and experimental (Dambournet et al. 2009) XRDs.

A slice was cut through the cooled structure of the TiO_2 nanosphere in order to reveal microstructures, which are depicted in figure 3.16. The blue colour depicts the upper layer of Ti^{4+} octahedra while the white colour shows the lower layer. Figure 3.16b shows a different orientation of microstructure for the nanosphere in order to view the layers clearly. The microstructures of nanosphere show zigzag and straight tunnels. More zigzag tunnels are found in the middle of the structure indicating a brookite phase, while the straight tunnels appear mostly at the side of the structure showing the present of rutile phase. We also observe the micro-twinning which suggest rutile phase. Some vacancies are observed on the right hand side of the microstructure in figure 3.16 (c).

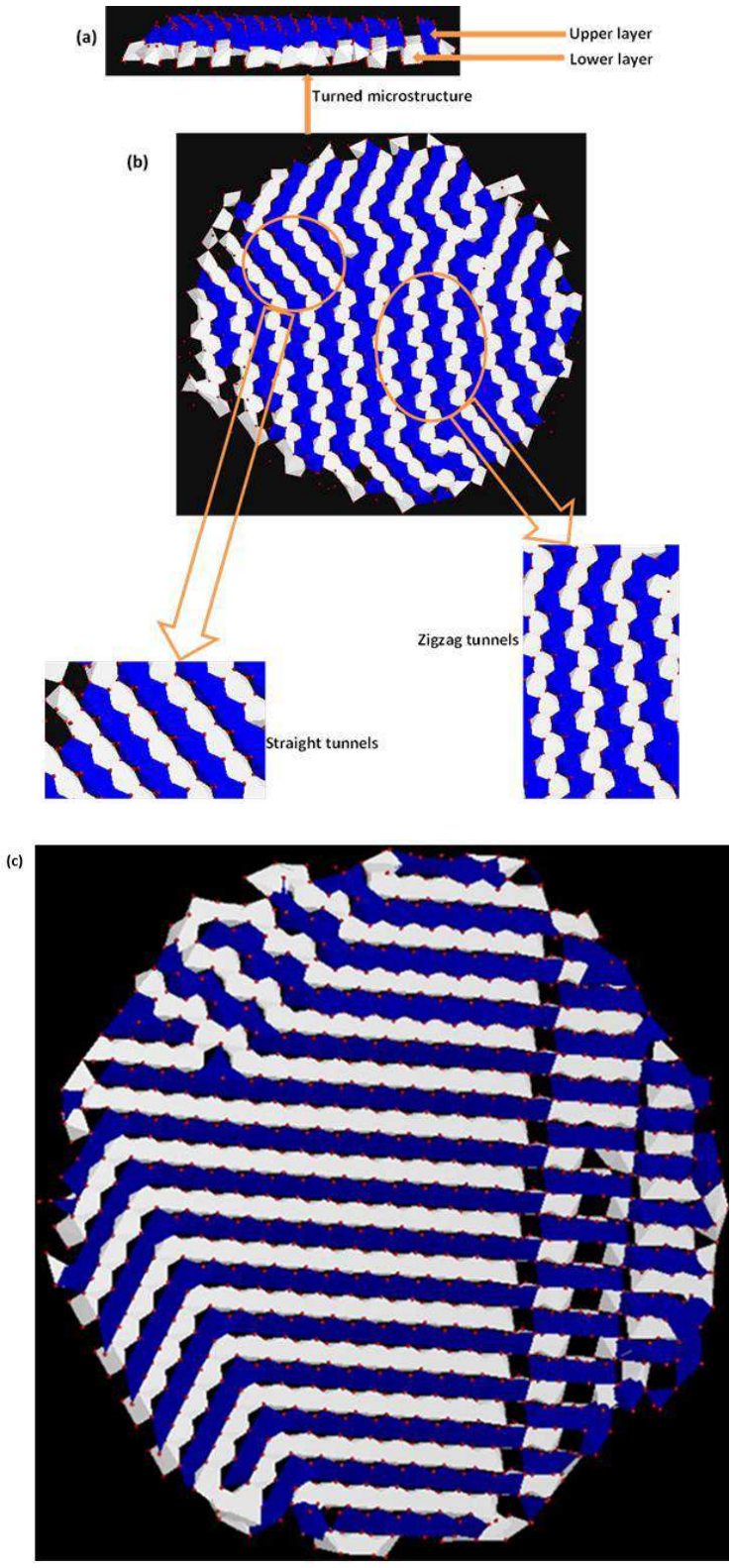

Figure 3.16: Microstructures of the TiO_2 nanosphere corresponding to different orientations; blue colour is the upper layer and white is the lower layer.

3.4.2 Titanium dioxide nanosheet structure

A nanosheet structure of TiO_2 corresponding to lattice a box of dimension 85 Å was generated by molecular dynamics from an amorphous nanosphere using the NPT ensemble. Before crystallising the nanosheet, RDFs were calculated and are illustrated in figure 3.17. Distinct peaks are observed which implies that the nanosheet was partially crystallised during its generation from the nanosphere. We continued to allow for full crystallisation by performing an NVT molecular dynamics calculation as was on the nanosphere in section 3.4.1. The calculated configuration energy as a function of time for

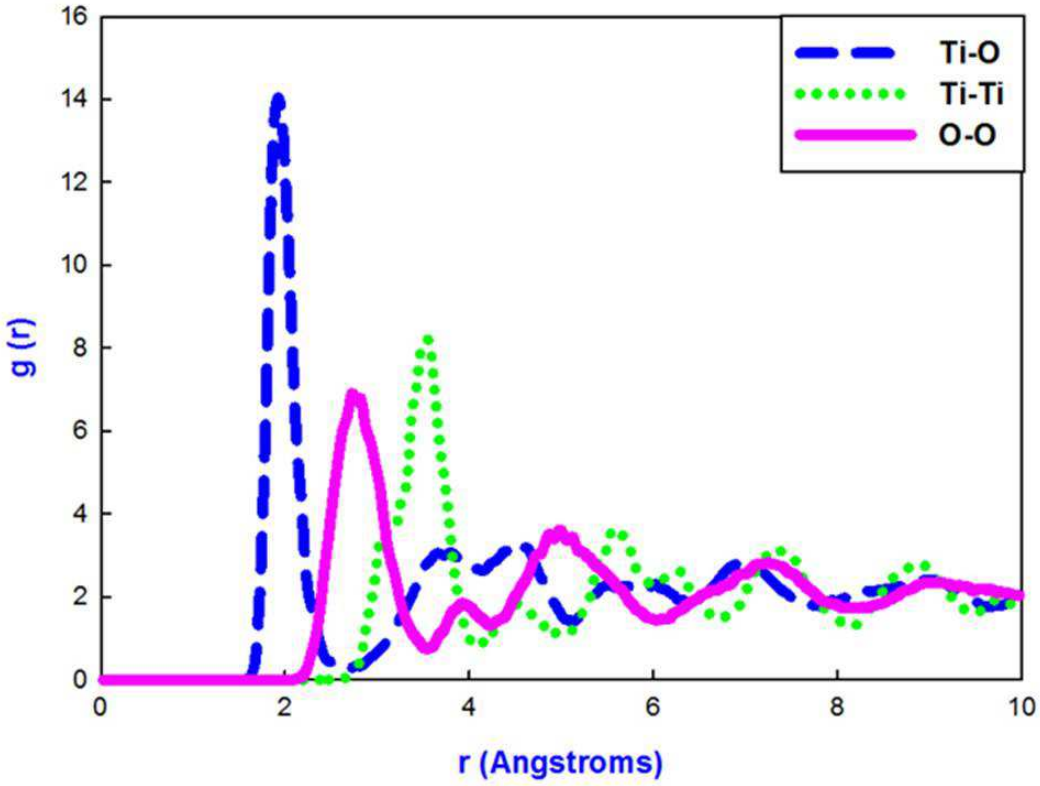

Figure 3.17: RDFs for the TiO_2 nanosheet before full recrystallisation at 2000 K.

the TiO_2 nanosheet during recrystallisation is shown in figure 3.18. The graph shows a constant energy from 0 to 1.5 ns followed by a slight drop from 1.5 to 2.25 ns. However, from 2.25 ns there is a sudden reduction of energy, amounting to 0.003×10^5 eV, which can be ascribed to full crystallisation or an annealing of a grain boundary since it is small. Above 2.5 ns the change in the configuration energy is insignificant.

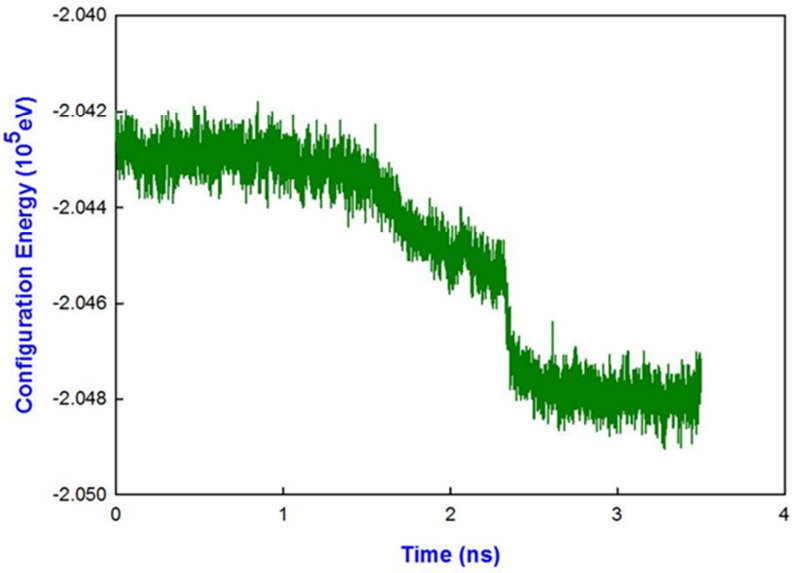

Figure 3.18: Calculated configuration energy as a function of time for TiO_2 nanosheet.

The partially crystallised (according to the RDFs) and fully recrystallised structures of nanosheet of TiO_2 are depicted in figures 3.19 (a) and (b) respectively. Some distinct crystalline patterns of recrystallised structure are marked with a blue circle. We have also sliced the recrystallised structure in order to observe clear patterns which are presented in figure 3.20.

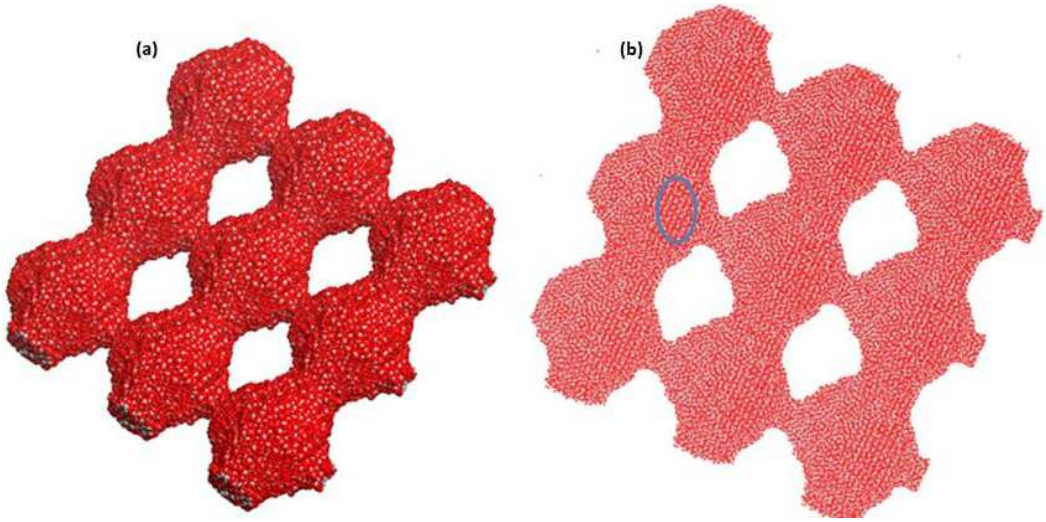

Figure 3.19: Structure of TiO_2 nanosheet (a) partially amorphised and (b) recrystallised.

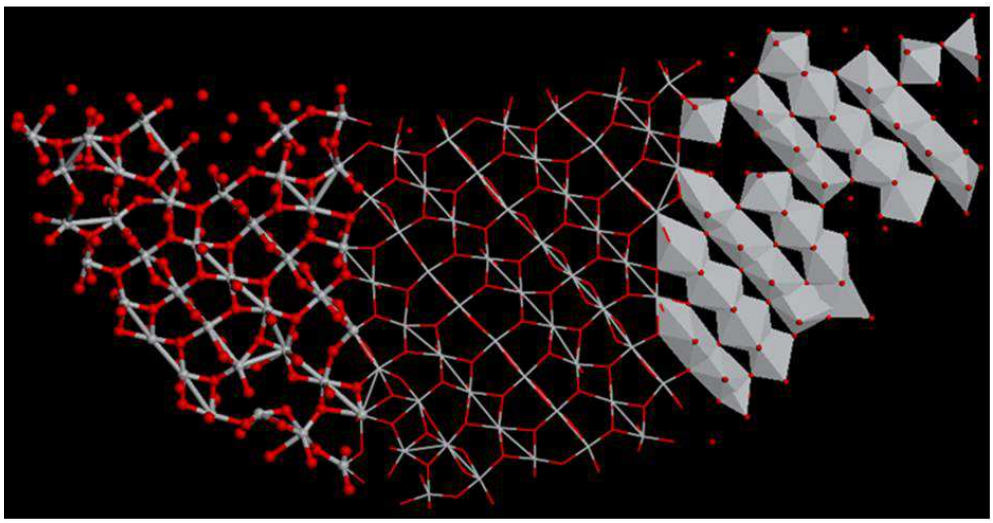

Figure 3.20: Recrystallised structure of TiO_2 nanosheet showing patterns.

The RDFs of the nanosheet after recrystallisation for Ti-O, Ti-Ti and O-O interactions are presented in figure 3.21. We observe a maximum peak at approximately 2.0 Å which is a contribution of Ti-O interaction. Between 2 and 4 Å sharp peaks are noted which are a contributions of Ti-Ti and O-O interactions; from 4 and 10 Å peaks contributed by Ti-O, Ti-Ti and O-O interactions are apparent. It can be deduced that the system has fully recrystallised since slightly sharper and higher RDF peaks are observed as compared to those before recrystallisation.

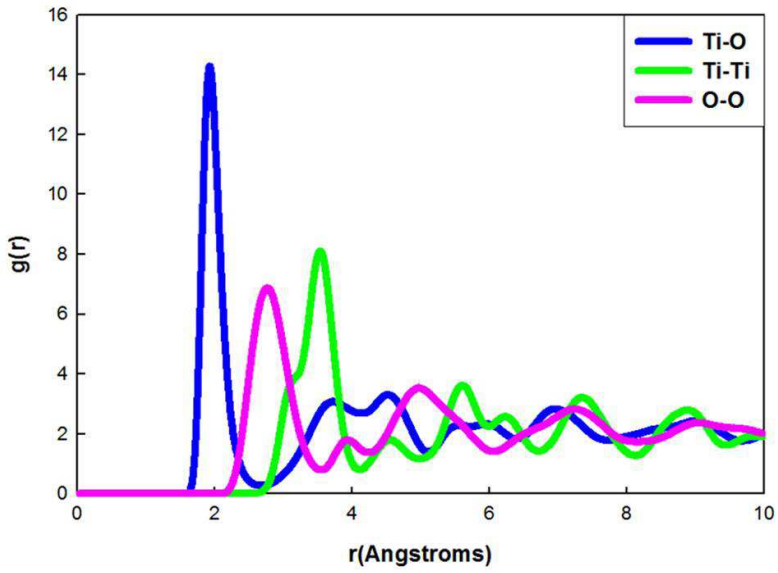

Figure 3.21: RDFs for TiO_2 nanosheet after recrystallisation at 2000 K.

The recrystallised structure of TiO_2 nanosheet was cooled using the procedure described in section 3.4.1 for the nanosphere. A cooled structure of nanosheet is given in figure 3.22; it shows some tunnels particularly on the side of the structure, which are not visible on the recrystallised nanosheet at 2000 K. Furthermore, we can observe grain boundaries on the nanosheet as illustrated by the magnified portion of the nanosheet in figure 3.23. Some grain boundaries are surrounded by a white circle.

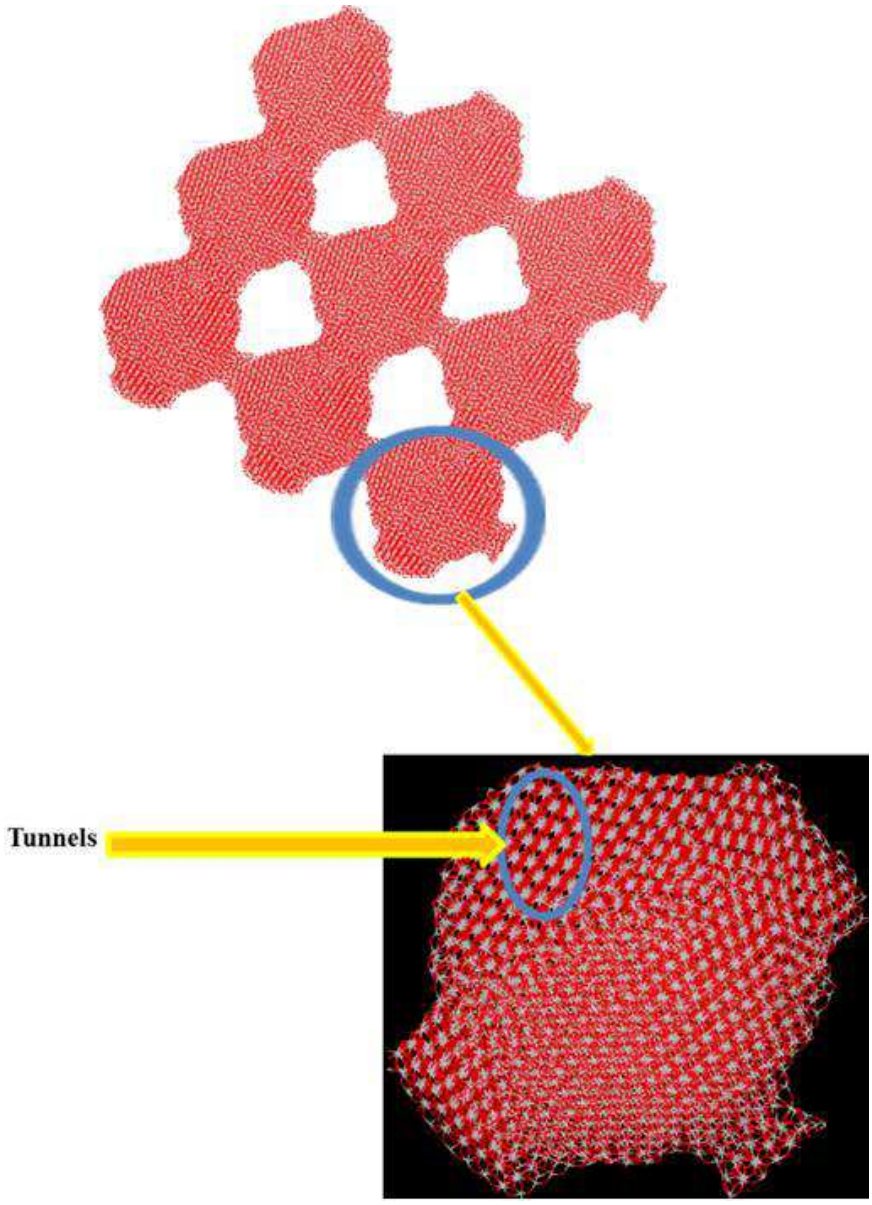

Figure 3.22: A cooled structure of TiO_2 nanosheet at 0 K.

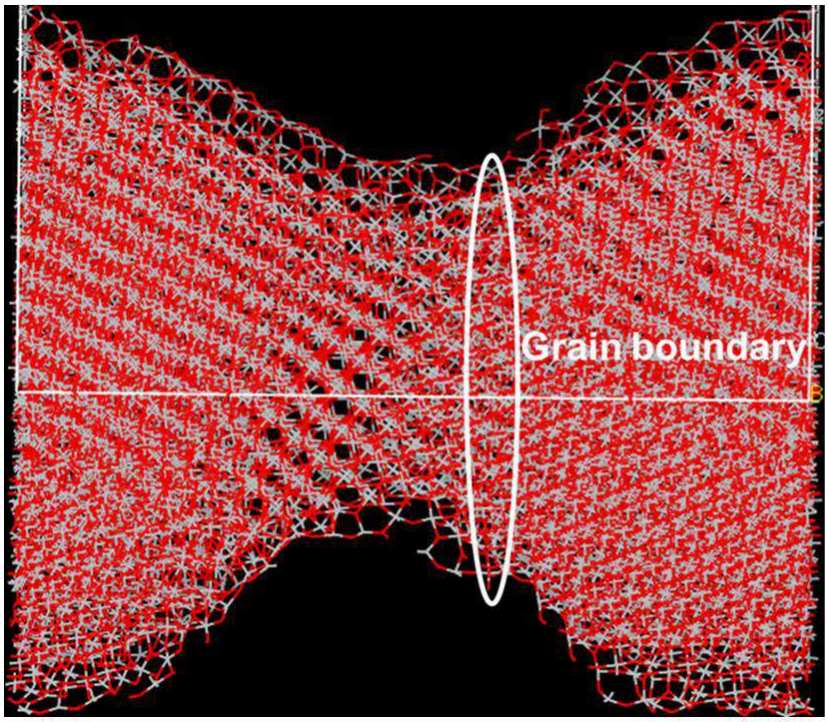

Figure 3.23: Magnified portion of TiO_2 nanosheet showing boundaries at 0 K.

The total RDFs of a cooled nanosheet are shown in figure 3.24 and it is apparent that as the temperature decreases the broadness of the peaks reduces and enhanced peak heights are noted. This implies that as the temperature is lowered the structure becomes more crystalline. Similarly to the nanosphere, a clear trend of sharp peaks is observed around 1.8 Å, with the highest peak occurring at 0 K followed by 500 K, then 1000 K and lastly 1500 K.

Microstructures of the nanosheet were created and are presented in figure 3.25. The blue colour depicts the upper layer of Ti^{4+} octahedra while the white colour is the lower layer of Ti^{4+}; and zigzag and the straight tunnels are observed. Straight 1D tunnel indicate the presence of the micro-twinned rutile polymorph whilst the zigzag patterns are related to the brookite phase. Figure 3.26 presents a comparison of our calculated microstructures of TiO_2 nanosheet with experimental high resolution transmission electron micrograph (HRTEM) of Wei et al. (2011). Experimental microstructures show straight tunnels which are much in accord with our calculated microstructures. The only difference is that

our calculated microstructures also contain zigzag tunnels which are not observed on the experimental microstructures. Few vacancies are noted on the sides of the microstructure.

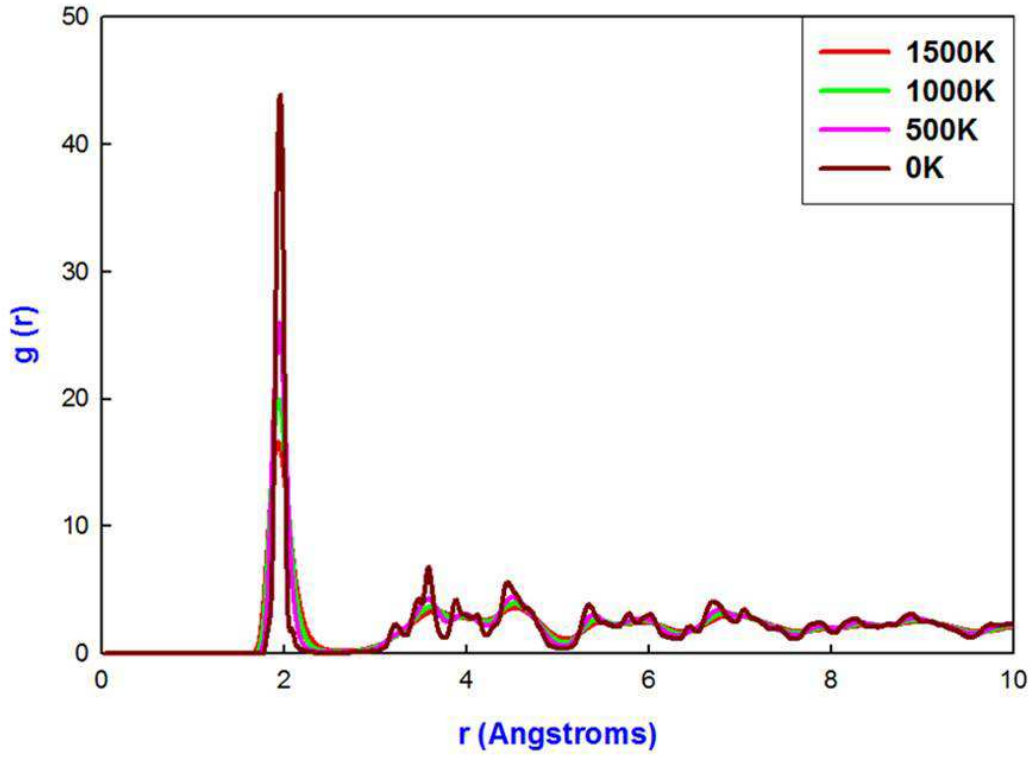

Figure 3.24: Total RDFs of the TiO_2 nanosheet at different temperatures.

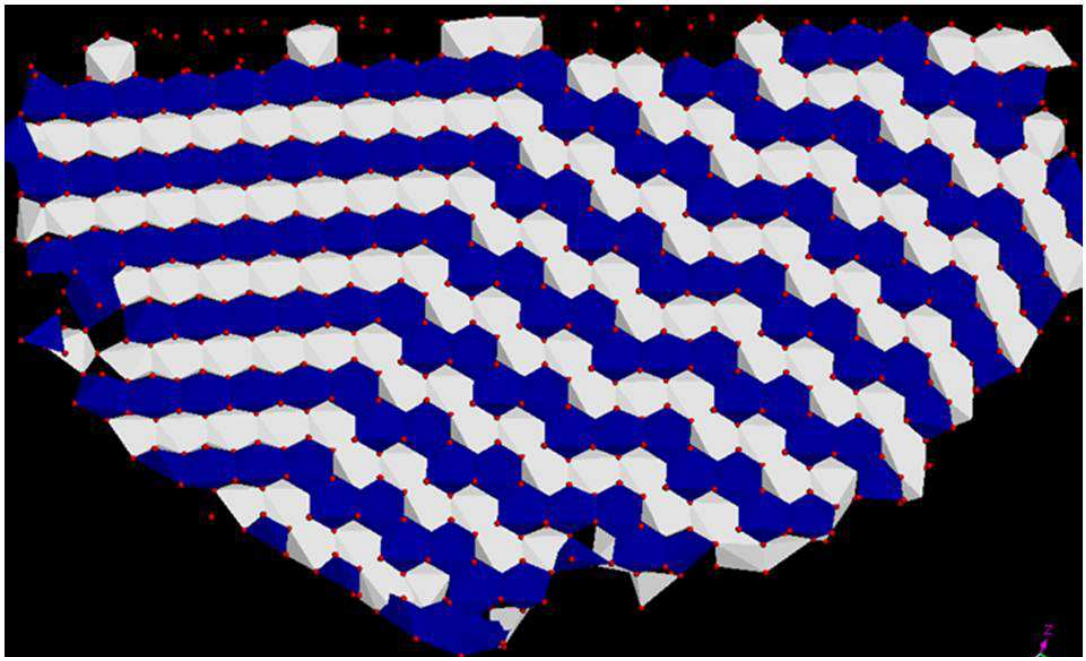

Figure 3.25: Simulated microstructure of the TiO_2 nanosheet at 0 K.

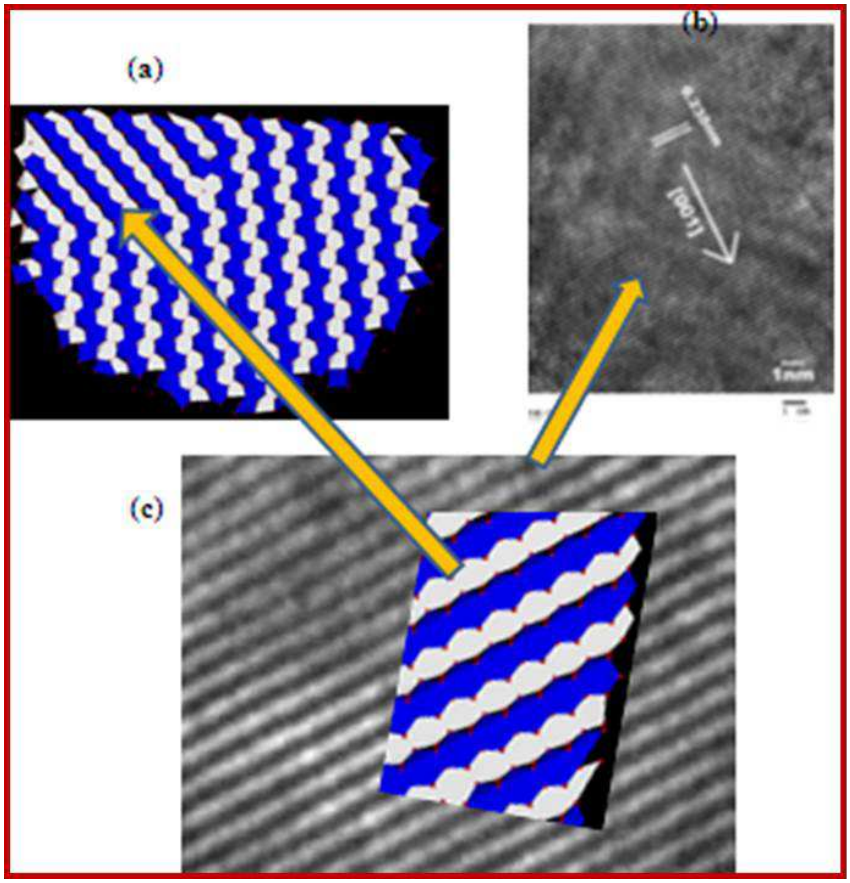

Figure 3.26: Microstructures of the TiO_2 nanosheet (a) this work, (b) experimental (Wei et al. 2011) and (c) Combination of (a) and (b).

Calculated and measured XRDs of the TiO_2 nanosheet are presented in figure 3.27. Calculated XRDs with copper Kα radiation source shows more resolved peaks than the one with Iron Kα radiation source. The copper generated XRD is generally better aligned with experimental results and suggests that our system has a brookite structural arrangement and has also peaks associated with the TiO_2: α-PbO_2 polymorph. Figure 3.28 shows a superimposition of experimental and simulated XRDs, which further confirms the presence of brookite, and TiO_2: α-PbO_2 polymorphs from corresponding sharp peaks at 27, 33, 37 and 42 °. Simulated XRD at 50 ° shows a smooth curve which tallies well with the rutile structure, and peaks at 37 and 57 ° accord well with all polymorphs. Peak at 67 ° correspond with rutile and TiO_2: α-PbO_2 polymorphs. Peaks were assigned using figure 1.3 and they reflect rutile and brookite model.

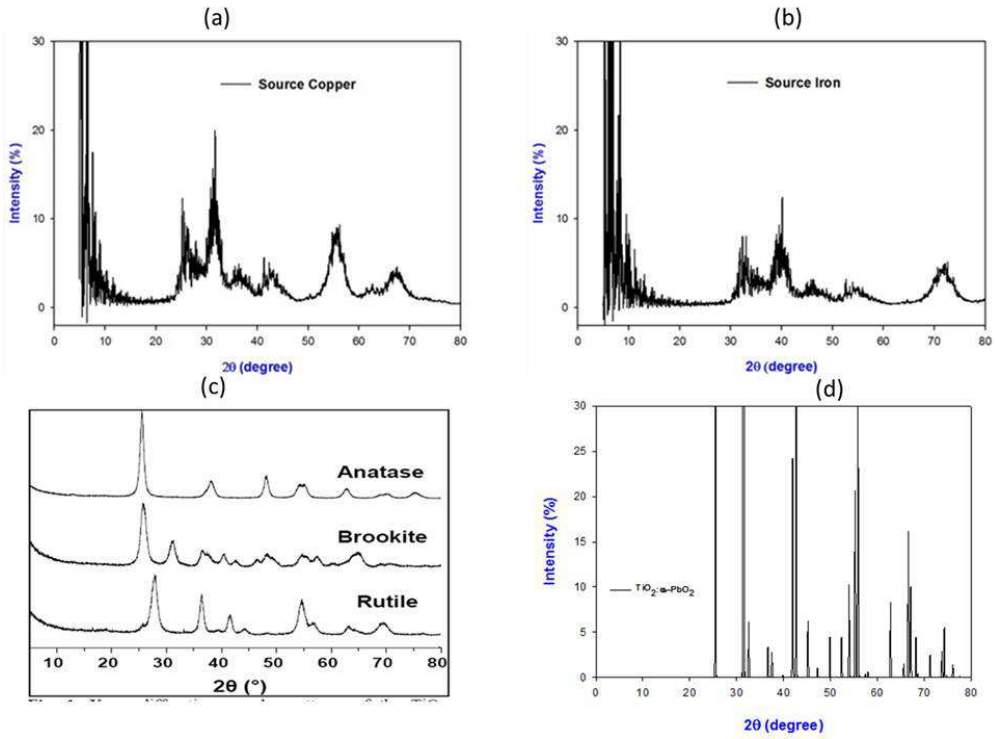

Figure 3.27: XRDs of TiO_2 nanosheet with source (a) Copper and (b) Iron, (c) experimental (Dambournet et al. 2009) and (d) TiO_2: α-PbO_2.

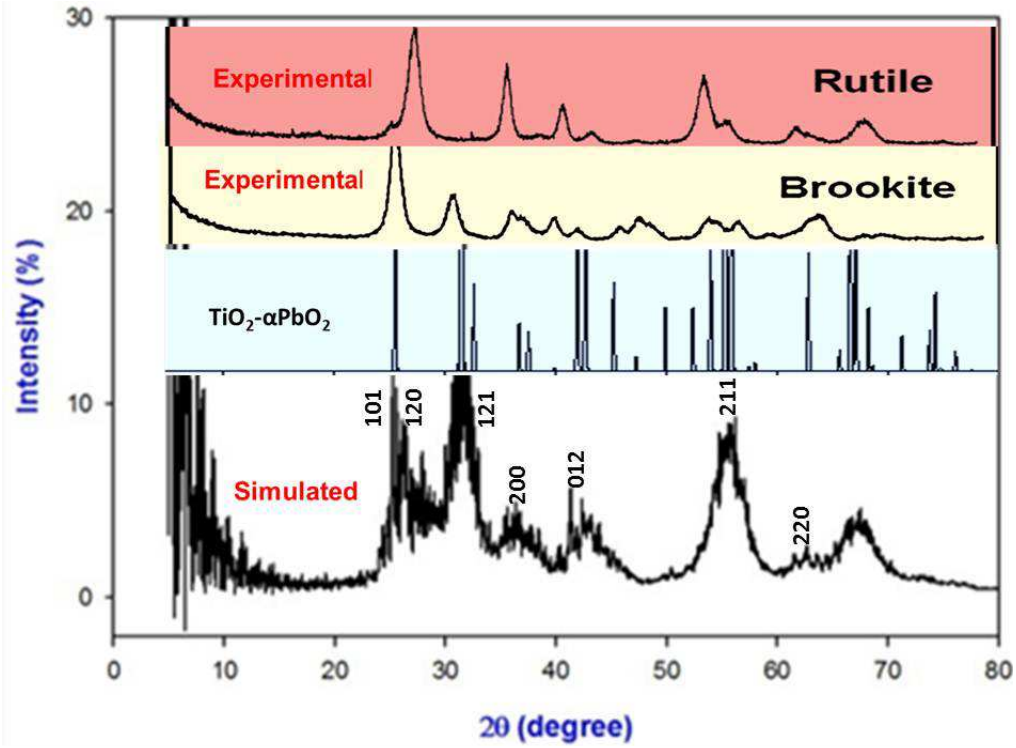

Figure 3.28: A comparison simulated TiO_2 nanosheet, calculated TiO_2: α-PbO_2 and experimental (Dambournet et al. 2009) XRDs.

3.4.3 Titanium dioxide of nanoporous structures

Two TiO_2 nanoporous structures, corresponding to lattice boxes of dimensions 60 and 66 Å were generated by molecular dynamics from an amorphous nanosphere using the NPT ensemble. Their RDFs are shown in figure 3.29 and 3.30, and they depict broader peaks and demonstrate that they are amorphous. The NVT ensemble was employed to recrystallise the nanoporous structures of TiO_2.

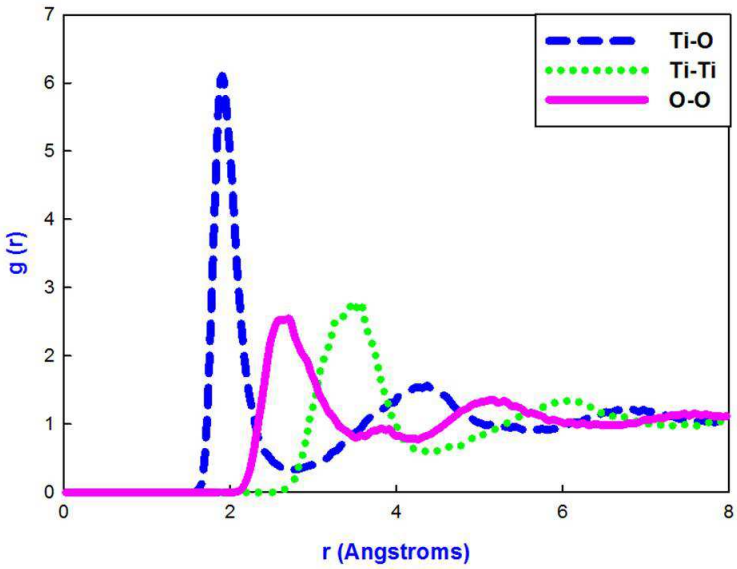

Figure 3.29: RDFs for the 60 Å TiO_2 nanoporous structure before recrystallisation.

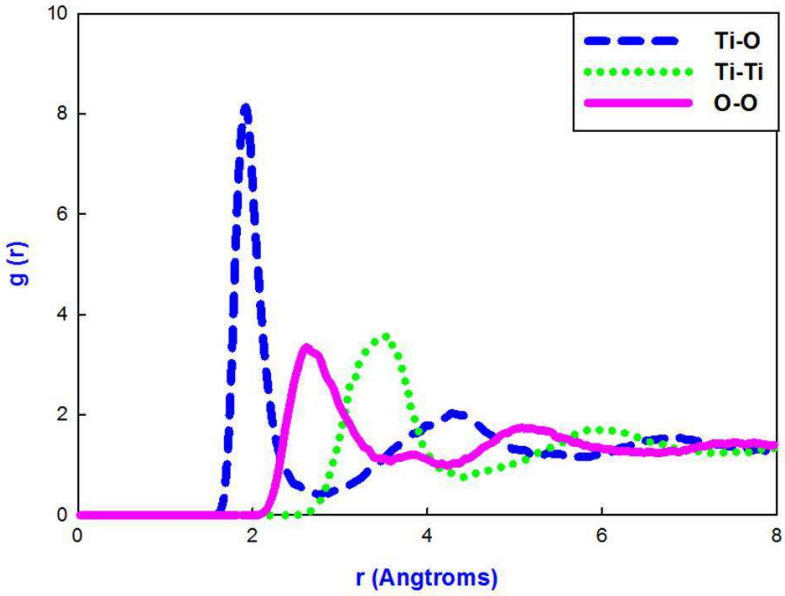

Figure 3.30: RDFs for the 66 Å TiO_2 nanoporous structure before recrystallisation.

The graphs of configuration energy as a function of time for the nanoporous structures of 60 and 66 Å are depicted in figures 3.31 and 3.32 respectively. For the nanoporous structure 60 Å, a phase change is observed between the times of 0 ns to 0.45 ns since there is a quick drop of energy from -2.0215 $x10^5$ eV to -2.0503 $x10^5$ eV. Such change is associated with the transition from amorphous to a crystalline phase. The significant change of energy subsequently levels off, and from 1.5 ns and it can be concluded that the nanoporous structure has recrystallised. In the case of the 66 Å nanoporous structure, the phase change is observed between time of 0 and 0.45 ns; a noticeable but steady drop of energy from -2.0154$x10^5$ to -2.0455$x10^5$ eV, is noted. Such phase change is also associated with the transition from amorphous to crystalline phase. As in the 60 Å nanoporous structure, after 2 ns the energy remains constant which suggests full recrystallisation. The nanoporous structure of 60 Å reflects recrystallisation with lower energy as compared to that of 66 Å, since it commences with energy of less than -2.0215 $x10^5$ eV while the other starts with energy of more than -2.0154 $x10^5$ eV. The energy as time graph of nanoporous structures 60 Å and 66 Å behave similarly to that of mesoporous and nanosheet of MnO_2 (Sayle et al. 2009).

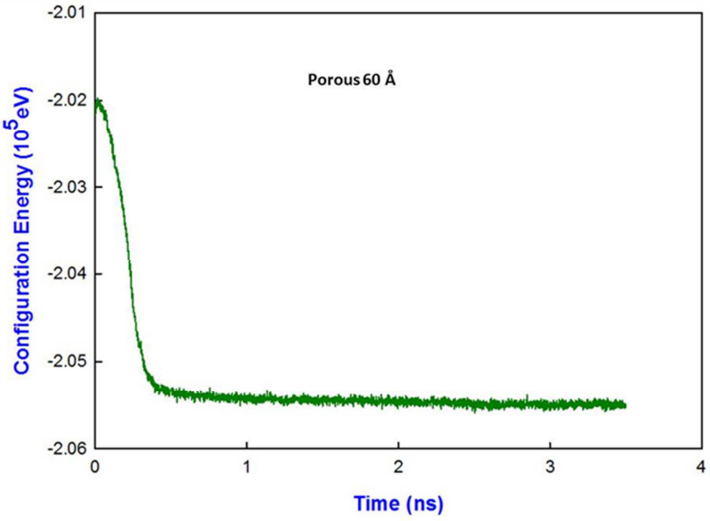

Figure 3.31: Calculated configuration energy as a function of time for TiO_2 nanoporous (60 Å).

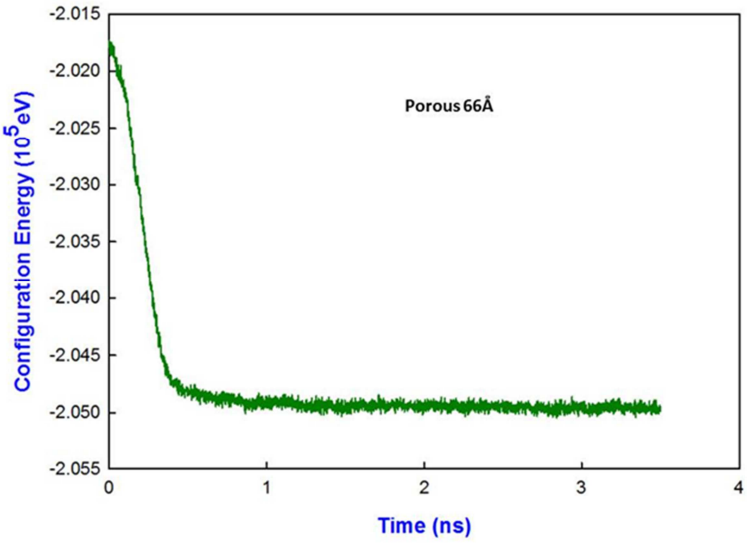

Figure 3.32: Calculated configuration energy as a function of time for TiO_2 nanoporous (66 Å).

Recrystallised nanoporous structures of TiO_2 are presented in figure 3.33, and all show crystalline patterns and have different sizes of channels; the nanoporous structure of 66 Å lattice box exhibits more tunnels and grain boundaries than that of 60 Å. An enlarged (66 Å) nanoporous structure is presented in figure 3.34, where circled areas indicate grain boundaries and tunnels and channels are clearly illustrated.

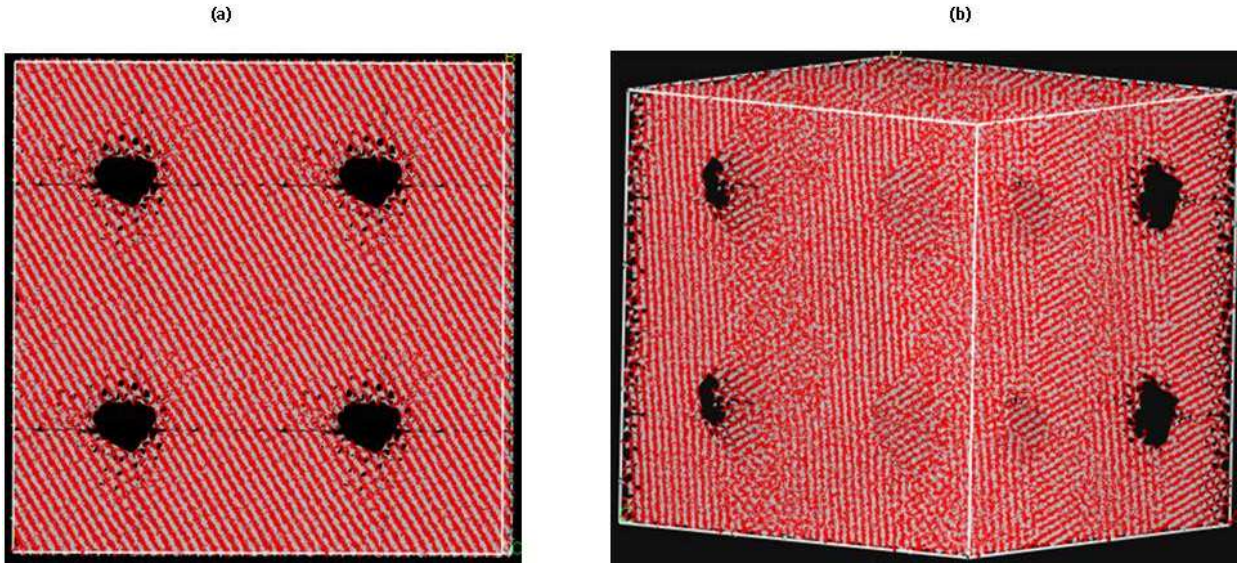

Figure 3.33: Recrystallised structures of the nanoporous TiO_2 corresponding to (a) 60 Å and (b) 66 Å lattice box.

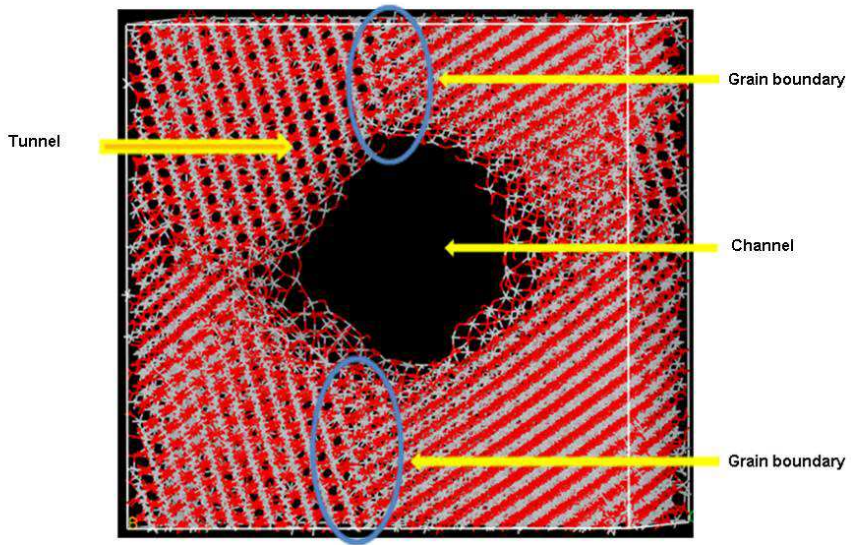

Figure 3.34: Magnified recrystallised structure of nanoporous TiO_2 (66Å) showing channels, tunnels and grain boundaries.

Simulated nanoporous structures are in good agreement with the experimental results. Figure 3.35 compares our simulated and TEM and HRTEM (Ren et al. 2010) nanoporous TiO_2 results; they both contain tunnels and channels. Some grain boundaries are observed on the simulated structure in figure 3.35 (a) and the experimental channel shape is in accord with the simulated structure.

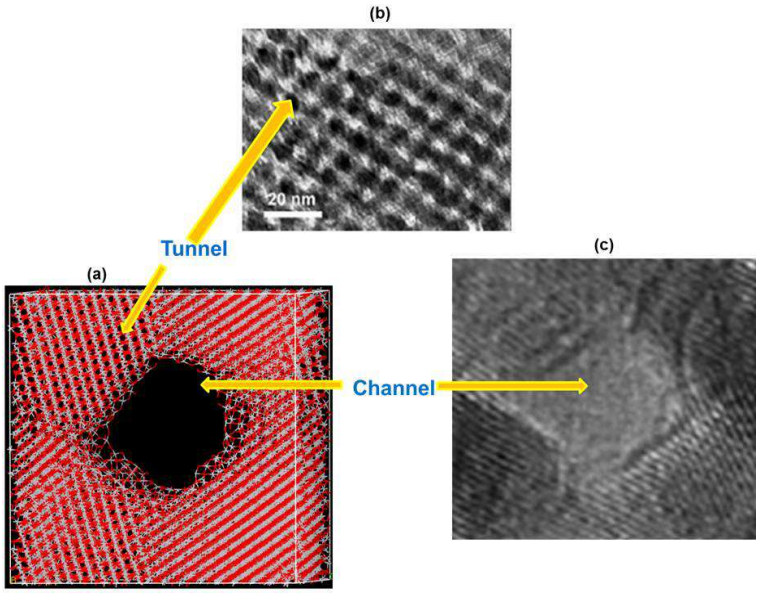

Figure 3.35: (a) Simulated and (b) measured (Ren et al. 2010) nanoporous structures of TiO_2. (c) An enlarged measured channel.

Calculated RDFs of the nanoporous structure after recrystallisation are shown in figures 3.36 and 3.37 for lattice boxes of 60 and 66 Å respectively; for Ti-O, Ti-Ti and O-O interactions only. The maximum peaks for both nanoporous structures are observed at 2.0 Å which is a contribution of Ti-O interaction with the 66 Å having the highest peak. Sharp peaks that are observed between 2 and 4 Å are contributions of Ti-Ti and O-O interactions. Other smaller peaks are observed from 4 to 10 Å which are contributions from Ti-O, Ti-Ti and O-O interactions. It can be surmised that our systems have recrystallised well since the peaks are well defined and we do not observe broader peaks.

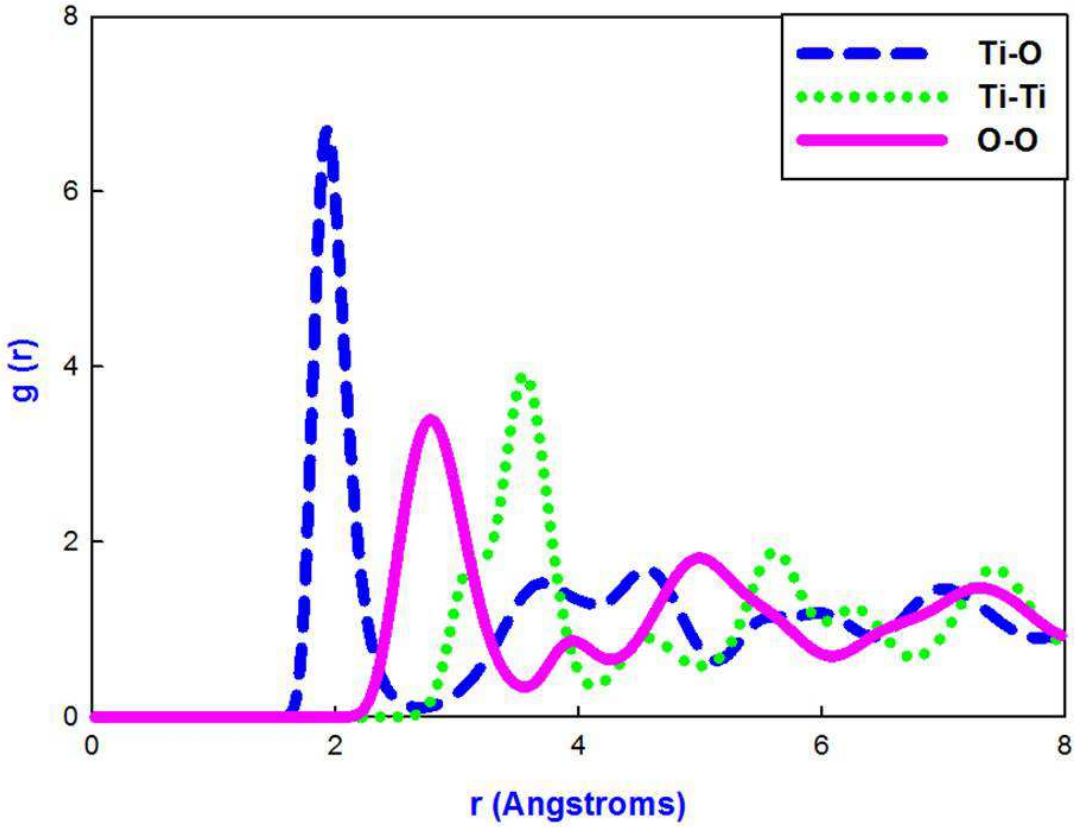

Figure 3.36: RDFs of TiO_2 nanoporous structure of 60 Å after recrystallisation at 2000 K.

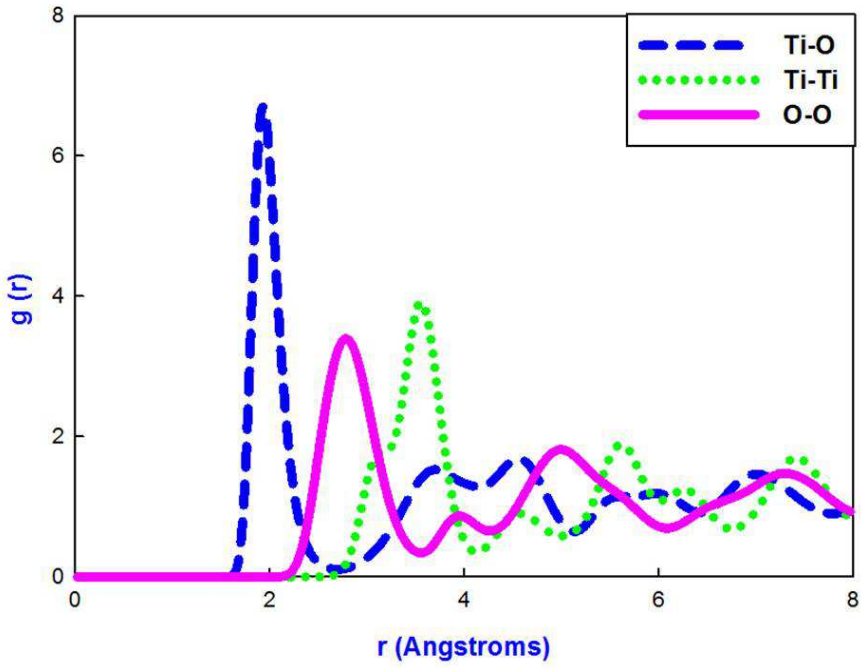

Figure 3.37: RDFs of TiO_2 nanoporous structure of 66 Å after recrystallisation at 2000 K.

The cooling process that was employed in section 3.4.1 was also used for the two nanoporous structures. Cooled crystallised TiO_2 nanoporous structures are shown in figure 3.38 where tunnels are quite distinct. The nanoporous structure 60 Å shows more tunnels than the 66 Å.

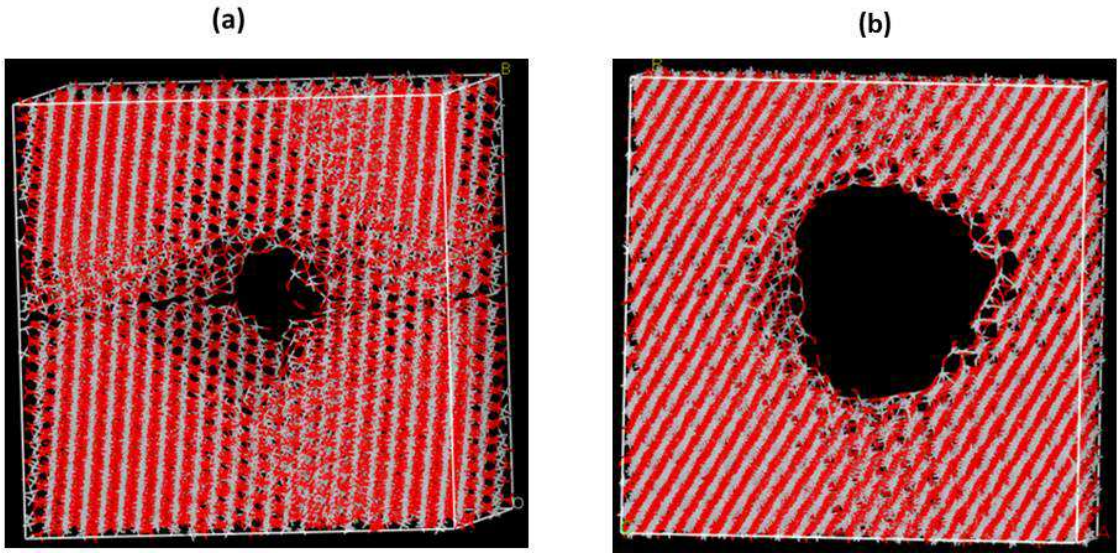

Figure 3.38: Cooled structures of crystallised TiO_2 nanoporous systems with (a) 60 Å and (b) 66 Å.

We have calculated the total RDFs of both cooled nanoporous structures and they are given in figures 3.39 and 3.40. As the temperature decreases the broadness of the peaks is reduced and this accompanied by increasing heights of peaks. Nanoporous structure of 60 Å has higher peaks as compared with those of 66 Å. However, both have sharp peaks, suggesting that they are well ordered.

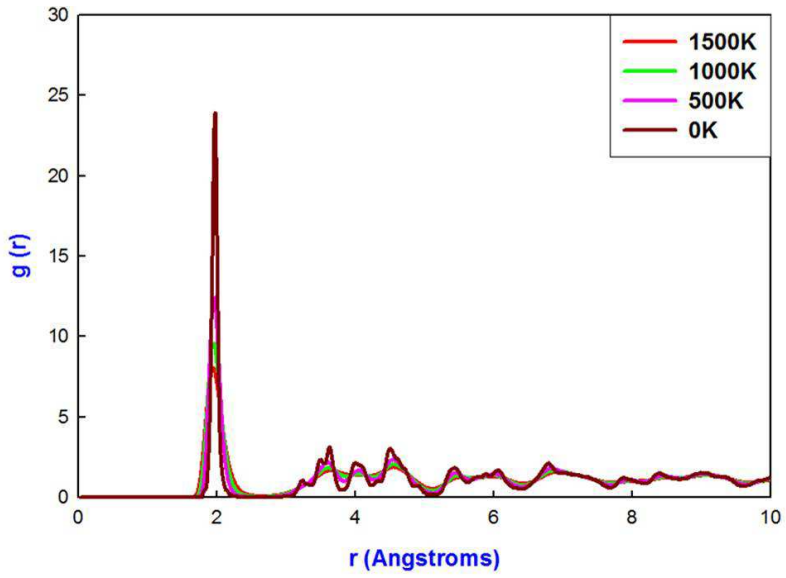

Figure 3.39: Total RDFs of recrystallised 60 Å nanoporous TiO_2 at different temperatures.

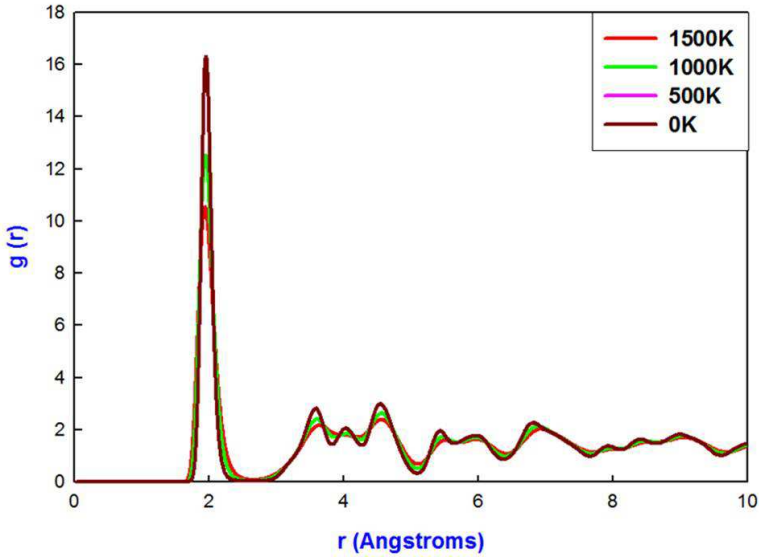

Figure 3.40: Total RDFs of recrystallised 66 Å nanoporous TiO_2 at different temperatures.

The microstructures of the TiO_2 nanoporous structure for 60 and 66 Å lattice boxes are presented in figures 3.41 and 3.42 respectively. The blue colour is associated with the upper layer of Ti^{4+} octahedra while the white colour is the lower layer of Ti^{4+} octahedra. The 60 Å microstructure shows more zigzag tunnels in the middle of the structure and the straight tunnels at the end of the structure. Microstructures of nanoporous structure of 66 Å were created by cutting the structure at different sides. The upper microstructure on figure 3.42 shows only zigzag tunnels while the lower microstructure on figure 3.42 shows zigzag tunnels in the middle and few straight tunnels at the end of the structure. The experimental (Wang et al. 2008) microstructure for high-resolution transmission electron microscopy (HRTEM) for nanoporous structure of TiO_2 is presented in figure 3.43. Our simulated microstructures correlate well with the measured results since all have zigzag tunnels. Figure 3.44 presents a combination of simulated and measured microstructures which compare well particularly in regard to their zigzag tunnels. The only difference is that our calculated microstructures, especially the one of 60 Å lattice box, contain straight tunnels which are currently not observed on the experimental microstructures. The presents of zigzag chains indicate the brookite domain whilst the straight chains show twinned rutile.

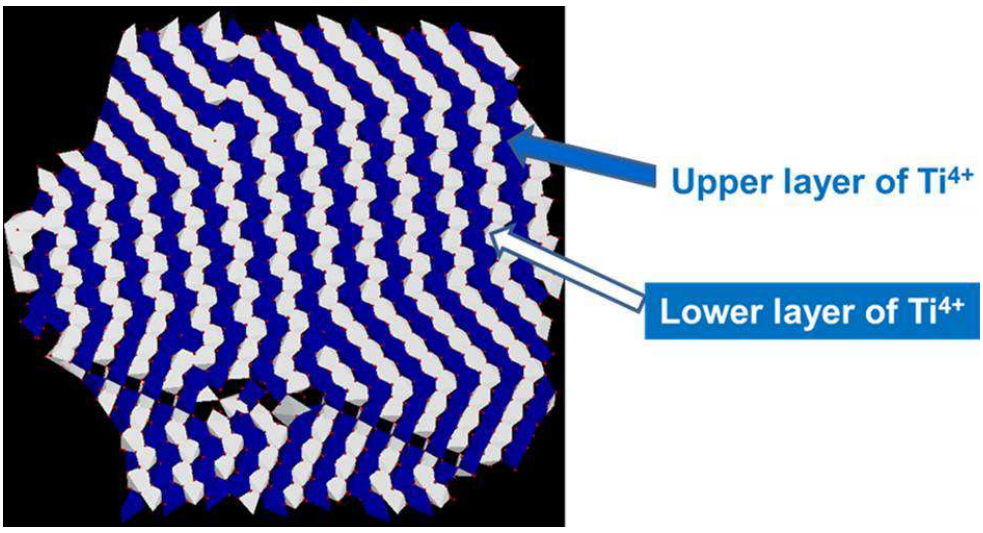

Figure 3.41: Microstructure of recrystallised TiO_2 nanoporous structure of 60 Å.

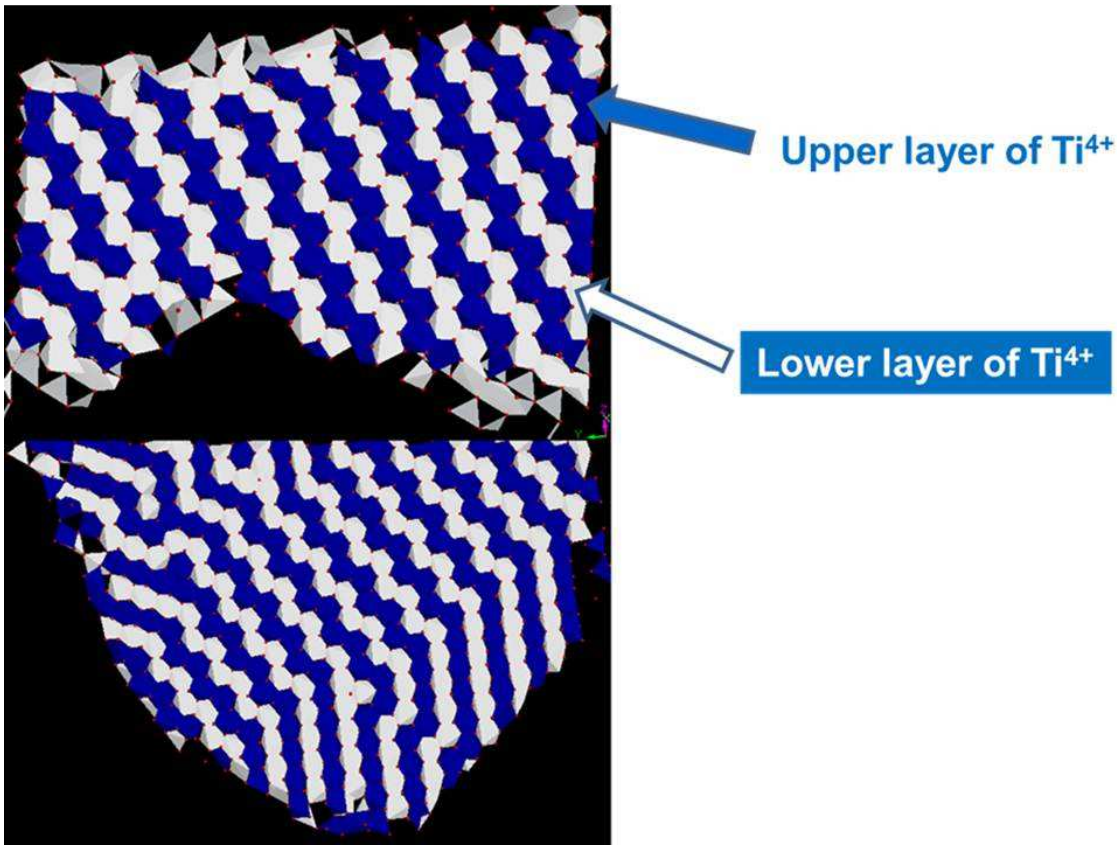

Figure 3.42: Microstructures of TiO_2 nanoporous structure of 66 Å size, viewed in different orientations.

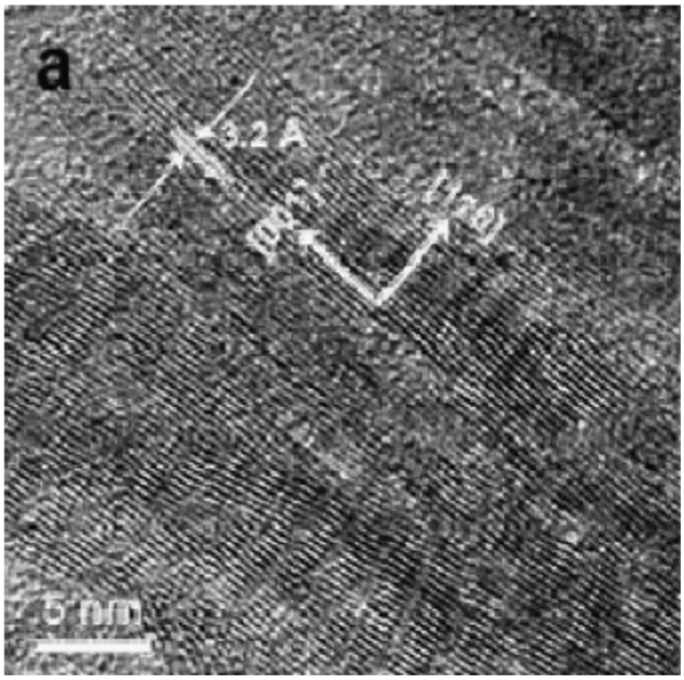

Figure 3.43: High-resolution TEM images of mesoporous TiO_2 (Wang et al. 2008).

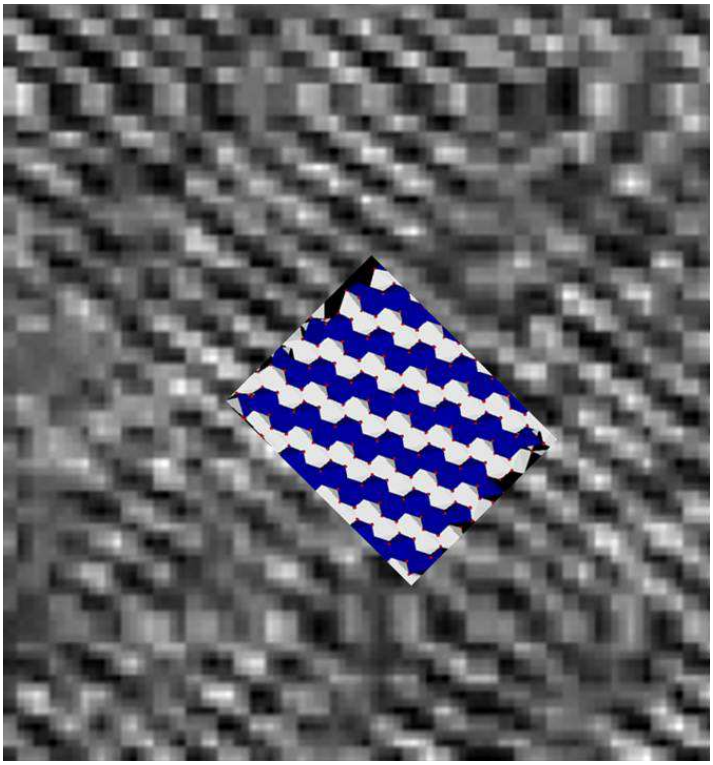

Figure 3.44: Combined simulated (in blue and white) and magnified measured HRTEM (Wang et al. 2008) microstructures of TiO_2 nanoporous.

XRD of nanoporous structure, calculated and simulated, are presented in figure 3.45. The copper radiation source shows more resolved peaks than iron radiation source. This implies that XRD for TiO_2 nanoporous must be calculated with the copper Kα radiation source since they are in accord with the experimental (Dambournet et al. 2009) data. By comparing the measured XRDs with the calculated ones, it is suggested that our system is aligned with the rutile and TiO_2: α-PbO_2 structural arrangement since it shows a similar peak in the vicinity of 67 °. A closer look at the experimental XRDs of rutile shows a similar peak to ours near 57 °. Simulated XRDs depict similar peaks of TiO_2: α-PbO_2 structure. XRDs of calculated, measured and TiO_2: α-PbO_2 are superimposed in figure 3.46 and 3.47, and they show a clear correspondence of peaks at 27, 33, 37, 42, 57 and 67 °. XRDs of both nanoporous structures are similar to each other. They show a combination of rutile and brookite structural arrangement. Peaks were assigned using figure 1.3 and they correspond to rutile and brookite polymorphs.

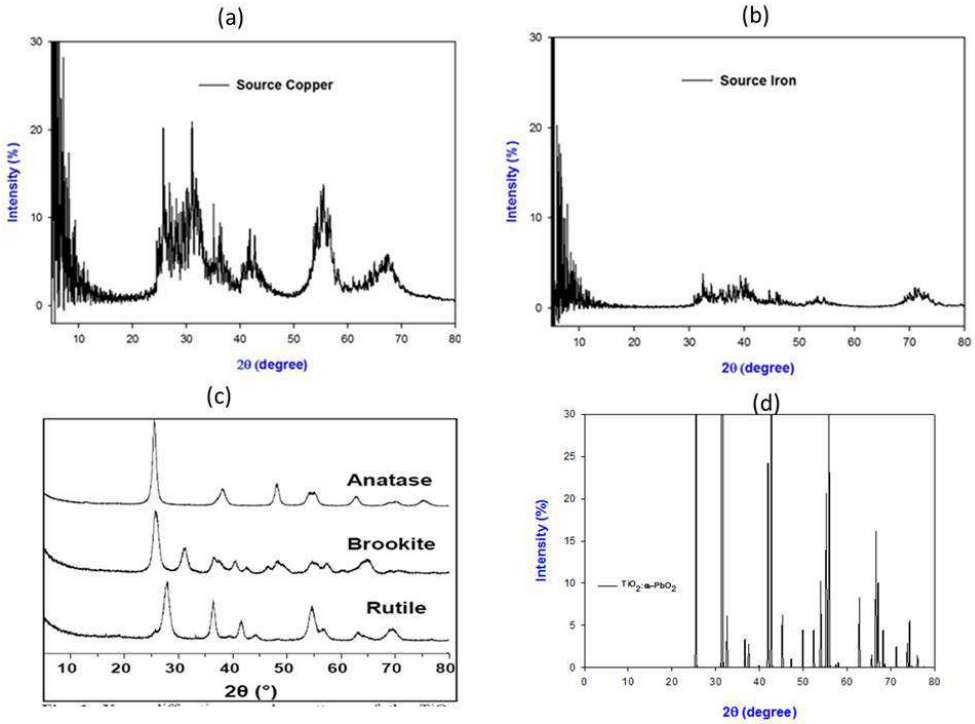

Figure 3.45: XRDs of simulated nanoporous structures from (a) copper, (b) iron sources, (c) experimental (Dambournet et al. 2009) (d) calculated TiO_2: α-PbO_2.

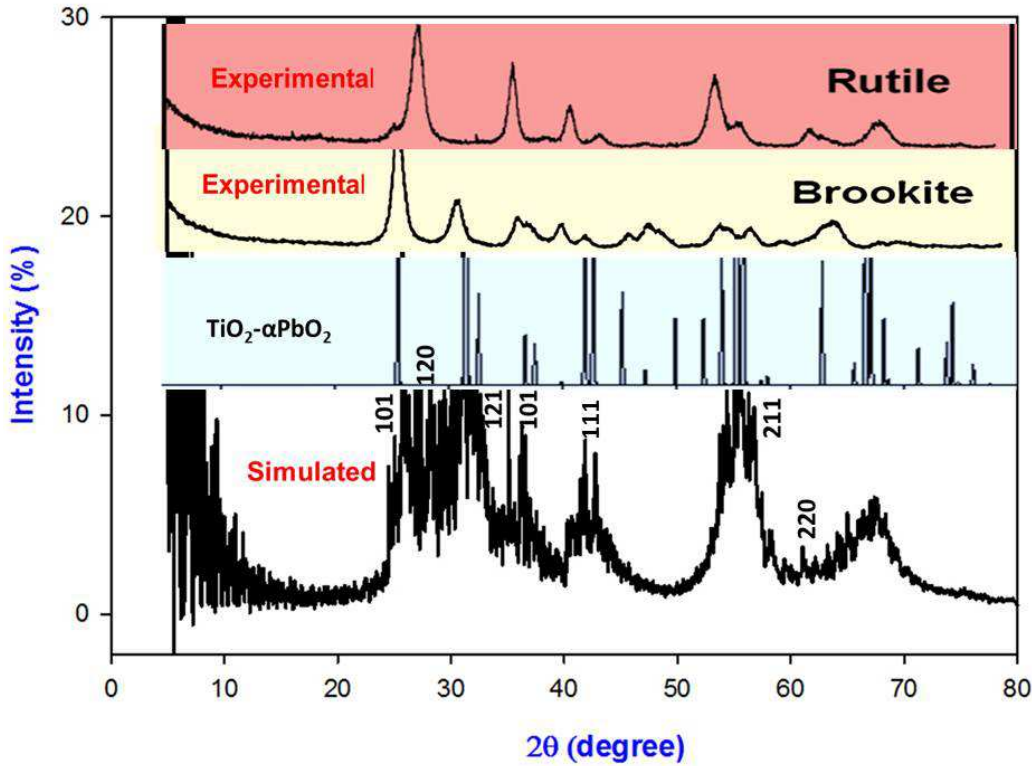

Figure 3.46: A comparison simulated TiO_2 nanoporous 60 Å, calculated TiO_2: α-PbO_2 and experimental (Dambournet et al. 2009) XRDs.

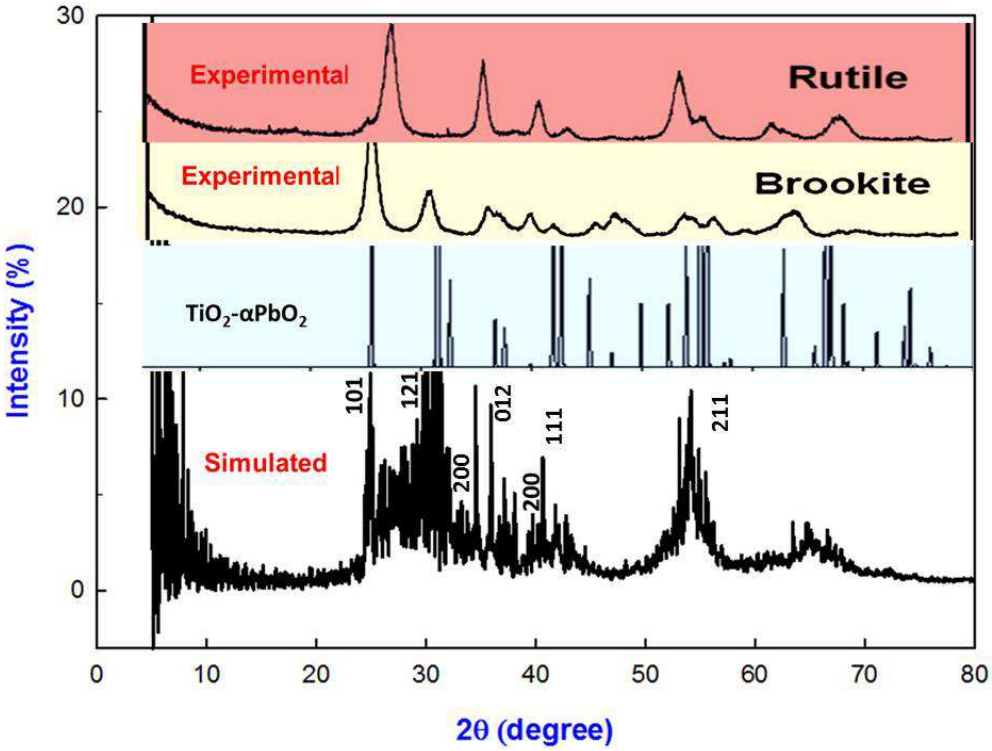

Figure 3.47: A comparison simulated TiO_2 nanoporous 66 Å, calculated TiO_2: α-PbO_2 and experimental (Dambournet et al. 2009) XRDs.

3.4.4 Titanium dioxide bulk structure

The bulk structure of TiO_2 was produced by running an NPT MD simulation on an amorphous nanosphere, to the lattice box of dimension 54 Å. Before recrystallising the bulk structure we have calculated radial distribution functions related to an amorphous phase which are shown in figure 3.48. We observe broader peaks indicating that the system is amorphous. The amorphous bulk structure of TiO_2 was recrystallised at 2000 K using NVT ensemble for 700000 steps with a time step of 0.005 ps. The graph of configuration energy as a function of time for TiO_2 bulk during recrystallisation is given in figure 3.49. In the period 0 to 0.35 ns there is a quick change of energy which shows a transition from an amorphous to a crystalline phase. The energy change during recrystallisation is from -2.033×10^5 to -2.063×10^5 eV corresponds to the latent heat of crystallisation. From 0.3 to 3.5 ns the change in energy is insignificant which indicates that a complete recrystallisation has occurred.

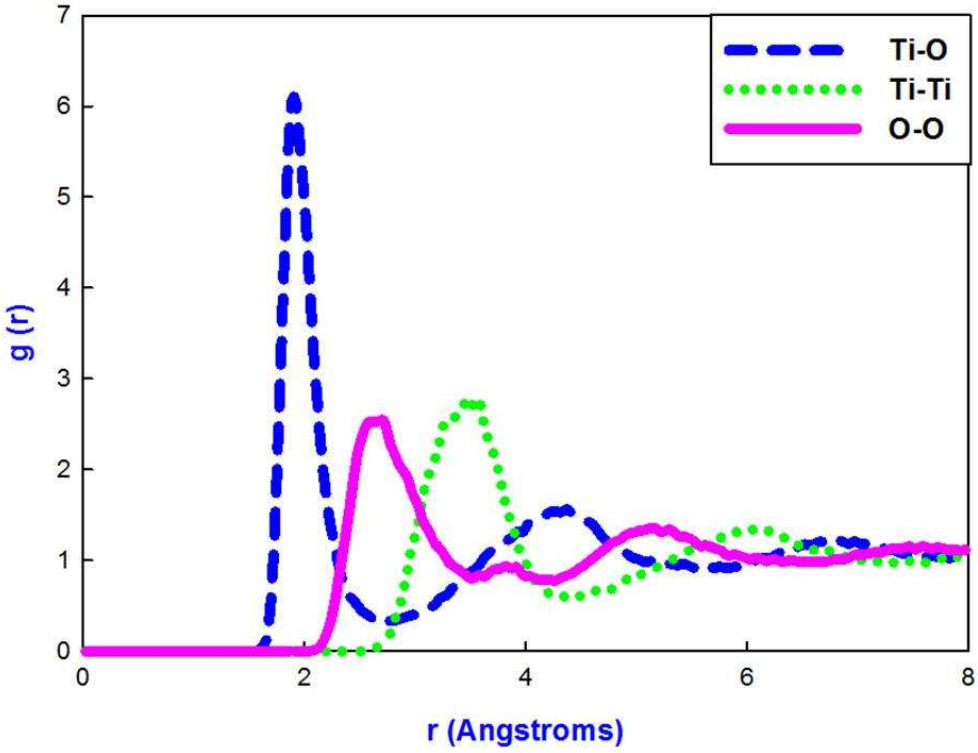

Figure 3.48: RDFs for TiO_2 bulk structure before recrystallisation at 2000 K.

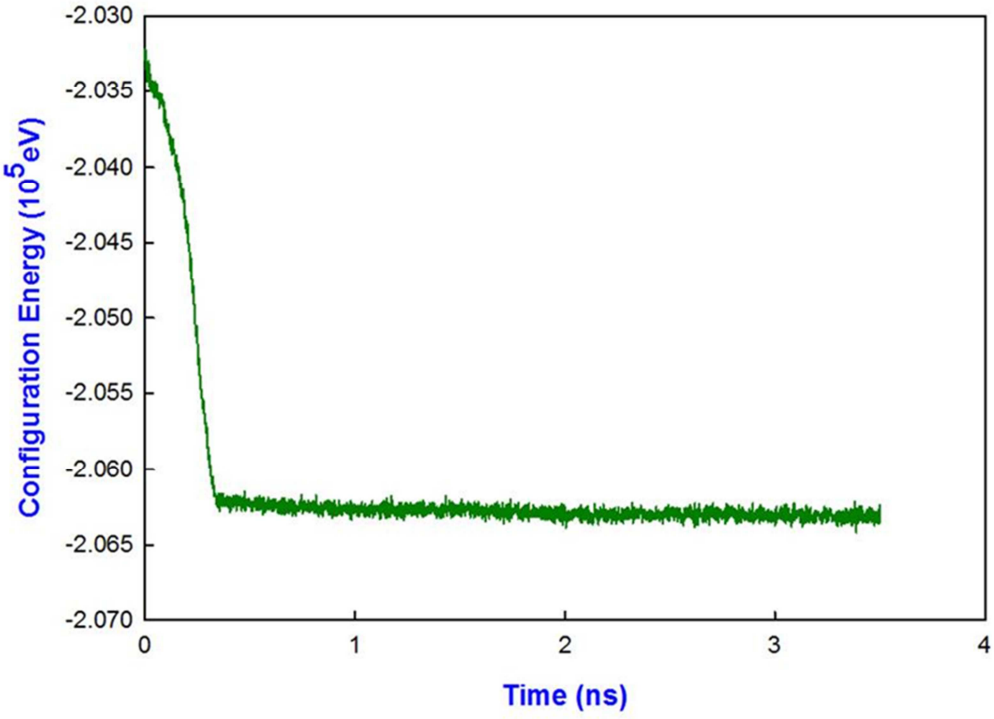

Figure 3.49: Calculated configuration energy as a function of time for the bulk structure of TiO_2 at 2000 K.

This graph behaves nearly to that of MnO_2 nanoparticle (Sayle et al. 2009). Figure 3.50 presents amorphised and recrystallised structures of the bulk. The ordered patterns observed in figure 3.50(b) suggest a crystallised bulk structure. Radial distribution functions of the bulk structure, after recrystallisation, for Ti-O, Ti-Ti and O-O interactions are shown in figure 3.51, and the sharp peaks confirm recrystallisation. At 2.0 Å we note a maximum peak which is a contribution of Ti-O interactions. The sharp peaks that are observed between 2.0 and 4.0 Å are a contribution of Ti-Ti and O-O respectively. After 4 Å, the peaks are a contribution of Ti-O, Ti-Ti and O-O interactions.

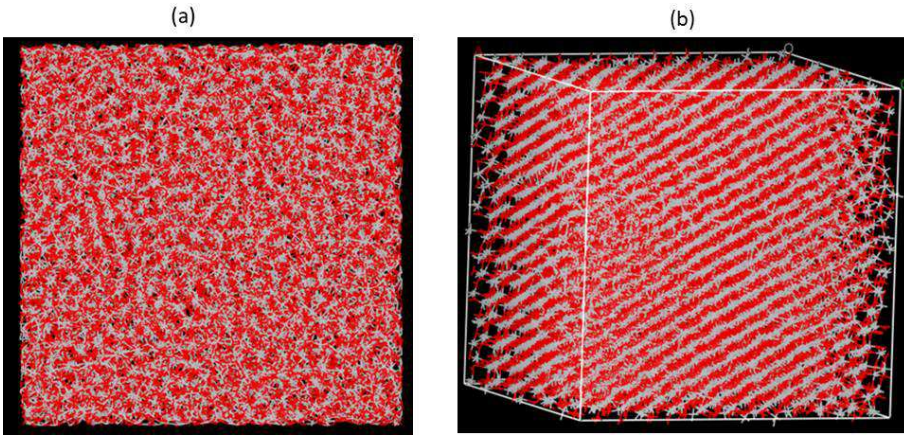

Figure 3.50: Bulk structures of TiO_2 (a) amorphised and (b) recrystallised phases at 2000 K.

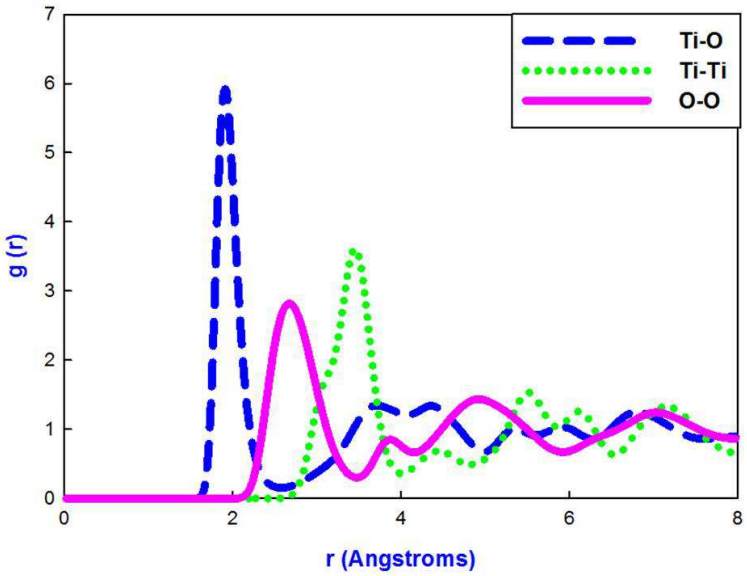

Figure 3.51: RDFs for TiO_2 bulk structure after recrystallisation at 2000 K.

We cooled the system gradually by running MD at 1500K for 500ps, 1000K for 250ps, 500K for 250ps then 0K for 500ps with a timestep of 0.005ps. The cooled structure of the bulk TiO_2 is given in figure 3.52, and tunnels are quite visible. The RDFs for cooled bulk TiO_2 are depicted in figure 3.53; they indicate that as the temperature decreases the broadness of the peak is reduced and the heights are enhanced indicating that the system is ordered. More shaper peaks are observed between separations of 2 and 7.5 Å. A plot of 0 K shows sharpest peaks than others which indicates crystallinity of the system.

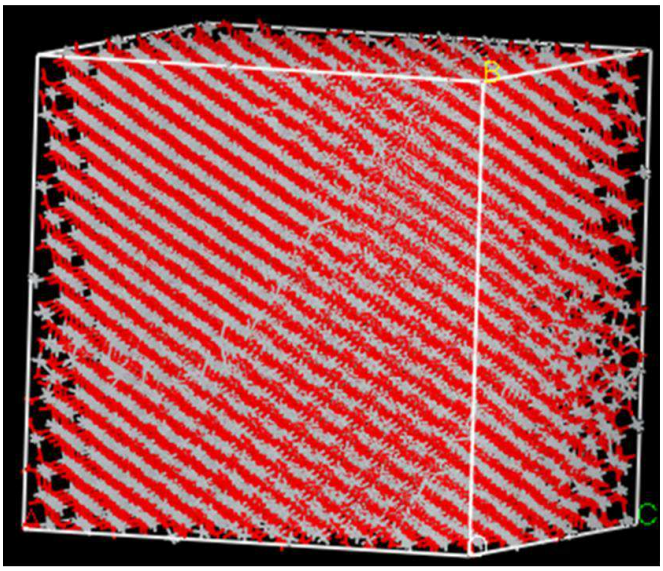

Figure 3.52: A cooled crystallised structure of bulk TiO_2 at 0 K.

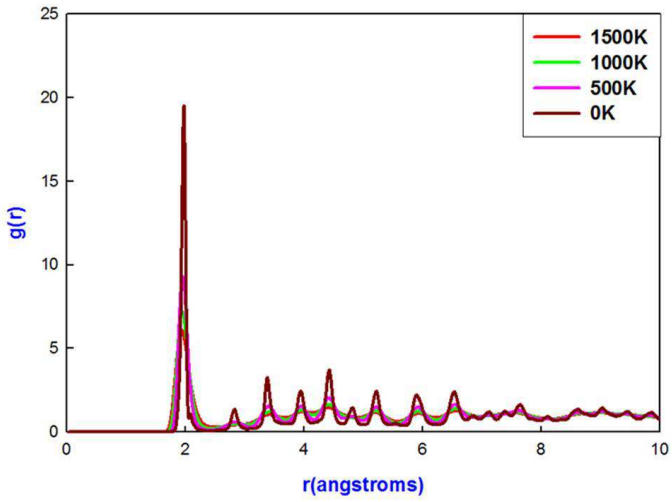

Figure 3.53: RDFs of the crystallised bulk TiO_2 at different temperatures.

Figure 3.54 shows the microstructures of the bulk TiO_2, where the blue chains depict the upper Ti^{4+} octahedra while white ones represent the lower layer of Ti^{4+} octahedra. The microstructure of the bulk TiO_2 features the zigzag and straight tunnels corresponding to brookite and twinned rutile polymorphs respectively and few vacancies, in figure 3.54a; and in a different orientation (figure 3.55b) rambling squares are depicted.

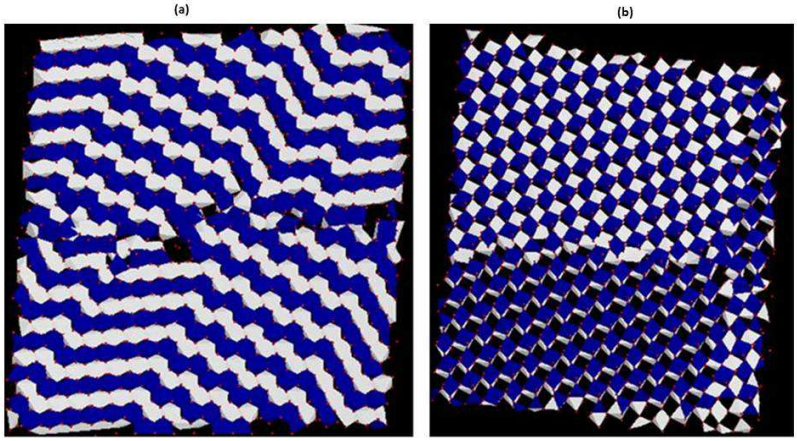

Figure 3.54: Microstructure of the cooled (0 K) crystallised bulk TiO_2 in different orientations.

We have calculated the XRDs of the simulated bulk TiO_2 with Cu and Fe radiations and they are presented in figure 3.55 together with the experimental results (Dambournet et al. 2009). Calculated XRDs with the Cu source show better resolved peaks and are more consistent with experiments than those of Fe, hence will be used in our discussions. Superimposed XRDs of simulated, measured TiO_2 and calculated TiO_2: α-PbO_2 is depicted in figure 3.56 and they show a clear correspondence of peaks. The first XRD peak of the simulated bulk TiO_2 between 20 and 30 ° corresponds well with those of the TiO_2: α-PbO_2 and brookite structures. The second peak between 30 and 35 ° is better aligned with that of the TiO_2: α-PbO_2 polymorph, whilst the third peak is closer to the three polymorphs, inclusive of rutile. The fourth peak and those nearer to the right correspond better with those of the TiO_2: α-PbO_2 structure than the brookite and rutile polymorphs. The smoother simulated curve around 50 ° is characteristic of the rutile

polymorph; including the distinct peak between 50 and 60 ° where fairly less intense peaks of brookite and TiO_2: α-PbO_2 is noted. The last broad peak of the simulated bulk structure above 60° incorporates elements of the brookite and rutile structures. Assigned peaks correspond to rutile and brookite model by figure 1.3.

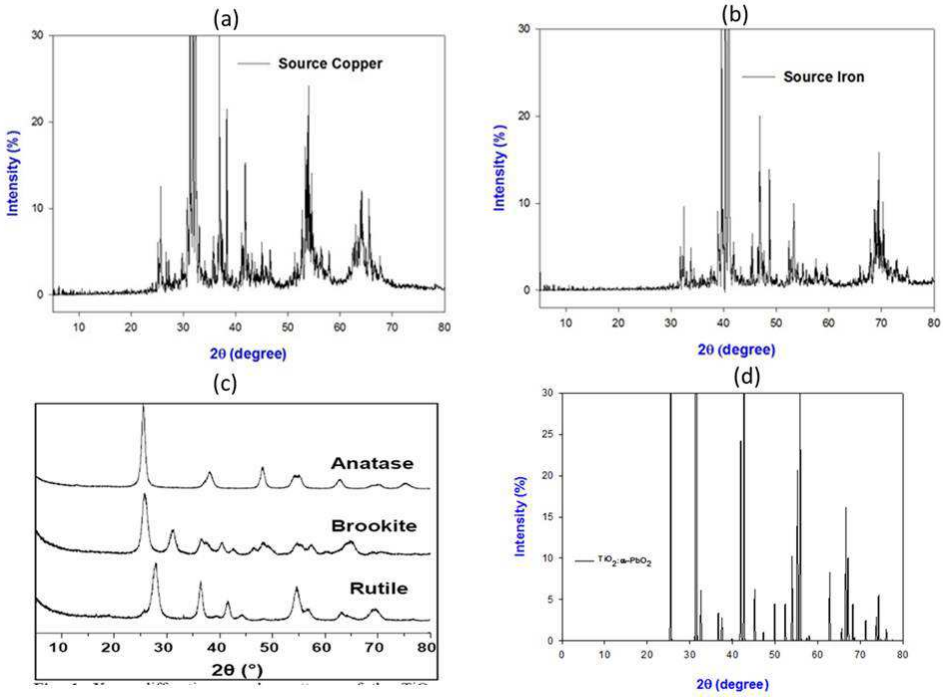

Figure 3.55: XRDs of TiO_2 bulk (a) copper and (b) iron source (c) experimental (Dambournet et al. 2009) and (d) calculated TiO_2: α-PbO_2.

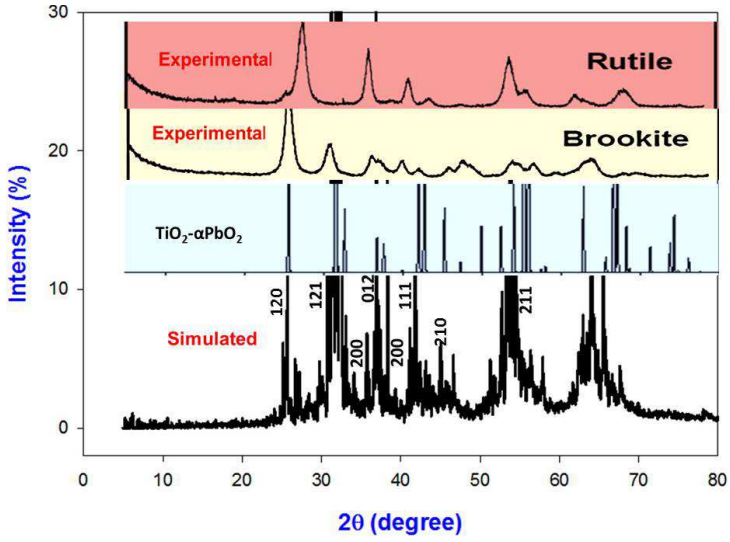

Figure 3.56: A comparison simulated TiO_2 bulk, calculated TiO_2: α-PbO_2 and experimental (Dambournet et al. 2009) XRDs.

3.5 Discussions

In this chapter the amorphisation recrystallisation method was employed to spontaneously generate simulated nanosheet, two nanoporous structures with channels of different sizes and bulk TiO_2 structures from an amorphous nanosphere. Prior to crystallisation the nanosphere, nanoporous and bulk architectures were completely amorphous whilst the nanosheet structure was partially amorphised. All nano-architectures were fully recrystallised, at 2000K, which was confirmed by their corresponding plots of configuration energy as a function of time and RDFs. Furthermore, nanostructures were cooled to 0 K and their related RDFs have well defined sharp peaks as compared to those at higher temperatures. Cooled nanoporous structures and their microstructures contain channels and tunnels consistent with those observed experimentally (Wang et al. 2008).

Microstructures of the TiO_2 nanosphere, nanoporous and nanosheet architectures display zigzag and straight tunnels, where the former are associated with the brookite and the latter with twinned rutile polymorph. Tunnels of the simulated nanosheet and nanoporous structure agree well with those of the experimental HRTEM (Wei et al. 2011) and TEM (Wang et al. 2008) micrographs respectively. The microstructures of the bulk TiO_2 also feature straight and zigzag tunnels and, in addition, exhibit rambling squares that suggest substantial rutile content. The latter patterns are scarce in other nano-architectures which have been used extensively in electrodes for Li-ion batteries. Hence, the presence of typical 1x1 rutile tunnels in simulated microstructures of the TiO_2 bulk architecture, could explain why the bulk form is not preferable for electrodes, as observed experimentally (Koudriachova et al. 2001). All microstructures of TiO_2 nanostructures exhibit certain features that are observable in MnO_2 (Sayle et al. 2005), they have twinned pyrolusite/rutile patterns and vacancies. Availability of tunnels

provides paths for lithium transport and storage in lithium ion batteries, as noted in the MnO_2 nano-architectures (Sayle et al. 2009).

Generally, the TiO_2 XRD patterns calculated with the copper source, show peaks that are satisfactorily aligned with experimental results (Dambournet et al. 2009). A comparison of the experimental and calculated XRDs of most simulated nano-architectures suggests the prevalence of the brookite polymorph in the generated structures. The brookite structure (PBCA) is very close to the TiO_2: α-PbO_2 structure (PBCN) and the latter were reported by Sayle and Sayle (2007) in simulated high-pressure crystallisation of TiO_2 nanoparticles. Indeed the experimental work of Reddy et al. (2006, 2007 and 2008) has reported the occurrence of the brookite phase in nanoparticles of TiO_2 and their aggregates. Furthermore, as mentioned in section 1.2, TiO_2 brookite is naturally occurring and has a structure consisting of edge- and corner-sharing TiO_6 octahedra, which form channels along the c axis (Bauer 1961). The dimensions of the channels are suitable to accommodate lithium ions (~0.76 Å). Furthermore, the presence of the rutile phase in the simulated nano-architectures has been observed, particularly from peaks corresponding to diffraction angles greater than 35^o. The microstructures of simulated TiO_2 nano-architectures show that this polymorph occurs predominantly in the twinned form, which also provide path for the transport of lithium ions, except for the bulk phase which includes the pure rutile phase. The XRDs patterns of simulated MnO_2 nano-architectures were calculated (Sayle et al. 2009a) and were found to predominantly depict pyrolusite type polymorph, in agreement with experimental results.

A careful analysis of our simulated TiO_2 nanosheet structure clearly indicates that it has exposed {001} surfaces, which are known to be highly reactive. This configuration is of great significance since it enhances the rate capability of the anode, as it shortens the Li

ion diffusion path and lowers insertion energy barriers on the active surface for Li ions (Ortiz et al. 2011). In addition, it enhances the electrolyte/electrode contact via the hollow structures. However, it is experimentally known that {001} surfaces are naturally unstable and tend to be dominated by the thermodynamically stable {101} facets. Recently, novel synthesis approaches of stabilising the less stable TiO_2 anatase surfaces, such as {001} (Young et al. 2008) and {100} (Wei et al. 2011) have been reported. Furthermore, nanosheets of the TiO_2–B polymorph have also been experimentally fabricated (Liu et al. 2012) and tend to ensure fast insertion and extraction of Li-ion due to its pseudocapacitive mechanism, while the porous structure with thin nanosheet wall effectively extends the interfacial zone and thus can greatly promote ionic transport and electrode reaction. The current simulations confirm that nanosheets with the predominant brookite and twinned rutile polymorphs are feasible. It is further interesting that, unlike other polymorphs, partly crystalline nanosheets were generated from an amorphous nanosphere, before crystallisation was allowed to commence; as depicted by its configuration energy vs. time curve. The change in such curve is small as compared to a full amorphisation to crystallisation transition, and is mainly ascribed to an annealing of a grain boundary.

The simulated TiO_2 nanoporous architecture structures (Figure 3.34) have distinct tunnels oriented parallel and perpendicular to the page and having zigzag and straight patterns (Figure 3.41 and 3.42). Such tunnels provide an excellent path for Li ion transport in the nanoporous structure. Electrodes of nanoporous structure materials for lithium batteries have short transport lengths for Li^+ ions due to their nano-sized grains (10–20 nm). The shape of the simulated channels appears similar to those on the electron microscope micrographs (Ren et al. 2010). The presence of the channels (5-10 nm) yields an easy access for electrolytes. Such nanoporous TiO_2 materials have high packing densities

unlike nanopowders, nanowires, nanorods and nanotubes. The storage performance and the packing density of the as-synthesized nanoporous TiO_2 are respectively reported to be five times and 6.6 better than the commercially available TiO_2 nanopowder (Saravanan et al. 2010).

In the case where ordered and uniform channels in the nanoporous TiO_2 exist the volume change during Li-ion insertion/de-insertion process can be conveniently accommodated. In addition, the three dimensional movement of Li ions in zigzag and straight tunnels contribute towards optimum expansion of electrodes. As with the porous MnO_2 (Sayle et al. 2009a, 2009b), it may be surmised that the tunnels and channels provide accessible paths for Li ions into the electrode, which will ultimately enhance the rate capability of related Li–ion batteries, and simultaneously enable many cycles to occur with reduced level of degradation because the host lattice is able to expand and contract symmetrically and uniformly, thus minimising the propensity for plastic deformation and fracture.

Chapter 4
Lithiation of TiO_2 nano-architectures

4.1. Introduction

In this chapter we present various nano-architectures of TiO_2 doped with different concentrations of lithium atoms. Amorphous nanostructures of TiO_2 that were produced in chapter 3 will be lithiated with different number of lithium atoms. Since higher concentrations impeded crystallisation (Dambournet et al. 2011) we will only consider lithiated structures with $50, 100$ and 300 lithium atoms. Amorphisation and recrystallisation technique will be employed to generate crystallised lithiated nanostructures. All recrystallised structures will be cooled, using the methods employed in the previous chapter and their RDFs will be calculated. Microstructures will also be presented, however only for cooled systems. We have noted from chapter 3 that XRDs using Cu source are in good accord with experimental results as compared to those of Fe. Hence we will calculate XRDs of cooled structures with the copper only source. As in the previous chapter we will compare our results with available experimental results.

4.2. Methodology

The potential models employed in this chapter are based on the Born model of ionic solids (Born et al. 1954) as in chapter 3. However, Ti^{4+}, Ti^{3+}, Li^{+} and O^{2-} ions interact via long-range Coulomb and short range interactions, given in table 4.1.

Table 4.1 Buckingham potentials used for lithiated TiO_2

Ion pair (ij)	A_{ij} (eV)	ρ_{ij} (Å)	C_{ij} (eV.Å6)
Ti^{3+}-O^{2-}	18645.840	0.1950	22.0000
Li^{+}-O^{2-}	426.48000	0.3000	0.00000
Ti^{3+}-Ti^{4+}	28707.210	0.1560	16.0000
Ti^{3+}-Ti^{3+}	33883.920	0.1560	16.0000

In this chapter we present and discuss the lithiated nanostructures of TiO_2. All produced nanostructures were lithiated with different number of lithium atoms.

4.3 Amorphisation and recrystallisation of lithiated TiO_2 nano-architectures.

This section will present and discuss the various lithiated nanostructures of TiO_2, generated by the amorphisation and recrystallisation strategy, as discussed in Section 2.3. The cooling method will be employed on all lithiated structures as in previous sections. Radial distribution functions after recrystallisation and cooling will also be presented. Configuration energy as a function of time will be shown in order to demonstrate when the nanostructures begin to recrystallise.

4.3.1 Lithiated structures of TiO_2 nanosphere

The RDFs of lithiated TiO_2 nanosphere with 50, 100 and 300 lithium atoms before recrystallisation are given in figure 4.1, while their structures are shown in figure 4.2. The RDFs show broader peaks indicating that the structures are amorphous. After lithiation we performed molecular dynamics simulation using the NVT ensemble, at 2000 K, for 700000 steps with a time step of 0.005 ps in order to recrystallise the structures.

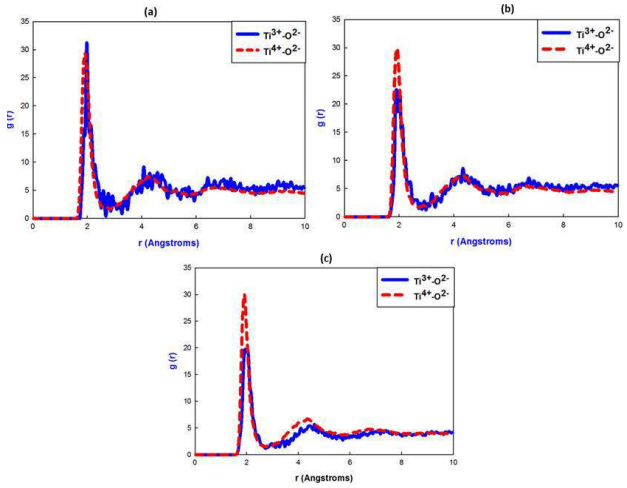

Figure 4.1: The RDFs of the TiO_2 nanosphere before recrystallisation with (a) 50, (b) 100 and (c) 300 lithium atoms.

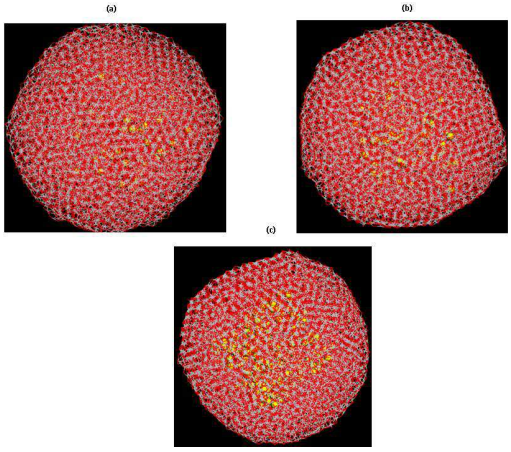

Figure 4.2: Lithiated structures of the TiO_2 nanosphere with (a) 50, (b) 100 and (c) 300 lithium atoms.

A plot of the configuration energy as a function of time for all lithiated nanospheres during recrystallisation is given in figure 4.3. The energy plot of the nanosphere with 50 lithium atoms shows an abrupt drop from 0 to 0.25 ns with configuration energy changing from -2.02×10^5 to -2.033×10^5 eV. In the period 0.25 to 0.8 ns there is a small change of energy which indicates that crystallisation of the structure is nearing an end. In the range 0.8 to 3.5 ns the energy remains constant which suggests that the lithiated

nanosphere is completely recrystallised. The configuration energy plot of the nanosphere with 100 lithium atoms exhibits an end of a plateau from 0 to 0.1 ns, which could be associated with a nucleation phase. An energy reduction, but more gentle than that of the 50 Li atom system, is noted from 0.1 to 0.65 ns with configuration energy varying from -2.007x10^5 to -2.033x10^5 eV. From 0.65 to 1.2 ns the energy is near constant which signals ends of crystallisation. From 1.2 to 3.5 ns the energy does not vary affirming a complete crystallisation. The slope of the configuration energy plot, for the 300 Li atoms nanosphere, reduces less steeply than those of lower concentrations, in the range 0 to 1.35 ns; with its magnitude changing from -1.983x10^5 to -2.012x10^5 eV. From 0.1.35 to 1.5 ns the energy tends to level off which reveal that the structure ceases to recrystallise. From 1.5 to 3.5 ns the energy is almost invariable which is an evidence of fully recrystallisation is. Hence, from all three plots we observe that there is an amorphous to crystalline transition caused by the sudden drop of energy. However, as more lithium atoms are introduced in the nanosphere it takes much longer time to fully recrystallise.

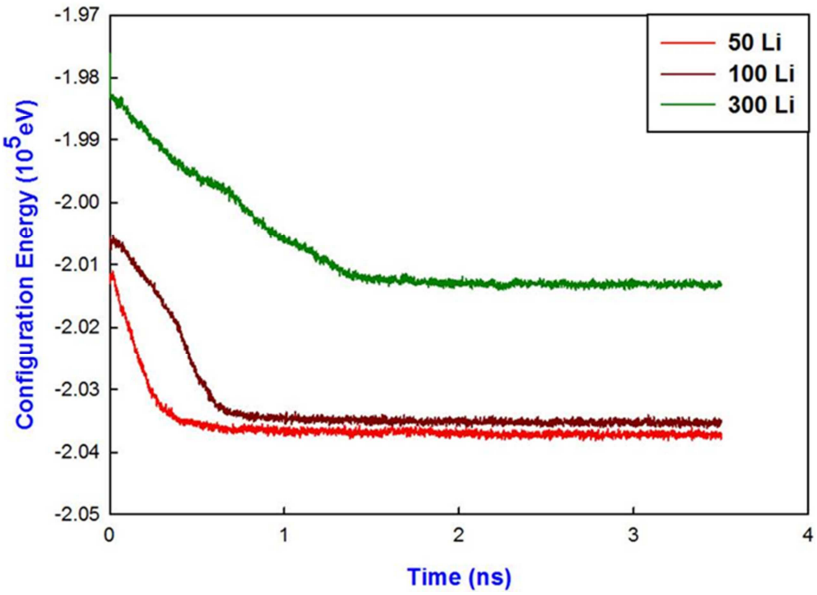

Figure 4.3: Calculated configuration energy as a function of time for the lithiated TiO_2 nanosphere.

Figure 4.4 shows the evolvement of the seed consisting of three layers of titanium atoms which are superimposed on each other. The movement of three Li atoms, labelled A, B and C is monitored from 500 to 1100 ps. At 500 ps the C atom is not visible since it is located in the lower layer. The C atom is noted in the middle layer, at 1000 ps, and the crystalline pattern grows in its vicinity. More Li atoms have started moving within the system. At 1100 ps atom C moved to the upper layer and most of the seed appears crystalline.

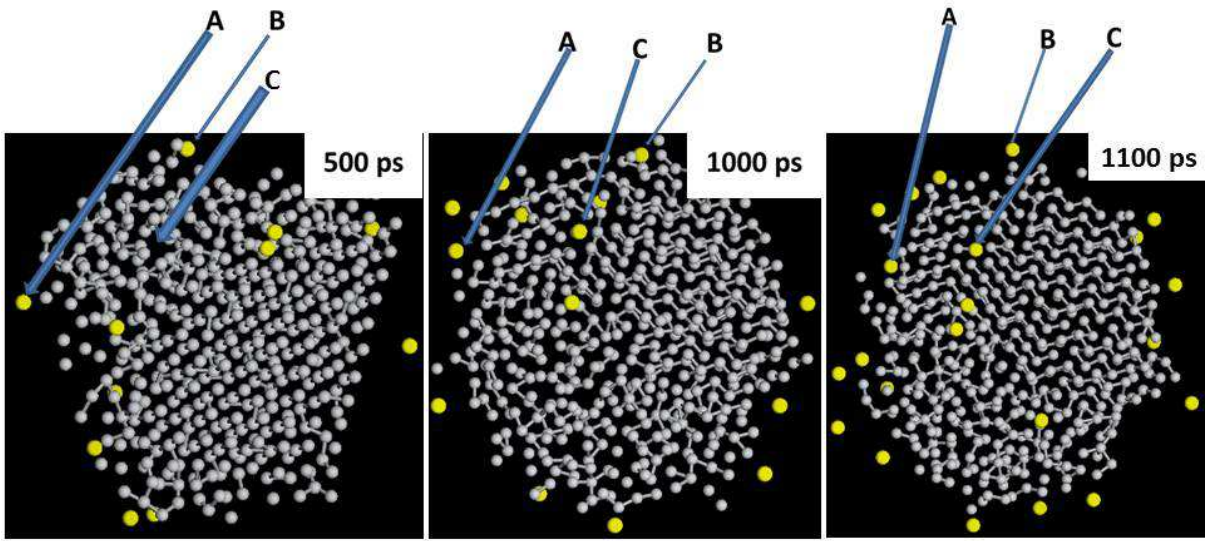

Figure 4.4: Molecular graphics for a slice of TiO_2 nanosphere with 300 Li, and consisting of three layers of titanium atoms. Li is coloured in yellow.

Recrystallised structures of lithiated nanosphere, with 50, 100 and 300 atoms are shown in figure 4.5. As crystallisation occurs some lithium atoms move out of the nanosphere or away. As to how many lithium atoms move out of the system and how many remain, depends on the number of lithium atoms originally in the system. As an example figure 4.5 (c) shows more lithium atoms that have moved outside the 300 Li atoms system than others with a lower number of lithium atoms.

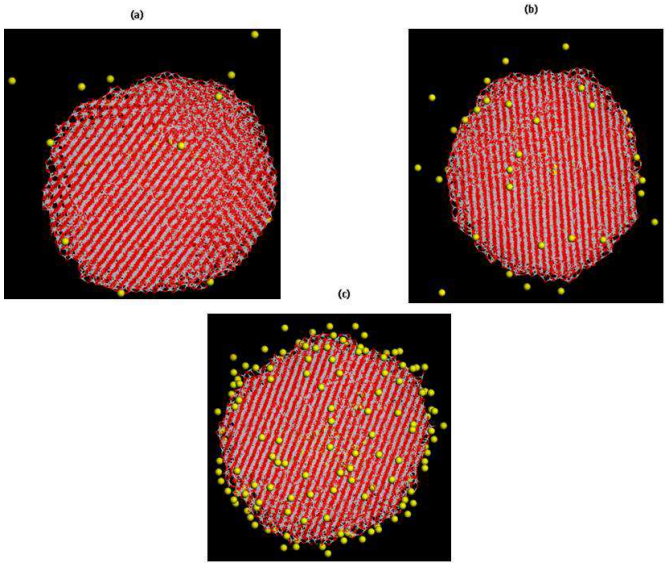

Figure 4.5: Recrystallised structures of lithiated nanosphere (a) 50, (b) 100 and (c) 300 lithium atoms.

Total radial distribution functions of all lithiated nanospheres after recrystallisation confirm that the systems have crystallised since we observe peaks at different distances (r). Total RDFs Ti^{3+}-O^{2-} and Ti^{4+}-O^{2-} interactions are presented in figures 4.6, 4.7 and 4.8 for lithiated nanosphere with 50, 100 and 300 lithium atoms respectively. The maximum sharp peak is observed at 2 Å for both interactions, with Ti^{4+}-O^{2-} being the highest and Ti^{3+}-O^{2-} the lowest. We observe other peaks at 3.8 and 4.5 Å for all systems. After a peak at 4.5 Å we can identify more peaks which are slightly broader than the peaks of unlithiated nanosphere. The total RDFs of the lithiated nanosphere with 300 lithium atoms have broadest peaks at 6, 7 and 9 Å as compared to lightly lithiated structures. This shows more lithium atoms tend to enhance the amorphous behaviour of the nanosphere and inhibit recrystallisation. The total RDFs of lithiated nanospheres have revealed this recrystallisation transition that the structures could not clearly show. Total RDFs of the nanosphere with 300 lithium atoms for both Ti^{3+}-O^{2-} and Ti^{4+}-O^{2-} interactions overlap more which is associated with increasing Ti^{3+} ions.

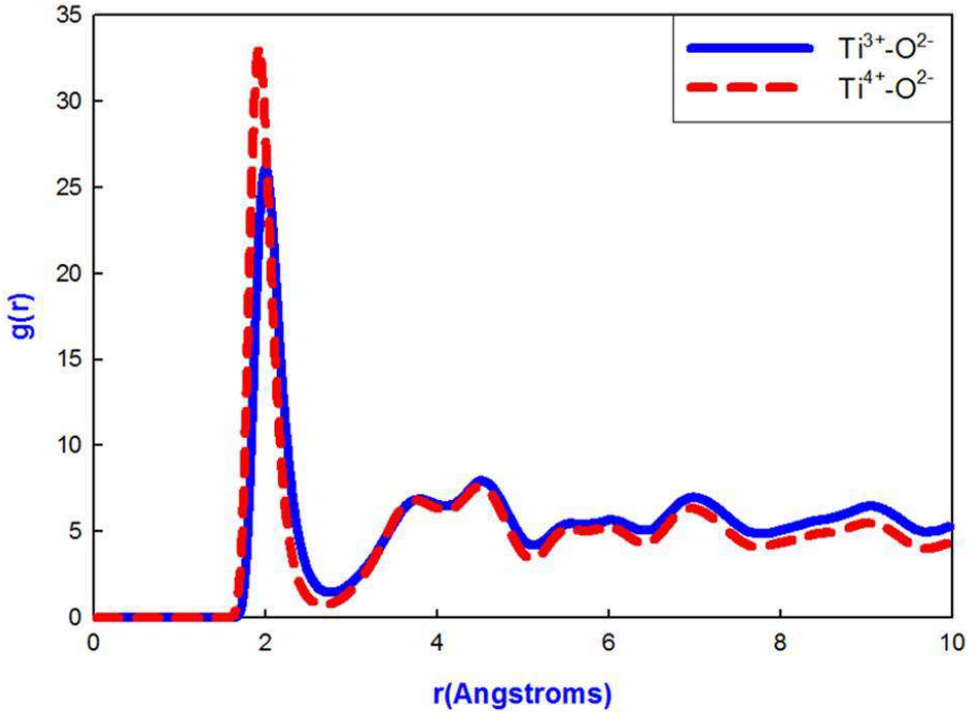

Figure 4.6: RDFs of the TiO_2 nanosphere with 50 lithium atoms at 2000 K.

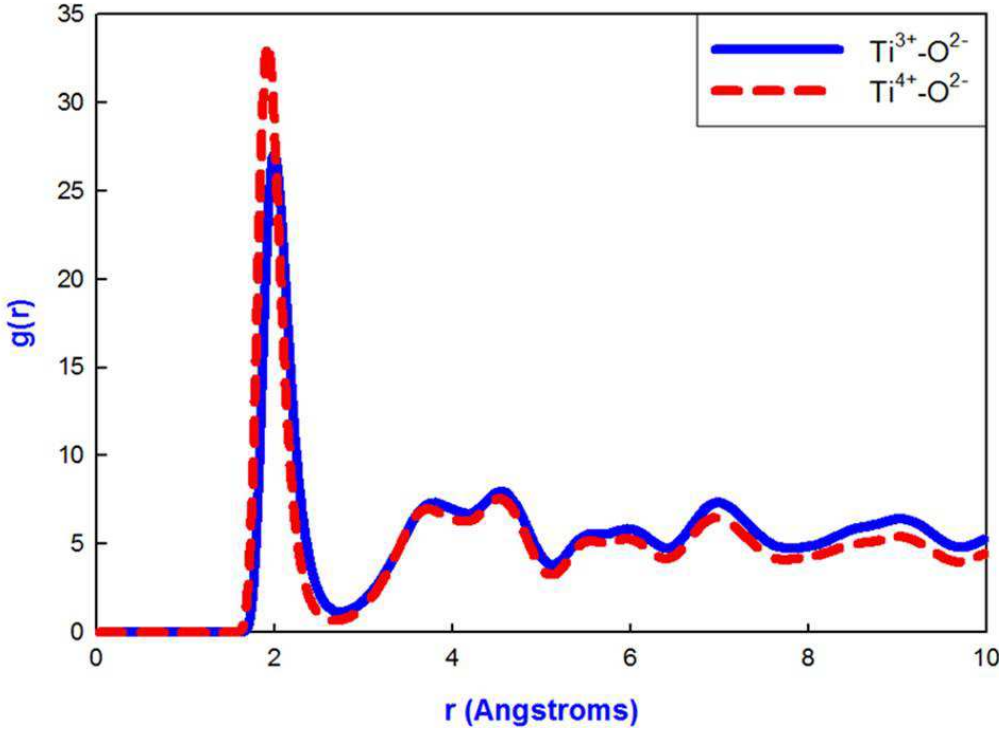

Figure 4.7: RDFs of the TiO_2 nanosphere with 100 lithium atoms at 2000 K.

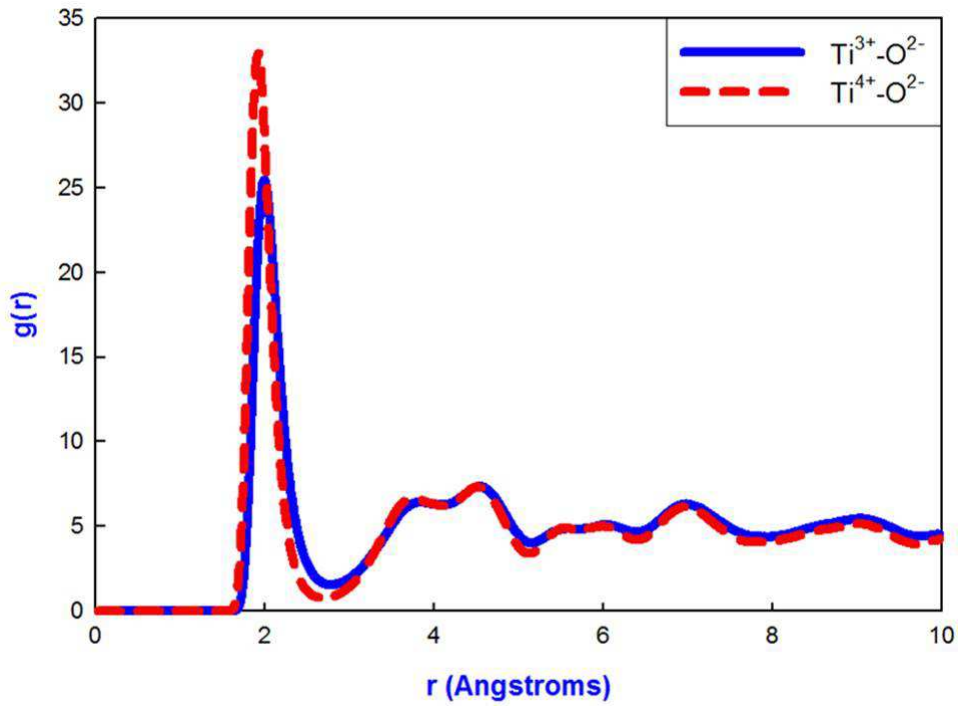

Figure 4.8: RDFs of the TiO_2 nanosphere with 300 lithium atoms at 2000 K.

As in the previous chapter we cooled the nanosphere gradually by firstly performing MD simulations for 500 ps at temperature of 1500 K, followed by a run for 250 ps at 1000 K, and lastly for 500 ps at temperature of 0 K. A cooled structure of the nanosphere with 50 lithium atoms is presented in figure 4.9. We observe patterns and some tunnels on the structure, and a few lithium atoms have moved out of the structure while other atoms remain inside. Total radial distribution functions of the nanosphere with 50 lithium atoms are presented in figure 4.10 (Ti^{3+}-O^{2-}) and figure 4.11 (Ti^{4+}-O^{2-}). They both show a similar behaviour that the system has been successfully cooled; this is partly evidenced by the decreases in the broadness of the peaks and in the increase of the height of the peak as the temperature is reduced. At approximately 2 Å we observe an expected trend where the 0 K peak is the highest and the 1500 K the lowest.

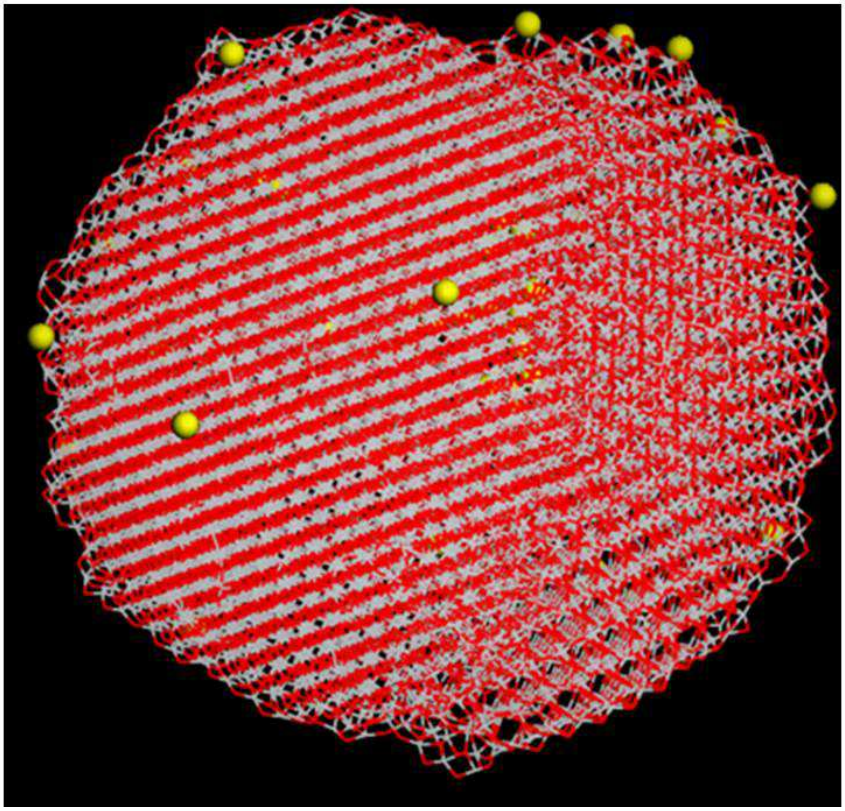

Figure 4.9: A cooled TiO_2 nanosphere structure with 50 lithium atoms.

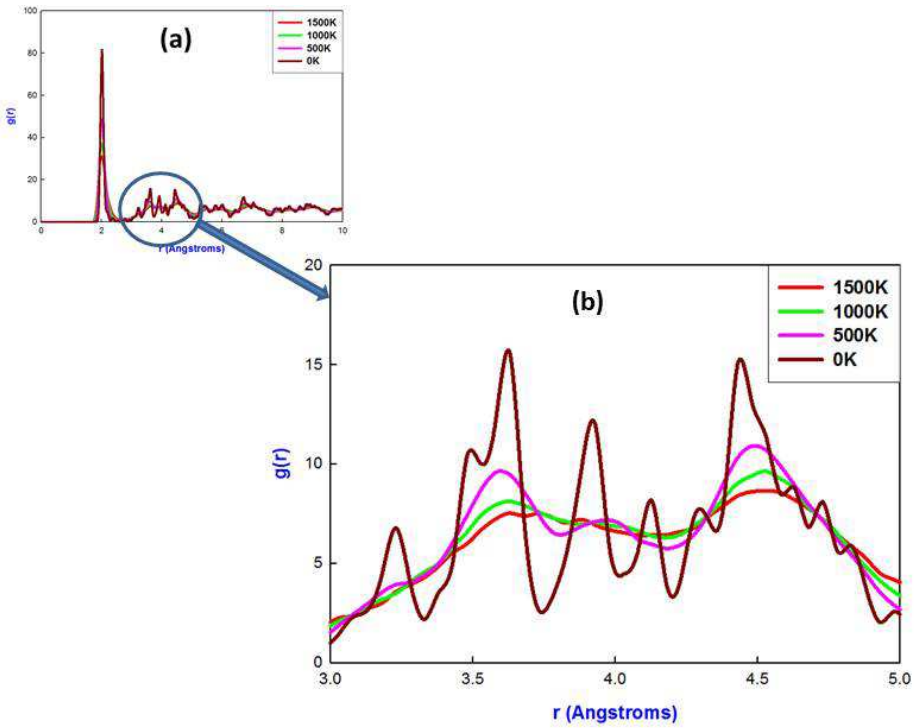

Figure 4.10: RDFs of Ti^{3+}-O^{2-} for the cooled TiO_2 nanosphere with 50 lithium atoms.

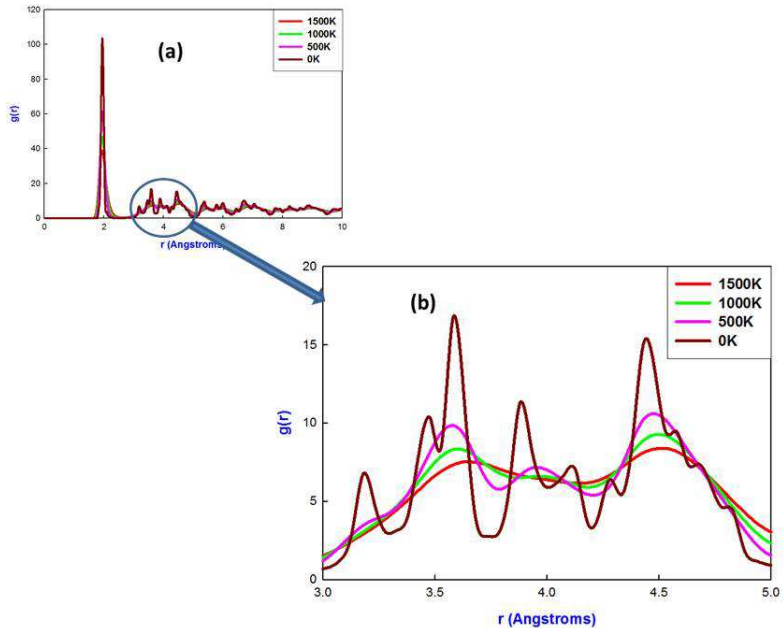

Figure 4.11: RDFs of Ti^{4+}-O^{2-} for the cooled TiO_2 nanosphere with 50 lithium atoms.

The cooled structure of the TiO_2 lithiated nanosphere with 50 lithium atoms was sliced in order to depict a microstructure which is presented in figure 4.12. The blue octahedra correspond to the upper layer of Ti^{4+}, and the white adjacent the lower layer and the lithium atoms are represented by yellow balls. The microstructure of the nanosphere shows zigzag tunnels which are associated with the brookite and the straight tunnels that are related to the twinned rutile polymorphs. Few vacancies are observed on the microstructure, and lithium atoms have moved into vacancies of the structure. A good anode requires the nanosphere to store optimum lithium atoms and provide pathways for their transport. Indeed the microstructure of the nanosphere reflects lithium atoms that are located in the tunnels.

Figure 4.13 depicts calculated, TiO_2: α-PbO_2 and measured (Dambournet et al. 2009) XRDs as compared to those of the simulated nanosphere. Two peaks just below and above 30 ° accord with the brookite and TiO_2: α-PbO_2 structures. At 37 and 57 °, observed peaks correspond to all measured structures. Simulated XRDs at 50 ° has a

smooth curve which accords with the rutile structure. At 67 ° we notice a peak which is in agreement with TiO_2: α-PbO_2 and rutile polymorphs. This implies that the lithiated TiO_2 nanosphere with 50 lithium atoms has a combination of brookite, TiO_2: α-PbO_2 and rutile structural arrangements. XRDs correspond to rutile and brookite model.

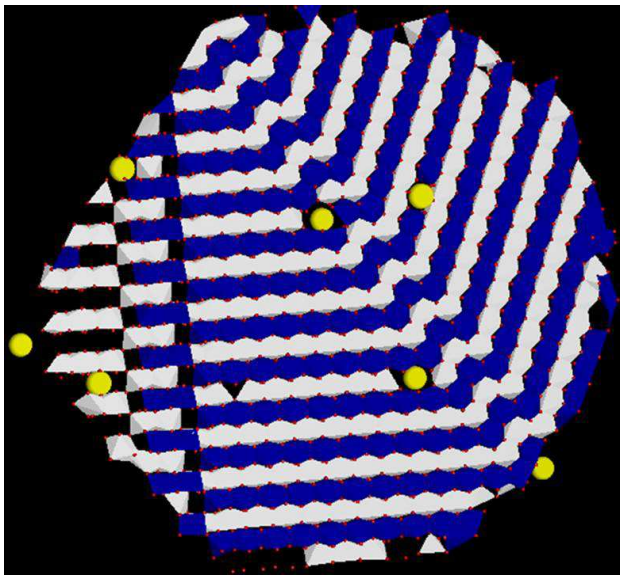

Figure 4.12: Microstructure of the TiO_2 nanosphere with 50 lithium atoms.

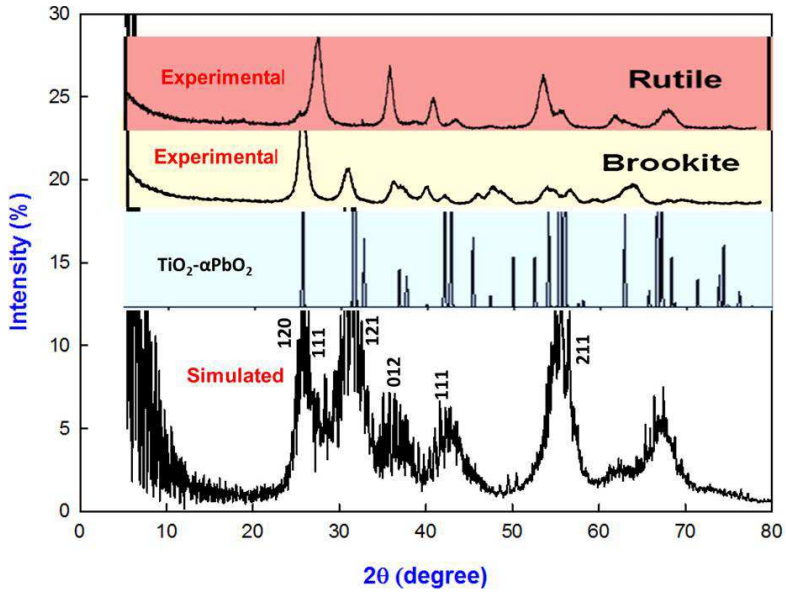

Figure 4.13: A comparison simulated TiO_2 nanosphere with 50 Li, calculated TiO_2: α-PbO_2 and experimental (Dambournet et al. 2009) XRDs.

The cooling procedure was also used on the recrystallised nanosphere of 100 lithium atoms and the corresponding structure is illustrated in figure 4.14. Clear patterns and more tunnels are observed throughout the systems. The nanosphere with 100 lithium atoms shows some lithium atoms have moved to the periphery of the system while others remain in the system. This structure has more tunnels as compared to that one with 50 lithium atoms. Total radial distribution functions of the system are presented in figure 4.15 (Ti^{3+}-O^{2-}) and figure 4.16 (Ti^{4+}-O^{2-}). They show similar trend of the peaks throughout the graph, especially near around peak of 2 Å. At peak of 2 Å we observe a clear trend of peaks as the smallest peak corresponds to the temperature of 1500 K, followed by the peak of temperature of 1000 K, then peak of 500 K and ultimately a peak of 0 K. Throughout the graphs of RDFs we observe a peak of 0 K being the sharpest and highest implying that the system has properly crystallised.

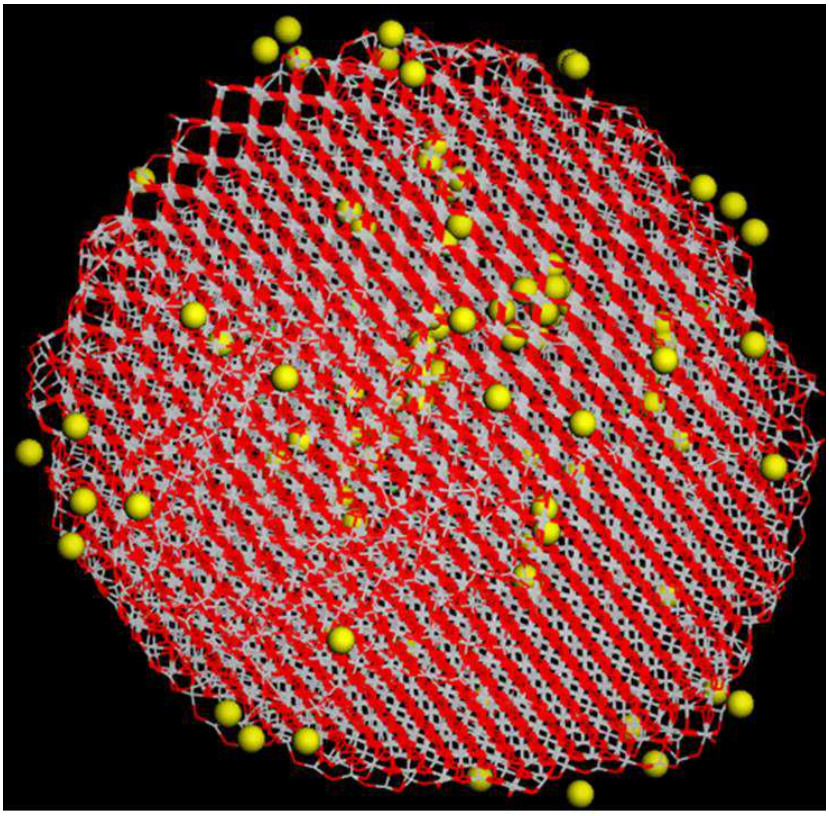

Figure 4.14: A cooled nanosphere structure with 100 lithium atoms.

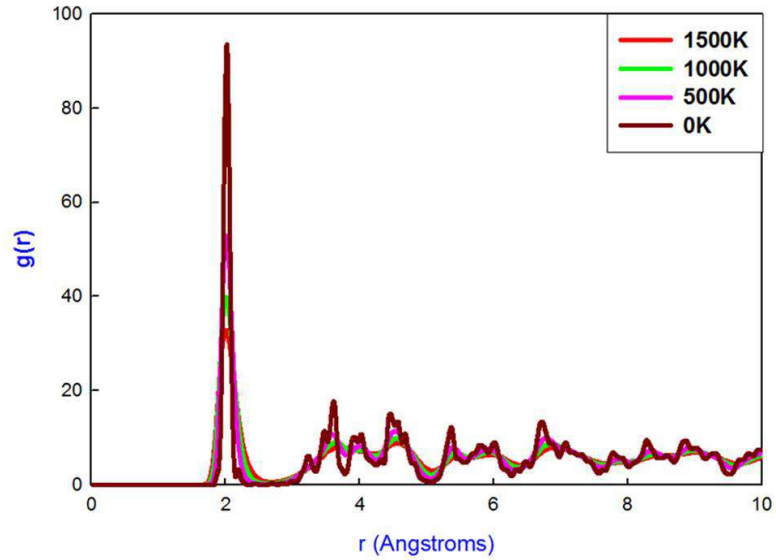

Figure 4.15: RDFs of Ti^{3+}-O^{2-} for the cooled nanosphere with 100 lithium atoms.

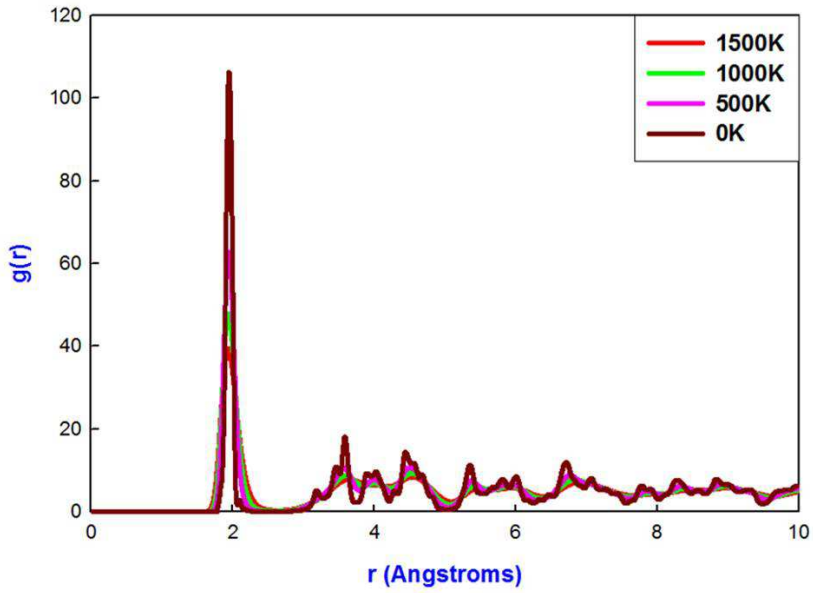

Figure 4.16: RDFs of Ti^{4+}-O^{2-} for the cooled nanosphere with 100 lithium atoms.

We have created microstructures of a nanosphere with 100 lithium atoms which are presented in figure 4.17. Microstructures of lithiated nanosphere are created in different directions in order to view different orientations of the structure. The blue colour is the upper layer of Ti^{4+}, the white colour is the lower layer of Ti^{4+} and yellow colour is the

lithium atoms. Straight tunnels which are associated with pyrolusite, zigzag tunnels which are associated with twinned pyrolusite, small defect cluster and vacancies are observed on the microstructures. It is apparent from the cooled structure of nanosphere, with 100 lithium atoms shown in figure 4.14, that some lithium atoms remains in the structure which indicates that the system has a storage capacity. Microstructures show some lithium atoms filled the vacancies and some moved out of the structure. Since we have increased number of lithium atoms from 50 to 100 we observe more lithium atoms moving in the vacancies and a few moving out of the system. Since our system shows that it can hold more lithium atoms for the storage and release some for transportation through vacancies or tunnels then TiO_2 nanosphere poses as a good candidate for an anode.

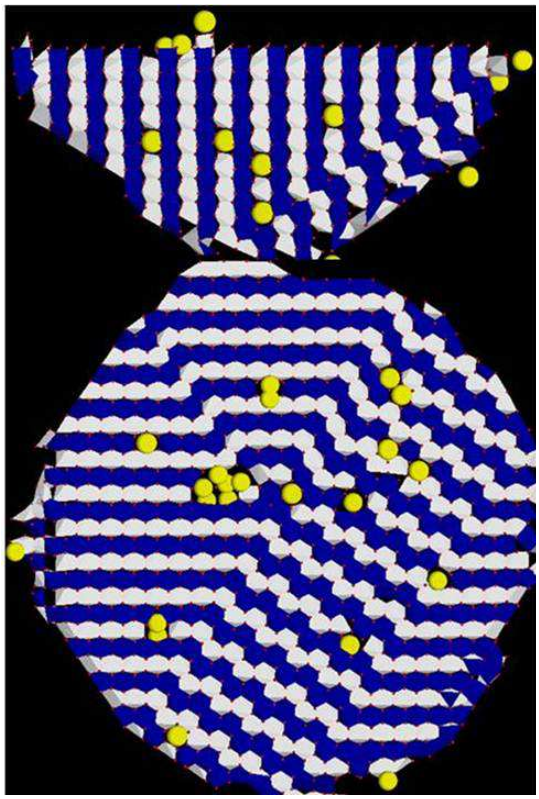

Figure 4.17: Microstructures of a cooled nanosphere with 100 lithium atoms.

XRDs of the simulated nanosphere with 100 lithium atoms, calculated TiO_2: α-PbO_2 and measured (Dambournet et al. 2009) are shown in figure 4.18. On comparing them, peaks correspond to XRDs for brookite and rutile. Two peaks below and above 30 ° correspond to the brookite and TiO_2: α-PbO_2, 37 and 42 ° peaks accord with the brookite, TiO_2: α-PbO_2 and rutile and at 57 ° the peak is associated with the brookite and TiO_2: α-PbO_2. A smooth curve around 50 ° matches the rutile XRDs. At 67 ° we note a peak in agreement with rutile and TiO_2: α-PbO_2. We conclude that the XRDs of the nanosphere with 100 lithium atoms contain brookite, TiO_2: α-PbO_2 and rutile structural arrangements. XRDs correspond to rutile and brookite model.

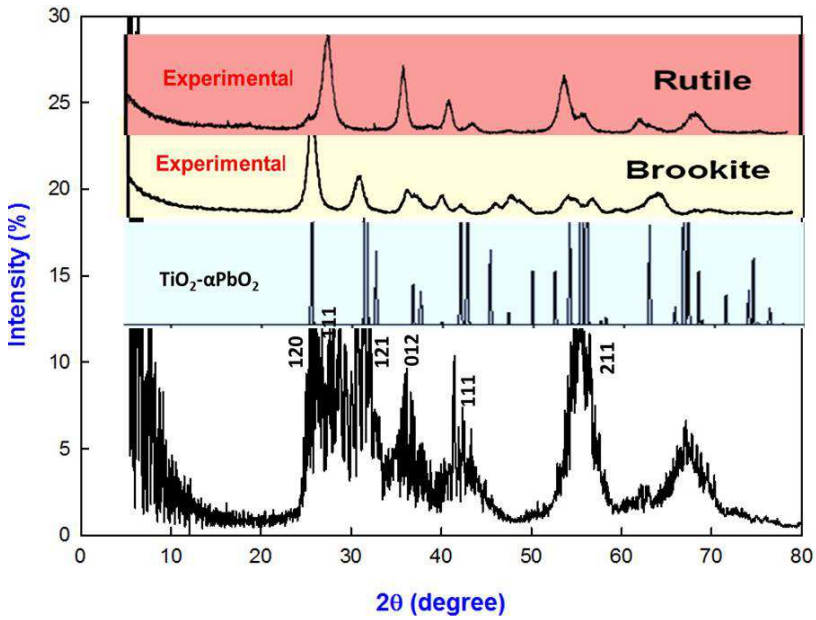

Figure 4.18: A comparison simulated TiO_2 nanosphere with 100 Li, calculated TiO_2: α-PbO_2 and experimental (Dambournet et al. 2009) XRDs.

A cooled nanosphere structure with 300 lithium atoms is presented in figure 4.19. Clear patterns can be observed on the structure. As in previous structures, with lower lithium concentration, it shows that a fraction of lithium atoms reside on the surface of the structure whilst more a retained in the system. Few vacancies are observed in the system.

Total radial distribution functions of the nanosphere with 300 lithium atoms are presented in figure 4.20 (Ti^{3+}-O^{2-}) and figure 4.21 (Ti^{4+}-O^{2-}). They show a similar behaviour and confirm that the system has been successfully cooled in crystalline form, as indicated by the trend of the peaks especially at 2 Å. The highest peak corresponds to 0 K and the lowest is associated with 1500 K.

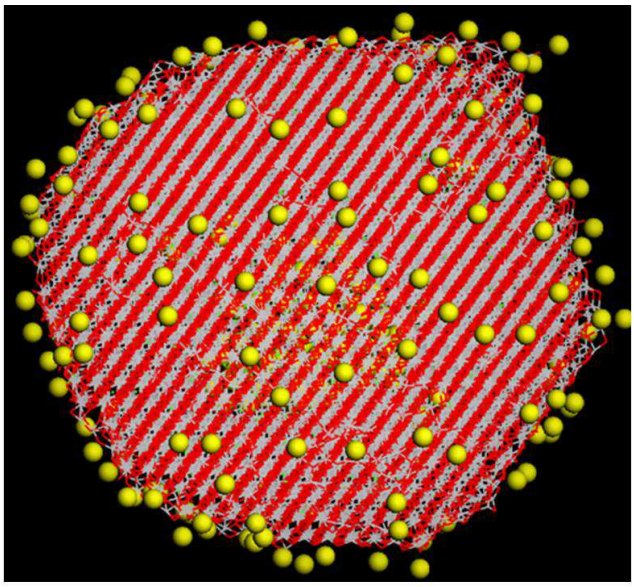

Figure 4.19: Structure of a cooled nanosphere with 300 lithium atoms.

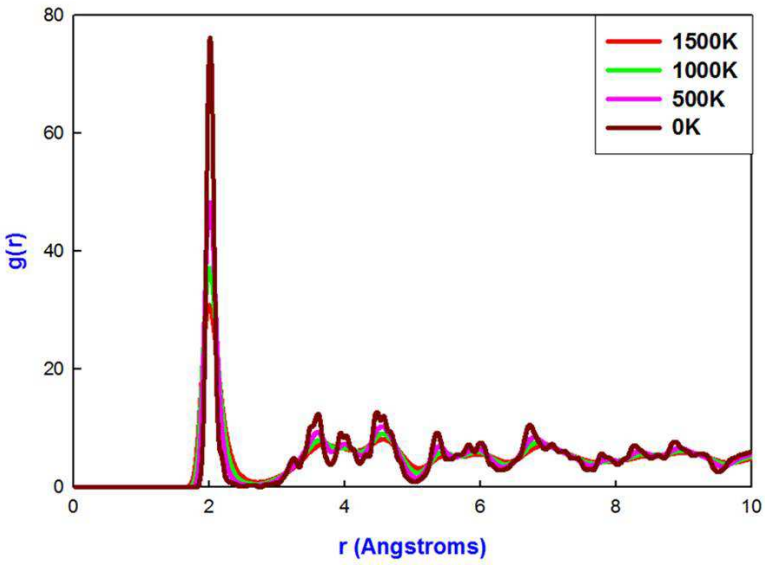

Figure 4.20: RDFs of Ti^{3+}-O^{2-} for the cooled nanosphere with 300 lithium atoms.

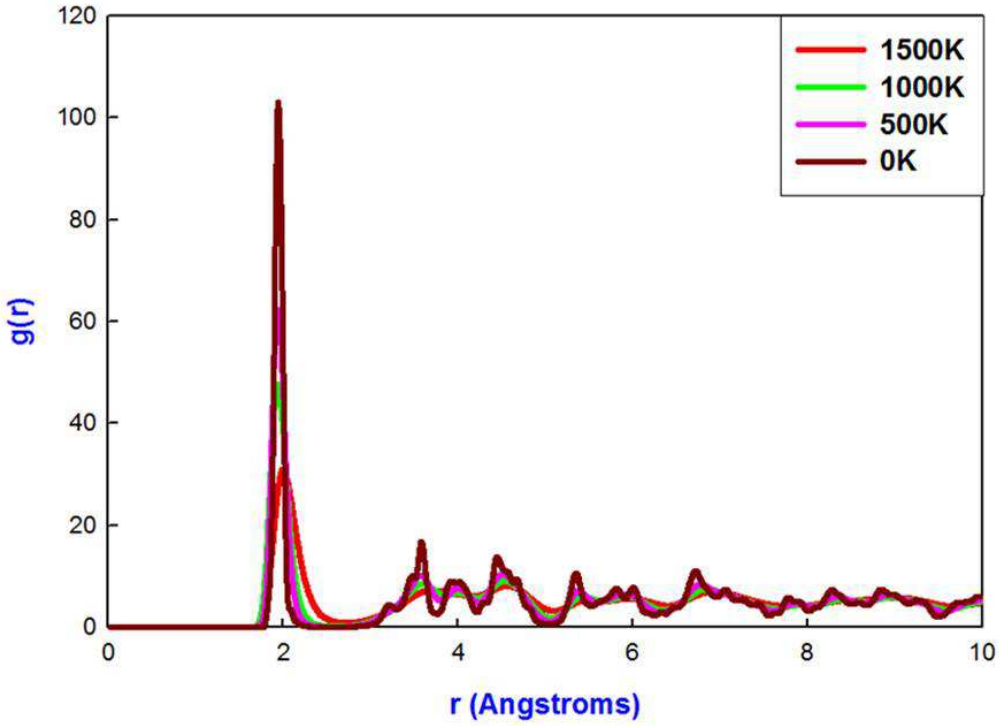

Figure 4.21: RDFs of Ti^{4+}-O^{2-} for the cooled nanosphere with 300 lithium atoms.

The microstructures of the nanosphere with 300 lithium atoms, in different directions, are depicted in figure 4.22. As in previous lithiated nanospheres we observe the following features in the microstructure: straight tunnels which are associated with the twinned rutile phase, zigzag tunnels which are related to the brookite polymorph and big defect cluster and few vacancies. A few lithium atoms are located at the edges of the system and those in the nanosphere are positioned in tunnels and have filled existing vacancies. XRDs for the simulated TiO_2 nanosphere with 300 lithium atoms, calculated TiO_2: α-PbO_2 and experimental (Dambournet et al. 2009) structures are shown in figure 4.23. At 27, 37 and 33 ° we observe two peaks corresponding to brookite and TiO_2: α-PbO_2 and at 42 ° there is a peak harmonized with the brookite, TiO_2: α-PbO_2 and rutile polymorphs. At 50 ° there is a smooth curve which accords with rutile and at 37 and 57 ° are peaks that agree with all polymorphs and at 67 ° the peak agrees with the TiO_2: α-PbO_2 and rutile structure.

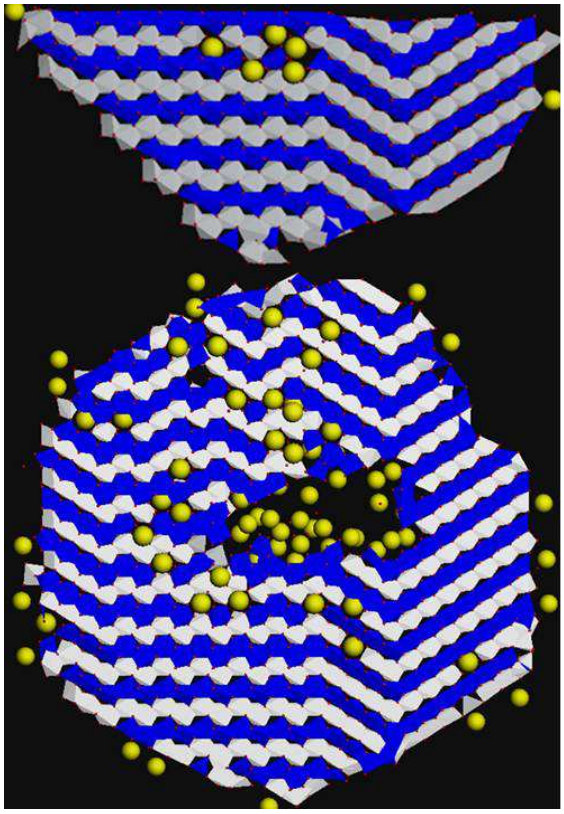

Figure 4.22: Microstructures of a cooled TiO_2 nanosphere with 300 lithium atoms.

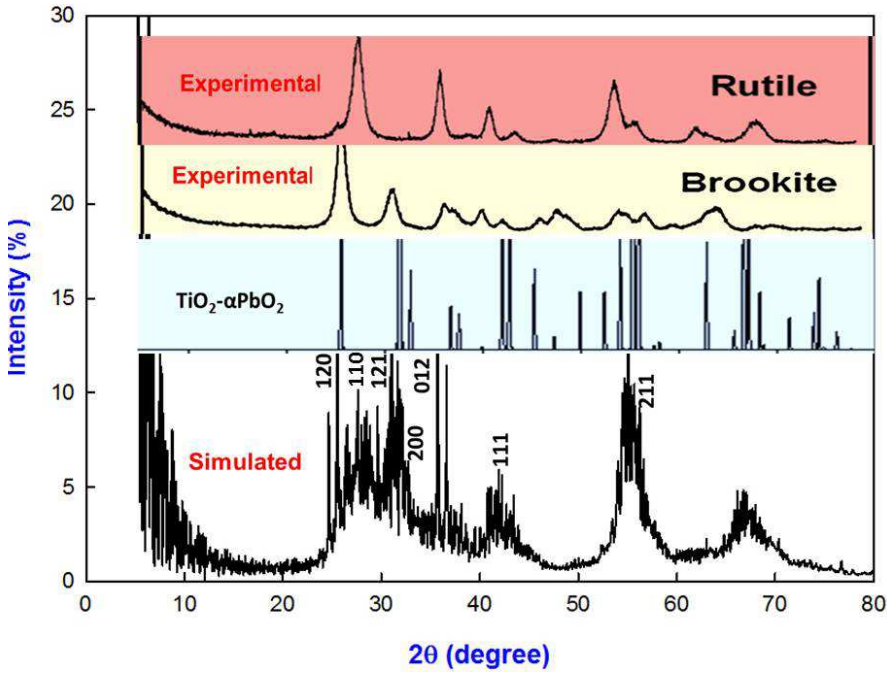

Figure 4.23: A comparison simulated TiO_2 nanosphere with 300 Li, calculated TiO_2: α-PbO_2 and experimental (Dambournet et al. 2009) XRDs.

4.3.2 Lithiated structures of TiO_2 nanosheet

The supercell structure of TiO_2 nanosheet was lithiated with different concentrations of lithium atoms namely 50, 100 and 300. Calculated RDFs before recrystallisation are depicted in figure 4.24 and they show slightly distinct peaks indicating partial crystallisation. Figure 4.25 gives lithiated structures of TiO_2 nanosheet.

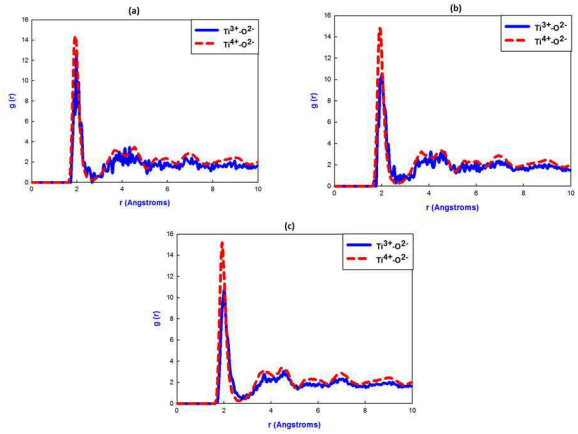

Figure 4.24: RDFs of the nanosheet of TiO_2 with (a) 50, (b) 100 and (c) 300 lithium atoms before recrystallisation.

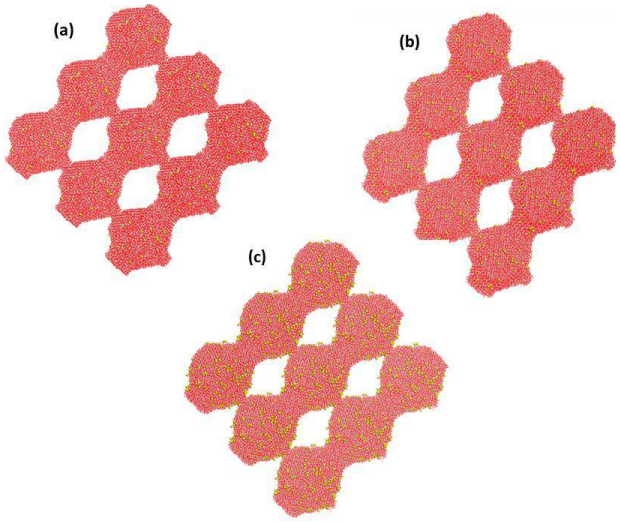

Figure 4.25: Supercell of TiO_2 nanosheets with (a) 50, (b) 100 and (c) 300 Li atoms, in a unit cell at 2000 K.

The graph of configuration energy as a function of time for all lithiated nanosheet structures is depicted in figure 4.26. It was noted that before the lithiated nanosheet was formally recrystallised it already showed certain crystalline patterns; hence the energy is not expected to change significantly. However, the plot of the nanosheet with 300 lithium atoms shows a small decrease at the beginning, suggesting that the system could be having more amorphous phase compared to those with lower lithium concentration. We can conclude that more lithium atoms in the nanosheet tend to enhance the content of the amorphous phase. A near constant energy is observed for all lithiated nanosheets as the simulation time increases, which suggests that systems do not undergo a significant change from partial to full crystallisation.

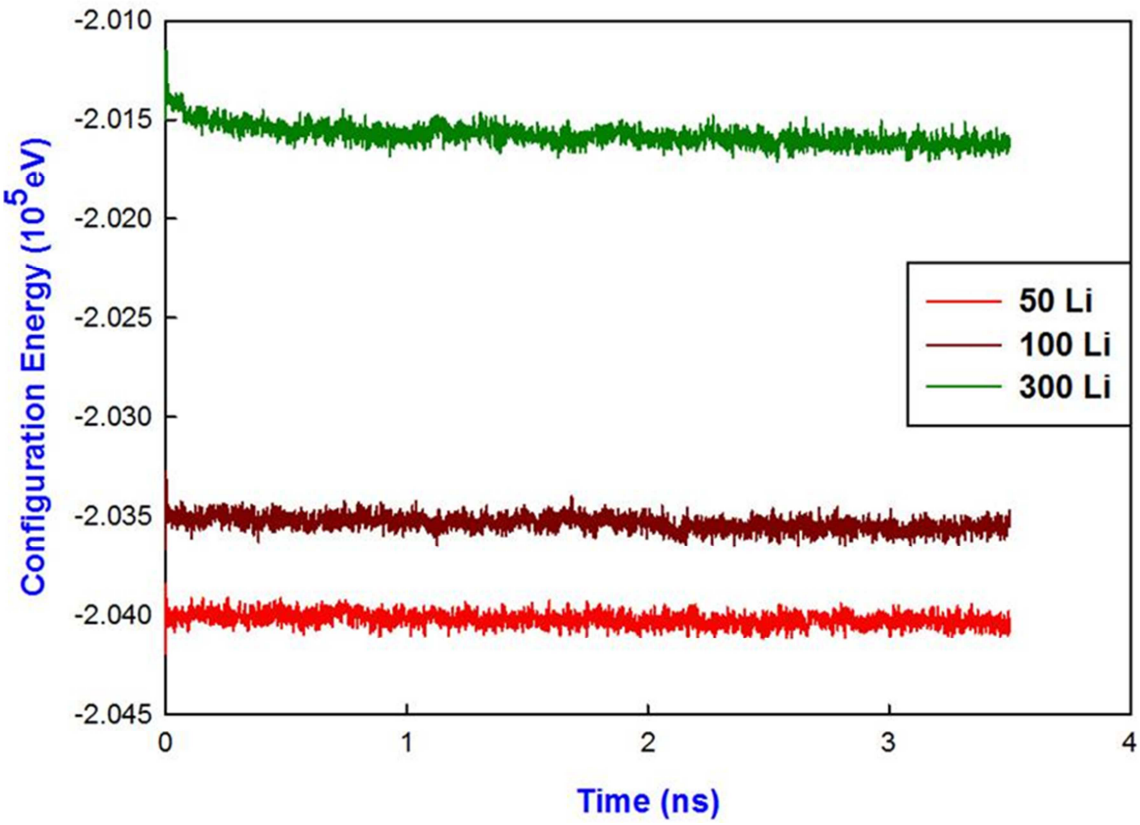

Figure 4.26: Calculated configuration energy as a function of time for the TiO_2 nanosheets with different concentrations of lithium.

Molecular dynamics simulation was performed on the lithiated structures using NVT ensemble in order to effect crystallisation. All lithiated structures show some patterns before we can recrystallise them. However, after recrystallisation the patterns are clearly visible on all structures, which indicate that the structures are fully recrystallised. Supercell recrystallised structures of lithiated nanosheet are illustrated in figure 4.27. After recrystallisation some lithium atoms have moved out of the system and others remained in the system as in the lithiated nanosphere.

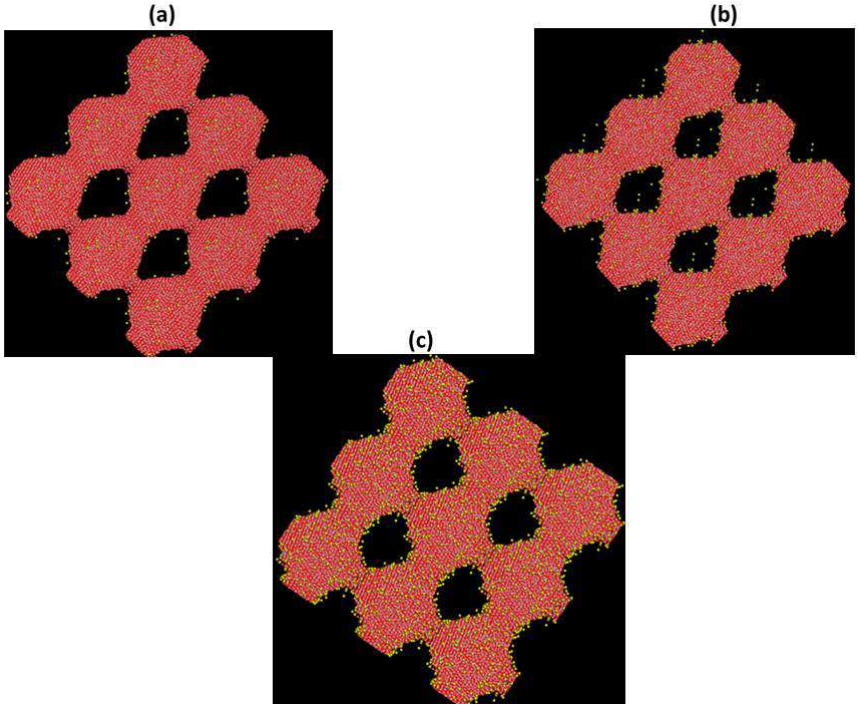

Figure 4.27: Supercell recrystallised structures of TiO_2 nanosheet with (a) 50, (b) 100 and (c) 300 lithium atoms in a unit cell at 2000 K.

Total radial distribution functions of the nanosheet after recrystallisation with varying concentrations of lithium atoms are illustrated in figures 4.28 to 4.30. They show a similar pattern as the RDFs before recrystallisation, but a slight difference can be observed as the RDFs after recrystallisation have sharper peaks. The maximum sharp peak is observed at a separation of 2 Å for both interactions with Ti^{4+}-O^{2-} interaction

being high and Ti^{3+}-O^{2-} low. At 4, 6 and 7 Å we also observe sharp peaks which confirm that complete recrystallisation has been attained. The peak at 9 Å is slightly broader and is similar to the peaks of RDFs of unlithiated nanosheets.

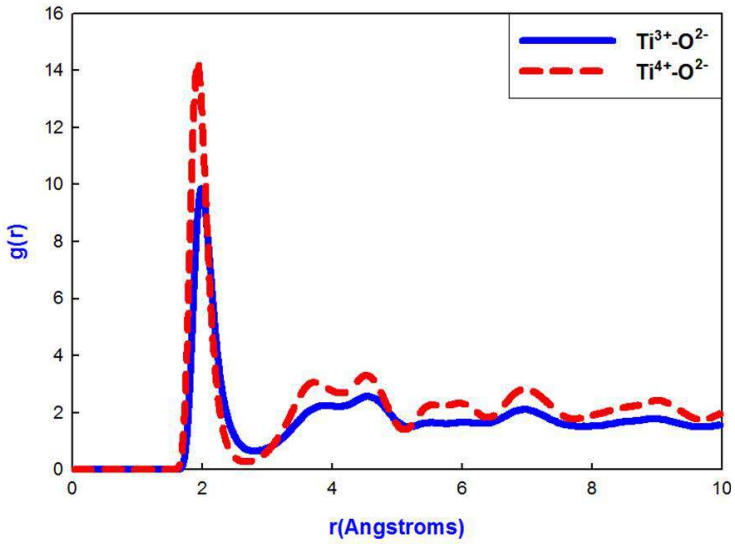

Figure 4.28: Total RDFs of a TiO_2 nanosheet with 50 lithium atoms after recrystallisation at 2000 K.

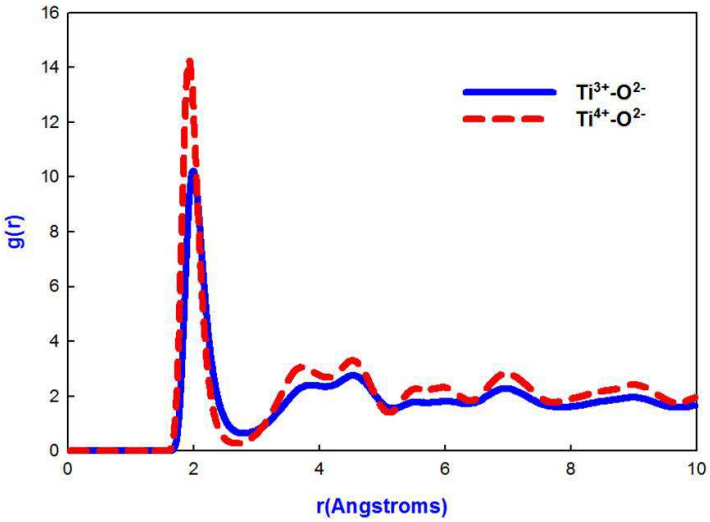

Figure 4.29: Total RDFs of a TiO_2 nanosheet with 100 lithium atoms after recrystallisation at 2000 K.

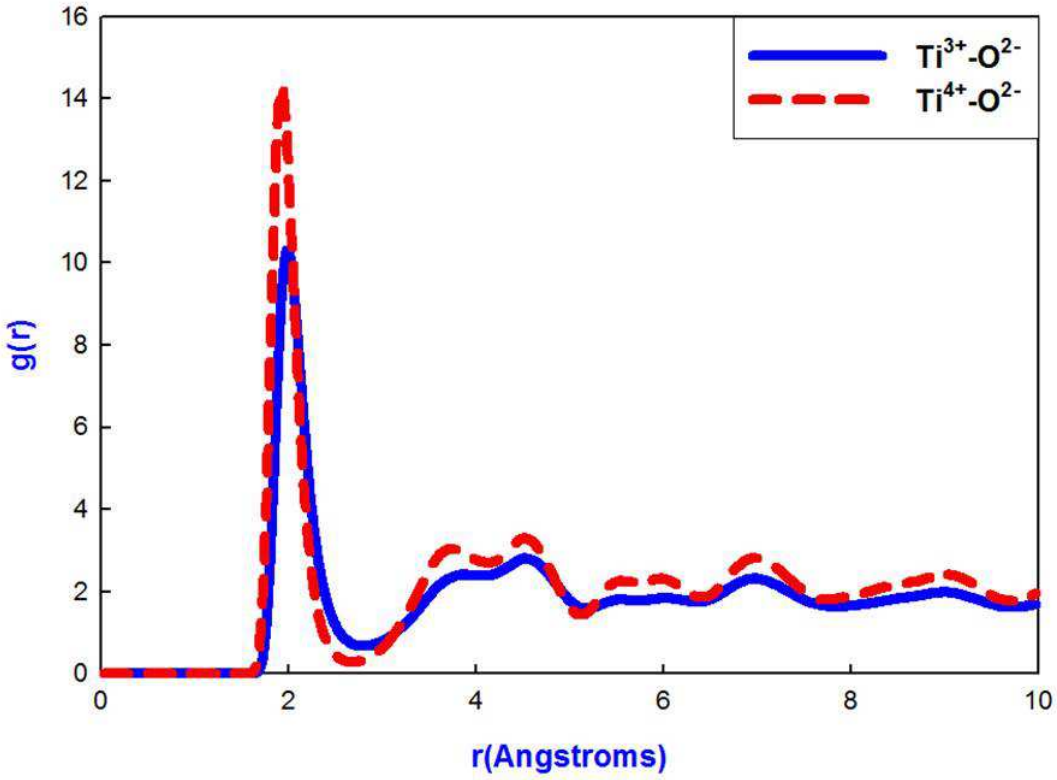

Figure 4.30: Total RDFs of the TiO_2 nanosheet with 300 lithium atoms after recrystallisation at 2000 K.

The recrystallised nanosheet with 50 lithium atoms was cooled and is shown in figure 4.31. More clear patterns are observed on the system and most lithium atoms are within the nanosheet as compared to recrystallised nanosheet at 2000 K in figure 4.27. Total radial distribution functions of the nanosheet of 50 lithium atoms for both interaction of Ti^{3+}-O^{2-} and Ti^{4+}-O^{2-} are delineated in figure 4.32 and 4.33 respectively. They both show a similar behaviour of the peaks, at a separation of 2 Å where peak heights increase temperature from 1500 to 0 K. They confirm that the system has been successfully cooled and retained crystallinity.

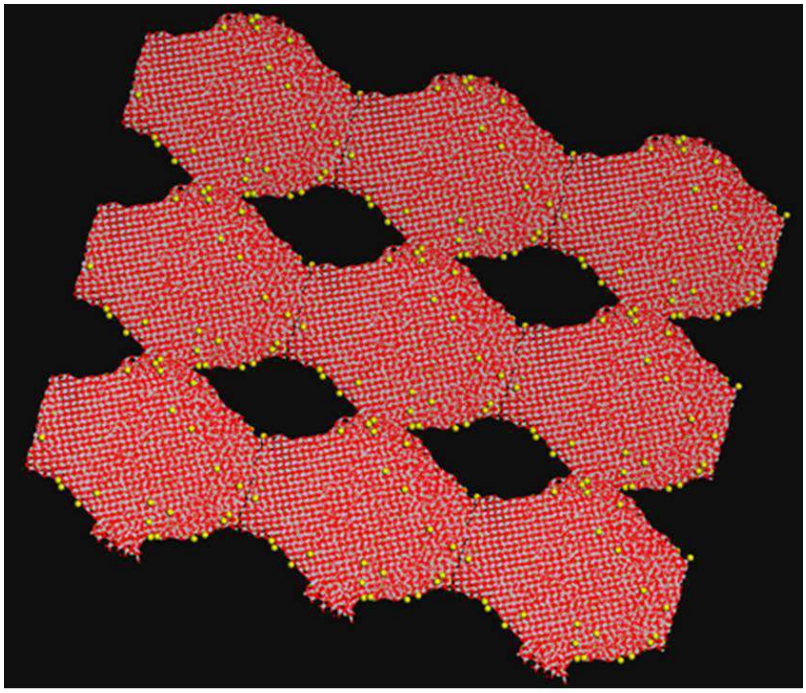

Figure 4.31: A cooled supercell structure of the TiO_2 nanosheet with 50 lithium atoms in a unit cell.

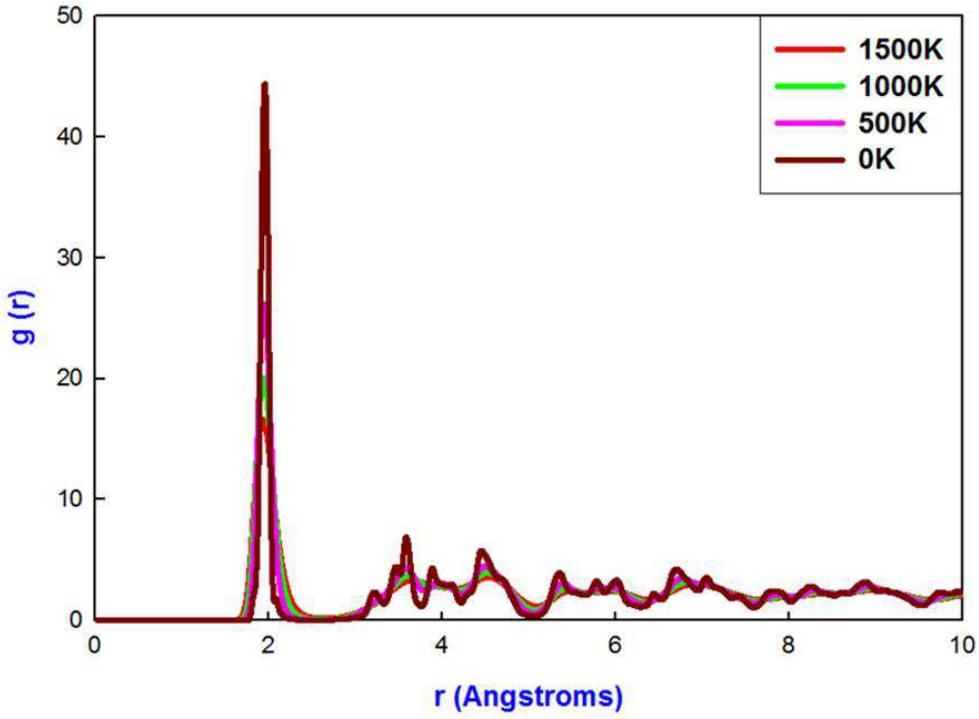

Figure 4.32: Total RDFs for Ti^{3+}-O^{2-} in the TiO_2 nanosheet with 50 lithium atoms at different temperatures.

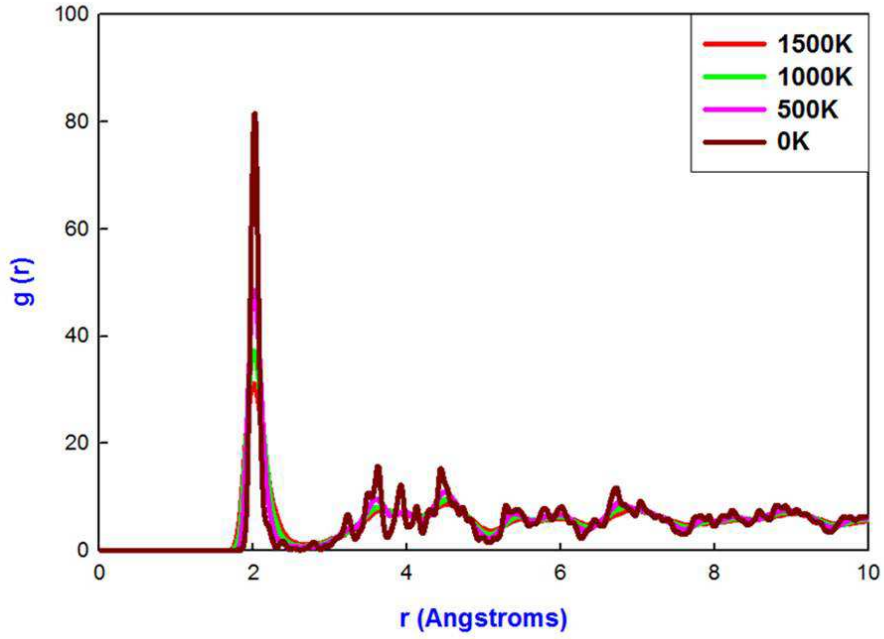

Figure 4.33: Total RDFs for Ti^{4+}-O^{2-} in the nanosheet with 50 lithium atoms at different temperatures.

A cooled TiO_2 nanosheet in figure 4.31 was sliced in order to view its microstructure, and this is given in figure 4.34. The blue colour is the upper layer of Ti^{4+}, the white colour is the corresponding lower layer and the yellow colour depicts lithium atoms. The microstructure of the nanosheet with 50 lithium atoms shows the stacking fault, straight tunnels which are associated with the twinned rutile, few zigzag tunnels which are related to the brookite structure and few vacancies. We observe one lithium atom which has moved into a vacancy. XRD patterns of calculated TiO_2: α-PbO_2 and experiments (Dambournet et al. 2009) are given in figure 4.35. Comparison of the XRDs of the simulated 50 lithium atoms nanosheet with experimental results, brookite, TiO_2: α-PbO_2 and rutile structural arrangements are suggested. At 27, 37 and 33 ° we observe two peaks corresponding to brookite, at 50 ° a smooth curve which accords with rutile and at 37 and 57 ° peaks which are similar to all polymorphs. At 67 ° there is a peak which can be ascribed to rutile and TiO_2: α-PbO_2.

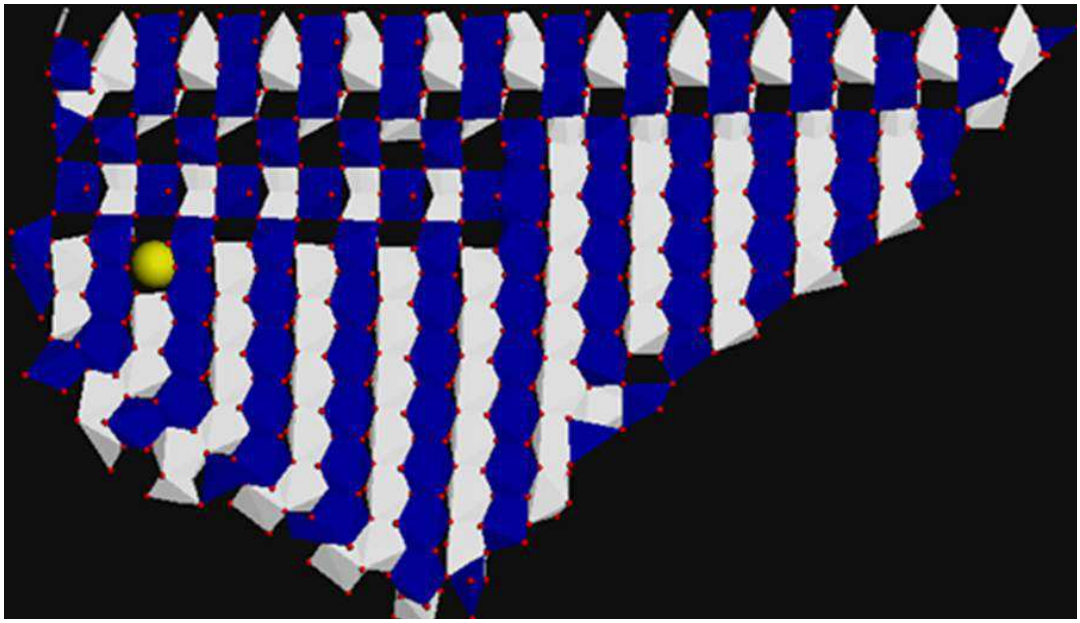

Figure 4.34: A microstructure of a cooled TiO_2 nanosheet with 50 lithium atoms.

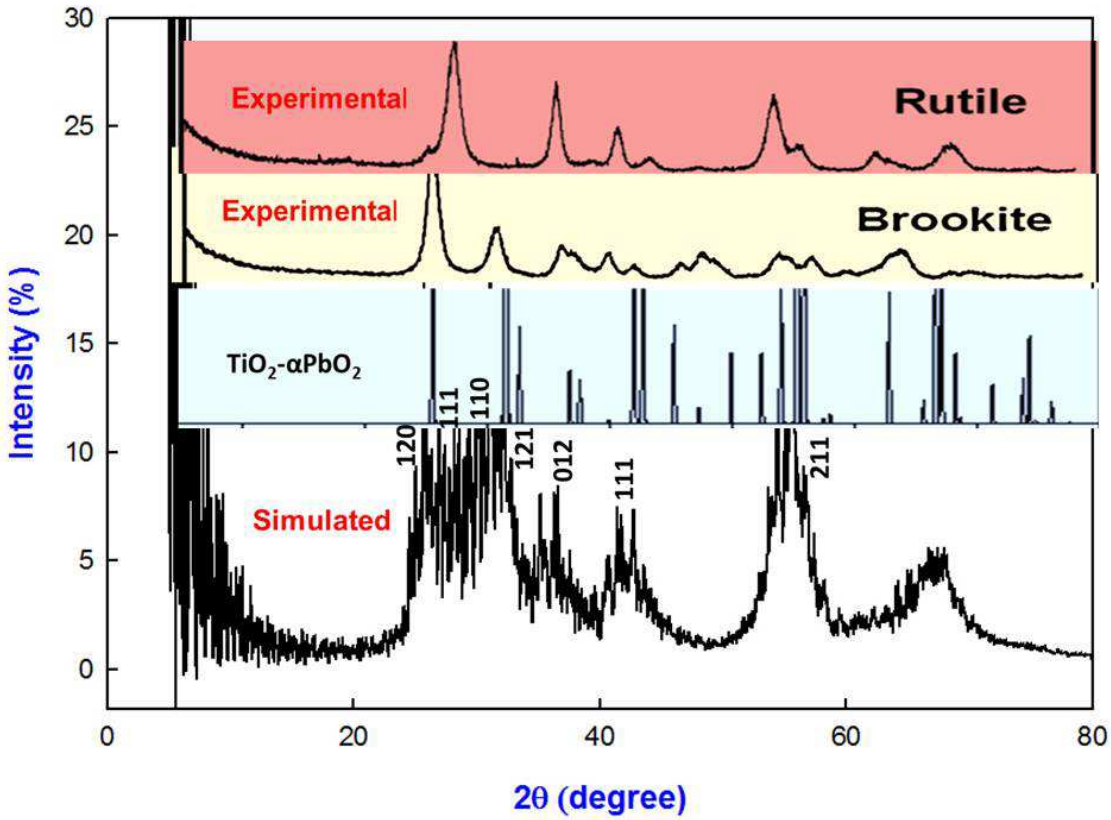

Figure 4.35: A comparison simulated TiO_2 nanosheet with 50 Li, calculated TiO_2: α-PbO_2 and experimental (Dambournet et al. 2009) XRDs.

MD simulation was also carried out to cool the recrystallised nanosheet with 100 lithium atoms which is shown in figure 4.36. Crystalline patterns are clearly observed on the structure and lithium atoms that had moved out of the structure at 2000 K have been re-incorporated in the nanosheet though few are still out.

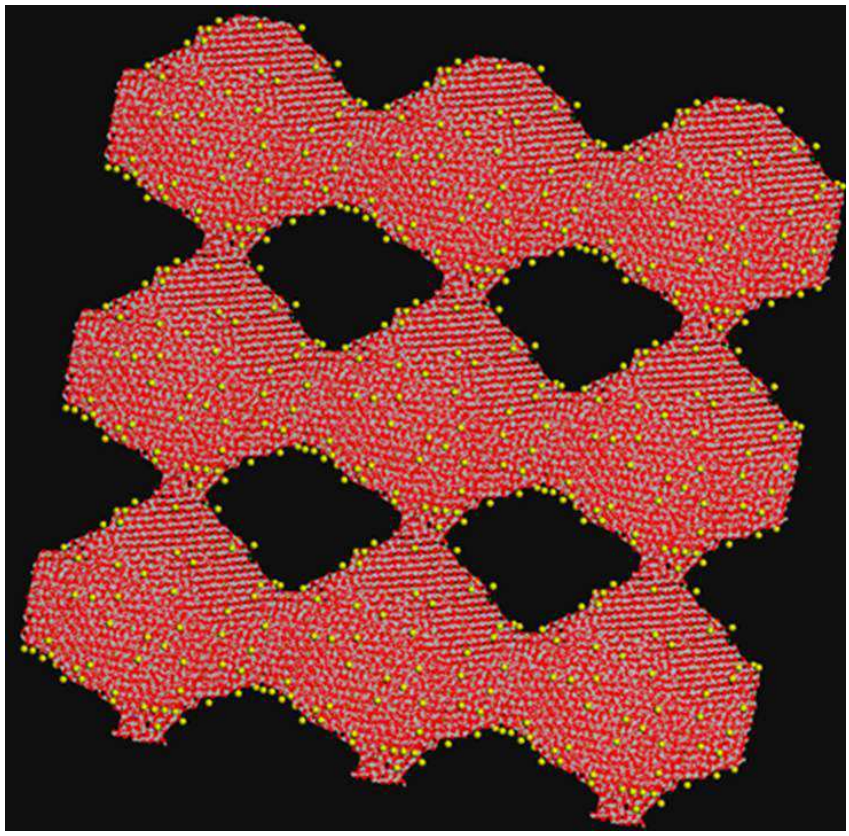

Figure 4.36: A cooled supercell structure of the TiO_2 nanosheet with 100 lithium atoms in a unit cell.

The calculated total RDFs of the system during cooling are given in figure 4.37 for (Ti^{3+}-O) and 4.38 (Ti^{4+}-O^{2-}) interactions. As in previous RDFs of the nanosheet with 50 lithium atoms, they show a similar trend at a separation of 2 Å for both graphs. The RDF plots corresponding to 0 K, have the sharpest and highest peaks than those at higher temperatures.

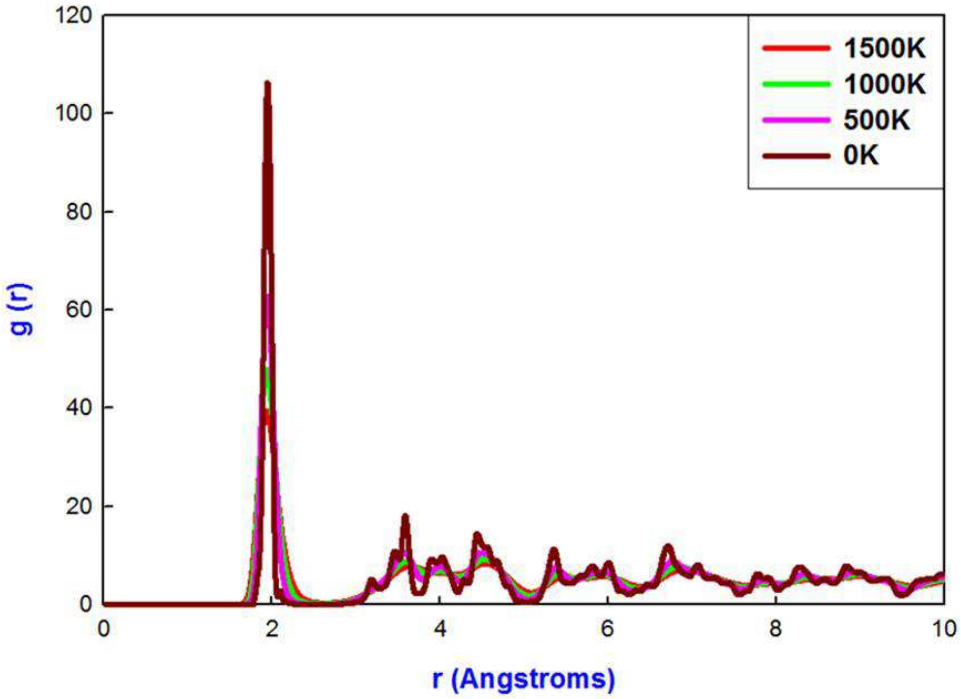

Figure 4.37: Total RDFs for Ti^{3+}-O^{2-} in the TiO_2 nanosheet with 100 Li at different temperatures.

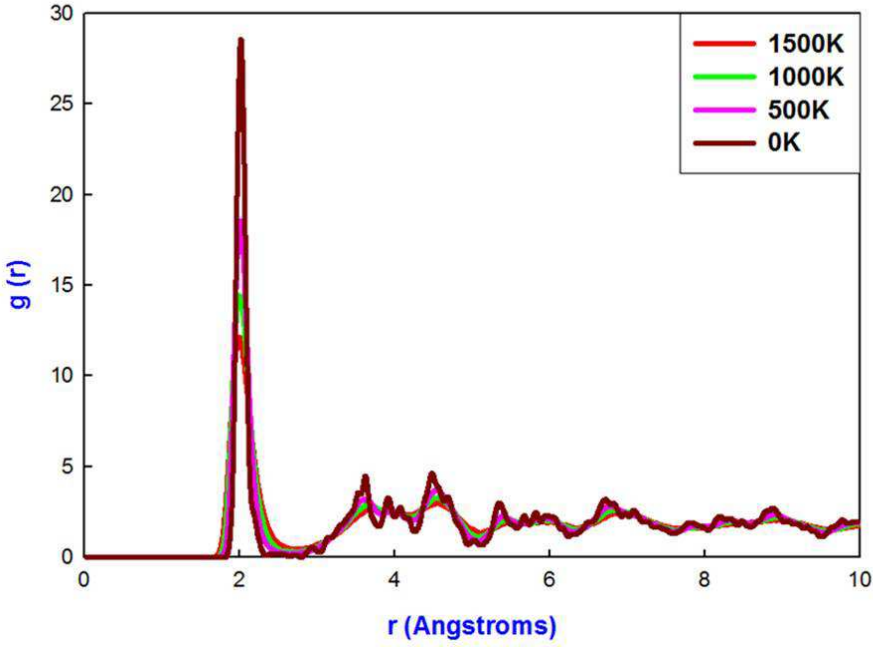

Figure 4.38: Total RDFs for Ti^{4+}-O^{2-} in the TiO_2 nanosheet with 100 lithium atoms at different temperatures.

Created microstructures of the nanosheet with 100 lithium atoms are shown in figure 4.39. The microstructures correspond to different orientations in order to view the arrangement of atoms in different directions. As previously indicated the blue colour is the upper layer of Ti^{4+}, the white colour is the lower layer of Ti^{4+} and the yellow colour depicts lithium atoms. Microstructures reveal the zigzag tunnels which are associated with the brookite structure, straight tunnels which are ascribed to the twinned rutile and few vacancies. Lithium atoms in the structure have filled vacancies of the system and some lithium atoms are located on the edge of the system. On comparing this microstructures with that of 50 lithium atoms more lithium atoms are inserted in the current system and the vacancies are not as many as in the nanosphere.

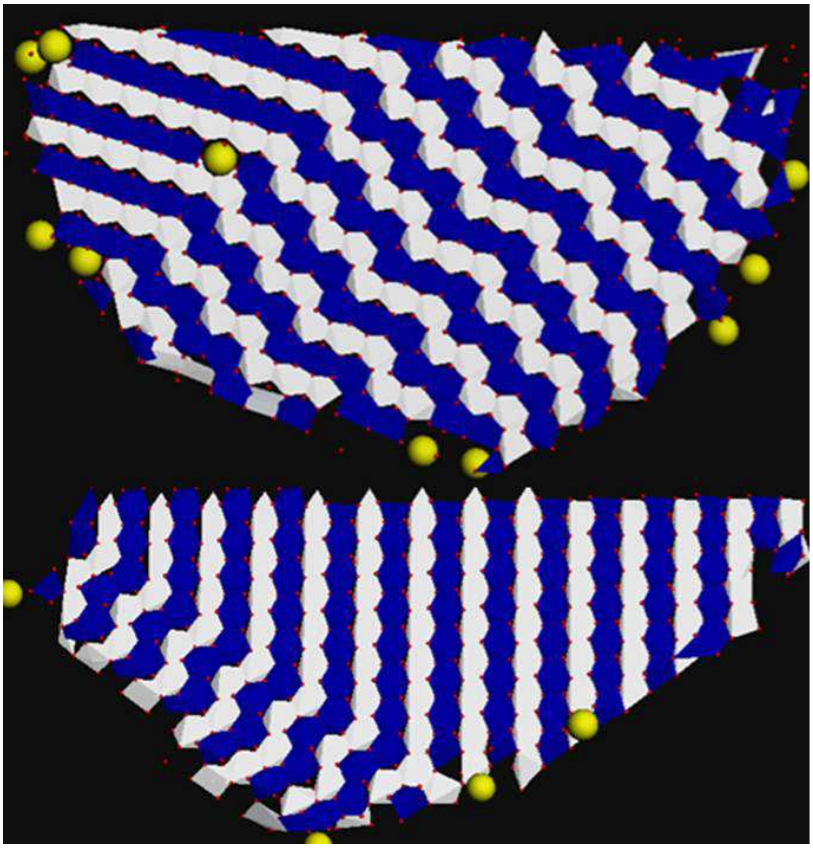

Figure 4.39: Microstructures of the TiO_2 nanosheet with 100 lithium atoms corresponding to two orientations.

Calculated TiO_2:α-PbO_2 and experimental (Dambournet et al. 2009) XRDs are depicted in figure 4.40. At 27, 33 and 37 ° there are peaks that resemble the peaks of brookite structural arrangements which is isostructural with TiO_2: α-PbO_2. At 42 ° we observe a peak corresponding to rutile and TiO_2: α-PbO_2 and at 50 ° there is a smooth curve which accords with rutile. Peaks at 37 and 57 ° match that of rutile, brookite and TiO_2: α-PbO_2. At 67 ° the peak is associated with rutile and TiO_2: α-PbO_2. A combination of rutile, TiO_2: α-PbO_2 and brookite polymorphs is suggested in the simulated nanosheet with 100 lithium atoms.

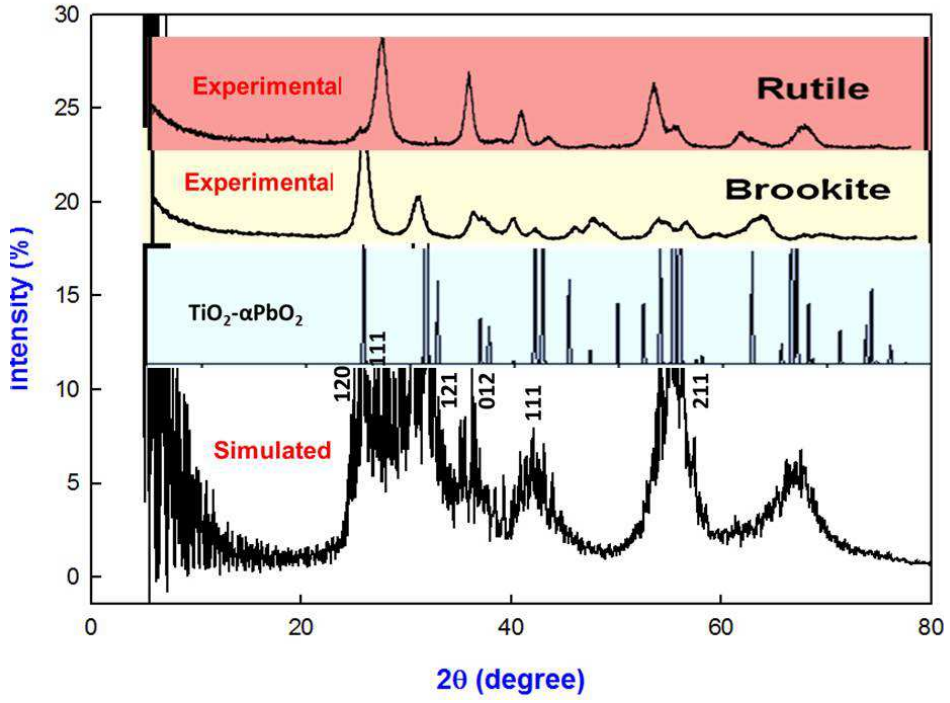

Figure 4.40: A comparison simulated TiO_2 nanosheet with 100 Li, calculated TiO_2: α-PbO_2 and experimental (Dambournet et al. 2009) XRDs.

We cooled the last lithiated nanosheet with 300 lithium atoms which is illustrated in figure 4.41. Lithium atoms that had moved away from the system after recrystallisation, at 2000 K, are now within the nanosheet after cooling, and more patterns are clearly visible on the system. Calculated RDFs of the system during cooling are presented in

figure 4.42 (Ti^{3+}-O^{2-}) and 4.43 (Ti^{4+}-O^{2-}). As in the previous RDFs of nanosheet with 50 and 100 lithium atoms, they show a similar pattern at 2 Å for both figures. The highest peak for all graphs correspond to 0 K and the lowest being that of temperature of 1500 K.

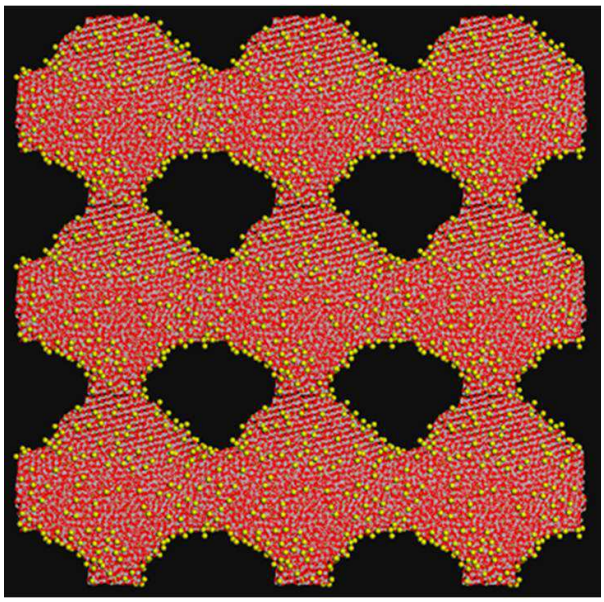

Figure 4.41: A cooled supercell structure of the TiO_2 nanosheet with 300 lithium atoms in a unit cell.

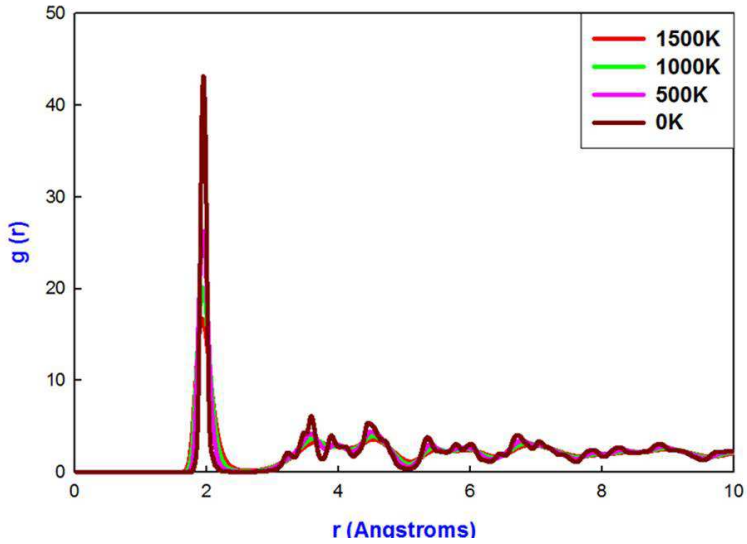

Figure 4.42: Total RDFs for Ti^{3+}-O^{2-} in the TiO_2 nanosheet with 300 lithium atoms at different temperatures.

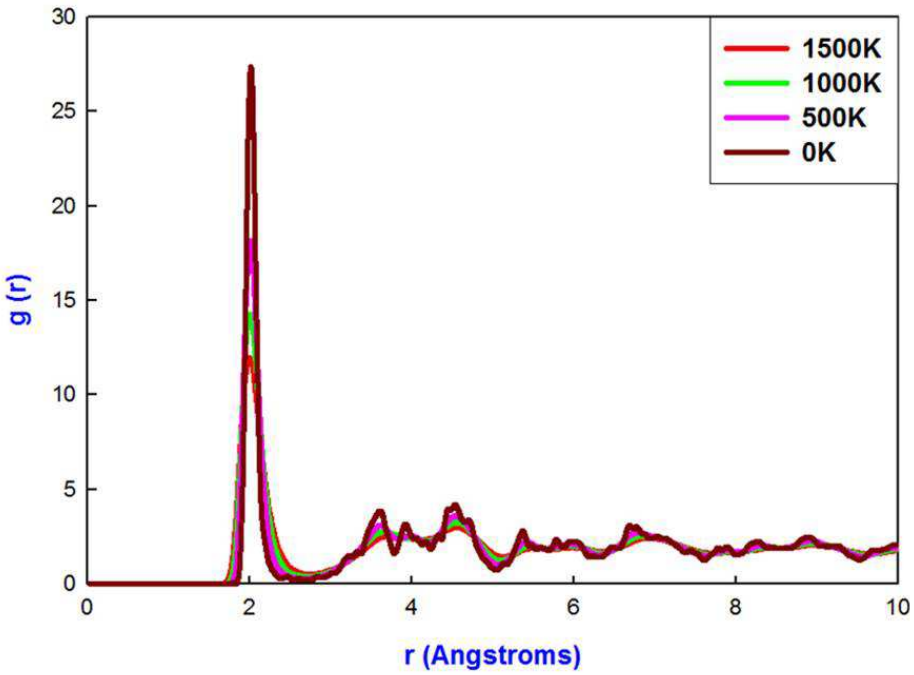

Figure 4.43: Total RDFs for Ti^{4+}-O^{2-} in the TiO_2 nanosheet with 300 lithium atoms at different temperatures.

As in the previous lithiated nanosheet we have also cut the nanosheet with 300 lithium atoms in order to view the microstructure. The microstructure is presented in figure 4.44, the blue colour is the upper layer of Ti^{4+}, the white colour is the lower layer of Ti^{4+} and the yellow colour is related to the lithium atoms. On the microstructure we observe the straight tunnels which are associated with the twinned rutile phase, zigzag tunnels related to the brookite polymorph and vacancies. Vacancies that are in the middle of the microstructure are filled with lithium atoms. We can observe more lithium atoms within the microstructure though some are on the edges of the nanosheet. As in previous systems we have calculated the XRDs for the simulated nanosheet with 300 lithium atoms. The calculated TiO_2: α-PbO_2 and experimental (Dambournet et al. 2009) XRDs are shown in figure 4.45, and are compared with the simulated nanosheet and the brookite, TiO_2: α-PbO_2 and rutile structures. Observed peaks at 27 °, 33 ° correspond to brookite and TiO_2:

α-PbO_2 at 37 ° to brookite and rutile and at 42 ° to mainly with rutile. The smooth curve at 50 ° is associated with the rutile phase and a peak at 57 ° corresponds with all polymorphs. A peak at 67 ° corresponds to TiO_2: α-PbO_2 and rutile polymorphs.

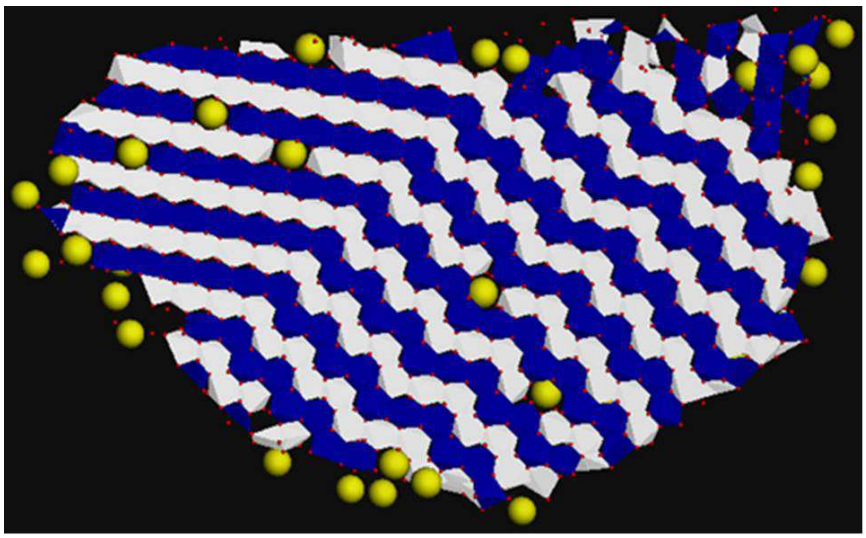

Figure 4.44: Microstructure of the TiO_2 nanosheet with 300 lithium atoms.

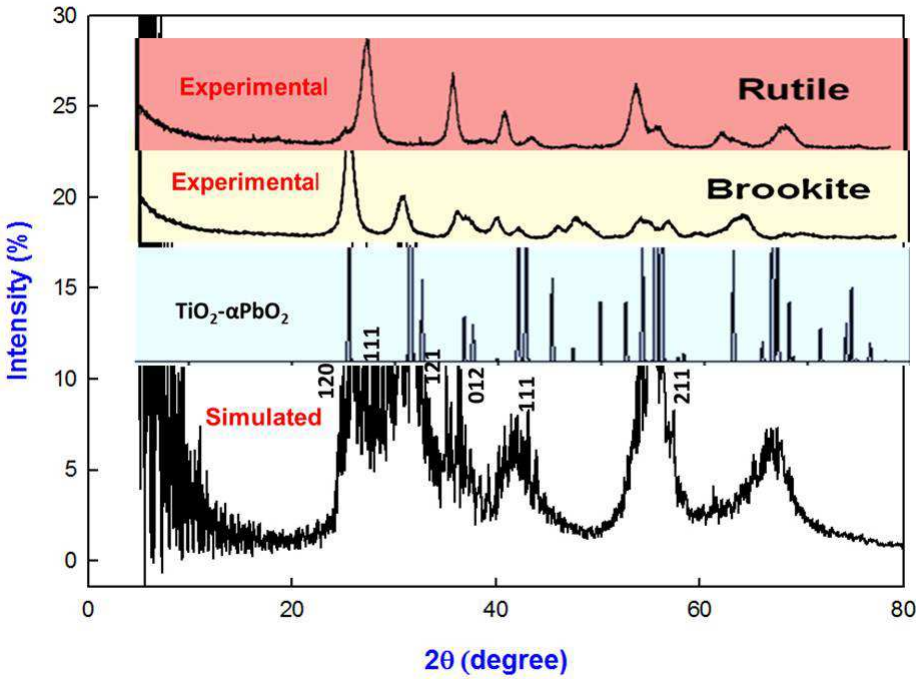

Figure 4.45: A comparison simulated TiO_2 nanosheet with 300 Li, calculated TiO_2: α-PbO_2 and experimental (Dambournet et al. 2009) XRDs.

4.3.3 Lithiated structures of TiO_2 nanoporous

We have lithiated the nanoporous structure of TiO_2 corresponding to the lattice vector of 66 Å with different concentration of lithium atoms i.e. 50, 100 and 300. Their radial distribution functions before crystallisation are shown in figure 4.46 and lithiated structures are illustrated in figure 4.47. RDFs of lithiated nanoporous TiO_2 with 50 lithium atoms shows some peaks indicating partial recrystallisation, and this followed by that of 100 lithium atoms. However, the nanoporous structure RDFs for the structure with 100 lithium atoms show broader peaks while that of 300 lithium atoms has no peaks, hence suggesting that the system is extensively amorphous. As more lithium atoms are added to the TiO_2 nanoporous structure the more amorphised it becomes.

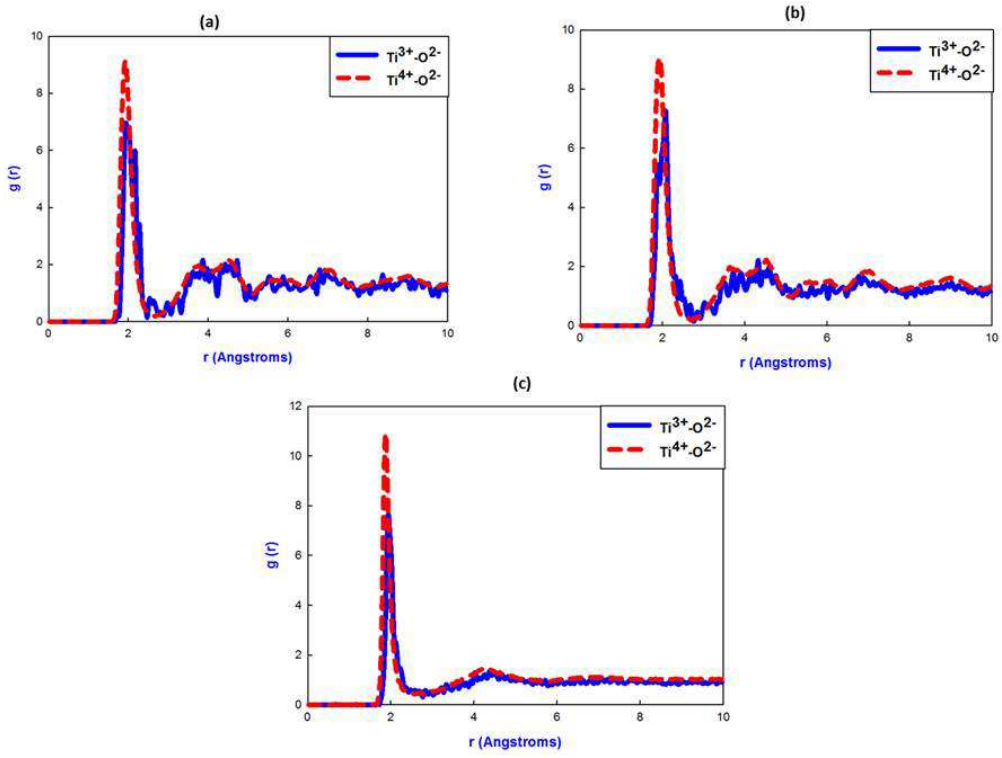

Figure 4.46: RDFs of the nanoporous TiO_2 (66 Å) before recrystallisation with (a) 50, (b) 100 and (c) 300 lithium atoms.

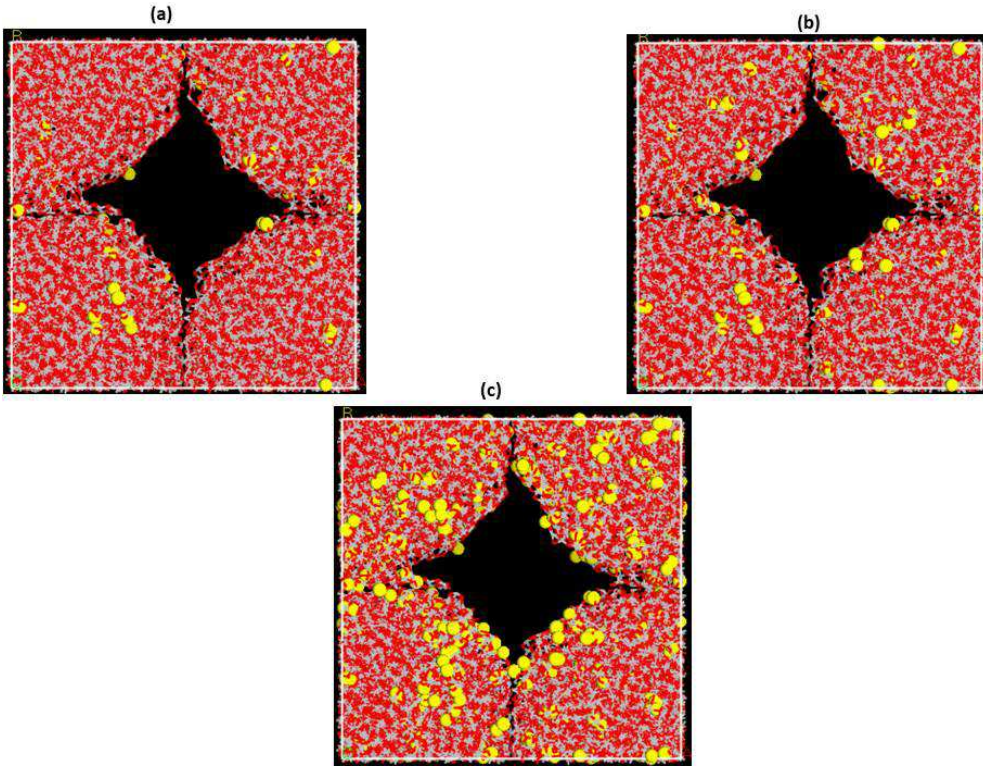

Figure 4.47: Amorphous lithiated TiO_2 nanoporous structures related to the lattice box of 66 Å.

The plots of the configuration energy as a function of time for nanoporous TiO_2, corresponding to the 66 Å lattice vector, and with 50, 100 and 300 lithium atoms, are given in figure 4.48. All energy plots show a distinct transition from an amorphous to a crystalline phase below 0.6 ns and the change in energy correspond to the latent heat of crystallisation. The energies of nanoporous structures with 50, 100 and 300 lithium atoms change from -2.013×10^5 to -2.0345×10^5, -2.008×10^5 to -2.038×10^5 and -1.997×10^5 to -2.017×10^5 eV respectively. An extended amorphous phase is noted as the lithium concentration is increased. It is further observed that beyond 0.6 ns the configuration energy tends to be constant which suggests that crystallisation has been completed. This plateau appears to commence earlier at lower lithium concentrations.

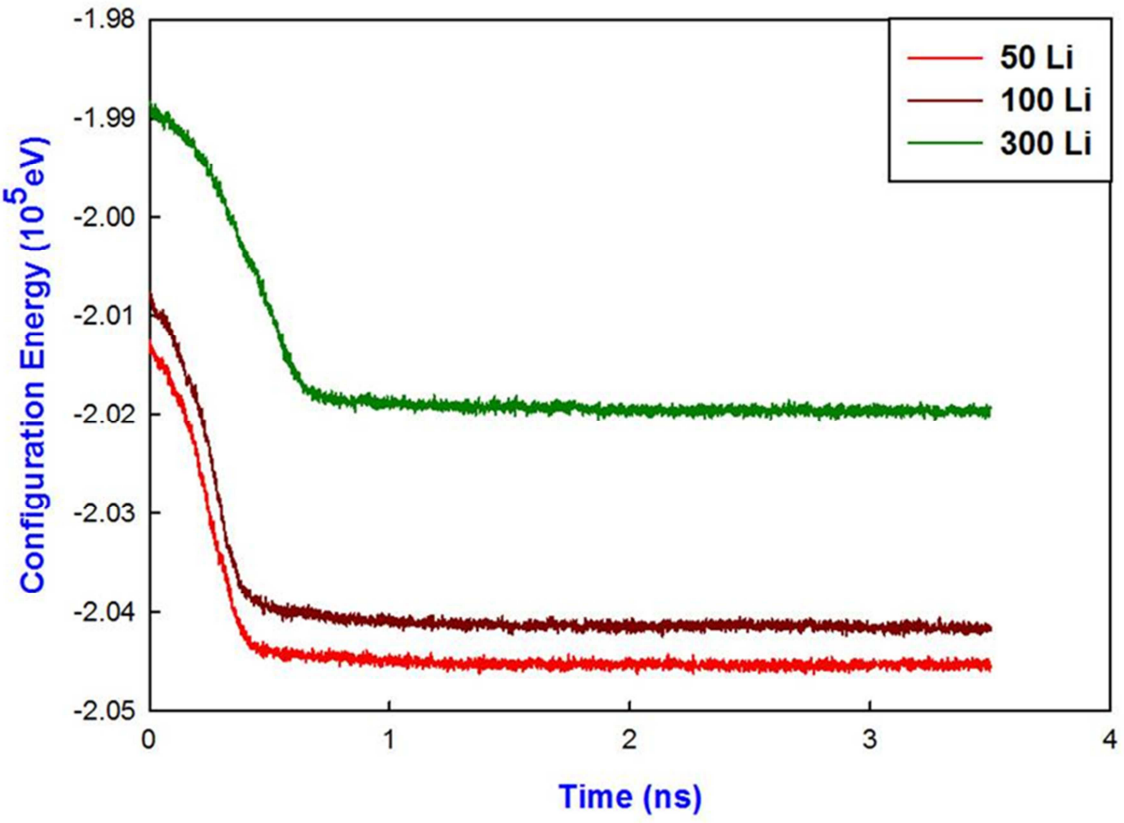

Figure 4.48: Calculated configuration energy as a function of time for the TiO_2 nanoporous 66 Å, at different lithium concentrations.

The nanoporous structures that are crystallised using the NVT ensemble, with different lithium concentrations, are given in figure 4.49. The structure of the nanoporous TiO_2 lithiated with 50 lithium atoms shows more clear patterns and some vacancies. The structure lithiated with 100 lithium atoms reveal some patterns, however, they are not clear as compared to those of 50 lithium atoms. Furthermore, the nanoporous structure with 100 lithium atoms displays some grain boundaries. The lithiated structure with 300 lithium atoms features clear crystalline patterns after recrystallisation and further reflects lithium atoms located on the edges of the channel as shown in figure 4.49(c).

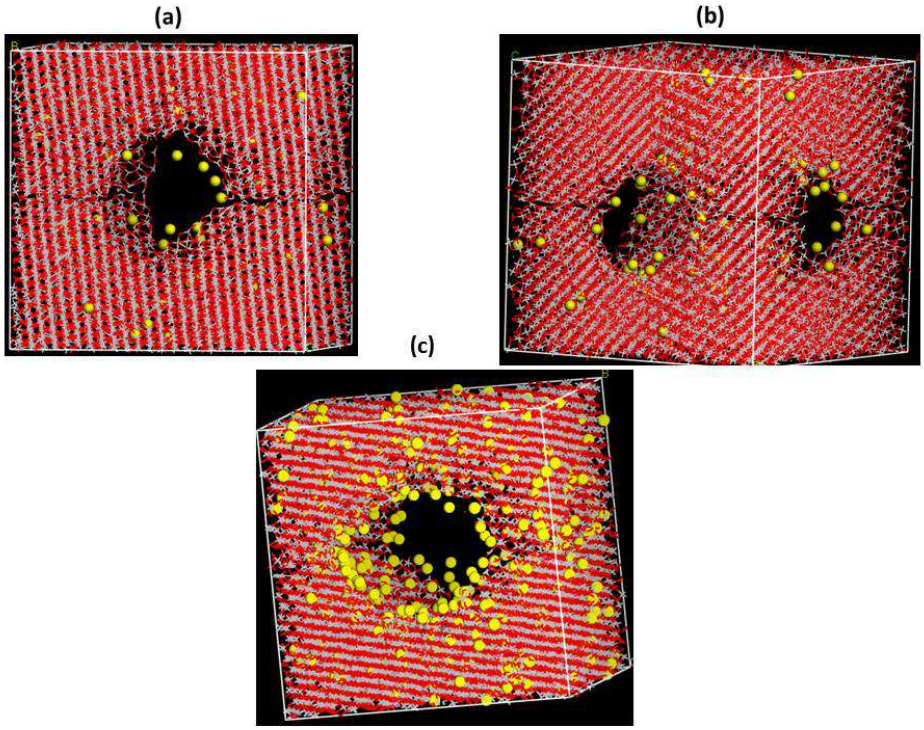

Figure 4.49: Recrystallised TiO_2 lithiated nanoporous structures related to the 66 Å at 2000 K, with different lithium concentration.

We calculated total RDFs for all lithiated nanoporous structures to check whether they consistent with the observed structures in figure 4.49. The total RDFs of Ti^{3+}-O^{2-} and Ti^{4+}-O^{2-} interactions after recrystallisation for all lithiated systems are presented in appendix E. They all show sharp peaks at a separation of 2 Å and after this separation, peaks are observed at 3.6, 4.5, 5.5, 6.0, 6.9 and 9.0 Å for all lithiated nanoporous structure with 66 Å lattice vector. This implies that the lithiated nanoporous structures have successfully recrystallised. The recrystallised nanoporous TiO_2 structure with 50 lithium atoms was cooled and is depicted in figure 4.50. We observe more vacancies next to the channel and lithium atoms are located closer to the inner edge of the channel and nanoporous structure than in the uncooled one; crystalline patterns are more distinct as compared with the ones at higher temperatures. Total radial distribution functions of the nanoporous structure during cooling are shown in appendix E. They show that the

nanoporous structure has cooled sufficiently since there is a clear trend of sharp peaks at 0K as compared to those at higher temperatures.

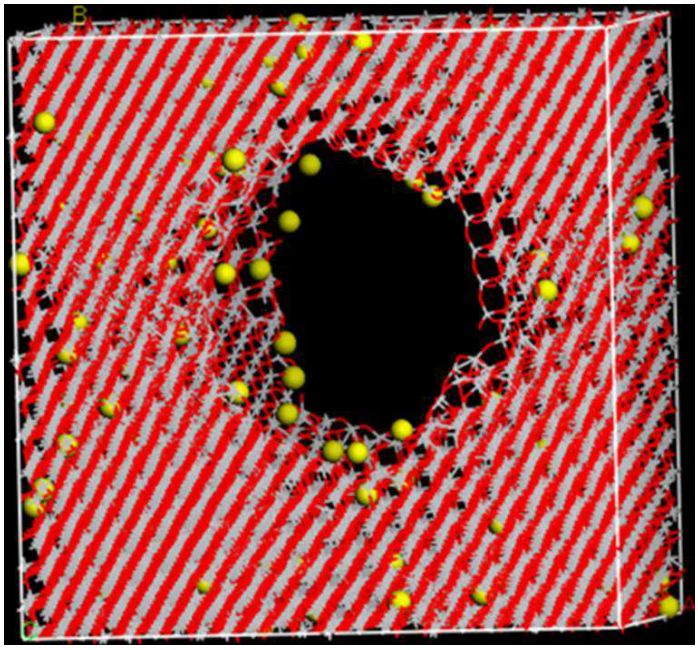

Figure 4.50: A cooled 66 Å TiO_2 nanoporous structure with 50 lithium atoms.

A slice showing the microstructure of the cooled 66 Å nanoporous structure with 50 lithium atoms is illustrated in figure 4.51. The blue octahedra correspond to the upper layer of Ti^{4+}, and the white to the lower adjacent layer and the lithium atoms are yellow in colour. We observe straight tunnels associated with the twinned rutile structure, zigzag tunnels to the brookite polymorph. The microstructure shows some lithium atoms on the channel and others in the tunnels of the nanoporous structure. In addition, few vacancies are noted on the microstructure. The calculated, TiO_2: α-PbO_2 and experimental (Dambournet et al. 2009) XRDs are superimposed in figure 4.52. More peaks of the simulated nanoporous structure are observed between 20 and 50 ° which agree with the XRDs of brookite and TiO_2: α-PbO_2 structures. At 27 and 3 ° peaks are associated with brookite, at 37 and 42 ° peaks accord mainly with brookite and rutile. At 50 ° there is a smooth curve corresponding to the rutile phase and a peak at 57 ° corresponds to all

polymorphs, and at 67 ° a peak matches the rutile and TiO_2: α-PbO_2 structures. Our calculated XRDs are mostly in accord with those of the experimental brookite and rutile.

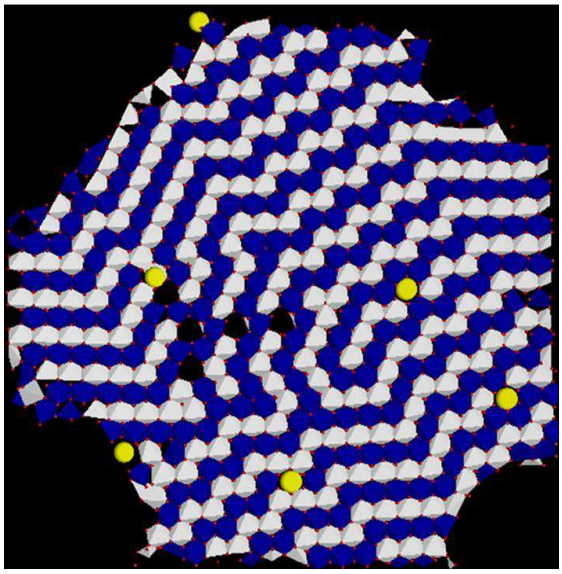

Figure 4.51: A microstructure of cooled 66 Å TiO_2 nanoporous structure with 50 lithium atoms.

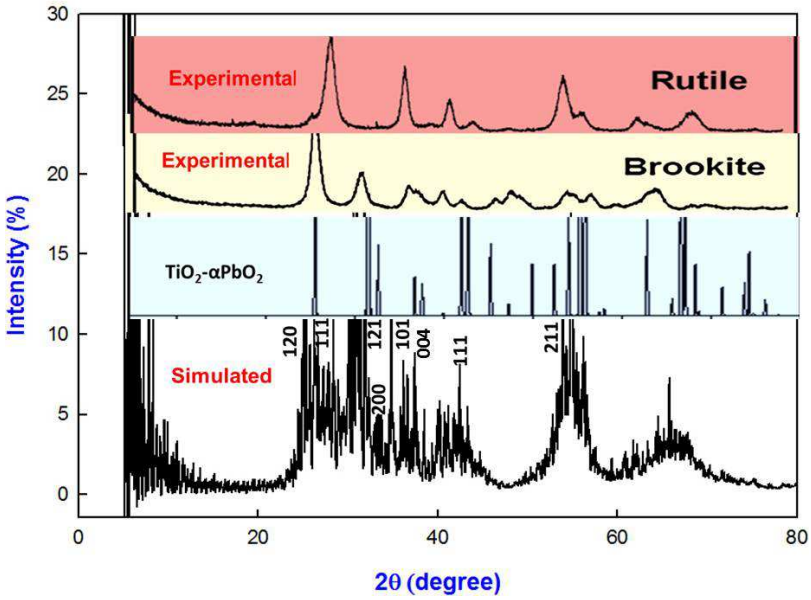

Figure 4.52: A comparison simulated TiO_2 nanoporous 66 Å with 50 Li, calculated TiO_2: α-PbO_2 and experimental (Dambournet et al. 2009) XRDs.

We have cooled the recrystallised 66 Å nanoporous structure with 100 lithium atoms and the structure is shown in figure 4.53. It shows more vacancies around the channel and some on the sides of the nanoporous structure. Crystalline patterns are clearly more visible as compared to those of the recrystallised structure at 2000 K. As the number of lithium atoms is increased, we now observe more atoms on the channel and more within the system. The total radial distribution functions of the nanoporous structure are presented in appendix E. For the peaks at 2 Å we note that the smallest peak corresponds to 1500 K and the highest peak to 0 K.

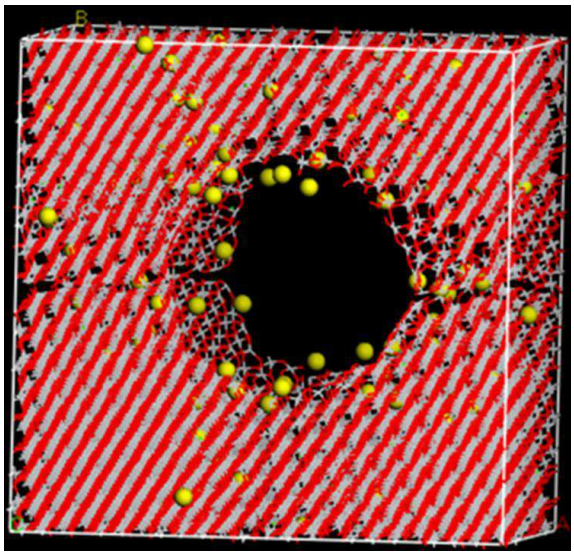

Figure 4.53: A cooled TiO_2 66 Å nanoporous structure with 100 lithium atoms.

The microstructure of the cooled 66 Å nanoporous structure is presented in figure 4.54 and shows straight tunnels which are associated with the twinned rutile, zigzag tunnels which are related with the brookite phase. Lithium atoms that are within the nanoporous structure are located in tunnels while some have moved to the channel. The nanoporous structure is suitable as an anode material since it can accommodate more lithium atoms. Calculated TiO_2: α-PbO_2 and experimental (Dambournet et al. 2009) XRDs are noted in figure 4.55. Peaks of the simulated nanoporous structure between 20 and 40 ° agree well

with the brookite and TiO_2: α-PbO_2 structural arrangements. A peak at 42 ° is aligned with brookite and TiO_2: α-PbO_2 arrangements. A smooth curve at 50 ° accords with the rutile phase and at 37 and 57 ° there are peaks corresponding to all polymorphs. At 67 ° there is a peak corresponding to XRDs of rutile and TiO_2: α-PbO_2. XRDs of simulated nanoporous structure with 100 lithium atoms aligned with brookite, TiO_2: α-PbO_2 and rutile polymorphs.

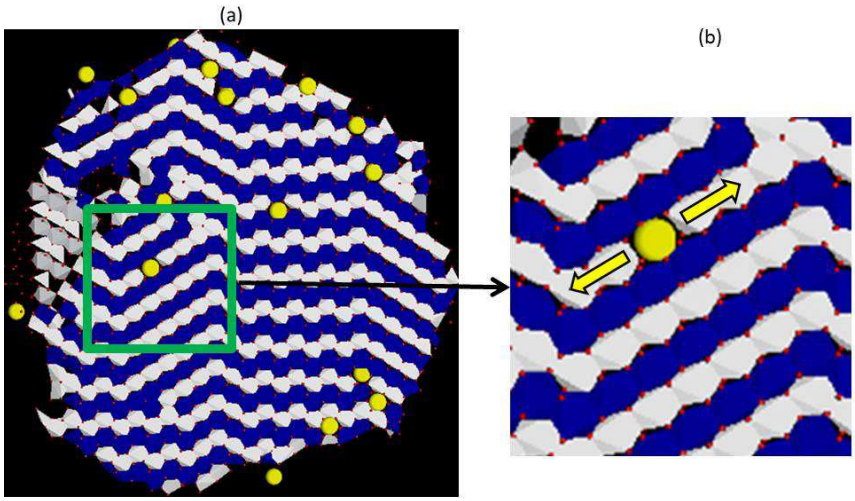

Figure 4.54: A microstructure of a cooled 66 Å TiO_2 nanoporous structure with 100 lithium atoms.

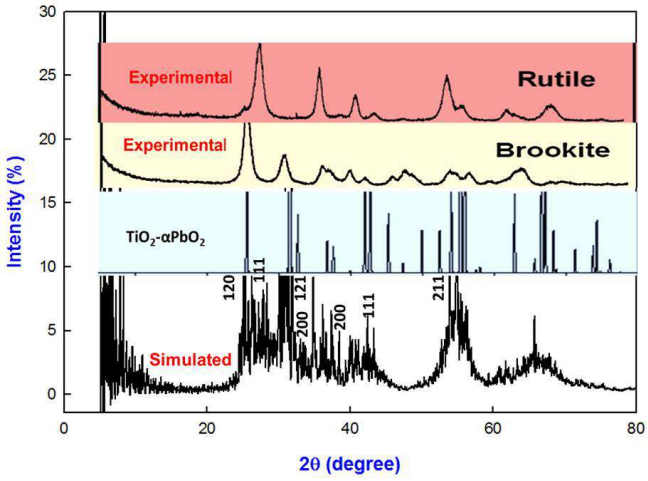

Figure 4.55: A comparison simulated TiO_2 nanoporous 66 Å with 100 Li, calculated TiO_2: α-PbO_2 and experimental (Dambournet et al. 2009) XRDs.

Figure 4.56 indicates the cooled nanoporous structures of 66 Å with 300 lithium atoms. Clear patterns and few tunnels are observed throughout the structure. It also shows lithium atoms at the edge of the channel and some that are located within the system. Radial distribution functions of the nanoporous structure during cooling are given in appendix E. The highest peak in both figures corresponds to 0 K and the lowest being that of 1500 K. It is observed that a plot of 0 K has sharp peaks which indicate that the nanoporous structure has been successfully cooled and retains crystallinity.

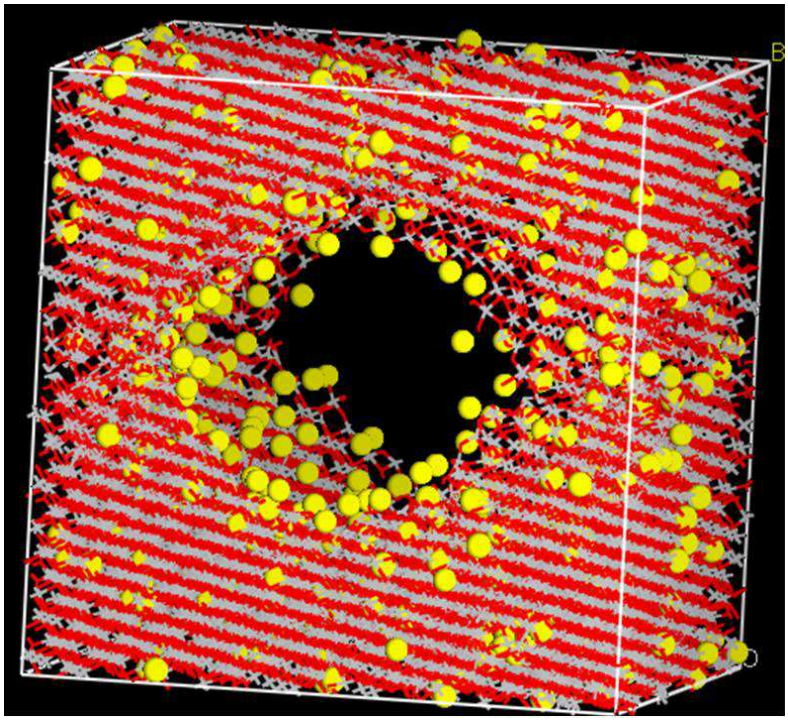

Figure 4.56: A cooled 66 Å TiO_2 nanoporous structure with 300 lithium atoms.

The sliced microstructure of 66 Å nanoporous with 300 lithium atoms is depicted in figure 4.57. The microstructure is characterized by zigzag tunnels which are related to the brookite structure and straight tunnels which are linked to the twinned rutile polymorph and vacancies. Lithium atoms have moved into the vacancies and some are located in the channels. Empty vacancies are very few as compared to the nanoporous structures

lithiated with 50 and 100 lithium atoms. This shows that the nanoporous can act as an anode material since it can holds more lithium atoms and transport them through channels, tunnels and existing vacancies. XRDs of the simulated nanoporous structure with 300 lithium atoms, calculated TiO_2: α-PbO_2 and experimental (Dambournet et al. 2009) are shown in figure 4.58. Observed peaks at 27, 33 and 37 ° correspond to brookite and TiO_2: α-PbO_2 structural arrangements. A smooth curve at 50 ° suggests a rutile structure. At 37 and 57 ° there are peaks accords well with all polymorphs. A simulated peak at 67 ° is similar to those of rutile and TiO_2: α-PbO_2 XRDs. This shows that the nanoporous structure accommodates the three polymorphs well.

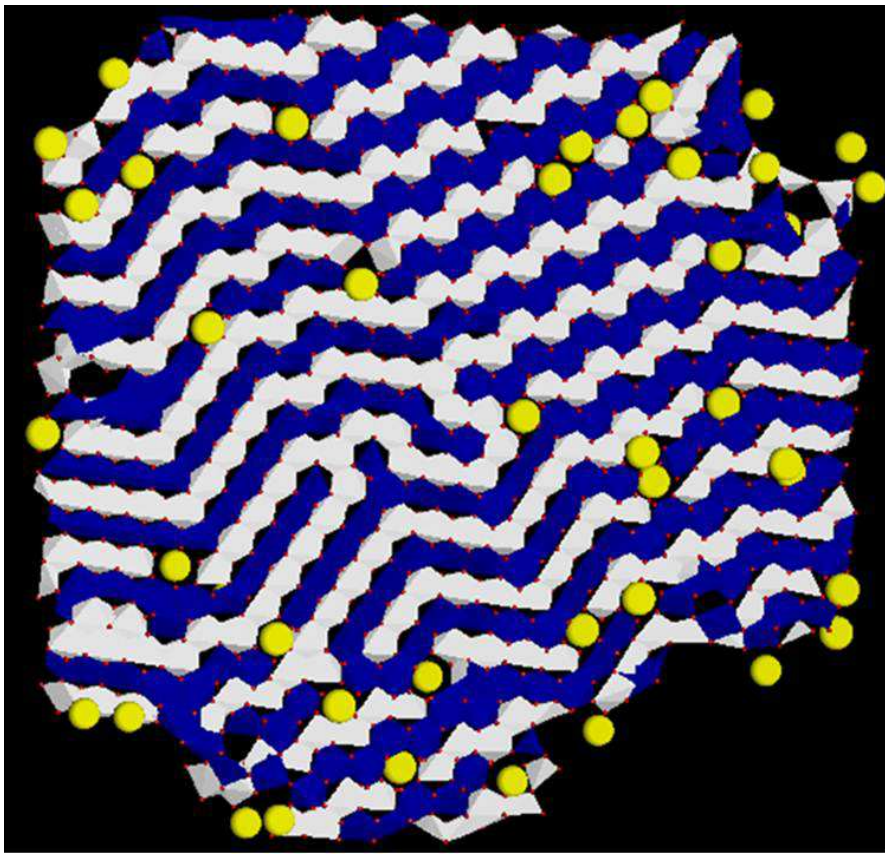

Figure 4.57: A microstructure of a cooled 66 Å TiO_2 nanoporous structure with 300 lithium atoms.

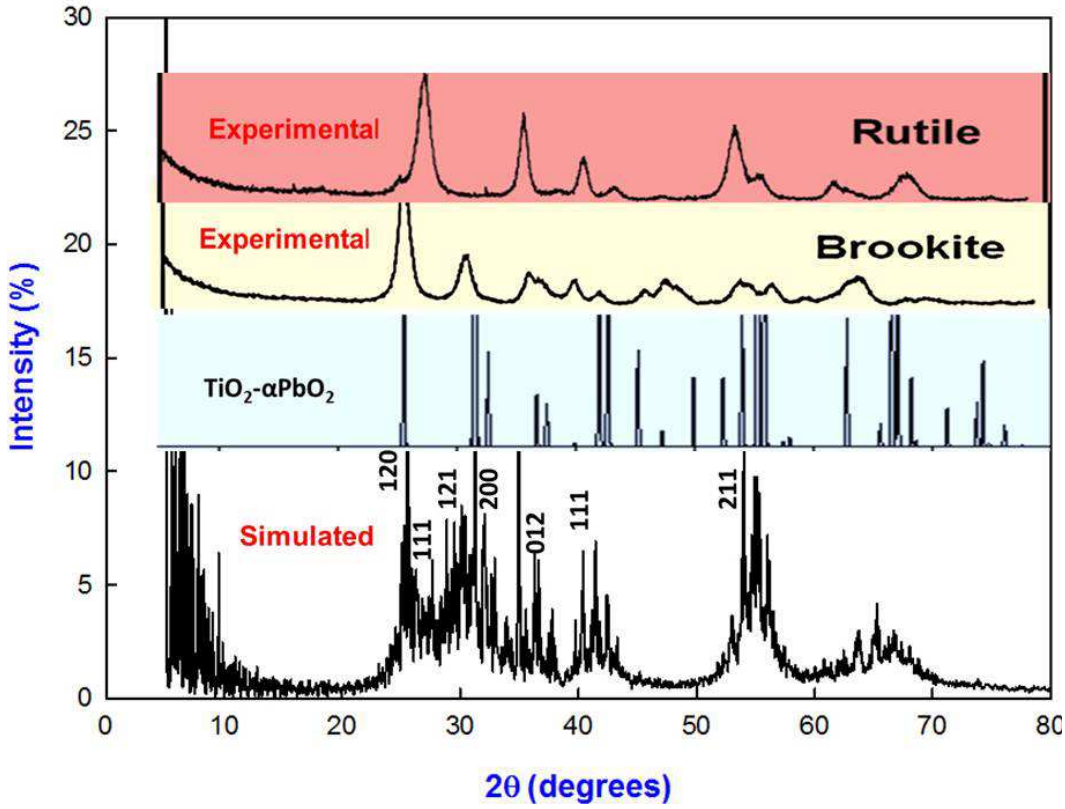

Figure 4.58: XRDs of the simulated TiO_2 nanoporous 66 Å having 300 Li, compared with calculated TiO_2: α-PbO_2 and experimental results (Dambournet et al. 2009).

4.3.4. Lithiated structures of the bulk TiO_2

The amorphous bulk structures of TiO_2 were lithiated with 50, 100 and 300 atoms. Their calculated radial distribution functions before recrystallisation are indicated in figure 4.59 while their structures are illustrated in figure 4.60. RDFs depict broader peaks suggesting an amorphous phase of the bulk structure. The RDFs of the bulk TiO_2 with 300 lithium atoms have broader peaks than others which imply that more lithium atoms enhance the presence of the amorphous phase.

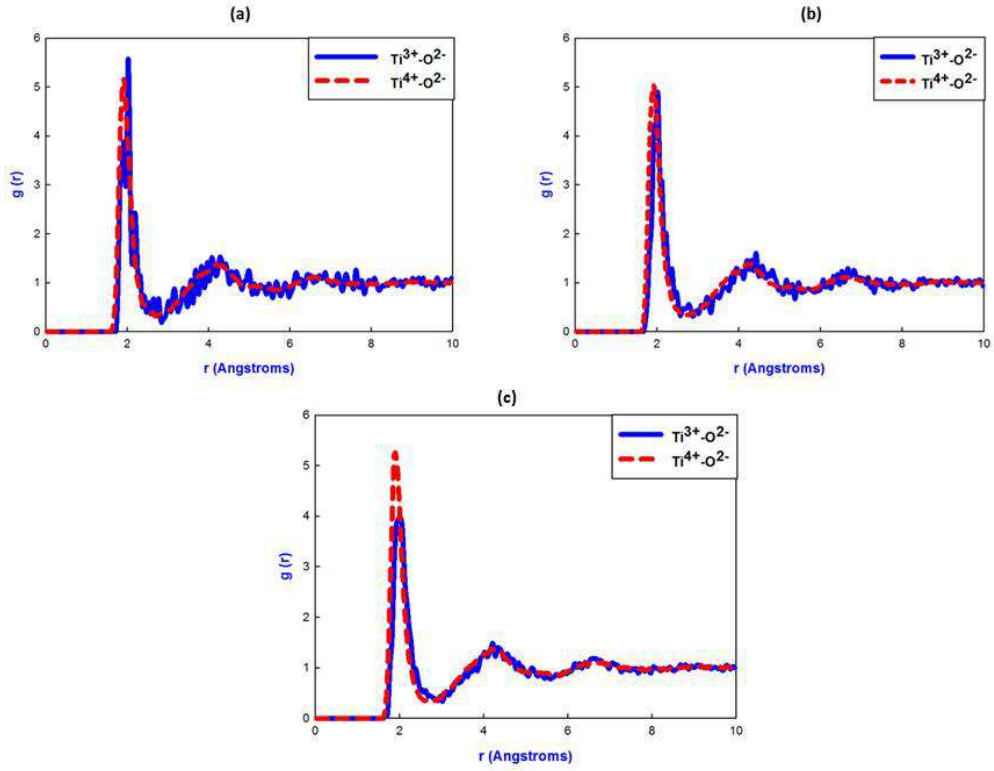

Figure 4.59: RDFs of the TiO_2 bulk before recrystallisation with (a) 50, (b) 100 and (c) 300 lithium atoms.

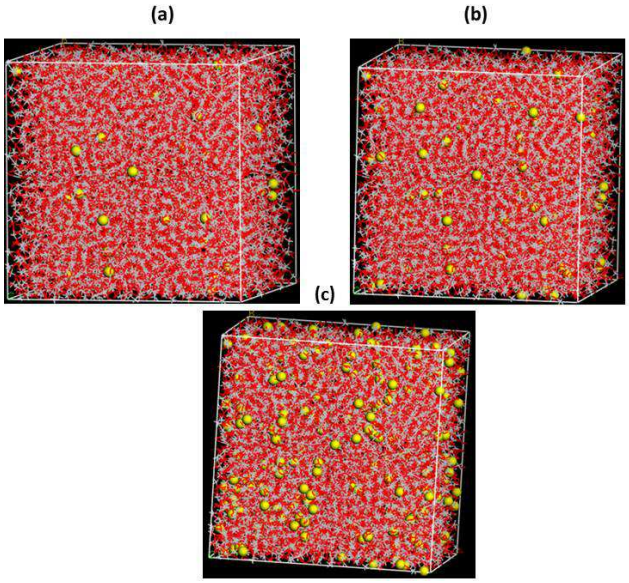

Figure 4.60: Lithiated amorphous structures of the bulk TiO_2 with (a) 50, (b) 100 and (c) 300 lithium atoms.

The graphs of the configuration energy as a function of time for lithiated bulk structures are displayed in figure 4.61. The energy plot of the bulk with 50 lithium atoms shows a sudden decrease from time of 0.15 to 0.42 ns which is associated with the transition from an amorphous to a crystalline phase. From 0.42 ns the graph is constant until 3.5 ns which suggest complete recrystallisation.

The configuration energy vs time plot of the bulk with 100 lithium atoms indicates that the amorphous region (A-B) is slightly extended. It subsequently exhibits an abrupt reduction from 0.125 to 0.25 ns which is linked to the transition from an amorphous to crystalline phase. After 0.25 ns the energy is invariable which shows that the system is recrystallised.

The plot of the bulk with 300 lithium atoms depict a small change in energy from 0 to 0.3 ns and this region (C-D) is more extend compared to that of 50 and 100 lithium structures. From 0.3ns we observe a sharp decrease of energy until 0.4 ns, which corresponds to an amorphous to crystalline transition. From 0.4 ns the energy is constant until 3.5 ns which suggest that the system is completely recrystallised. The magnitude of the energy reduction for all three systems is equivalent to the latent heat of crystallisation. On comparison, the configuration energy shows that bulk structure with 50, 100 and 300 lithium atoms require 0.0625, 0.125, 0.3 ns respectively to undergo an amorphous to crystalline transition. The extended amorphous regions in figure 4.61 i.e. A to B and C to D, cause the structure to demand long time to crystallise, this agrees well with the experimental report (Dambournet et al. 2011), that lithiation of a brookite structure tends to enhance the presence of an amorphous phase.

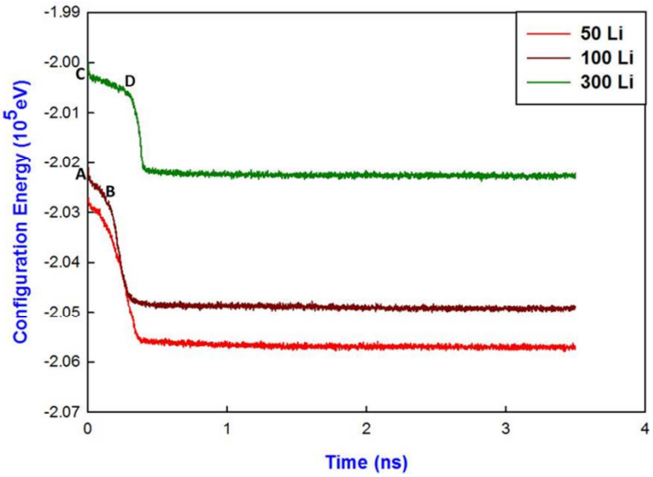

Figure 4.61: Calculated configuration energy as a function of time for the TiO_2 bulk structure.

We have further crystallised a TiO_2 bulk structure from a second amorphous nanosphere, generated from the nanosphere with gas atoms, as discussed in section 3.3. The graph is depicted in figure 4.62. The purpose of showing the variation of the configuration energy change with time of these lithiated structures are their well-defined and extended amorphous and nucleation stages which so vividly demonstrates the delayed crystallisation by an increase in the lithium content.

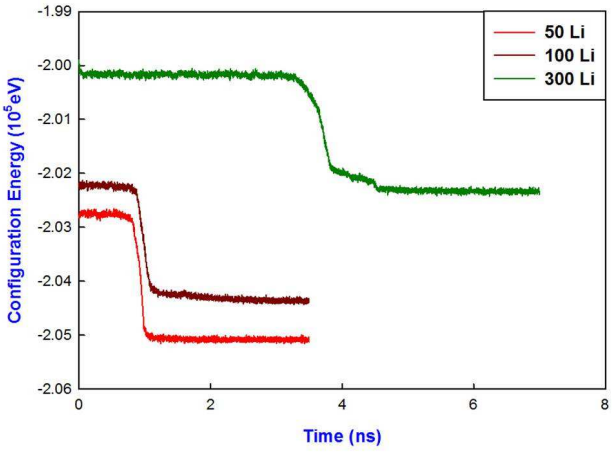

Figure 4.62: Plots of calculated configuration energy as a function of time for the TiO_2 bulk structure, corresponding to 50, 100 and 300 lithium's, which were generated from a different amorphous nanosphere, as that of figure 3.60.

As in previous sections, after lithiation, the structures were crystallised by an MD simulation using the NVT ensemble, at a temperature of 2000 K, for 700000 steps with a time step of 0.005 ps. Recrystallised TiO_2 lithiated bulk structures are shown in figure 4.63, and clear patterns are observed at all concentrations indicating a complete crystallisation of the bulk.

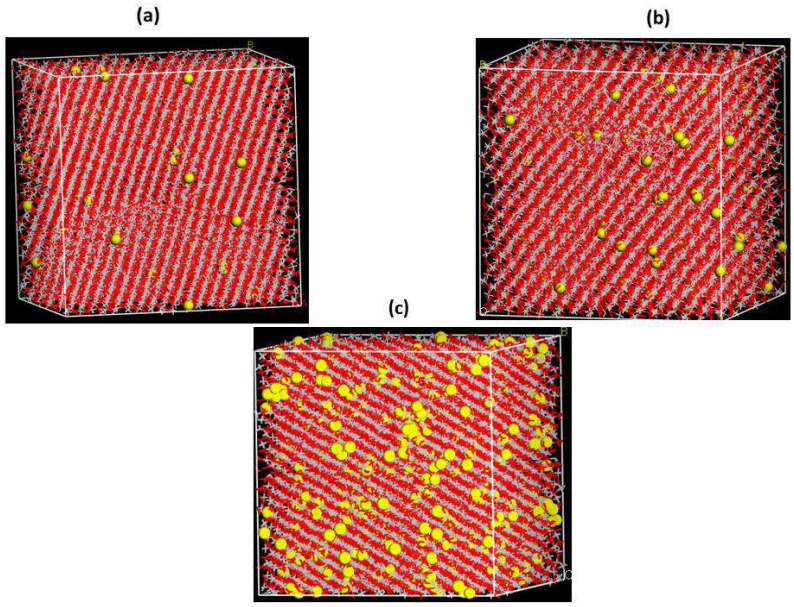

Figure 4.63: Recrystallised bulk structures of TiO_2 with (a) 50, (b) 100 and 300 lithium atoms at 2000 K.

The total RDFs of bulk TiO_2 with 50, 100 and 300 lithium atoms for Ti^{3+}-O^{2-} and Ti^{4+}-O^{2-} interactions are shown in appendix E. They behave similarly for all the structures; the highest peaks are observed at a radial distance of 2 Å and more peaks are noted at 4.3, 5.1, 6.0, 6.9, 7.5 and 9.0 Å. This confirms that the bulk structures have recrystallisation. Molecular dynamics calculations were performed to cool all the crystallised lithiated bulk as was done for other TiO_2 nano-architectures. A cooled bulk structure with 50 lithium atoms is shown in figure 4.64 and depicts clearer patterns and tunnels, with lithium atoms located within the system. The total radial distribution functions of the bulk with 50

lithium atoms at different temperatures, for both Ti^{3+}-O^{2-} and Ti^{4+}-O^{2-} interactions, are reflected in appendix E. Peak heights increase as the temperature is reduced from 1500 to 0 K and sharper peaks are noted at lower temperatures.

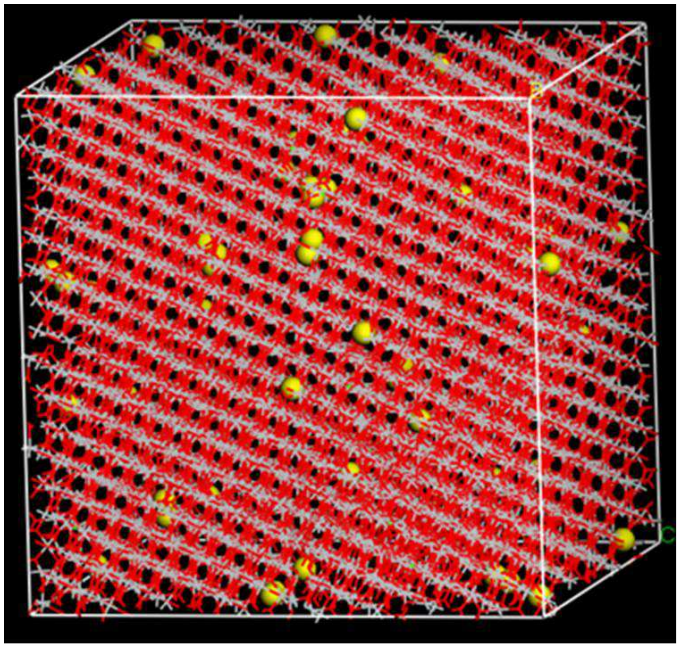

Figure 4.64: Cooled structure of the bulk TiO_2 with 50 lithium atoms.

The microstructure of the bulk with 50 lithium atoms is illustrated in figure 4.65 and it shows no octahedra straight or zigzag tunnels as in other nano-architectures, hence suggesting limited tunnels. Lithiation of the bulk TiO_2 appears to have destroyed most tunnels that were observed in the pure bulk and lithium atoms have filled the vacancies that are within the system. The simulated bulk structure, TiO_2: α-PbO_2 and experimental (Dambournet et al. 2009) XRDs are depicted in figure 4.66. Simulated diffractions show sharp peaks than the experimental ones. At 27, 3, 42 and 62 ° peaks tend to agree with brookite and TiO_2: α-PbO_2. At 37 and 56° they correspond to all polymorphs. At 67 ° they are aligned with the rutile structure.

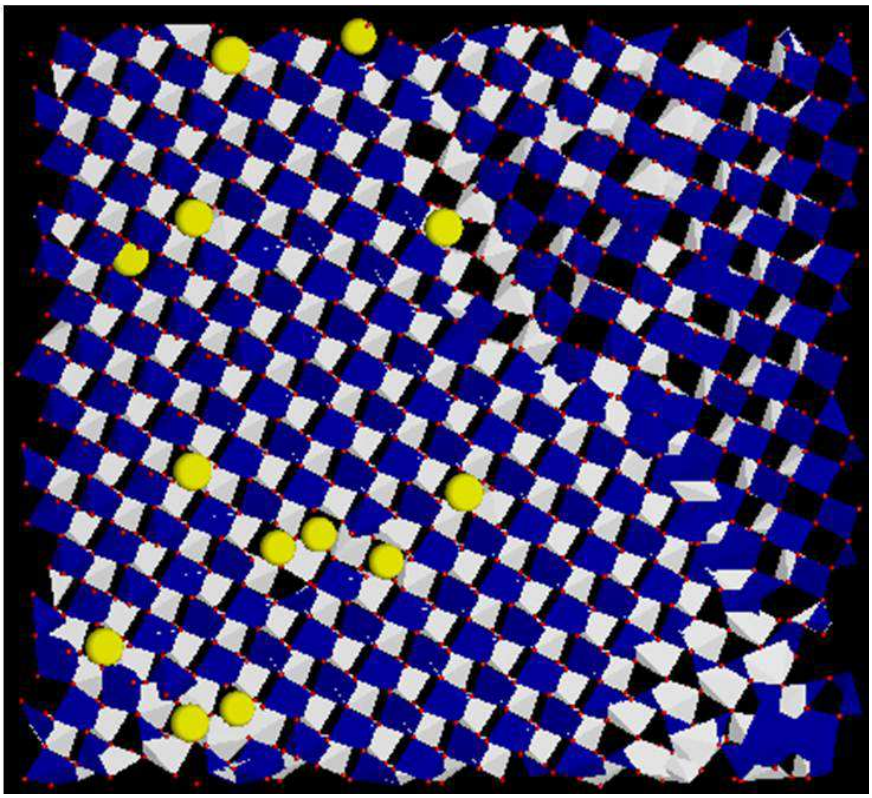

Figure 4.65: Microstructure of the cooled lithiated bulk TiO_2 with 50 lithium atoms.

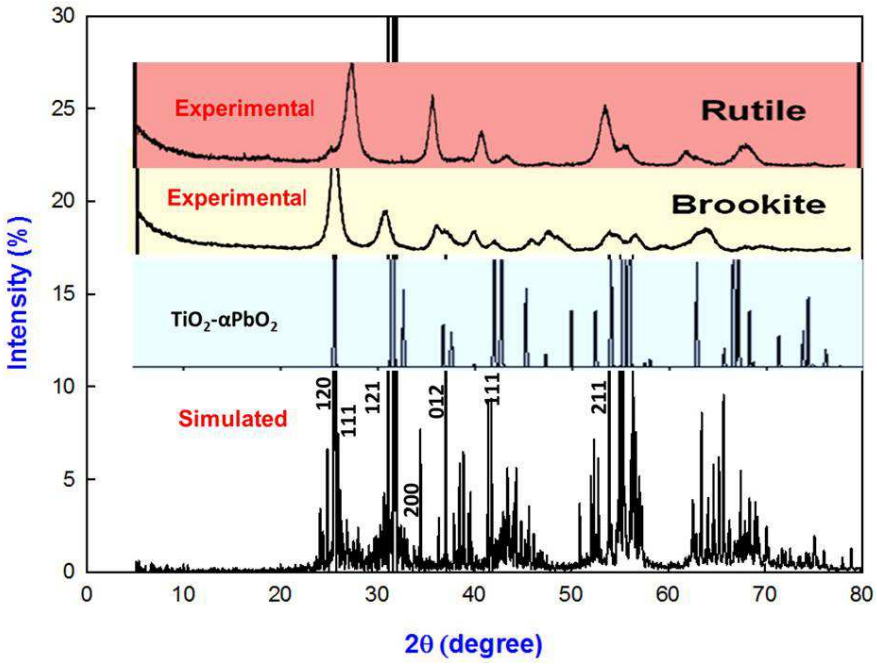

Figure 4.66: XRDs of simulated TiO_2 bulk with 50 Li, TiO_2: α-PbO_2 and experiments (Dambournet et al. 2009).

The cooling procedure was applied to the recrystallised bulk TiO_2 with 100 lithium atoms and the corresponding structure is shown in figure 4.67. More tunnels are observed throughout the structure especially in the middle as compared to the recrystallised bulk at 2000 K. Total RDFs of the system are illustrated in appendix E. They show a similar trend of the peaks throughout the graph, especially around peak of 2 Å. The peaks are higher and sharper at lower than at higher temperatures.

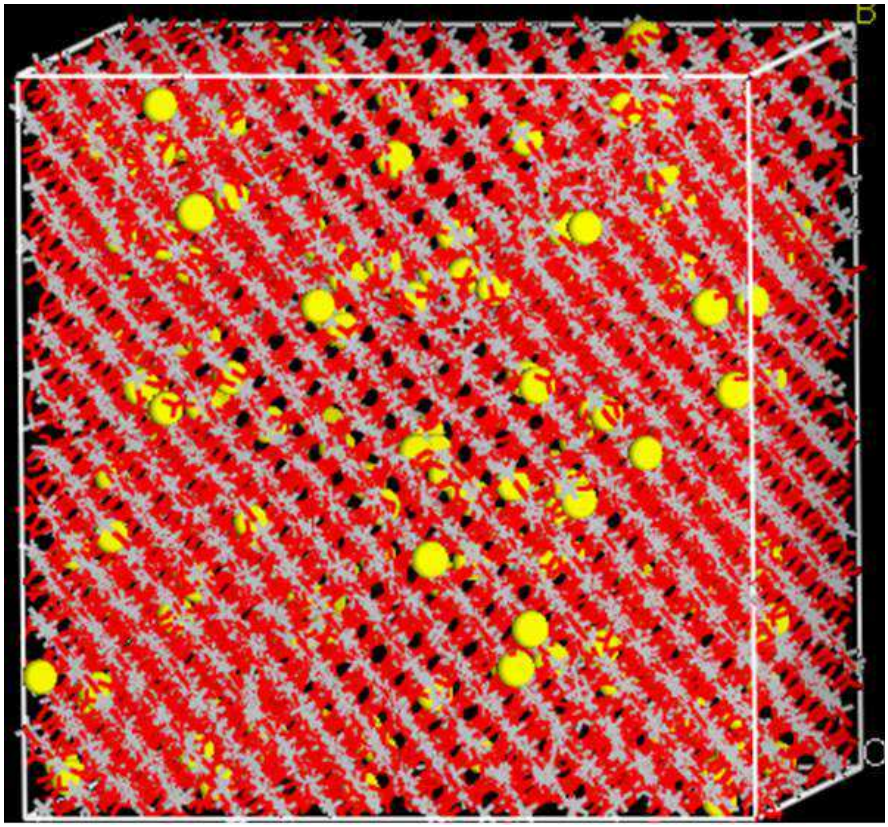

Figure 4.67: Cooled structure of the bulk TiO_2 with 100 lithium atoms.

A simulated microstructure of the bulk TiO_2 with 100 lithium atoms is shown in figure 4.68. Tunnels are not observed on the system and lithium atoms are occupying the vacancies. The microstructure depicts complex defects almost through the whole system.

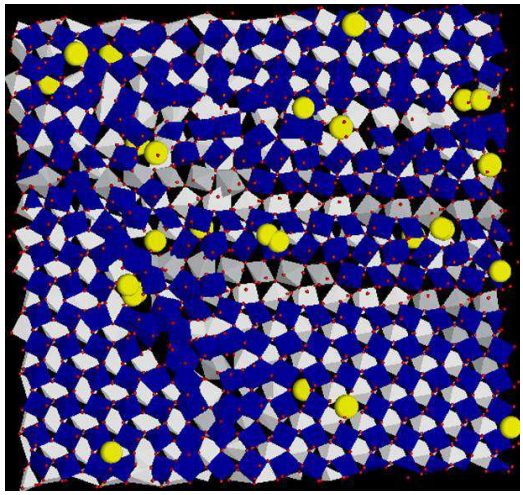

Figure 4.68: Microstructure of a cooled lithiated bulk TiO_2 with 100 lithium atoms.

Simulated XRDs for the bulk, TiO_2: α-PbO_2 and experiments (Dambournet et al. 2009), which are superimposed, are given in figure 4.69. They show peaks that mainly correspond to experimental results of brookite, rutile and to the calculated TiO_2: α-PbO_2 structure between 25 and 70 °. The peak usually observed at 27 ° has disappeared. At 37, 57 and 63 ° peaks are associated with brookite, rutile and TiO_2: α-PbO_2 structures, whilst at 67 ° a peak is associated with the rutile and TiO_2: α-PbO_2 polymorphs.

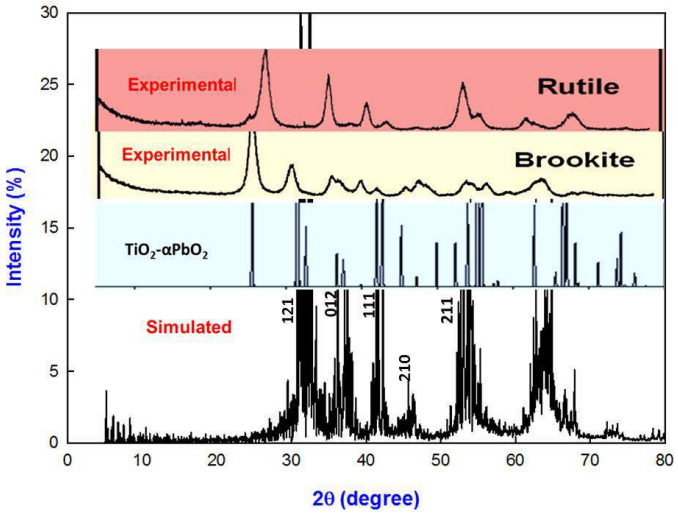

Figure 4.69: XRDs of the bulk simulated TiO_2 with 100 Li, TiO_2: α-PbO_2 and experiments (Dambournet et al. 2009).

A cooled structure of the bulk with 300 lithium atoms is given in figure 4.70 and clear patterns are observed and more visible as compared to that of recrystallised structure at 2000 K. Few tunnels are observed at the edge of the bulk. Total radial distribution functions of the bulk with 300 lithium atoms are illustrated in appendix E. The peaks are lower and broader at higher than at lower temperatures.

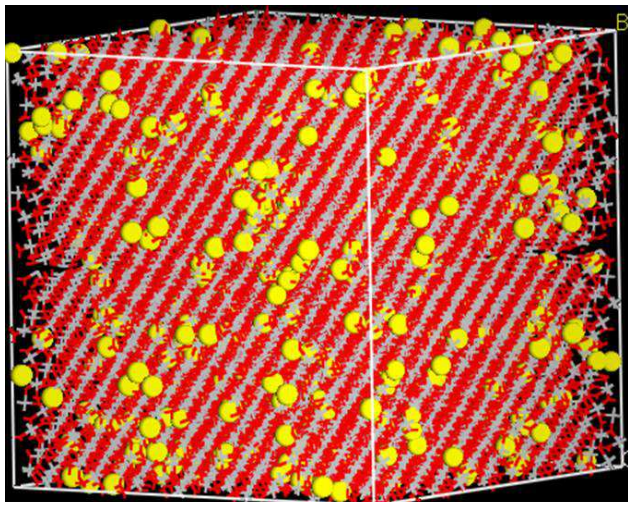

Figure 4.70: Cooled structure of the bulk TiO_2 with 300 lithium atoms.

Simulated microstructure of the bulk with 300 lithium atoms is depicted in figure 4.71. More lithium atoms are clustering and no patterns or tunnels are observed on the microstructure. The lower layer of Ti^{4+} octahedra is not clearly visible as compared to that of the bulk with 50 and 100 lithium atoms. The bulk structure for 300 Li atoms has short twinned tunnels unlike those of 50 and 100 Li atoms; hence it shows that the structure is rutile since the micro twinning is associated with rutile structural arrangement. In figure 4.72, XRDs of the bulk structure with 300 atoms are compared to those calculated from TiO_2: α-PbO_2 structure and the experimental results (Dambournet et al. 2009). Simulated bulk TiO_2 shows sharp peaks while the measured ones are broader. Peaks at 27, 33, 37 and 65 ° are aligned with the brookite structure, although the one at 27 ° is very small. At 33, 37, 45, 63 and 67 ° peaks correspond to the TiO_2: α-PbO_2

structure. Peaks at 37, 54 and 63° and a smooth curve around 50° are aligned with the rutile structure. Hence all three polymorphs are present in the simulated bulk with 300 lithiums.

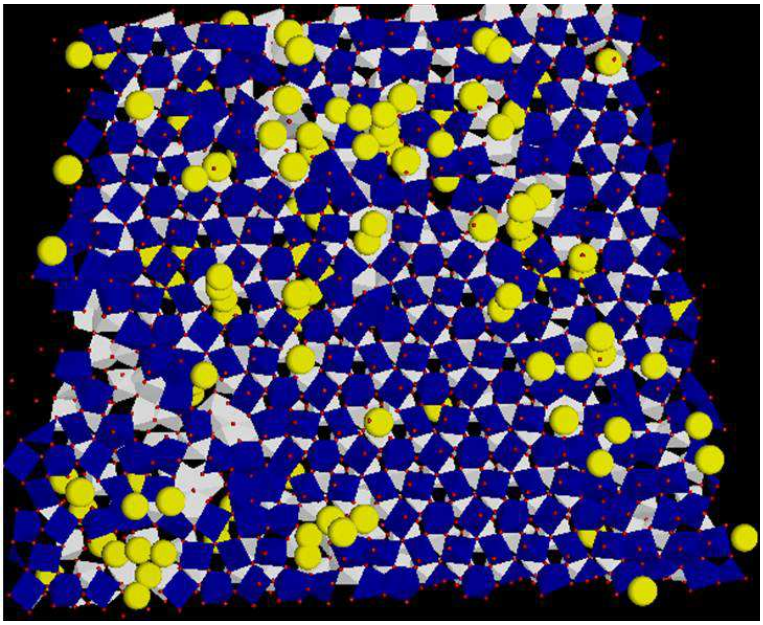

Figure 4.71: Microstructure of the lithiated bulk TiO_2 with 300 lithium atoms.

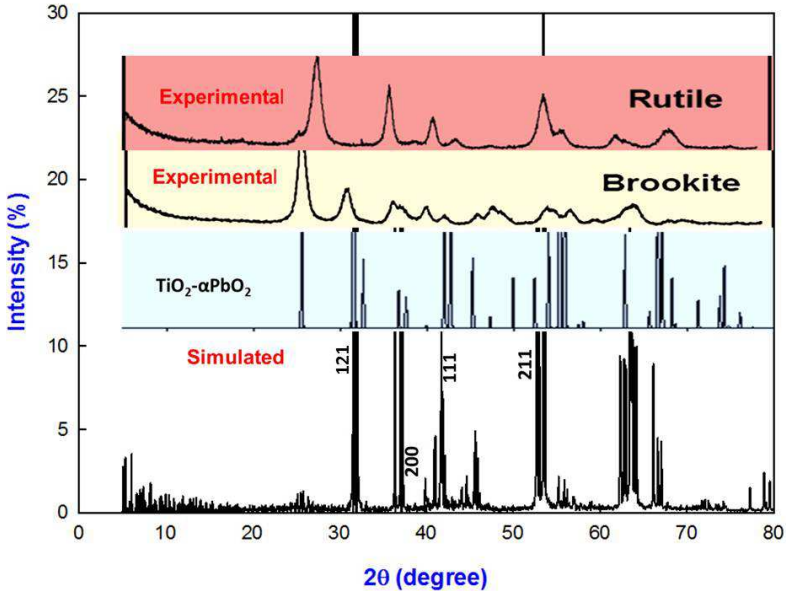

Figure 4.72: A comparison simulated TiO_2 bulk with 300 Li, calculated TiO_2: α-PbO_2 and experimental (Dambournet et al. 2009) XRDs.

4.4 Discussions

All amorphous nano-architectures of TiO_2 were inserted with 50, 100 and 300 Li ions. It has, however, been observed that the nanosheet was partially crystalline before and after lithiation. Such partial crystallinity is confirmed by an almost constant plot of configuration energy as a function of time. Lithiated nanostructures were successfully crystallised and cooled as evidenced by their configuration energy vs. time and RDFs plots. After recrystallisation and cooling, most Li ions are located within systems which indicates that TiO_2 nano-architectures can host Li ions; consistent with simulation studies on nanoporous of MnO_2 (Sayle et al. 2009b).

On the other hand, it has been noted that immediately after crystallisation some of the lithium atoms reside outside the nano-architectures. Quantification for the nanosphere, as an example, shows that for a nanosphere with 50 lithiums, 18 lithiums moved out and 32 remained. In the case of 100 lithium atoms system, 43 lithiums moved out and 57 remained and for 300 lithiums nanosphere 180 moved out and 120 remained. However, on cooling, the lithium atoms are re-incorporated into the nanosphere, with a few remaining outside. It is suggested that during crystallisation, the TiO_2 crystallises into the brookite and twinned rutile structures and as each amorphous Ti or O species adhere and extend the crystal at the crystallisation front, the Li is pushed out as it does not extend the brookite and twinned rutile crystal structure. However, on cooling, there are 1D tunnels that the Li can move through hence it is surmised that the Li at the surface then moves into the 1D tunnels exposed at the surface. The same argument can be extended to other TiO_2 nano-architectures.

Calculated XRDs of simulated nanosphere, nanoporous, bulk and nanosheet TiO_2 display peaks which accord well with the brookite, rutile and TiO_2: α-PbO_2 structural

arrangements. Superimposed XRDs of lithiated nano-architectures are shown in appendix C, where those of the nanosphere appear to be least affected by the increase of Li concentration. In other architectures XRD peaks at higher angles, especially 57 and 67 ^{o}, appear broader for the nanosheet (associated with reduced crystallinity) at higher lithium concentrations. Furthermore, they tend to shift to lower values for the nanoporous with increasing content of lithium, which could be partly ascribed to an increase of the rutile phase. In regard to the bulk TiO_2 the first peak at 27 ^{o} associated with the brookite structure disappears at higher lithium concentrations. In addition, peaks at 57 and 67 ^{o} shift to lower values and a new peak emerges on the right of the latter; all such changes suggest an increase of the rutile polymorph, in agreement with observed changes on the microstructures of the bulk TiO_2.

We now discuss the observed impact of lithiation on nucleation and crystallisation of the various nano-architectures of TiO_2. A comparison of plots of configuration energy against time for pure (Figure 3.8) and lithiated (Figure 4.3) TiO_2 nanosphere shows a short nucleation period in the former which appears to be diminished in the latter, hence suggesting that lithiation accelerates crystallisation, especially for the 50 Li atom system. However, as the Li concentration is increased to 100 and 300 Li atoms, crystallisation appears to be suppressed as evidenced by the reduced slope of the energy vs. time plots. In the nanoporous structures, lithiation appears to extend the nucleation phase and the reduced rate of crystallisation is quite pronounced in the 300 Li doped system. The manifestation of the delayed crystallisation by lithiation is quite distinct in the bulk TiO_2. Indeed extended nucleation phases are displayed and these tend to increase with increasing Li content. In all nano-architectures, crystallisation was not achieved at higher Li concentrations; particularly over simulation times equivalent to

and higher than those used in the current work; perhaps this could be feasible for very long periods of simulations.

Discussions above clearly point to the promotion of amorphisation by lithiation in most TiO_2 nano-architectures, and in particular within the context of simulated structures with predominantly brookite polymorph. This behaviour is confirmed by experimental investigations, where XRD studies on different stages of Li insertion and de-insertion reactions suggest that the Brookite framework is amorphised during discharge, with a partial recovery of the crystallinity upon (re)charging (Reddy et al. 2008). A further investigation, involving a combined PDF and DFT approaches, clearly indicated that the TiO_2 connectivity within the brookite framework remains intact upon lithium intercalation (Dambournet et al. 2011). The flexibility of the framework with five-fold coordination environment for the Li ion, which, in part, allows it to accommodate the Li ions, is also responsible for the broadening of the Bragg reflections and apparent reported amorphisation. On the contrary lithiation appears not to substantially perturb or annihilate partial crystallinity of the TiO_2 nanosheet, at equivalent concentrations, since no nucleation phase is observed in the configuration against time curve. As mentioned in section 1.3 under literature review, the synthesis of TiO_2 nanosheets is very recent as compared to other nano-architectures and is reckoned to have excellent rate capabilities (Dylla et al. 2012).

A comparison of microstructures for pure and lithiated bulk TiO_2 after crystallisation and annealing is quite informative. The observed microstructures of pure TiO_2 reveal various patterns; twinned straight and zigzag tunnels (Figure 3.54) and ordinary 1x1 tunnels. However, in the 50 Li doped bulk TiO_2 the twinned patterns are not obvious. On the contrary Li ions appear to be trapped in the 1x1 tunnels, and what is more interesting the 2x1 tunnels that tended to occur in the ramsdellite MnO_2 are visible. As the Li

content is increased to 100 and 300 shorter tunnels of Ti octahedra are noted, but they do not appear accommodate Li ions; on the contrary they seem to be located in the Ti vacancies. An increase in the rutile type 1x1 tunnels with concentration is in good agreement with XRD results which suggest enhanced rutile polymorph.

Microstructures of the nano- sphere, sheet and porous TiO_2 architectures respond differently to Li insertion when compared to the bulk. Most display straight and zigzag tunnels in the pure phase, associated with the twinned rutile and brookite polymorphs respectively, and such patterns are mostly retained after Li is inserted at varying concentrations, i.e. from 50 to 300 Li. The Li ion is predominantly located in such tunnels, as demonstrated by both upper and lower layers formed by Ti octahedra. This could suggest that the tunnels of the nano-architectures are robust and flexible enough to accommodate Li ion and to allow its passage as it diffuses in an electrode. The bulk structure appears not be conveniently providing such path, hence its poor performance when used in electrodes for Li-ion batteries. Such nano-architectural attributes are further elucidated by advantages associated with nanoscaling which were discussed extensively in Section 1.3 on literature review. In addition, the supremacy of nanoporous over nanoparticle architecture has also been outlined, in most polymorphs, since the former has characteristic grains as well as pores nearly in the same scale. Similar trends have been noted in simulation studies of Li insertion into various nano-architectures of MnO_2 (Sayle et al. 2009a,b and Maphanga et al. 2011).

Chapter 5

Conclusions and Recommendations

5.1 Conclusions

This is the first study where various simulated nano-architectures of TiO_2 i.e. nanosphere, nanosheet, nanoporous and bulk have been successfully generated, at different lattice box sizes with the bulk being the smallest, using amorphisation recrystallisation method. We obtained two nanoporous structures at lattice boxes 60 Å and 66 Å. They mainly differ by channel size with the nanoporous of lattice box 60 Å having the small channel and nanoporous of lattice box 66 Å having a larger one. All grown nanostructures have recrystallised, as shown by their RDFs, structures and graphs of configuration energy against time. However, the configuration energy as a function of time graphs show a clear amorphise-crystallisation transition for the nanosphere, two nanoporous and bulk architectures. Such transition was not distinct for the nanosheet, since it was partially crystallised before the actual crystallisation with an NVT ensemble was carried out. XRDs of TiO_2 nanostructures were calculated using copper and iron source, and those of copper agree better with the experimental results. All calculated X-ray diffractions of our structures suggest that the systems are mostly of brookite, TiO_2: α-PbO_2 (isostructural with brookite) and twinned rutile structural arrangements.

Microstructures of nanostructures have predominantly straight tunnels, which are associated with the twinned rutile type and zigzag tunnels, which are related to the brookite structure. The tunnels are formed by titanium octahedra in which lithium can be

inserted. The simulated microstructures of the nanosheet and nanoporous structures are in good accord with the experimental high resolution transmission electron microscope images. Some microstructures have vacancies which can be filled by lithium atoms.

Amorphisation and recrystallisation technique has also been successfully employed, for the first time, to generate nano-architectures of TiO_2 with different lithium concentrations. Plots of the total RDFs and configuration energy vs. time for lithiated nanospheres confirm that systems have crystallised. The change of the configuration energy shows an amorphise-crystalline transition and can estimate the latent heat of crystallisation. Cooling of all lithiated nanospheres where successful as confirmed by their sharp RDFs. Microstructures of lithiated nanospheres show that the systems can host and transport atoms which suggest that it can be a good anode material. Their XRDs confirm a brookite structural arrangement and they are accord with those of TiO_2: α-PbO_2.

Lithiated nanosheets have all recrystallised, this is confirmed by their RDFs and their structures. Configuration energy was constant throughout and there is no obvious amorphous-crystalline transition since after lithiation the structures show patterns. All lithiated nanosheets were cooled gradually and have sharp RDFs peaks. Nanosheets have been characterised by XRD and correspond to the brookite and rutile TiO_2 when compared with the experimental results. They also show similar peaks as those of TiO_2: α-PbO_2. Created microstructures show a good anode material since the system appears to host and transport lithium.

All lithiated nanoporous structures related to the lattice box of 66 Å have recrystallised, which is confirmed by their RDFs. The plot of the configuration energy as a function to time changed as a confirmation of amorphous-crystalline transition. RDFs of all lithiated

nanoporous structures confirm that the systems have cooled gradually. Nanoporous have been characterised by XRD and correspond to the brookite and rutile TiO_2 when compared with the experimental, and they are accord with the x-ray of TiO_2: α-PbO_2. Created microstructures show a good promising anode material since the system can host and transport ions.

Lithiated bulk structures have crystallised which is confirmed by their RDFs. Configuration energies as a function of time shows a transition of amorphise to crystalline phase. The microstructures of the cooled structures show very limited defined tunnels. Lithiated bulk cannot act as an anode material; this might be the reason for not having much work on bulk as an anode material. XRDs also confirm the presence elements of the three polymorphs noted in other nano-structures, although some of the peaks associated with the brookite and TiO_2: α-PbO_2 structures tend to disappear at higher concentrations.

Generally, it can be concluded that XRDs and microstructures of simulated nano-architectures concur well on types of TiO_2 polymorphs that are present. The insertion of higher lithium concentrations in TiO_2 nano-architectures appears to extend the amorphous phase and delay crystallisation, and this behaviour has been noted experimentally for the brookite TiO_2.

On the whole the current study, which has employed the amorphisation and recrystallisation method, has, for the first time, succeeded to spontaneously generate simulated nanosphere, nanosheet, nanoporous and bulk structures of TiO_2. It has further provided, at an atomistic level, valuable structural insights that account for the promotion and suppression of Li ion transport in TiO_2; hence explaining why certain nano-architectures serve as good candidates for lithium ion battery anode, whereas others,

particularly the bulk phase do not. The generation and characterisation of such simulated structures have laid a solid foundation and opened an avenue for the prediction of conditions under which such electrodes will undergo electrochemical and mechanical failure.

5.2 Recommendations

In the current simulations, lithiation has been affected by crystallising lithiated amorphous structures for various nano-architectures, which is equivalent to chemical lithiation. It is recommended that in the future crystalline nano-architectures of TiO_2 be lithiated and related changes in mechanical properties, which influence the lifespan of battery electrodes, be studied. Such an approach will be equivalent to electrochemical lithiation and it tends to accommodate higher concentrations of lithium.

Bibliography

Akimoto J., Gotoh Y.,Oosawa Y., Nonose N., Kumagai T., Aoki K. and Takei H. 1994. Topotactic oxidation of ramsdellite-type $Li_{0.5}TiO_2$, a new polymorph of titanium dioxide: TiO_2(R). J. Solid State Chem. **113,** 27 - 36.

Alder B. J. and Wainwright T. E. 1957. Phase Transition for a hard sphere system. J. Chem. Phys. **27,** 1208 – 1209.

Arico A. S., Bruce P., Scrosati B. Tarascon J.M. and van Schalkwijk W. 2005. Nanostructured materials for advanced energy conversion and storage devices. Nat. Mater. **4,** 366 - 377.

Armstrong A. R., Armstrong G., Canales J. and Bruce P. G. 2005a. TiO_2-B nanowires as negative electrodes for rechargeable lithium batteries. J. Power Sources. **146**(1-2), 501 – 506.

Armstrong A. R., Armstrong G., Canales J., Garcia R and Bruce P. G. 2005b. Lithium-Ion Intercalation into TiO_2-B Nanowires. Adv. Mater. **17** (7), 862 – 865.

Armstrong G., Armstrong A. R., Canales J and Bruce P. G. 2006. TiO_2(B) Nanotubes as Negative Electrodes for Rechargeable Lithium Batteries. Batteries, Fuel Cells and Energy Conversion. Electrochem. Solid-State Lett. **9**(3), A139 – A143.

Armstrong G., Armstrong A. R., Canales J. and Bruce P. G. 2005c. Nanotubes with the TiO_2-B. Chem. Commun. 2454 – 2456.

Augustsson A., Henningsson A., Butorin S. M., Siegbahn H. Nordgren J. and Guo J.-H. 2003. Lithium ion insertion in nanoporous anatase TiO_2 studied with RIXS. J. Chem. Phys. **119,** 3983 – 3987.

Balachandran D., Morgan D., Ceder G. and van de Walle A. 2003. First-principles study of the structure of stoichiometric and Mn-deficient MnO_2. J. Solid State Chem. **173** (2), 462 – 475.

Balaya P., Saravanan K.,Hariharan S., Ramar V., Lee H. S., Kuezma M., Devaraj S., Nagaraju D. H. Ananthanarayanan K. and Mason C. W. 2011.Nanostructured mesoporous materials for lithium-ion battery applications. SPIE; http://dx.doi.org/10.1117/12.884460.

Barbe C. J., Arendse F. P., Jirousek M., Lenzmann F., Shklover V. and Gratzel M. 1997. Nanocrystalline Titanium Oxide Electrodes for Photovoltaic Applications, J. Am. Ceram. Soc. **80,** 3157 - 3171.

Baudrin E., Cassaignon S., Koelsch M., Jolivet J. –P., Dupont L. and Tarascon J. –M. 2007. Structural evolution during the reaction of Li with nano-sized rutile type TiO_2 at room temperature. Electrichem. Commun. **9,** 337 – 342.

Bauer V. W. H. 1961. Atomabstände und Bindungswinkel im Brookit, TiO_2. Acta Cryst. **14,** 214 – 216.

Berger H., Tang H. and Levy F. 1993. Growth and Raman spectroscopic characterization of TiO_2 anatase single crystals. J. Cryst. Growth. **130,** 108 - 112.

Borghols W. J. H., Wagemaker M., Lafont U., Kelder E. M. and Mulder F. M. Impact of Nanosizing on Lithiuated Rutile TiO_2. Chem. Mater. **20,** 2949 – 2955.

Born M. M. and Huang K. 1954. Dynamic Theory of Crystal Lattices, Oxford University Press, Oxford, U.K.

Bruce P.G., Scrosati B. and Tarascon J.M. 2008. Nanomaterials for Rechargeable Lithium Batteries. Angew. Chem. Int. Ed. **47,** 2930 - 2946.

Brus L. E. 1984. Electron-electron and electron-hole interactions in small semiconductor crystallites: The size dependence of the lowest excited electronic state. J. Chem. Phys. **80,** 4403 - 4409.

Cava R. J., Murphy D. W., Zahurak S., Santoro A. and Roth R. S. 1984. The crystal structures of the lithium-inserted metal oxides $Li_{0.5}TiO_2$ anatase, $LiTi_2O_4$ spinel, and $Li_2Ti_2O_4$. J. Solid State Chem. **53** (1), 64 – 75.

Chen J. S. and Lou X. W. 2010. The superior lithium storage capabilities of ultra-fine rutile TiO_2 nanoparticles. J. Power Sources. **195**(9), 2905 – 2908.

Chen X. and Mao S. S. 2007. Titanium dioxide nanomaterials: Synthesis, properties, modifications and applications. Chem. Rev. **107,** 2891 - 2959.

Cheng W-Y., Deka J. R., Chiang Y-C., Rogeau A. and Lu S-Y. 2012. One-step, Surfactant-Free Hydrothermal Method for syntheses of Mesoporous TiO_2 Nanoparticle Aggregates and Their Applications in High Efficiency Dye-Sensitized Solar Cells. Chem. Mater. **24**(16), 3255 – 3262.

Cho J. Y., Nam W. H., Lim Y. S., Seo W-S., Park H-H. and Lee J. Y. 2012. Bulky mesoporous TiO_2 structure. RSC Adv. **2,** 2449 – 2453.

Choi M. G., Lee Y-G., Song S-W. and Kim K. M. 2010. Lithium-ion battery anode properties of TiO_2 nanotubes prepared by the hydrothermal synthesis of mixed (anatase and rutile) particles. Electrochim. Acta. **55**(20), 5975 – 5983.

Chou S-L., Wang J-Z., Liu H-K. and Dou S-X. 2011. Rapid Synthesis of $Li_4Ti_5O_{12}$ Microspheres as Anode Materials and Its Binder Effect for Lithium-Ion Battery. J. Phys. Chem. C **115**, 16220 – 16227.

Dambournet D., Belharouak I. and Amine K. (2010). Tailored Preparation Methods of TiO_2 Anatase, Rutile, Brookite: Mechanism of Formation and Electrochemical Properties. Chem. Mater. **22**(3), 1173 – 1179.

Dambournet D., Belharouak I. and Amine K. 2009. Nanosized TiO_2 anatase, rutile and brookite anodes for Li-ion batteries. Electrochem. Soc. **215,** No.1.

Dambournet D., Chapman K. W., Koudriachova., Chupas P. J. Belharouak I. and Amine K. 2011. Combining the pair distribution function and computational methods to understand Lithium insertion in brookite (TiO_2). Inorg. Chem. **50,** 5855 - 5857.

Deng D., Kim M. G., Lee J. Y. and Cho J. 2009. Green energy storage materials: Nanostructured TiO_2 and Sn-based anodes for lithium-ion batteries. Energy Environ. Sci. **2** (8), 818 – 837.

Deng Q., Wei M., Ding X., Jiang L., Ye B. and Wei K. 2008. Brookite-type TiO_2 nanotubes. Chem. Commun. 3657 – 3659.

Dick B. G. and Overhauser A. W. 1958. Theory of the dielectric constants of alkali halide crystals. Phys. Rev. **112,** 90 - 103.

Djerdj I. and Tonejc A. M. 2006. Structural investigations of nanocrystalline TiO2 samples. J. Alloy Compd. **413**,159 – 174.

Dong S., Wang H., Gu L., Zhou X., Liu Z., Han P., Wang Y., Chen C., Cui G. and Chen L. 2011. Rutile TiO_2 nanorod arrays directly grown on Ti foil substrates towards lithium-ion micro-batteries. Thin Solid Films. **519**(18), 5978 – 5982.

Dylla A. G., Xiao P., Henkelman G. and Stevenson K. J. 2012. Morphological Dependence of Lithium Insertion in Nanocrystalline TiO_2(B) Nanoparticles and Nanosheets. J. Phys. Chem. Lett. **3**(15), 2015 – 2019.

Efros A. L and Efros A. L. 1982. Interband absorption of light in a semiconductor sphere. Sov. Phys. Semicond. **16,** 772 - 775.

Estruga M., Domingo C. and Ayllón J. A. 2010. Low-temperature and ambient-pressure sybthesis of TiO_2(B). Mater. Lett. **64**(21),2357 – 2359.

Ewald P. P. 1921. The calculation of optical and electrostatic grid potential. Ann. d. Phys. **64,** 253 - 287.

Exnar I., Kavan L., Haung S. Y. and Grätzel M. 1997. Novel 2v rocking-chair lithium battery based on nano-crystalline titanium dioxide. J. Power sources. **68**(2), 720 – 722.

Fahmi A., Minot C., Silvi B. and Causa M. 1993. Theoretical analysis of the structures of titanium dioxide crystals. Phys. Rev. B. **4,** 11717 - 11724.

Fang H. T., Liu M., Wang D. W., Sun T. Guan D. S., Li F. Zhou J., Sham T. K. and Cheng H. M. 2009. Comparison of the rate capability of nanostructured amorphous and anatase TiO_2 for lithium insertion using anodic TiO_2 nanotube arrays. Nanotechnology. **20**, 2257011 – 2257017.

Fattakhova-Rohlfing D., Wark M., Brezesinski T., Smarsly B. M. and Rathousky J. 2006. High Organized Mesoporous TiO_2 Films with Controlled Crystallinity: A Li-Insertion Study. Adv. Funct. Mater. **17,** 123 – 132.

Feist T. P. and Davies P. K. 1992. The soft chemical synthesis of TiO_2(B) from layered titanates. J. Solid State Chem. **101**(2), 275 – 295.

Fu L. J., Zhang T., Cao Q., Zhang H. P. and Wu Y. P. 2007. Preparation and characterization of three-dimensionally ordered mesoporous titania microparticles as anode material for lithium ion battery. Electrochem. Commun. **9**, 2140 – 2144.

Fujishima A. and Honda K. 1972 Electrochemical photolysis of water at a semiconductor electrode. Nature. **238,** 37 - 38.

Fukushima K. and Yamada I. 1989. Electrical properties of TiO_2 films deposited by a reactive-ionized cluster beam. J. Appl. Phys. **65,** 619 - 623.

Furukawa H., Hibino M. and Honna I. 2004. Electrochemical properties of nanostructured amorphous, sol-gel-synthesized TiO_2/acetylene black composite electrodes. J. Electrochem. Soc. **151,** A527 - A531.

Gao X. P., Lan Y., Zhu H. Y., Liu J. W., Ge Y. P., Wu F. and Song D. Y. 2005. Electrochemical Performance of Anatase Nanotubes Converted from Protonated Titanate Hydrate Nanotubes. Electrochem. Solid State Lett. **8**(1), A26 – A29.

Gao X.P., Zhu H.Y., Pan S.H., Lan Y., Wu F. and Song D.Y. 2004. Preparation and electrochemical characterization of anatase nanorods for lithium-insertion electrode material J. Phys. Chem. B. **108,** 2868 - 7282.

Gligor F. and de Leeuw S. W. 2006. Lithium diffusion in rutile structured titania. Solid State Ionics. **26 – 32**, 2741 – 2746.

Gong X. Q. and Selloni A. 2005. Reactivity of anatase TiO_2 nanoparticles: the role of the minority (001) surface. J. Phys. Chem. B. **10**9, 19560 – 19562.

Guo Y. G., Hu Y. S. and Maier J. 2006. Synthesis of hierarchically mesoporous anatase spheres and their application in lithium batteries. Chem.Commun. **26**, 2783 - 2785.

Guo Y. G., Hu Y. S., Sigle W. and Maier J. 2007. Superior electrode performance of nanostructured mesoporous TiO_2 (anatase) through efficient hierarchical mixed conducting networks. Adv. Mater. **19,** 2087 - 2091.

Haines J. and Leger J. M. 1993. X-ray diffraction study of TiO2 up to 49 GPa. Physica B: Phys. Condens. Matter. **192,** 233 - 237.

Haller G. L. and Resasco D. E. 1989. Metal-support interaction: Group VIII metals reducible oxides. Adv. Catal. **36,** 173 - 235.

Hansen J. –P and McDonald I. R. 1990. Theory of simple liquids. 2nd Edition, Academic Press: London.

Hardwick L. J., Holzapfel M., Novák P., Dupont L and Baudrin E. 2007. Electrochemical lithium insertion into anatase-type TiO_2: An in situ Raman microscopy investigation. Electrochim Acta. **52**(17), 5357 – 5367.

Hartman P., Lee D-K., Smarsly B. M. and Janek J. 2010. Mesoporous TiO_2: Comparison of Classical Sol-Gel and Nanoparticle Based Photoelectrodes for the Water Splitting Reaction. ACS Nano. **4**(6), 3147 – 3154.

He B. L., Dong B. and Li H. L. 2007. Preparation and electrochemical properties of Ag-modified TiO_2 nanotube anode material for lithium-ion battery. Electrochem. Commun. **9,** 425 - 430.

Henningsson A., Rensmol H., Sandell A., Siegbahn H., Sodergren S., Lindsrom H. and **H**agfeldt A. 2003. Electronic structure of electrochemically Li-inserted TiO_2 studied with synchrotron radiation electron spectroscopies.J. Chem. Phys. **118**, 5607 – 5612.

Henrich V. E. and Cox A. F. 1993. The surface science of metal oxides. Cambridge University press.

Hibino M., Abe K., Mochizuki M. and Miyayama M. 2004. Amorphous titanium oxide electrode for high-rate dischsrge and charge. J. Power Sources. **126,** 139 - 143.

Hirshes M. 2004. Nanoscale materials for energy storage. Mater. Sci. Eng., B **108,** 1 - 178.

Hosaka N., Sekiya T., Satoko C., and Kurita S. 1997. Optical properties of single crystal anatase TiO_2. J. Phys. Soc. Jpn. **66,** 877- 880.

Hou L., Wang P., Kong F., Park H., Kobiro K. and Ohama T. 2013. Mesoporous TiO_2 nanoparticles: A new material for biolistic bombardment. Phycological Research. **61**(1), 58 – 60.

Hu Y. S., Kienel L., Guo Y. G. and Maier J. 2006. High lithium electroactivity of nanometer-sized rutileTiO_2. Adv. Mater. Technol. **18,** 1421-1426.

Hwang K-J., Cho D. W., Lee J-W and Im C. 2012. Preparation of nanoporous TiO_2 electrodes using different mesostructured silica templates and improvement of the photovoltaic properties of DSSCs. New J. Chem. **36,** 2094 – 2100.

Jansen A. N., Kahaian A. J., Kepler K. D., Nelson P. A., Amine K., Dees D. W., Vissers D. R. and Thackeray M. M. 1999. Development of a high-power lithium-ion battery. J. Power Sources. **81/82,** 902 - 905.

Jiang C. H., Honma I., Kudo T. and Zhou H. S. 2007a. Nanocrystalline rutile TiO_2 electrode for high-capacity and high-rate lithium storage. Electrochem. Solid-State Lett. **10**(5)**,** A127 - A129.

Jiang C. H., Honma I., Kudo T. and Zhou H. S. 2007b. Particles size dependence of the lithium storage capacity and high rate performance of nanocrystalline anatase TiO_2 electrode. J. Power sources. Volume **166,** 239 - 243.

Jung H-G., Oh S. W., Ce J., Jayaprakash N. and Sun Y-K. 2009. Mesoporous TiO_2 nano networks: Anode for high power lithium battery applications. Electrochem. Commun. **11**(4), 756 – 759.

Kang J. W., Kim D. H., Mathew V., Lim J. S., Gim J. H. and Kim J. 2011. Particle Size Effect of Anatase TiO_2 Nanocrystals for Lithium-Ion Batteries. Batteries and Energy Storage. J. Electrochem. Soc. **158**(2), A59 – A62.

Kavan L., Fattakhova D. and Krtill P. 1999. Lithium insertion into mesoscopic and single-crystal TiO_2 (rutile) electrodes. J. Electrochem. Soc. **146,** 1375-1379.

Kavan L., Grätzel M., Gilbert S. E., Klemenz C. and Scheel H. J. 1996. Electrochemical and Photoelectrochemical Investigation of Single-Crystal Anatase. J. Am. Chem. Soc. **118,** 6716 - -6723.

Kavan L., Grazel M., Rathousky J. and Zukal A. 1996. Nanocrystalline TiO_2 (anatase) electrodes surface morphology, adsorption, and electrochemical properties. J. Electrochem. Soc. **143,** 394 - 400.

Kavan L., Kratochvilová K. and Grätzel M. 1995. Study of nanocrystalline TiO_2 (anatase) electrode in the accumulation regime. J. Electroanal. Chem. **394**, 93 – 102.

Kavan L., Rathouskỳ J., Grätzel M., Shklover V. and Zukal A. 2000. Surfactant-Templated TiO_2 (Anatase): Characteristic Features of Lithium Insertion Electrochemistry in Organized Nanostructures. **104,** 12012 – 12020.

Kavan L., Rathousky J., Gratzel M., Shklover V. and Zukal A. 2001. Mesoporous thin film TiO_2 electrodes. Microporous Mesoporous Mater. **44 -45,** 653 – 659.

Kerisit S., Rosso K. M., Yang Z. and Liu J. 2010. Computer Simulation of the Phase Stabilities of Lithiated TiO_2 Polymorphs. J. Phys. Chem. C. **114**(44), 19096 – 19107.

Kgatwane K. M. 2011. Atomistic simulation studies of lithiated MnO_2 nanostructures. (Thesis write-up for Msc to PhD conversion.)

Khomane R. B. 2011. Microemulsion-mediated sol-gel synthesis of mesoporous rutile TiO_2 nanoneedles and its performance as anode material for Li-ion batteries. J. Colloid Interface Sci. **356**(1), 369 – 372.

Kim J. and Cho J. 2007. Rate Charaxteristics of Anatase TiO**2** Nanotubes and Nanorods for Lithium Battery Anode Materials at Room Temperature. J. Electrochem. Soc. **154**(6), A542 – A546.

Kittel C. 1971. Introduction to Solid State Physics. John wiley, New York. 1- 766.

Knauth P. and Tuller H. L. 1999. Electrical and defect thermodynamics properties of nanocrystalline titanium dioxide. J. Appl. Phys. **85**, 897 – 902.

Koudriachova M. V., de Leeuw S. W. and Harrison N. M. 2002. Density-functional simulations of lithium intercalation in rutile. Phys. Rev. B Condens. Matter Mater Phys. **65,** 235423-1 – 235423-12.

Koudriachova M. V., de Leeuw S. W. and Harrison N. M. 2004a. First-principles study of H intercalation in rutile TiO_2. Phys. Rev. B Condens. Matter Mater Phys. **70**(16)**,** 165421-1 – 165421-5.

Koudriachova M. V., de Leeuw S. W. and Harrison N. M. 2004b. Orthorhombic distortion on Li intercalation in anatase. Phys. Rev. B Condens. Matter Mater Phys. **69,** 054106-1 – 054106-6.

Koudriachova M. V., Harrison N. M. and de Leeuw S. W. 2001. Effect of Diffusion on Lithium Ontercalation in Titanium Dioxide. Phys. Rev. Lett. **86**, 1275 – 1278.

Koudriachova M., Harrison N. M. and de Leeuw S. W. 2003. Diffusion of Li-ions in rutile. An ab initio study. Solid state Ionics. **157**(1-4), 35 – 38.

Kubiak P., Geserick J., Hüsing and Wohlfahrt-Mehrens M. 2008. Electrochemical performance of mesoporous TiO_2 anatase. J. Power Source. **175,** 510 – 516.

Kuhn A., Amandi R. and Carcia-Alvarado F. 2001. Electrochemical Lithium insertion in TiO_2 with the ramsdellite structure. J. Power Sources. **92,** 221 - 227.

Lafont U., Carta D., Mountjoy G., Chadwick A. V. and Lelder E. M. 2010. In situ structural changes upon electrochemical lithium insertion in nanosized anatase TiO_2. J. Phys. Chem. C,. **114,** 1372 - 1378.

Lai C., Zhang H. Z., Li G. R. and Gao X. P. 2011. Mesoporous polyaniline/TiO_2 microspheres with core-shell structure as anode materials for lithium ion battery. J. Power Sources. **196**(10), 4735 – 4740.

Lan Y., Gao X. P. Zhu H. Y., Zheng Z. F., Yan T. Y., Wu F., Ringe S. P. and Song D. Y. 2005. Titanate Nanotubes and Nanorods Prepared from Rutile Powder. Adv. Funct. Mater. **15**(8), 1310 – 1318.

Latroche M., Brohan R., Marchand R. and Tournoux M. 1989. New hollandite oxides:TiO_2(H) and $K_{0.06}TiO_2$. J. Solid State Chem. **81,** 78 - 82.

Lazzeri M., Vittadini A. and Selloni A. 2001. Structure and energetics of stoichiometric TiO_2 anatase surfaces. Phys. Rev. B. **63**, 155409-1 – 155409-9.

Lee D. -H., Park J. –G., Choi K. J., Choi H. –J. and Kim D. –W. 2008. Preparation of Brookite-Type TiO_2/Carbon Nanocomposite Electrodes for Application to Li Ion Batteries. Eur. J. Inorg. Chem. **2008,** 878 – 882.

Li J. R., Tang Z. L. and Zhang Z. T. 2005. Preparation and novel lithium intercalation properties of titanium oxide nanotubes. Electrochem. Solid-State Lett. **8,** A316 - A319.

Liang Y., Gan S., Chambers S. A. and Altman E.I. 2001. Surface structure of anatase TiO_2(001): Reconstruction, atomic steps, and domains. Phys. Rev. B. **63,** 235402-1 – 235402-2.

Lindstrom H., Sodergren S., Solbrand A., Rensmo H., Hjelm J., Hagfeldt A. and Lindquist S. E. 1997. Li+ ion insertion in (anatase).2.Voltammetry on nanoporous films. J. Phys. Chem. B. **101,** 7717 - 7722.

Linsebigler A. L., Lu G., Yates J. T. 1995. Photocatalysis on TiO_2 surfaces: Principles, Mechanisms and Selected Results. Chem. Rev. **95,** 735- 758.

Liu B., Deng D., Lee J. Y. and Aydil E. S. 2010a. Oriented Single-crystalline TiO_2 nanowires on titanium foil for lithium ion batteries. J. Mater. Res. **25**(8), 1588 – 1594.

Liu G., Wang L., Yang H. G., Cheng H-M. and Lu G. Q. 2010b. Titania-based photocatalysts-crystal growth, doping and heterostructruring. J. Mater. Chem. **20,** 831 – 843.

Liu H., Bi Z., Sun X-G., Unocic R. R., Paranthaman M. P., Dai S. and Brown G. M. 2011. Mesoporous TiO_2-B Microspheres with Superior Rate Performance for Lithium Ion Batteries. Adv. Mater. **23**, 3450 – 3454.

Liu S, Li J, Shen Q, Cao Y, Guo X, Zhang G, Feng C, Zhang J, Liu Z, Steigerwald ML, Xu D and Nuckolls C. 2009. Mirror-image photoswitching of individual single-walled carbon nanotube transistors coated with titanium dioxide. Angew Chem Int Ed, **48,** 4759 – 4762.

Liu S., and Jaroniec M. 2011. Anatase TiO_2 with dominant high-energy {001} facets: Synthesis, properties and applications. Chem Mater, **23,** 4085 – 4093.

Liu S.,Jia H., Han L., Wang J., Gao P., Yang J. and Che S. 2012b. Nanosheet Constructed Porous TiO_2-B for Advanced Lithium Ion Batteries. Adv. Mater. **24,** 3201 – 3204.

Liu S-H. and Syu H-R. 2012a. One-step fabrication of N-doped mesoporous TiO_2 nanoparticles by self-assembly for photocatalytic water splitting under visible light. Appl. Energy. **100,** 148 – 154.

Liu Z., Hong L. and Guo B. 2005. Physicochemical and electrochemical characterization of anatase titanium dioxide nanoparticles. J. Power Sources. **143**(1-3), 231 – 235.

Macklin W. J. and Neat R. J. 1992. Performance of titanium dioxide-based cathodes in a lithium polymer electrolyte cell. Solid State Ionics. **53-56,** 694 – 700.

Mackrodt W. C. 1999. First Principles Hartree-Fock Description of Lithium Insertion in Oxides. J. Solid State Chem. **142,** 428 – 439.

Maphanga R. R., Ngoepe P. E., Sayle T. X. T. and Sayle D. C. 2010. Amorphisation and recrystallisation study of lithium insertion in manganese dioxide. Phys. Chem.Chem. Phys. **13,** 1307 -1313.

Marchand R., Brohan L. and Tournoux M. 1980. TiO_2(B) a new form of titanium dioxide and the potassium octatitanate $K_2Ti_8O_{17}$. Mater. Res. Bull. **15**(8), 1129 – 1133.

Marchand R., Brohan R. and Tournoux M. 1980. TiO_2 (B) a new form of titanium dioxide and the potassium octatitanate $K_2Ti_8O_{17}$. Mater. Res. Bull. **15,** 1129 - 1133.

Matsui M. and Akoagi M., 1991. Molecular dynamics simulation of the structural and physical properties of the four polymorphs of TiO_2. Mol. Simulat. **6,** 239 - 245.

Moriguchi I., Hidaka R., Yamada H., Kudo T., Murakami H. and Nakashima N. 2006. A mesoporous nanocomposite of TiO_2 and carbon nanotubes as a high-rate Li-intercalation electrode material. Adv. Mater. **18,** 69 - 73.

Murphy D. W., Cava R. J., Zahurak S. M. and Santoro A. 1983. Ternary Li_xTiO_2 phases from insertion reactions. Solid State Ionics. **9-10,** 413 – 417.

Muscat J., Swammy V. and Harison N. M. 2002. First-principles calculations of the phase stability of TiO_2. Phys. Rev. B Condens. Matter mater Phys. **65**(22), 224112-1 – 224126-15.

Nazer L. F., Goward G., Leroux F., Duncan M., Huang H., Kerr T. and Gaubicher J. 2001. Nanostructures materials for energy storage. Int. J. Inorg. Mater. **3,** 191 - 200.

Noailles L. D., Johnson C. S., Vaughey J. T. and Thackeray M. M. 1999. Lithium insertion into hollandite-type TiO_2. J. Power Sources. **81/82** 259 - 263.

Nose S. 1984. A molecular dynamics method for simulations in the canonical ensemble. Mol. Phys. **52,** 255 – 268.

Nuspl G., Yoshizawa K. and Yamabe T. 1997. Lithium intercalation in TiO_2 modifications. J. Mater. Chem. **7** (12), 2529 – 2536.

O'Regan B. and Gratzel M. 1991. A low-cost, high-efficiency solar cell based on dye-sensitized colloidal TiO_2 films. Nature. **353,** 737 – 740.

Ogata T., Ogasawara K., Munetoh S. and Motooka T. 2009 to be published. Molecular dynamics simulations of void Morphology in crystalline Silicon: Temperature dependence.

Oh S. W., Park S-H and Sun Y-K. 2006. Hydrothermal synthesis of nano-sized anatase TiO_2 powders for lithium secondary anode materials. J. Power Sources. **161**(2), 1314 – 1318.

Ohzuku T., Kodama T. and Hirai T. 1985. Electrochemistry of anatase titanium dioxide in lithium nonaqueous cells. J. Power Sources. **14** 153 – 166.

Ohzuku T., Takehara Z. and Yoshizwa S. 1979. Nonaqueous lithium/titanium dioxide cell. Electrochim. Acta. **24**(2)**,** 219 - 222.

Okuya M., Nakade K. and Kaneko S. 2002. Porous TiO_2 thin films synthesized by a spray pyrolysis deposition (SPD) technique and their application to dye-sensitized solar cells. Sol Energy Mater. Sol. Cells. **70,** 425 – 435.

Ollis D. F., Pelizzetti E. and Serpone N. 1989. Heterogeneous photocatalysis in the environment: Application to water purification. In photocatalysis, fundamentals and applications. John Wiley & Sons: New York. 603 - 637.

Olsen J. S., Gerward L. and Jiang J. Z. 1999. On the rutile/ α-PbO_2-type phase boundary of TiO_2. J. Phys. Chem. Solids. **60** 229 - 233.

Olson C. L. Nelson F. and Islam M. S. 2006. Defect Chemistry, Surface Structures and Lithium Insertion in Anatase TiO_2. J. Phys. Chem. B **110,** 9995 – 10001.

Park N.-G, van de Lagemaat J. and Frank A. J. 2000. Comparison of Dye-Sensitized Rutile- and Anatase-Based TiO_2 Solar Cells. J. Phys.l Chem. B. Volume **104,** 8989 - 8994.

Parry D. E. 1975. The electrostatic potential in the surface region of an ionic crystal. Surf. Sci. **49,** 433 - 440.

Patra A. K., Das S. K. and Bhaumik A. 2010. Self-assembled mesoporous TiO_2 spherical nanoparticles by a new templating pathway and its enhanced photoconductivity in the presence of an organic dye. J. Mater. Chem. **21,** 3925 – 3930.

Payne M. C., Teter M. P., Allan D. C., Arias T. A. and Joannopoulos J. D. 1992. Interactive minimization techniques for ab initio total-energy calculations: molecular dynamics and conjugate gradients. Rev Mod Phys 64 (4), 1045 – 1097.

Peng T-Y., Fan K., Zhao D., Yu L-J. and Li R-J. 2012. Effects of Oxide Modifications on Photoelectrochemical Properties of Mesoporous TiO_2 Nanoparticles Electrodes for Dye-Sensitized Solar Cells. Chin. J. Chem. Phys. **25**(5), 609 – 616.

Poizot P., Laruelle S., Grugeon S., Dupont L. and Tarascon J-M. 2000. Nano-sized transition-metal oxides as negative-electrode materials for lithium-ion batteries. Nature **407**, 496 – 499.

Qiao H., Tao D., Wang Y., Cai Y., Huang F., Tang X., Wei J. and Wei Q. 2010. Electrochemical charge storage of flowerlike rutile TiO_2 nanorods. Chem. Phys. Lett. **490**(4-6), 180 – 183.

Reddy M. A., Kishore M. S., Pralong V., Varadaraju U. V. and Raveau B. 2007. Lithium intercalation into nanocrystalline brookite TiO_2. Electrochem. Solid-State Lett. **10,** A29 - A31.

Reddy M. A., Kishore M. S., Pralong V., Caignaert V., Varadaraju U. V. and Raveu B. 2006. Room temperature synthesis and Li insertion into nanocrystalline rutile TiO_2. Electrochem. Commun. **8,** 1299 - 1303.

Reddy M. A., Pralong V., Varadaraju U. V. and Raveau B. 2008. Crystallite Size Constraints on Lithium Insertion into Brookite TiO_2. Electrochem. Solid-State Lett. **11**, A132 – A134.

Ren Y., Hardwick L. J. and Bruce P. G. 2010. Lithium intercalation into mesoporous anatase with an ordered 3D pore structure. Angew. Chem. Int. Ed. **49**, 2570 - 2574.

Reyes-Coronado, Rodriguez-Gattorno G., Espinosa-Pesqueira M. E., Cab C., deCoss R. and Oskam G. 2008. Phase-pure TiO_2 nanoparticles: anatase, brookite and rutile. Nanotechnology. **19**, 145605 (1 – 10).

Sanjines R., Tang H., Berger H., Gozzo F., Margaritondo G. and Levy F. 1994. Electronic structure of anatase TiO_2 oxide. J. Appl. Phys. **75,** 2945 - 2951.

Saravanan K., Ananthanarayanan K. and Balaya P. 2010. Mesoporous TiO_2 with high packing density for superior lithium storage. Energy Environ. Sci. **3**, 939 – 948.

Sayle D. C. and Johnston R. L. 2003. Evolutionary techniques in atomistic simulation: thin films and nanoparticles. Curr. Opin. Solid State Mater. Sci. **7,** 3 - 12.

Sayle D. C. and Sayle T. X. T. 2007. High-Pressure Crystallisation of TiO_2 Nanoparticles. J. Comput. Theor. Nanosci. **4,** 299 – 308.

Sayle D. C. and Watson G. W. 2001a. Structural exploration of thin-film oxide interfaces via "simulated amorphisation and recrystallisation. Surf. Sci. **437**, 97 – 107.

Sayle D. C. and Watson G. W. 2001b. The Atomistic structures of MgO/SrTio3(001) and BaO/SrTiO3(001) using simulated amorphisation and recrystallisation. J. Phys. Chem. B, 1**05**, 5506 – 5514.

Sayle D. C. and Watson G. W. 2002a. Amorphisation and recrystallisation of an MgO cluster supported on BaO(100). J. Phys. Chem. B. **106,** 3916 – 3925.

Sayle D. C. and Watson G. W. 2002b. Atomistic structures of 25000-Atoms oxide nanoparticles supported on an oxide substrate. J. Phys. Chem. B. **106** 10793 - 10807.

Sayle D. C. Maicaneanu S. A. and Watson G. W. 2002c. Atomistic models for CeO_2 (111), (110) and (100) nanoparticles, supported on yttrium stabilised zirconia. J. Am. Chem. Soc. **124,** 11429 - 11439.

Sayle T. X. T., Catlow C. R. A., Maphanga R. R., Ngoepe P. E. and Sayle D. C. 2005. Generating MnO_2 nanoparticles using simulated amorphisation and recrystallisation. J. Am. Chem. Soc. **127,** 12828 - 12837.

Sayle T. X. T., Catlow C. R. A., Maphanga R. R., Ngoepe P. E. and Sayle D. C. 2006. Evolving microstructure in MnO_2 using Amorphisation and recrystallisation. J.Crys. Growth. **294,** 118 – 129.

Sayle T. X. T., Maphanga R. R., Ngoepe P. E. and Sayle D. C. 2009a. Predicting the electrochemical properties of MnO_2 nanomaterials used in rechargeable Li batteries; Simulating nanostructure at the atomistic level. J. Am. Chem. Soc. **131,** 6161 - 6173.

Sayle T. X. T., Ngoepe P. E. and Sayle D. C. 2009b. Simulating mechanical deformation in nanomaterials with application for energy storage in nanoporous architectures. Am. Chem. Soc. Nano. **3,** 3308 - 3314.

Sayle T. X. T., Parker S. C. and Sayle D. C. 2004. Shape of CeO_2 nanoparticles using simulated Amorphisation and recrystallisation. Chem.Commun. **21,** 2438 – 2439.

Sayle T. X. T., Parker S. C. and Sayle D. C. 2006. Ionic conductivity in nano-scale CeO_2/YSZ heterolayers. J. Mater. Chem. **16,** 1067 – 1081.

Sayle T.X.T., Catlow C. R. A., Sayle D. C., Parker S. C. and Harding J. H. 1993. Computer simulation of thin heteroepitaxial ceramic interfaces using a near-coincidence-site lattice theory. Phil. Mag. **A**, 68, 565 – 573.

Sekiya T., Ichimura K., Igarashi M. and Kurita S. 2000. Absorption spectra of anatase single crystals heat-treated under oxygen atmosphere. J. Phys. Chem. Solids. **61,** 1237 - 1242.

Sekiya T., Igarashi M., Kurita S., Takekawa S. and Fujisawa M. 1998. Structure dependence of reflection spectra of TiO_2 single crystals. J. Electron Spectrosc. Relat. Phenom. **92,** 247 - 250.

Simons P. Y. and Dachille F. 1967. The structure of TiO_2II, a high-pressure phase of TiO_2. Acta Crystallogr. **23,** 334 - 336.

Smith W. and Forster T. R. 1996. http://www.dl.ac.uk/TCSC/Software/DLPOLY.

Södergren S., Siegbahn H., Rensmo H., Lindström H., Hagfeldt A. and Lindquist S-E. 1997. Lithium Intercalation in Nanoporous Anatase TiO_2 Studied with XPS. J. Phys. Chem. B **101,** 3087 – 3090.

Sorantin P. I. and Schwarz K. 1992. Chemical bonding in rutile-type compounds. Inorg. Chem. **31,** 567 - 576.

Stashans A., Lunell S., Bergström R., Hagfeldt A. and Lindquist S-E. 1996. Theoretical study of lithium intercalation in rutile and anatase. Phys. Rev. B **53,** 159 – 170.

Su X., Wu Q-L., Zhan X., Wu J., Wei S. and Guo Z. 2012. Advanced titania nanostructures and composites for lithium ion battery. J. Mater Sci. **47,** 2519 – 2534.

Sudant G., Baudrin E. Larcher D. and Tarascon J. M. 2005. Electrochemical lithium reactivity with nanotextured anatase-type. J. Mater. Chem. **15**(12), 1263 – 1269.

Sun X. D., Ma C. L., Wang Y. D. and Li H. D. 2004. Ai_{13}-pillared anatase TiO_2 as a cathode for a lithium battery. Nanotechnology. **15,** 1535 - 1538.

Sushko M. L., Rosso K. M. and Liu J. 2010. Size Effects on Li+/Electron Conductivity in TiO_2 Nanoparticles. J. Phys. Chem. Lett. **1**(13), 1967 – 1972.

Sutton A. P. and Balluffi R. W. 1987. Overview no. 61 on geometric criteria for low interfacial energy. Acta Metal. **35** (9), 2177 – 2201.

Tang H. and Levy F. 1994a. Electronic properties of anatase TiO_2 Investigated by electric and optical measurements on single crystals and thin films. Ecole Polytechnique Federale De Lausanne.

Tang H., Levy F., Berger H. and Schmit P. E. 1995. Urbach tail of anatase TiO_2. Physical Review B. Condens. Matter Mater. Phys. **52,** 7771 - 7774.

Tang H., Prasad K., Sanjines R., Schimit P. E. and Levy 1994b Electrical and optical properties of TiO_2 anatase thin films. J. Appl. Phys. **75,** 2042 - 2047.

Tang J. and Endo J. 1993. P-T boundary of α-PbO_2 type and baddeleyite type high-pressure phases of titanium dioxide. J. Am. Ceram. Soc. **76,** 796 - 798.

Tang Y., Yang L. Qiu Z. and Huang J. 2009. Template-free synthesis of mesoporous spinel lithium titanate microspheres and their application in high-rate lithium ion batteries. J. Mater. Chem. **19**, 5980 – 5984.

Tsuji T., Nakanishi M., Mizuki T., Tsuji M., Doi T., Yahiro T. and Yamaki J. 2009. Preparation of nano-sized functional materials using laser ablation in liquids. **255**(24), 9626 – 9629.

Van de Krol R., Goossens A. and Schoonman J. 1999. Spatial Extent of Lithium Intercalation in Anatase TiO_2. J. Phys. Chem. B **103,** 7151 – 7159.

Vegard L. 1916. Results of crystal analysis. Philos. Mag. **32,** 505 - 515.

Wagemaker M., Borghols W. J. H. and Mulder F. M. 2007. Large impact of particle size on insertion reactions. A case for anatase Li_xTiO_2. J. Am. Chem. Soc. **129,** 4323 - 4327.

Wand D., Choi D., Yang Z., Viswanathan V.V. Nie Z., Wang C., Song Y., Zhang J. and Liu J. 2008. Synthesis and Li-Ion Insertion Properties of High Crystalline Mesoporous Rutile TiO_2. Chem. Mater. **20**, 3435 – 3442.

Wang J., Polleux J., Lim J. and Dunn B. 2007. Pseudocapacitive Contributions to Electrochemical Energy Storage in TiO_2 (Anatase) Nanoparticles. J. Phys. Chem. C **111**(40), 14925 – 14931.

Wang J., Wang J., Wang Z. and Zhang F. 2009. A Template-Free Method toward Urchin-Like Polyaniline Microspheres. Macromol. Rapid Commun. **30** (8), 604 – 608).

Wang K., Wei M., Morris M. A., Zhou H. and Holmes J. D. 2007. Mesoporous Titania Nanotubes: Their Preparation and Application as Electride Materials for Rechargeable Lithium Batteries. Adv. Mater. **19**(19), 3016 – 3020.

Wang Q., Wen Z. and Li J. 2006. Solvent-Controlled Synthesis and Electrochemical Lithium Storage of One-Dimensional TiO_2 Nanostructures. Inorg. Chem. **45**(17), 6944 – 6949.

Wang Q., Wen Z. H. and Li J. H. 2006. A hybrid supercapacitor fabricated with a carbon nanotube cathode and a TiO_2-B nanowire anode. Adv. Funct. Mater. **16,** 2141 - 2146.

Wang X., Xie K., Li J., Lai Y., Zhang Z. and Liu Y. 2011. Synthesis and electrochemical performance of TiO_2-B as anode material. J. Cent. South Univ. Technol.(Engl. Ed.) **18**(2), 406 – 410.

Wang Z. Y., Liu S. Z., Chen G. and Xia D. G. 2007. Preparation and Li-intercalation properties of mesoporous anatase-TiO_2 spheres. Electrochem. Solid State Lett **10**(3)**,** A77 - A80.

Wei X., Liu J., Chua Y. Song J. and Liu X. 2011. Fabrication of O (Dye)-Terminated Anatase TiO_2 Nanosheets for Dye Sensitized Solar Cells. Energy Environ. Sci. **4,** 2054 - 2057.

Wessel C., Zhao L., Urban s., Ostermann R., Djerdj I., Smarsly B. M., Chen L., Hu Y-S. and Sallard S. 2011. Ionic-Liquid Synthesis Route of TiO_2(B) Nanoparticles for Functionalized Materials. Chem. Eur J. **17**(3), 775 – 779.

Wilhelm O., Pratsinis S. E., de Chambrier E., Crouzet M. and Exnar I. 2004. Electrochemical performance of granulated titania nanoparticles. J. Power Sources. **134**(2), 197 – 201.

Wu Q. L. and Rankin S. E. 2011. Tuning the Mesopore Size of Titania Thin Films Using a Polymeric Swelling Agent. J. Phys. Chem. C **115**(24), 11925 – 11933.

Wu Q. L., Subramanian N. and Rankin S. E. 2011. Hierarchically Porous Titania Thin Film Prepared by Controlled Phase Separation and Surfactant Templating. Langmuir. **27**(15), 9557 – 9566.

Yamada H., Yamato T., Moriguchi I. and Kudo T. 2004. Porous TiO_2 (anatase) electrodes for high-power batteries. Chem. Lett. **33,** 1548 - 1549.

Yan J., Song H., Yang S. and Chen X. 2009. Effect of heat treatment on the morphology and electrochemical performance of TiO_2 nanotubes as anode materials for lithium-ion batteries. **118**(2-3), 367 – 370.

Yang Z., Choi D., Kerisit S., Rosso K. M., Wang D., Zhang J., Graff G. and Liu J. 2009. Nanostructures and lithium electrochemical reactivity of lithium titanites and titanium oxides: A review. J. Power Sources. **192**, 588 – 598.

Yang H. G., Sun C. H., Qiao S. Z., Liu J. Z. Smith S. C. Cheng H. M. and Lu G. Q. 2008. Anatase TiO_2 Single crystals with a large percentage of reactive facts. Nature **453**, 638 – 641.

Yang M. –C, Lee Y. –Y, Xu B. Powers K. and Meng Y. S. 2012. TiO_2 flakes as anode materials for Li-ion batteries. J. Power Sources. **207**, 166 – 172.

Yang Z., Choi D., Kerisit S., Rosso K. M., Wang D., Zhang J., Graff G. and Liu J. 2009. Nanostructures and lithium electrochemical reactivity of lithium titanites and titanium oxides: A review. J. Power Sources. **192,** 588 – 598.

Yoon S. and Manthiram A. 2011. Hollow Core-Shell Mesoporous TiO_2 Spheres for Lithium Ion Storage. J. Phys. Chem. **115**(19), 9410 – 9416.

Zachau-Christiansen B., West K., Jacobsen T. and Atlung S. 1988. Lithium insertion in different TiO_2 modifications. Solid State Ionics. **28-30,** 1176 - 1182.

Zaslavskii A. I. and Tolkachev S. S. 1952. The structure of alpha modification of lead dioxide. Zh. Fiz. Khim. **26,** 743 – 752.

Zhang H. and Banfield J. 2000. Understanding polymorphic phase transformation behaviour during growth of nanocrystalline aggregates: Insights from TiO_2. J. Phys. Chem. B **104** (15), 3481 – 3487.

Zhou H. S., Li D. L., Hibino M. and Honma I. 2005. A self-ordered, crystalline-class, mesoporous nanocomposite for use as a lithium-based storage device with both high power and high energy densities. Angew. Chem. Int. Edit. **44,** 797 - 802.

Zhou Y-K., Cao L., Zhang F-B., He B-L. and Li H-L. 2003. Lithium Insertion into TiO_2 Nanotube Prepared by the Hydrothermal Process BATTERIES, FUEL CELLS AND ENERGY CONVERSION. J. Electrochem. Soc. **150** (9), A1246 – A1249.

Zhu G-N., Wang C-X. and Xia Y-Y. 2011. Structural transformation of layered hydrogen trititanate ($H_2Ti_3O_7$) to TiO_2(B) and its electrochemical profile for lithium-ion intercalation. J. Power Sources. **196** (5), 2848 – 2853.

Zukalova M., Kalbac M., Kavan L., Exnar I. and Graetzel M. 2005. Pseudocapacitive lithium storage in TiO_2(B). Chem. Mater. **17** (5)**,** 1248 - 1255.

Appendix A

Publications

M. G. Matshaba, P. E Ngoepe and D. C Sayle, Generating nanostructures of titanium dioxide (TiO_2) using armophisation recrystallisation method, Materials Modelling Centre, Department of Physics, University of Limpopo (Turfloop Campus), SA. To be published soon.

M. G. Matshaba, P. E Ngoepe and D. C Sayle, Atomistic simulation of lithiated nanostructured of titanium dioxide (TiO_2), Materials Modelling Centre, Department of Physics, University of Limpopo (Turfloop Campus), SA. To be published soon.

Appendix B

Papers presented at the conferences

Local

M.G. Matshaba*, P. E. Ngoepe* and D. C. Sayle[#] "Atomistic simulations studies of TiO_2 nanostructures." Centre for High Performance Competing (CHPC) Meeting 2010 December 07 – December 09. Westin Grand Hotel, Cape Town, South Africa (SA).

***** *Materials Modelling Center, School of Physical and Mineral Sciences, University of Limpopo, SA.*

[#] *Cranfield University, Defence Academy of the United Kingdom, Shrivenham, Swindon, UK.*

M. G. Matshaba*, P. E. Ngoepe* and D. C. Sayle[#] "Amorphisation and recrystallisation of pure and lithiated titanium dioxides". A 60th birthday conference in honour of Prof. P. E. Ngoepe 2013 January 8th – 9th. R40 University of Limpopo Turfloop Campus, South Africa (SA).

* *Materials Modelling Center, School of Physical and Mineral Sciences, University of Limpopo, SA.*

[#] *Cranfield University, Defence Academy of the United Kingdom, Shrivenham, Swindon, UK.*

International

Malili Matshaba*, Phuti Ngoepe* and Dean Sayle[#] "Atomistic simulation studies of nanostructured TiO_2" American Physical Society (APS) March Meeting 2012 February 27 - March 2. Boston Convention Center, Massachusetts, United States of America (USA).

***** *Materials Modelling Center, School of Physical and Mineral Sciences, University of Limpopo, SA.*

[#] *Cranfield University, Defence Academy of the United Kingdom, Shrivenham, Swindon, UK.*

M.G. Matshaba*, P. E. Ngoepe* and D. C. Sayle[#] "Atomistic simulations studies of TiO_2 nanostructures" International Battery Association (IBA) Meeting 2011 April 12 – April 15. One and Only, Cape Town, South Africa (SA).

* *Materials Modelling Center, School of Physical and Mineral Sciences, University of Limpopo, SA.*

[#] *Cranfield University, Defence Academy of the United Kingdom, Shrivenham, Swindon, UK.*

Phuti Ngoepe*, Malili Matshaba* and Dean Sayle[#] "Atomistic Simulation Studies of the Bulk Lithiated TiO_2" American Physical Society (APS) March Meeting 2013 March 18 – March 22. Baltimore, Maryland, United States of America (USA).

* *Materials Modelling Center, School of Physical and Mineral Sciences, University of Limpopo, SA.*

[#] *Cranfield University, Defence Academy of the United Kingdom, Shrivenham, Swindon, UK.*

Appendix C

X-ray diffractions of unlithiated and lithiated nanostructures combined in the same axis.

C1: X-ray diffractions of nanosphere

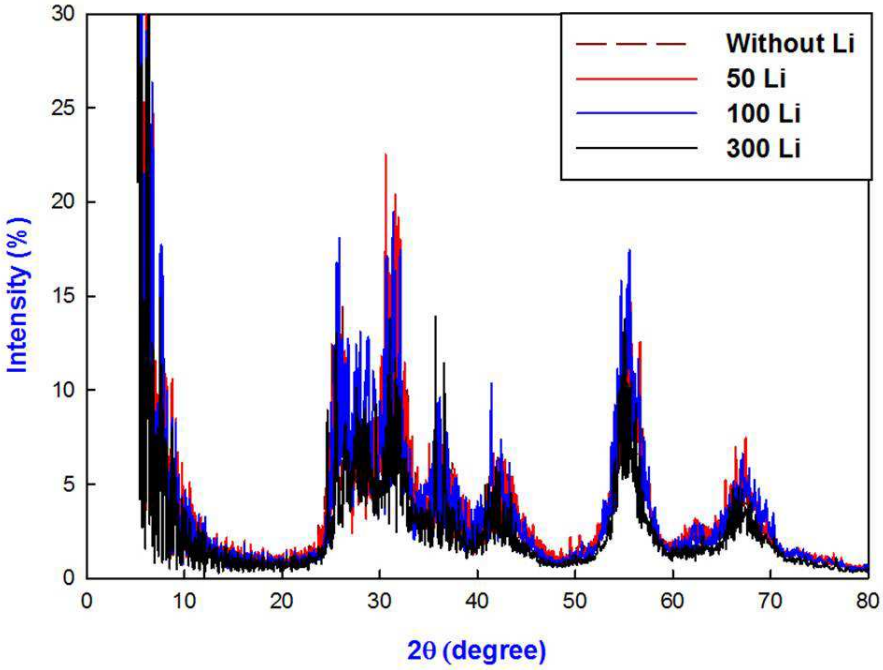

C2: X-ray diffractions of nanosheet

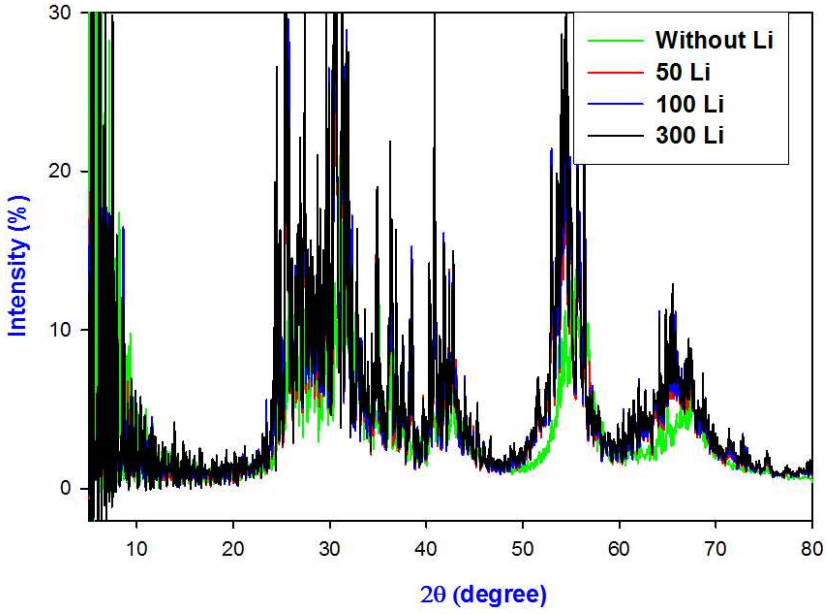

C3: X-ray diffractions of nanoporous (Lattice box 66Å)

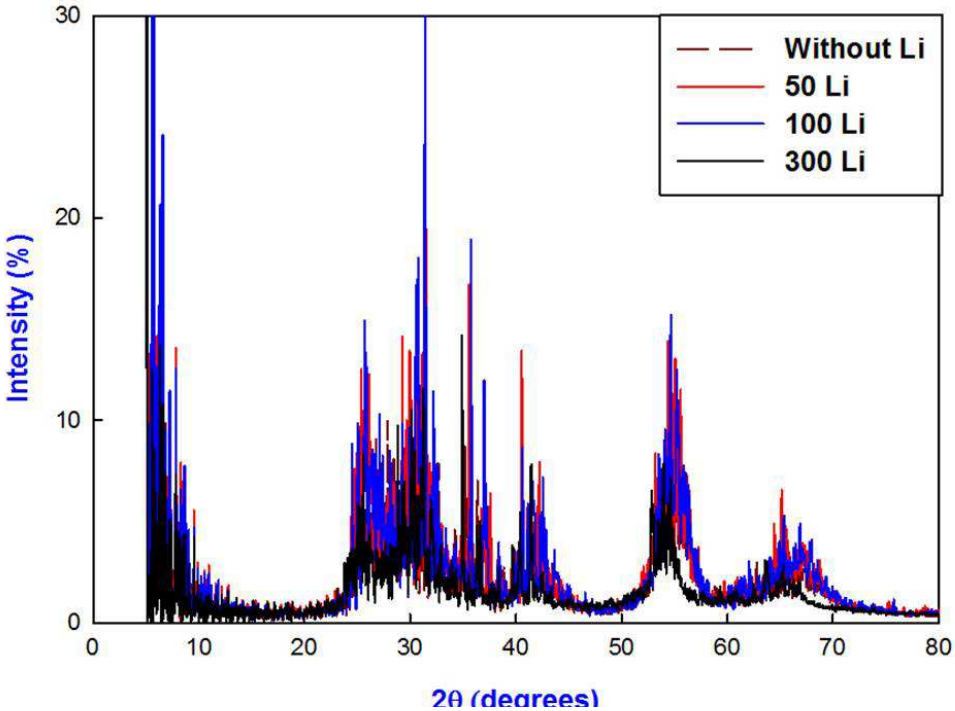

C4: X-ray diffractions of bulk

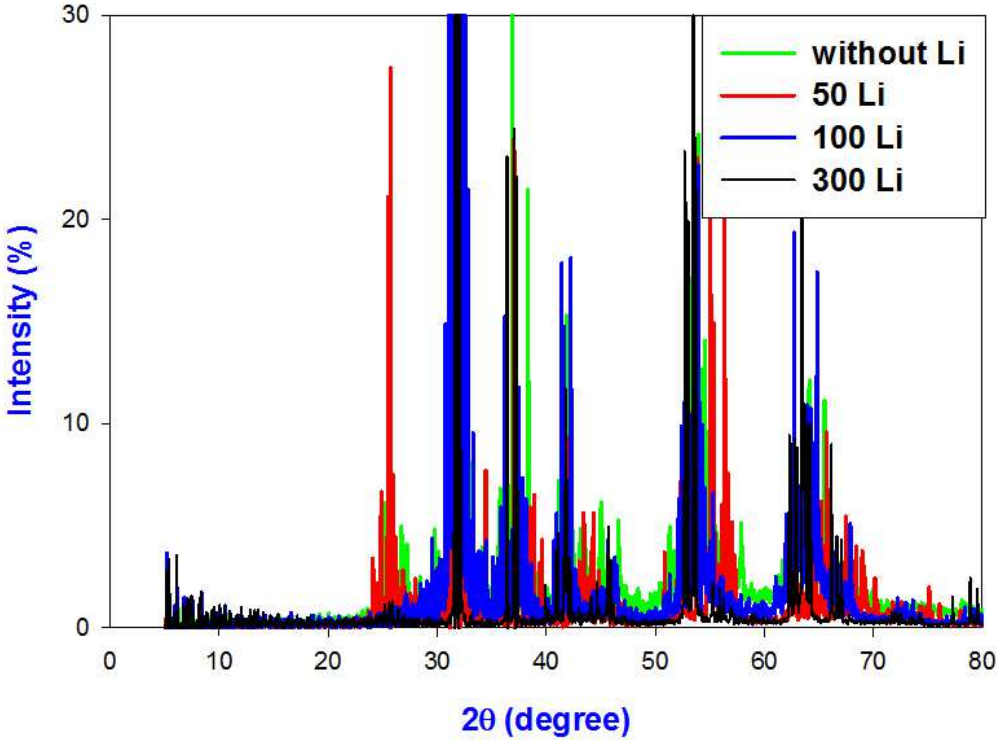

Appendix D

Snapshots showing the progress of nucleation and crystal growth.

D1:TiO_2 nanosphere.

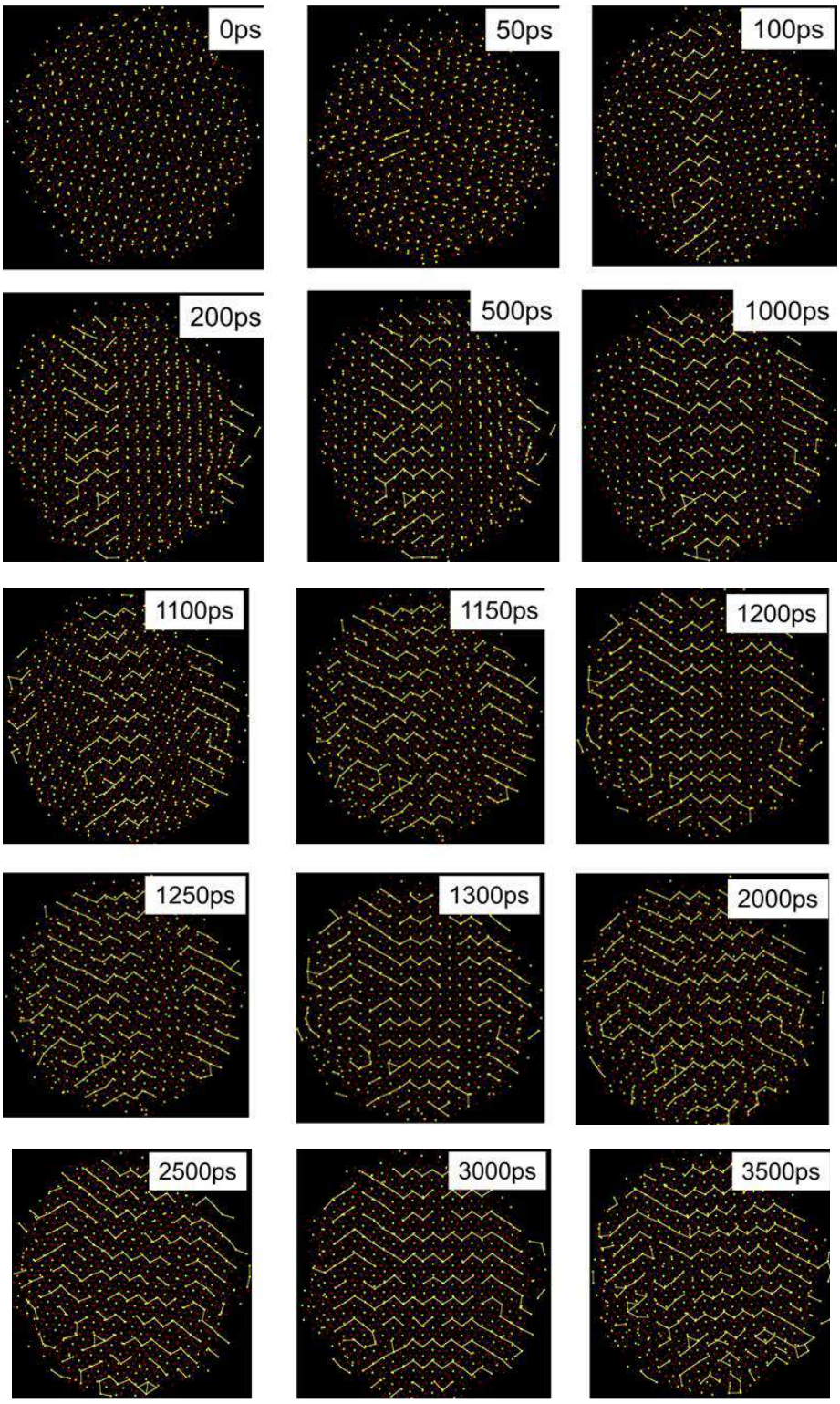

D2:TiO_2 nanosphere with 300 lithium atoms.

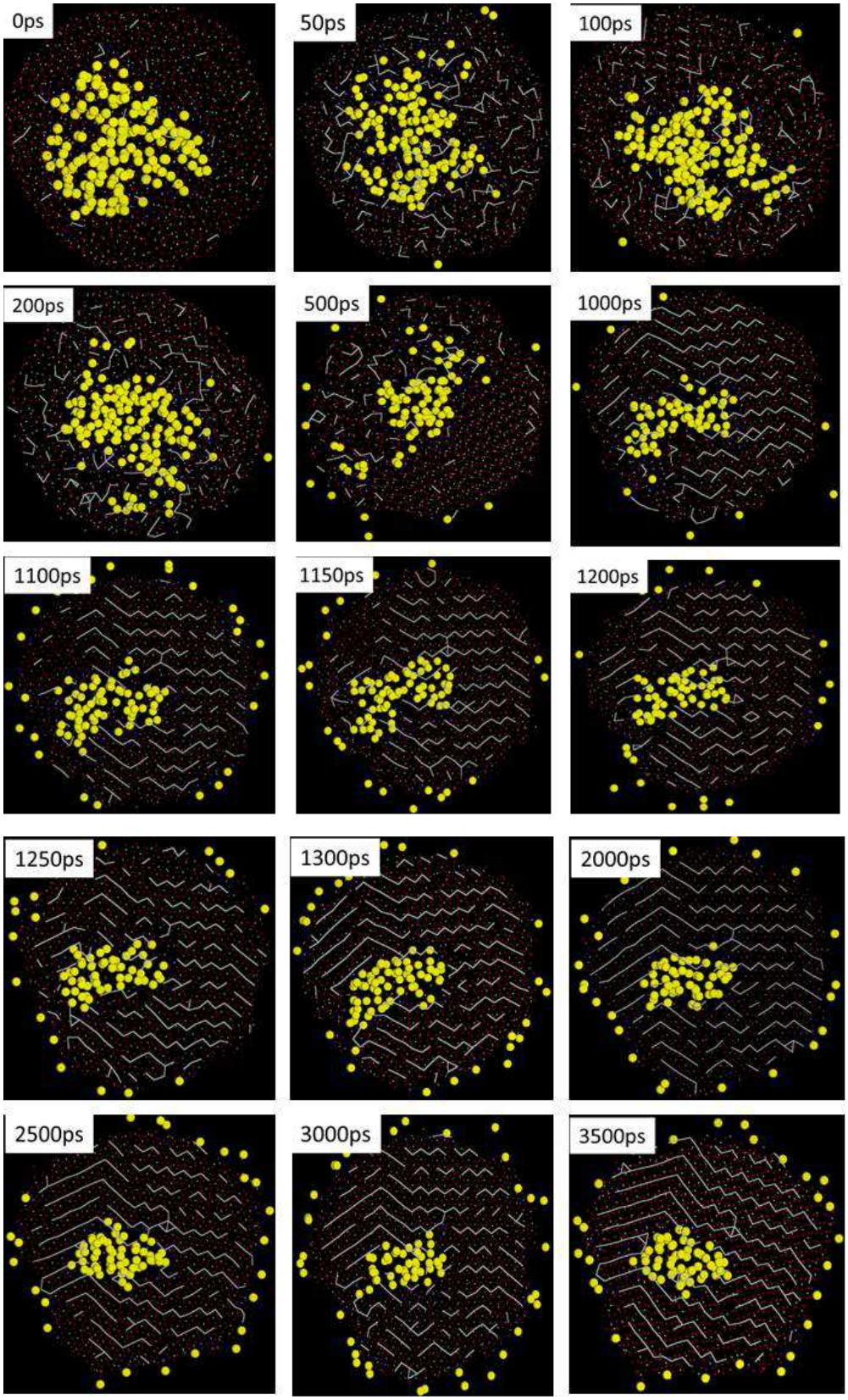

Appendix E

Radial distribution functions of lithiated nanoporous and bulk after recrystallisation and during cooling

E1: RDFs of the TiO_2 nanoporous structure (related to 66 Å) with 50 lithium atoms after recrystallisation at 2000 K.

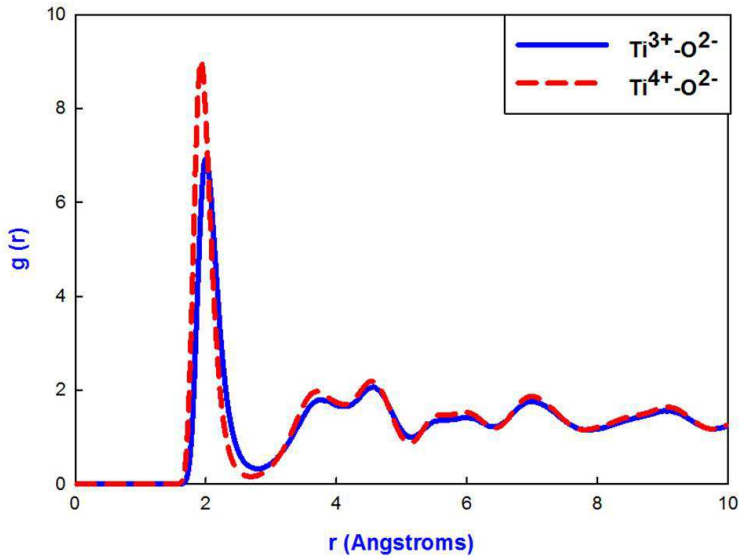

E2: RDFs of the TiO_2 nanoporous structure (related to 66 Å) with 100 lithium atoms after recrystallisation at 2000 K.

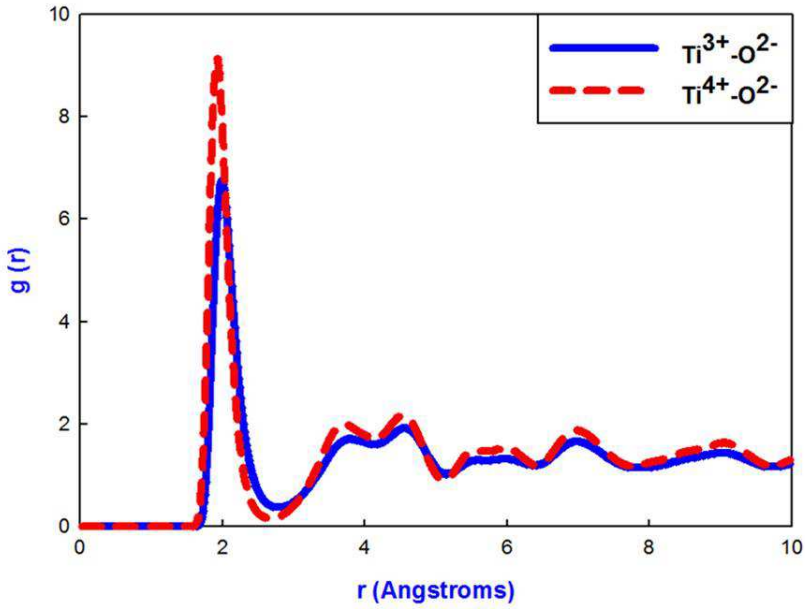

E3: RDFs of the TiO_2 nanoporous structure (related to 66 Å) with 300 lithium atoms after recrystallisation at 2000 K.

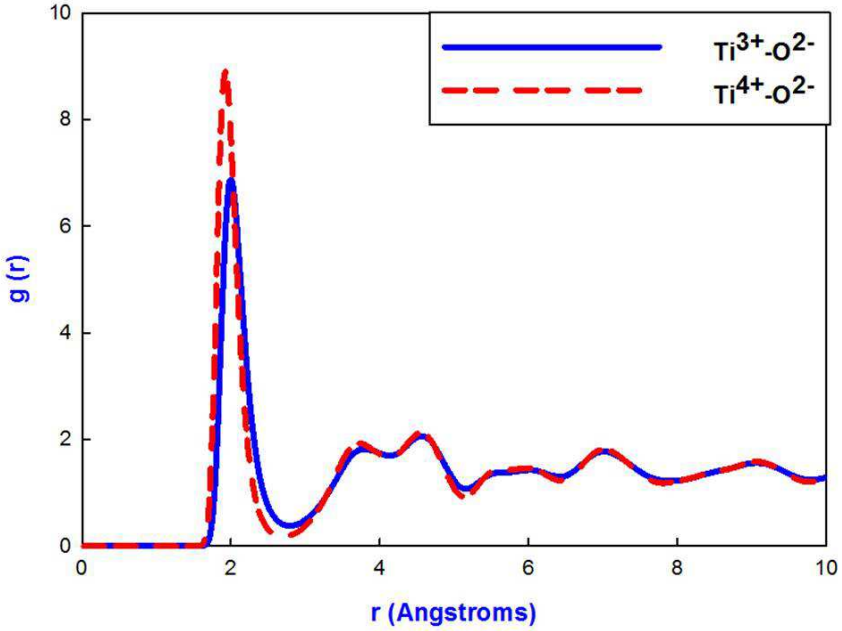

E4: Total RDFs of the bulk TiO_2 with 50 lithium atoms after recrystallisation at 2000 K.

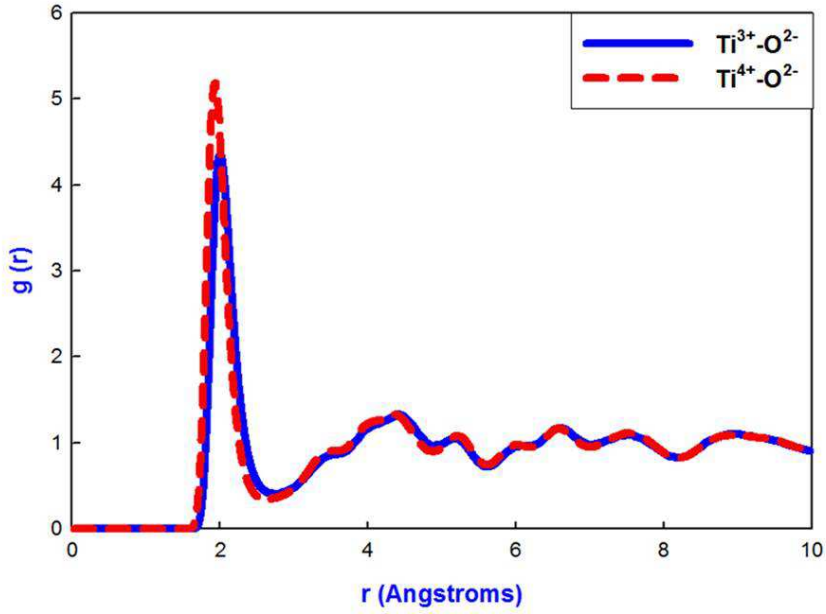

E5: Total RDFs of the bulk TiO_2 with 100 lithium atoms after recrystallisation at 2000 K.

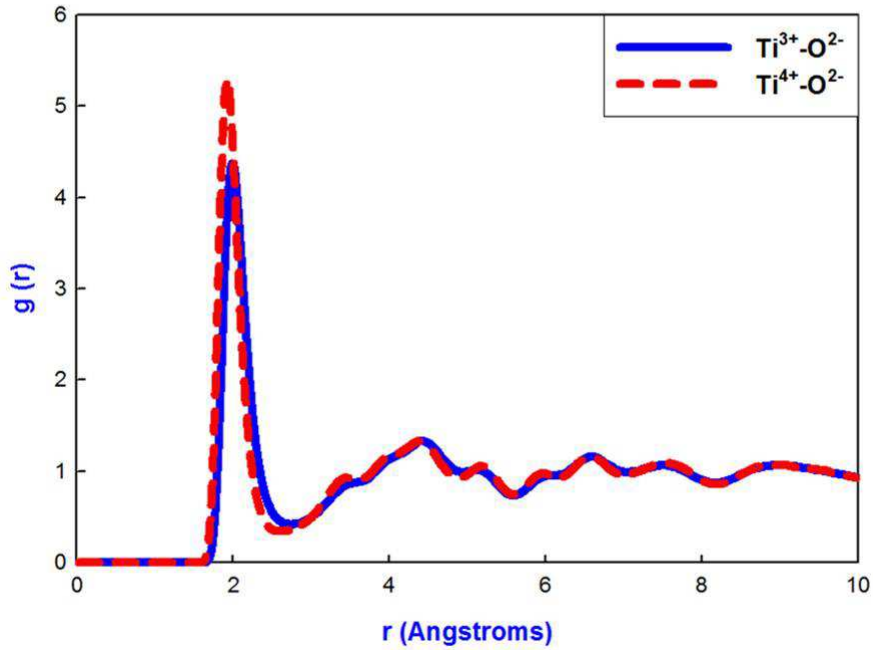

E6: Total RDFs of the bulk TiO_2 with 300 lithium atoms after recrystallisation at 2000 K.

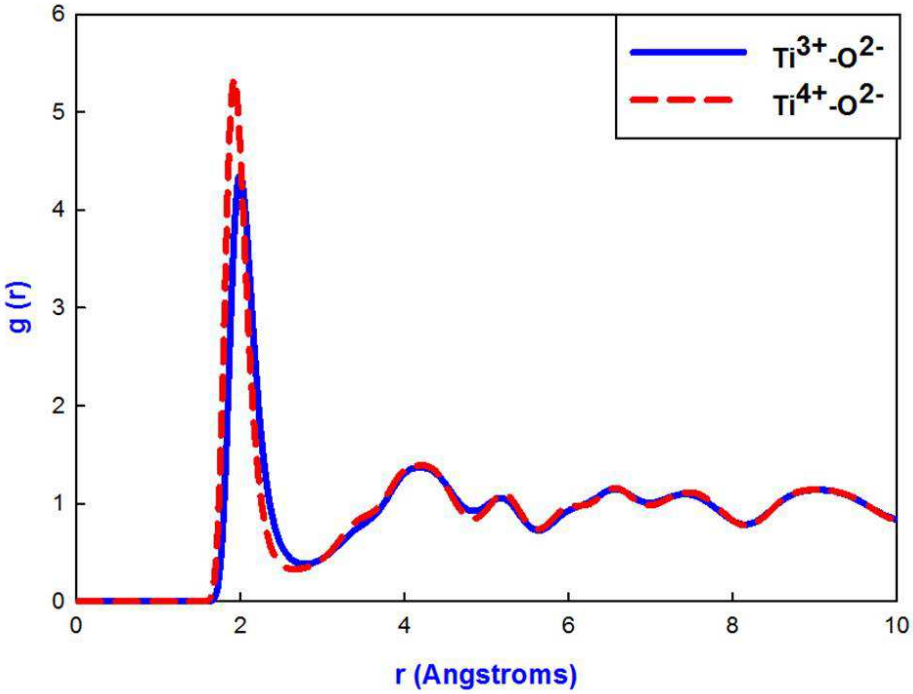

E7: Total RDFs of TiO_2 for the Ti^{3+}-O^{2-} interaction, at different temperatures, in the 66 Å cooled nanoporous structure, with 50 lithium atoms.

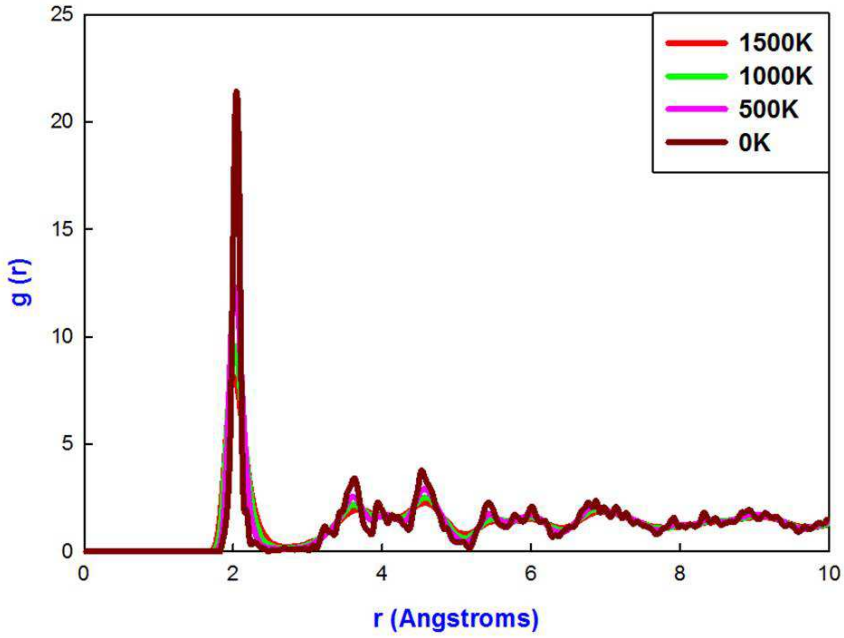

E8: Total RDFs of TiO_2 for the Ti^{4+}-O^{2-} interaction, at different temperatures, in the 66 Å cooled nanoporous structure, with 50 lithium atoms.

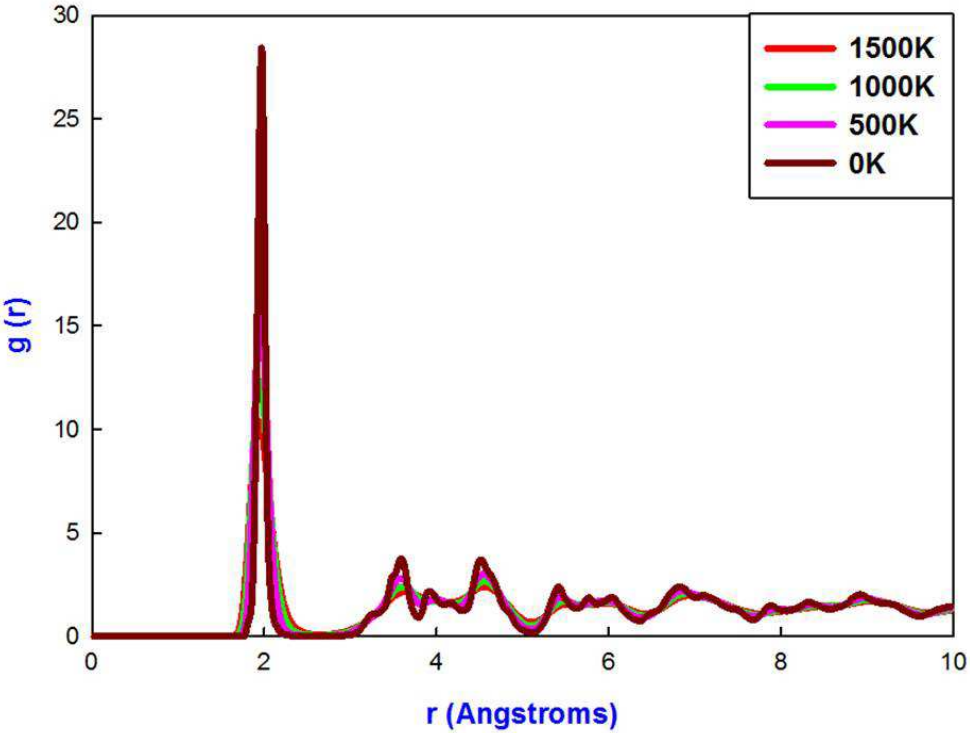

E9: Total RDFs for the Ti^{3+}-O^{2-} interaction, at different temperatures, in the 66 Å cooled TiO_2 nanoporous structure, with 100 lithium atoms.

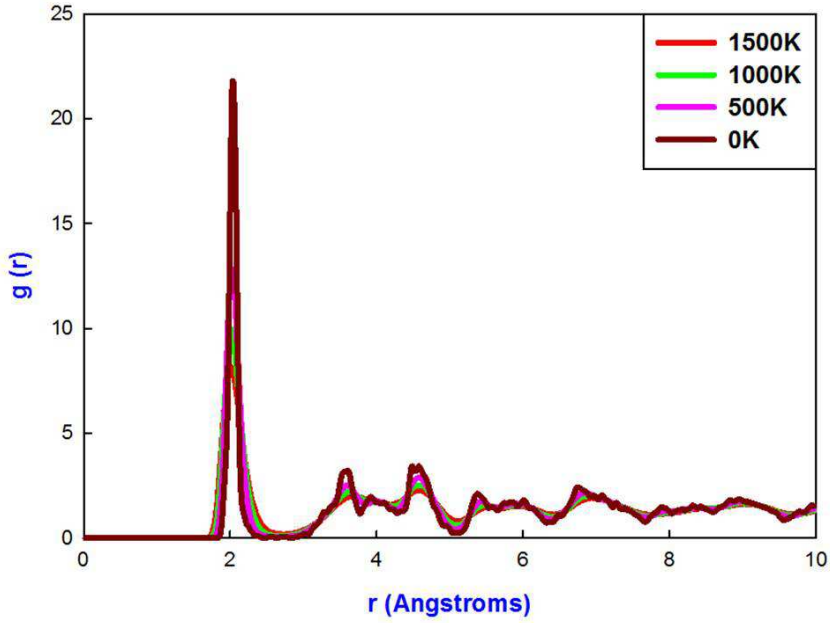

E10: Total RDFs for the Ti^{4+}-O^{2-} interaction, at different temperatures, in the 66 Å cooled TiO_2 nanoporous structure, with 100 lithium atoms.

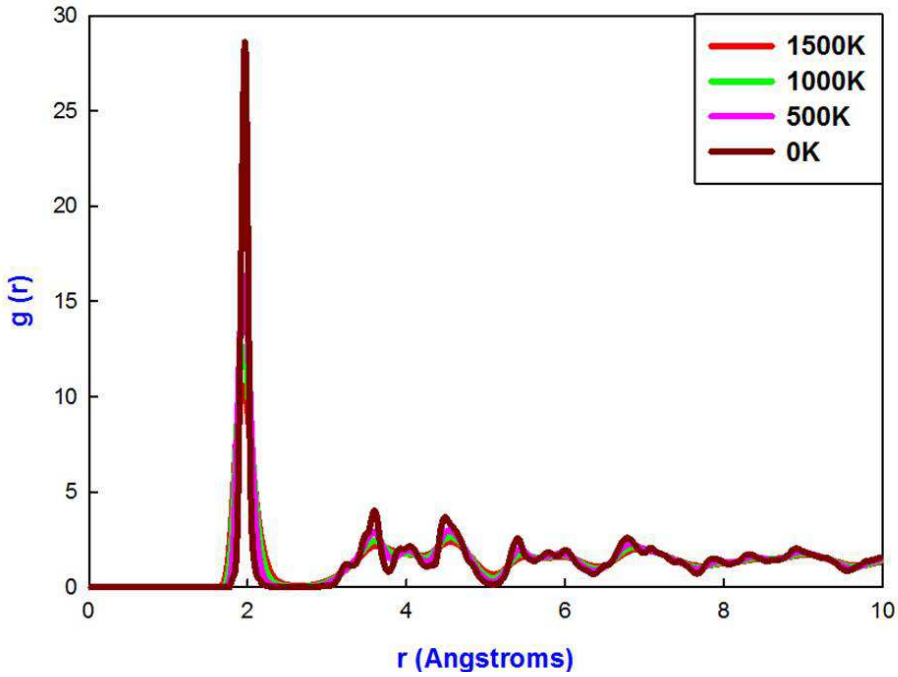

E11: Total RDFs for the Ti^{3+}-O^{2-} interaction, at different temperatures, in the 66 Å cooled TiO_2 nanoporous structure, with 300 lithium atoms.

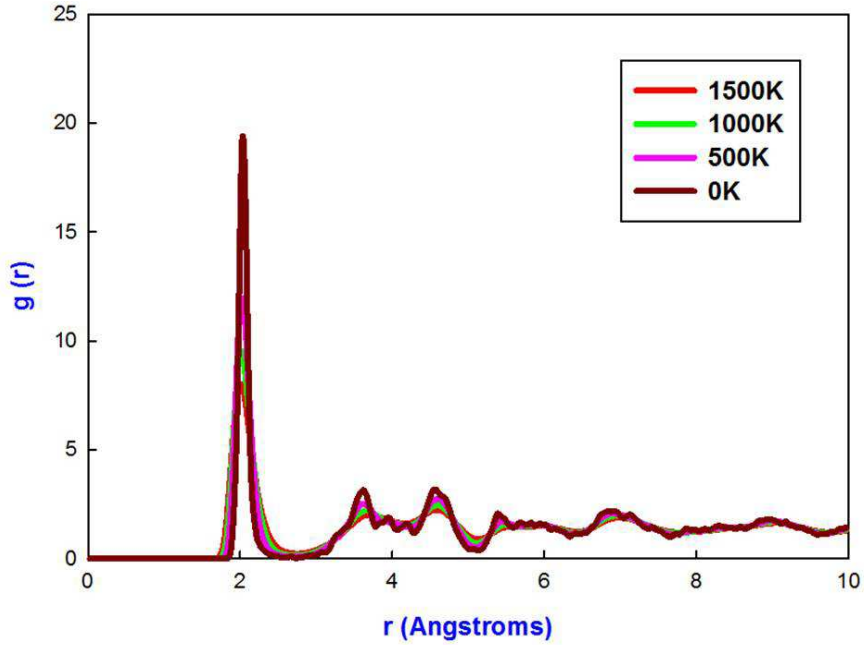

E12: Total RDFs for the Ti^{4+}-O^{2-} interaction, at different temperatures, in the 66 Å cooled TiO_2 nanoporous structure, with 300 lithium atoms.

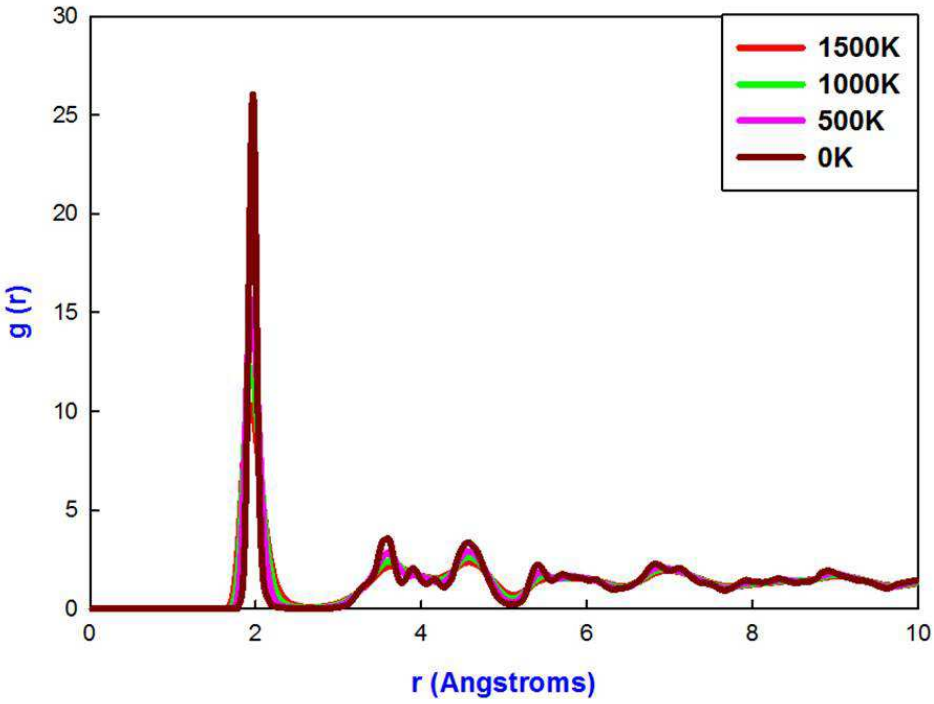

E13: Total RDFs for the Ti^{3+}-O^{2-} interaction, at different temperatures, in the cooled bulk structure, with 50 lithium atoms.

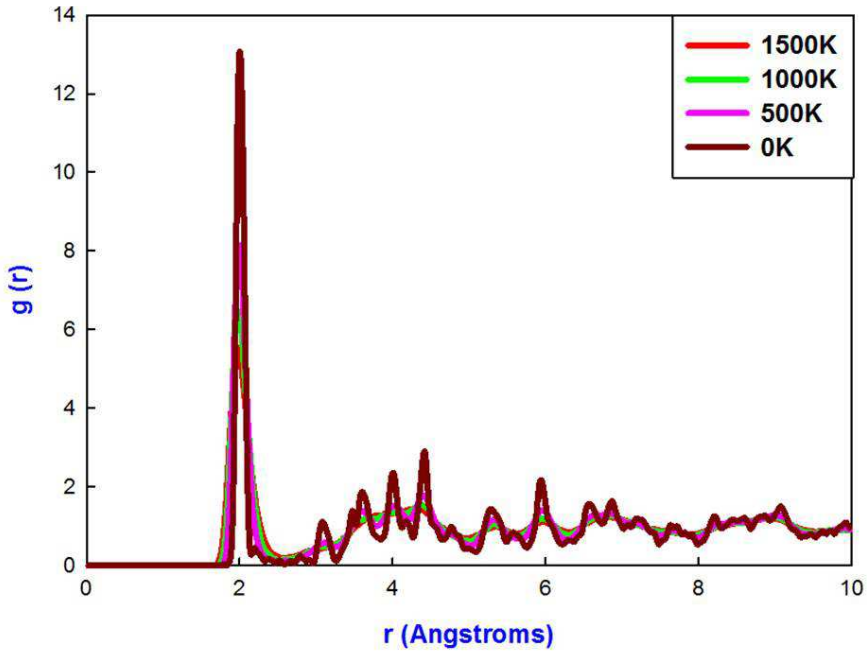

E14: Total RDFs for the Ti^{4+}-O^{2-} interaction, at different temperatures, in the cooled bulk TiO_2, with 50 lithium atoms.

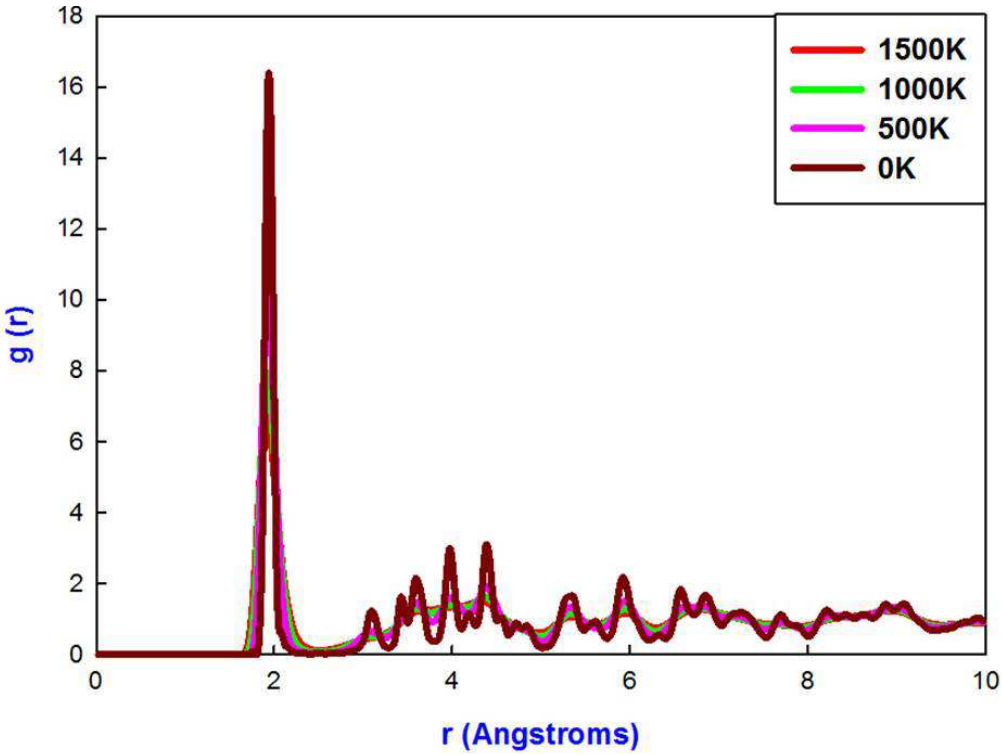

E15: Total RDFs for the Ti^{3+}-O^{2-} interaction, at different temperatures, in the cooled bulk structure, with 100 lithium atoms.

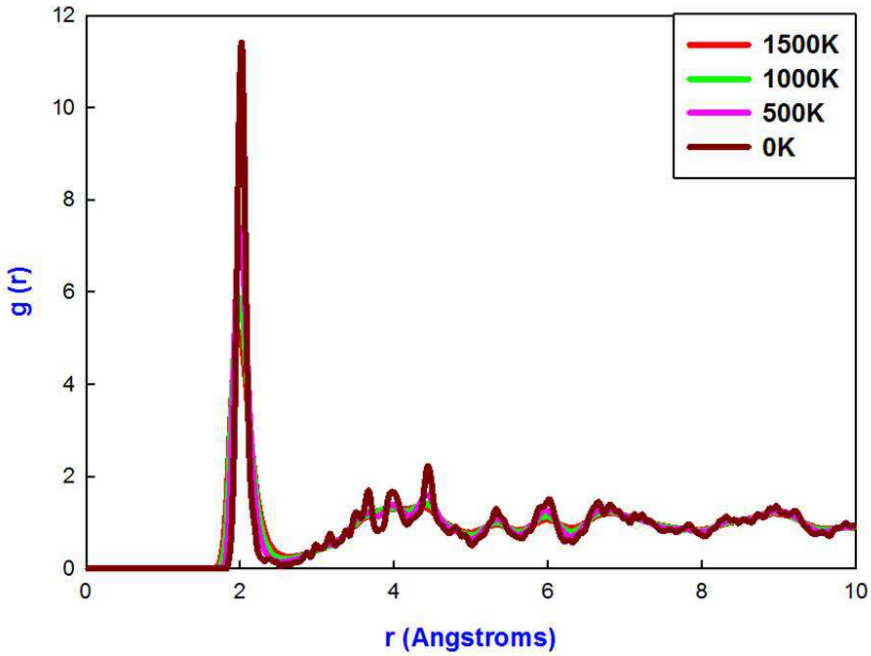

E16: Total RDFs for the Ti^{4+}-O^{2-} interaction, at different temperatures, in the cooled bulk structure, with 100 lithium atoms.

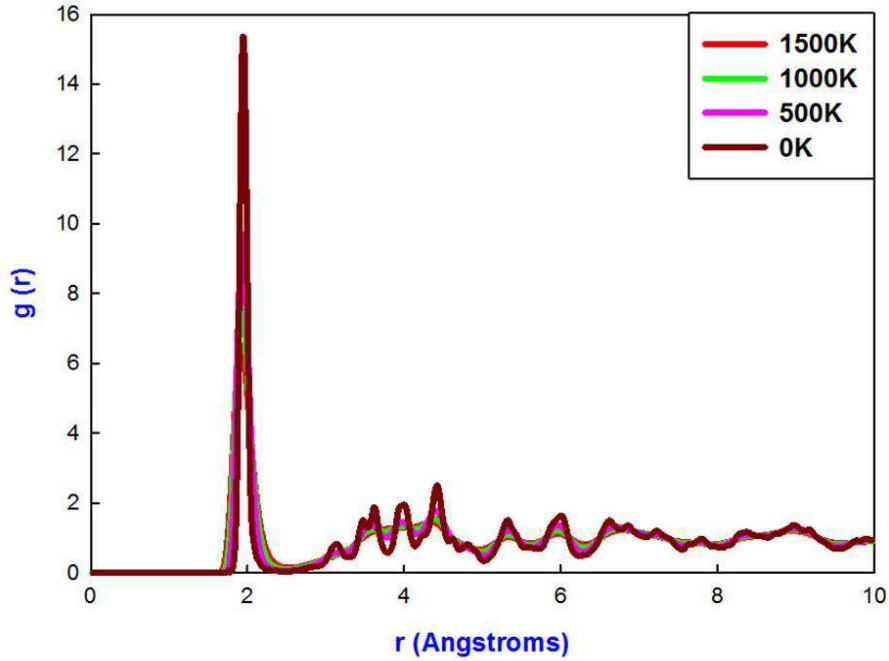

E17: Total RDFs for the Ti^{3+}-O^{2-} interaction, at different temperatures, in the cooled bulk structure, with 300 lithium atoms.

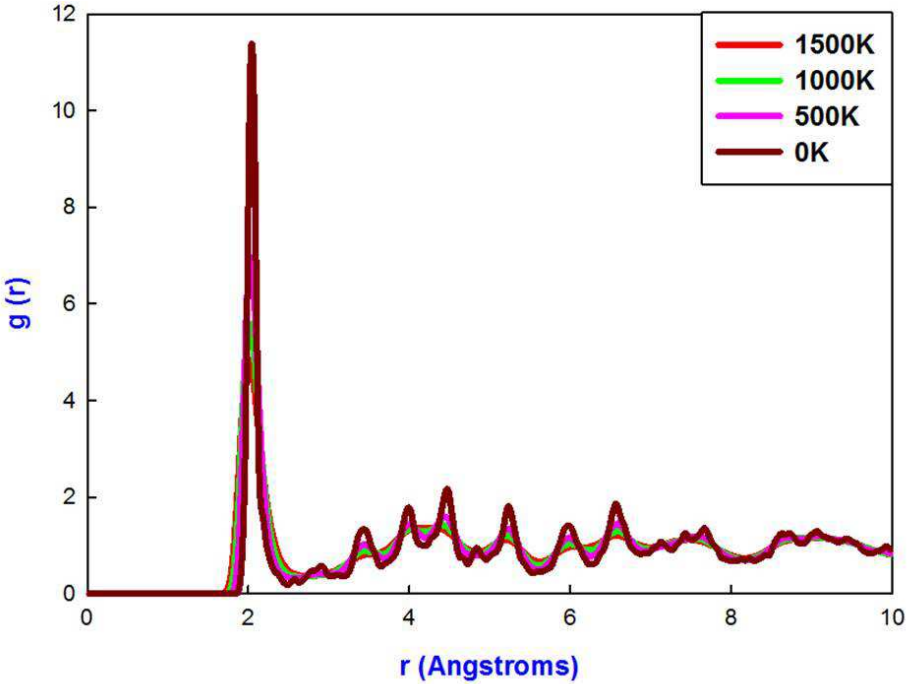

E18: Total RDFs for the Ti^{4+}-O^{2-} interaction, at different temperatures, in the cooled bulk structure, with 300 lithium atoms.